

ALMA MATER STUDIORUM
UNIVERSITÀ DEGLI STUDI DI BOLOGNA

Dipartimento di Fisica e Astronomia

DOTTORATO DI RICERCA IN
ASTROFISICA

Ciclo XXXI

**Mapping of the intra-cluster medium
out to the virial radius**

Dottorando:

Vittorio Ghirardini

Supervisore:

Stefano Etori

Coordinatore:

Francesco R. Ferraro

Esame finale anno 2019

Settore Concorsuale: 02/C1 - Astronomia, Astrofisica, Fisica della Terra e dei Pianeti

Settore Scientifico Disciplinare: FIS/05 - Astronomia e Astrofisica

Science is the belief in the ignorance of experts

R.P. Feynman

ABSTRACT

In this thesis, I study the thermodynamic properties of the intracluster medium out to the virial radius, making use of a unique combination of dedicated *XMM-Newton* exposures and *Planck* maps, thus exploiting the capabilities of multi-wavelength observations, to constrain at an unprecedented level the thermodynamic properties in a complete sample of galaxy clusters. I will explore in detail their self-similar properties, their radial dependence, and their implication. This work provides an important legacy value for any future studies of galaxy cluster until the next generation of X-ray telescopes comes along.

- In Chapter 1 the present knowledge on the observable properties of galaxy clusters in the literature are presented within a well defined cosmological framework.
- In Chapter 2 a review of the current understanding of the thermodynamic properties of the intracluster medium is introduced, with possible selection biases.
- In Chapter 3, I present the X-COP project that has been the focus of the PhD work, with sample selection, the main goals, and the main sample properties. I will also introduce the reader to the X-COP like analysis, with applications of novel techniques.
- In Chapter 4 I will present the analysis of Abell 2319 as a pilot study for X-COP.
- In Chapter 5 the results for the entire X-COP sample regarding the main information on the thermodynamic properties and their intrinsic scatter are presented.
- In Chapter 6 the results on the hydrostatic mass profiles in X-COP are presented, exploring several mass models and comparing with other mass probes.
- In Chapter 7 the contamination from non thermal pressure support in the X-COP sample is estimated, comparing the mass bias with the *Planck* cluster count bias.

- In Chapter 8 the polytropic state of the intracluster medium in the X-COP cluster sample and some important consequences are presented.
- In Chapter 9 I will explore another project performed on a sample of high redshift clusters observed with *Chandra*, investigating their evolution upon redshift.
- In Chapter 10 I will summarize the main finding of this thesis, draw the final conclusions, and present a few future scenario I am involved in.
- In Chapter 11 I will present the report on the activities carried out during the PhD.

TABLE OF CONTENTS

Abstract	v
1 Introduction	1
1.1 Cosmological framework	3
1.2 Formation and evolution of galaxy clusters	6
1.2.1 Growth of structure	7
1.2.2 Spherical collapse model	8
1.2.3 Hydrostatic equilibrium	9
1.3 Observational properties of galaxy clusters	10
1.3.1 Galaxy clusters in optical	11
1.3.2 Galaxy clusters in X-rays	12
1.3.3 Galaxy clusters in Microwaves	12
1.3.4 Galaxy clusters in Radiowaves	13
1.4 Mass measurement of clusters	14
1.4.1 Velocity dispersion	14
1.4.2 Lensing	14
1.4.3 Thermodynamics	15
2 Physics of the intracluster medium	17
2.1 Selection effects	19
2.2 Thermodynamic properties	22
2.2.1 Density	23
2.2.2 Temperature	24
2.2.3 Pressure	25

2.2.4	Entropy	26
2.2.5	Gas fraction	27
2.2.6	Chemistry	28
2.2.7	The polytropic state of the ICM	29
3	The XMM Cluster Outskirts Project (X-COP)	31
3.1	The X-COP cluster sample	33
3.2	<i>XMM-Newton</i> data analysis	35
3.2.1	Data reduction	36
3.2.2	Image extraction and preparation	37
3.2.3	Point source subtraction	38
3.2.4	Surface brightness profiles	38
3.2.5	Spectral extraction	39
3.2.6	Spectral modeling	40
3.3	Non-X-ray background modelling	41
3.3.1	Model	42
3.3.2	Blank-sky dataset and modelling	42
3.4	<i>Planck</i> data analysis	43
3.4.1	Data reduction	44
4	The XMM Cluster Outskirts Project (X-COP): Thermodynamic properties of the Intracluster Medium out to R_{200} in Abell 2319	51
4.1	Introduction	53
4.2	<i>XMM-Newton</i> Analysis	53
4.2.1	Spatial analysis	54
4.2.2	Spectral analysis	56
4.2.3	Results of the spectral fitting	57
4.2.4	Comparison with <i>Chandra</i> data	58
4.3	<i>Planck</i> analysis	59
4.4	Joint X-ray–SZ analysis of the thermodynamic properties	61
4.4.1	Clumpiness profile	61
4.4.2	Temperature profile	62
4.4.3	Systematic uncertainties on the temperature profile	63
4.4.4	Pressure profile	65
4.4.5	Hydrostatic mass	66
4.4.6	Systematic uncertainties on the hydrostatic mass	69
4.4.7	Likelihood for the mass reconstruction	70

4.4.8	Entropy profile	71
4.5	Analysis in azimuthal sectors	73
4.5.1	Thermodynamic properties	73
4.5.2	Azimuthal scatter and clumpiness	75
4.5.3	Thermodynamic quantities in azimuthal sectors	79
4.6	Characterizing the hydrostatic bias	83
4.6.1	Gas mass fraction and the non-thermal contribution	83
4.6.2	Effects of the hydrostatic bias on the rescaled profiles	86
4.7	Summary and conclusions	88
5	The universal thermodynamic properties of the intracluster medium over two decades in radius in the X-COP sample	91
5.1	Introduction	93
5.2	Dataset and analysis procedures	93
5.2.1	The X-COP project	93
5.2.2	<i>XMM-Newton</i> data analysis	93
5.2.3	Deprojection and gas density profiles	93
5.2.4	<i>Planck</i> data analysis	96
5.2.5	Consistency between X-ray and SZ pressure measurements	96
5.2.6	Comparison between MILCA and forward-modeling pressure profiles	97
5.2.7	Mass estimates	98
5.3	Thermodynamic properties	99
5.3.1	Fitting procedure	99
5.3.2	Density	100
5.3.3	Pressure	104
5.3.4	Temperature	108
5.3.5	Entropy	111
5.3.6	Scatter	115
5.3.7	Mass-induced scatter in thermodynamic profiles	116
5.3.8	CC vs NCC	118
5.4	Discussion	125
5.4.1	Systematic uncertainties	125
5.4.2	Regular outskirts	126
5.4.3	Self-similarity of the profiles	128
5.5	Conclusion	129

6	Hydrostatic mass profiles in X-COP galaxy clusters	131
6.1	Introduction	133
6.2	The total gravitating mass with the Hydrostatic Equilibrium Equation . . .	133
6.2.1	Comparison among different mass models with the <i>backward</i> method	135
6.2.2	Reference mass model: <i>backward</i> method with NFW mass model .	137
6.2.3	Comparison among different methods and systematic errors	140
6.3	Comparison with mass estimates from scaling laws, weak lensing and galaxy dynamics	143
6.4	Comparison with predictions from the Emergent Gravity scenario and MOND	145
6.5	Conclusions	146
7	Non-thermal pressure support in X-COP galaxy clusters	149
7.1	Introduction	151
7.2	Data analysis	151
7.2.1	Hydrostatic masses and gas fraction	151
7.3	Methodology	152
7.3.1	Parameters of the universal gas fraction	152
7.3.2	Baryon depletion factor	153
7.3.3	Stellar fraction	154
7.3.4	Cosmological parameters and estimated universal gas fraction . . .	155
7.3.5	Non-thermal pressure fraction	156
7.4	Results	157
7.4.1	Non-thermal pressure fraction in X-COP clusters	157
7.4.2	Comparison with <i>Planck</i> SZ masses	161
7.5	Discussion	163
7.5.1	Systematic uncertainties	163
7.5.2	Implications on the thermalization of the ICM	164
7.5.3	Implications for cosmology	166
7.6	Conclusion	167
8	The polytropic state of the intracluster medium in the X-COP sample	169
8.1	Introduction	171
8.2	The polytropic equation	171
8.2.1	Relations between gas pressure, gas density and radius	172
8.2.2	Functional form for pressure against density	175
8.2.3	Application of the functional form $P(n)$ in mass reconstruction . . .	175
8.3	A polytropic NFW model for the gas	177

8.3.1	NFW polytropic model with $\Gamma(r)$	181
8.3.2	Derivation of $\Gamma(r)$	182
8.4	Conclusions	184
9	Entropy and pressure profiles in X-ray galaxy clusters at $z > 0.4$	185
9.1	Introduction	187
9.2	The method to reconstruct $K(r)$ and $P(r)$	187
9.3	Data Analysis	190
9.3.1	Fitting procedure for the entropy profile	191
9.3.2	No rescaling	193
9.3.3	Rescaling using K_{500}	194
9.3.4	Rescaling using the gas fraction	195
9.4	Discussion	198
9.4.1	Self-similarity	198
9.4.2	Angular resolution effect	199
9.4.3	Bimodality	200
9.4.4	Evolution with redshift	201
9.4.5	Pressure	202
9.4.6	Polytropic index	205
9.5	Conclusion	208
10	Summary and Conclusions	209
10.1	Summary	211
10.2	Conclusions	213
10.3	Work produced	215
11	Report on the activities	
	carried out during the PhD	217
11.1	Research Activities	219
11.2	Workshops, conferences, and meetings	220
11.3	Talks	220
11.4	Periods spent Abroad	221
11.5	Schools and internal courses	221
11.6	Publications	221
	References	223
	List of figures	251

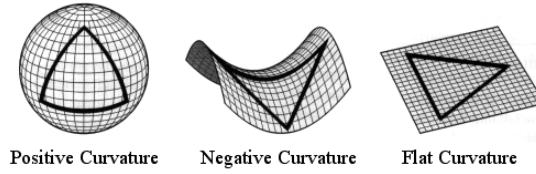
INTRODUCTION

1.1 Cosmological framework

In an isotropic and homogeneous Universe, which is either contracting or expanding, the general form of the metric is described by the Friedmann–Lemaître–Robertson–Walker (FLRW) metric.

$$ds^2 = c^2 dt^2 - a^2(t) \left(\frac{dr^2}{1 - kr^2} + r^2(d\theta^2 + \sin^2 \theta d\phi^2) \right) \quad (1.1)$$

where $a(t)$ is the scale factor describing the evolution of the universe and k is the curvature parameter, which can be either positive, zero, or negative, as schematically illustrated here:



In general relativity the dynamic of the Universe is described by the Einstein equations, which illustrate how matter changes the space-time geometry of the Universe

$$-\frac{8\pi G}{c^4} T^{\mu\nu} = G^{\mu\nu} + \Lambda g^{\mu\nu} \quad (1.2)$$

where $T^{\mu\nu}$ is the energy-momentum tensor. For a perfect fluid, characterized only by its density ρ and its pressure p , the energy-momentum tensor takes the following form:

$$T^{\mu\nu} = \left(\rho + \frac{p}{c^2} \right) u^\mu u^\nu - p \eta^{\mu\nu} \quad (1.3)$$

where u^μ is the 4-vector velocity field, and $\eta^{\mu\nu}$ is the Minkowski metric, $\eta^{\mu\nu} = \text{diag}(1, -1, -1, -1)$. Thus in the reference frame at rest with respect to the perfect fluid, $T^{\mu\nu}$ takes the matrix form

$$T^{\mu\nu} = \begin{bmatrix} \rho & 0 & 0 & 0 \\ 0 & p & 0 & 0 \\ 0 & 0 & p & 0 \\ 0 & 0 & 0 & p \end{bmatrix}$$

Therefore, the Einstein equations, Eq. (1.2) are expressed by the two Friedmann's equations

$$H^2 = \left(\frac{\dot{a}}{a} \right)^2 = \frac{8\pi G}{3} \rho - \frac{kc^2}{a^2} + \frac{\Lambda c^2}{3} \quad (1.4)$$

$$\dot{H} + H^2 = \frac{\ddot{a}}{a} = -\frac{4\pi G}{3} \left(\rho + 3\frac{p}{c^2} \right) + \frac{\Lambda c^2}{3} \quad (1.5)$$

The Hubble parameter, defined by $H = \frac{\dot{a}}{a}$, measures the expansion rate of the Universe. Combining the two Friedmann's equations it is possible to compute the formula for energy conservation in this cosmological framework.

$$\dot{\rho} + 3\frac{\dot{a}}{a} \left(\rho + \frac{p}{c^2} \right) = 0 \quad (1.6)$$

However generally in the literature it is preferred to use only the first Friedmann equation, Eq. (1.4), and combine it with an equation of state

$$p = \omega \rho c^2 \quad (1.7)$$

where ω is a constant which is usually called itself "equation of state". In general for every ω , we can find the evolution, as function of the scale factor a , for the density by substituting Eq. (1.7) in Eq. (1.6):

$$\rho = \rho_0 \cdot a^{-3(1+\omega)} \quad (1.8)$$

where $\rho_0 \equiv \rho$ when $a = 1$, i.e. at present time we measure the density ρ_0 . In particular for cold matter, i.e. when $p \ll \rho c^2$ determines $\omega = 0$, the scaling of its matter density goes with $\rho_m \propto a^{-3}$. On the contrary in the case of radiation (or ultra hot matter), i.e. when $p = \frac{\rho c^2}{3}$ implies $\omega = 1/3$, its density scales with $\rho_r \propto a^{-4}$. Moreover we define the following densities

$$\rho_\Lambda = \frac{\Lambda c^2}{8\pi G} \quad \text{and} \quad \rho_k = \frac{3kc^2}{8\pi G} \quad \text{and} \quad \rho_c = \frac{3H_0^2}{8\pi G} \quad \text{and} \quad \Omega_x = \frac{\rho_x}{\rho_c} \quad (1.9)$$

where ρ_c is the critical density of the Universe, and the subscript "x" indicates the specific density we are referring to (matter, radiation, dark energy, curvature).

Thus the first Friedmann equation, Eq. 1.4, can be rewritten as:

$$E^2(z) = \left(\frac{H}{H_0} \right)^2 = \Omega_m a^{-3} + \Omega_r a^{-4} + \Omega_k a^{-2} + \Omega_\Lambda \quad (1.10)$$

Finally, considering that the expansion of the universe, governed by the scale factor a , produces a redshift in the spectrum of photons $z = \frac{\Delta\lambda}{\lambda} = (1+a)^{-1}$, we can write the first Friedmann equation as:

$$E^2(z) = \left(\frac{H}{H_0} \right)^2 = \Omega_m (1+z)^3 + \Omega_r (1+z)^4 + \Omega_k (1+z)^2 + \Omega_\Lambda \quad (1.11)$$

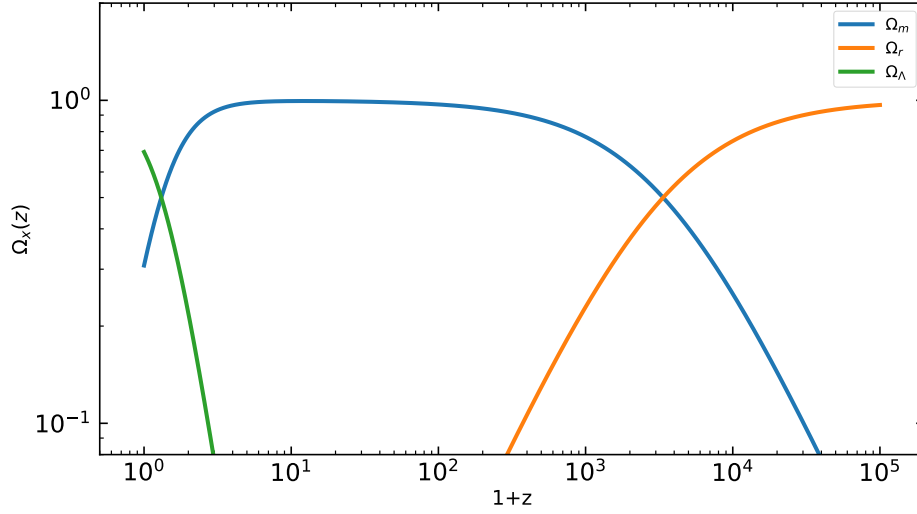


Fig. 1.1 Evolution of the energy densities with redshift. The blue, orange, and green lines represents the evolution of the matter density Ω_m , the radiation density Ω_r , and the dark energy density Ω_Λ components respectively in a Λ CDM cosmological framework with parameters as measured by *Planck* (Planck Collaboration et al., 2016e).

In Fig. 1.1 the evolution of each of these components with redshift are displayed, where $\Omega_x(z)$ are simply the value at present time multiplied by their evolution with redshift and renormalized by $E^2(z)$:

$$\Omega_m(z) = \Omega_m \frac{(1+z)^3}{E^2(z)}, \quad \Omega_r(z) = \Omega_r \frac{(1+z)^4}{E^2(z)}$$

$$\Omega_k(z) = \Omega_k \frac{(1+z)^2}{E^2(z)}, \quad \text{and} \quad \Omega_\Lambda(z) = \Omega_\Lambda \frac{1}{E^2(z)}$$

In the concordance model, or Λ CDM model, the aforescribed cosmological parameters take the values implied by observations of the cosmic microwave background (CMB), which are found by *Planck* (Planck Collaboration et al., 2016e) to be

$$\left\{ \begin{array}{l} H_0 = 67.8 \pm 0.9 \text{ km s}^{-1} \text{Mpc}^{-1} \\ \Omega_m = 0.308 \pm 0.012 \\ \Omega_\Lambda = 0.692 \pm 0.012 \\ |\Omega_k| < 0.005 \\ \Omega_r = (9.15 \pm 0.36) \cdot 10^{-5} \\ \omega = -1.006 \pm 0.045 \end{array} \right. \quad (1.12)$$

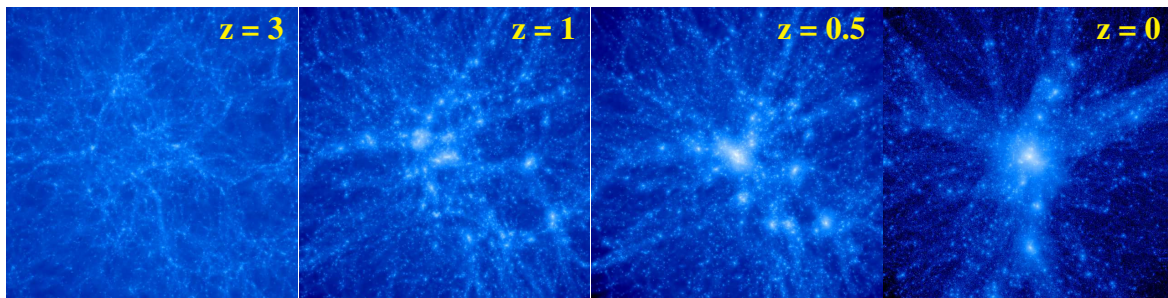


Fig. 1.2 Evolution of a dark matter density field around a cluster.

1.2 Formation and evolution of galaxy clusters

In the hierarchical structure formation scenario, galaxy clusters grow through a sequence of mergers and accretion of smaller systems from the primordial density fluctuations to form the massive structures we observe today. Their growth is driven mainly by gravity, therefore by the dark matter that dominates the gravitational potential, thus the formation and evolution can be approximated by models of dissipationless dark matter collapse, predicting correlations between basic cluster properties. One of the most remarkable and successful model is the self-similar model of clusters (Kaiser, 1986), that despite its simplicity is able to reproduce several of the observed properties.

Kaiser (1986) describe the thermodynamics of the intracluster medium (ICM) as being entirely determined by gravitational processes, assuming spherical symmetry and hydrostatic equilibrium. In this model, clusters with the same mass and at the same redshift are identical, with observable properties scaling with mass and redshift following well defined power laws

$$\begin{cases} L_X \propto M^{4/3} E(z)^{7/3} \\ kT \propto M^{2/3} E(z)^{2/3} \end{cases}$$

The complete description of cluster formation and evolution requires modeling the non-linear processes during the gravitational collapse, and the correct treatment of the dissipative baryonic component (see Kravtsov and Borgani, 2012, for a detailed review on the formation and evolution of galaxy clusters). Pristine gas falls into the dark matter potential well and is progressively heated to high temperatures of $10^7 - 10^8$ K, such that the majority of the baryons end up in the form of a fully ionized plasma, the intracluster medium. This low entropy gas falls toward the centre of the cluster, getting compressed up to a point when cooling becomes efficient; this feeds star formation and accretion on the supermassive black

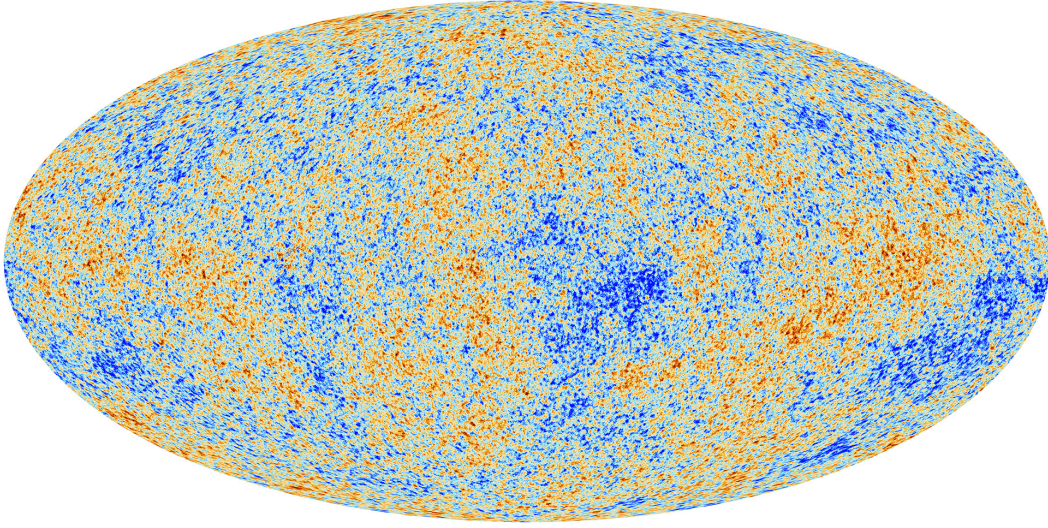


Fig. 1.3 The anisotropies of the cosmic microwave background as observed by *Planck*.

hole, which in turn results in an energetic feedback due to supernovae (SNe) or active galactic nuclei (AGN) activity.

1.2.1 Growth of structure

In 1965 Penzias and Wilson detected a signal coming from all over the sky, with spectral feature very close to a perfect black body spectrum with temperature of about 2.7 K, thus with emission peaking in the microwaves (from Wien's displacement law $\lambda_{max} \approx \frac{2.9 \cdot 10^{-3} \text{ K m}}{T}$). Through the years more refined instruments have looked at this cosmic microwave background (CMB), finding that the temperature is not uniform, but fluctuates around the mean by a fractional difference of only 10^{-5} . Fig. 1.3 shows these temperature fluctuations as observed by *Planck*. These tiny temperature fluctuations correspond to regions of slightly different densities, which represent the seeds of all future structures. Once this primordial density fluctuations are set, they begin to grow linearly. These density fluctuations are characterized by a density contrast

$$\delta(\mathbf{x}) = \frac{\rho(\mathbf{x}) - \bar{\rho}_m}{\bar{\rho}_m} \quad (1.13)$$

where $\bar{\rho}_m$ is the mean mass density of the Universe.

Assuming that the statistical properties of the primordial density fluctuation are a uniform and isotropic Gaussian field, a power spectrum $P(k)$ is a complete statistical description of the initial perturbations. During the initial phase, each fluctuation mode $\delta(k)$ grow independently at the same rate, evolving according to the linear growth factor $D_+(a)$. Once the amplitude

of these fluctuation approaches the unity, the linear model fails at reproducing cluster growth, and further evolution requires numerical simulations with detailed astrophysical model for all the phenomena taking place.

1.2.2 Spherical collapse model

The simplest model for collapse is a uniform sphere slightly denser than the surrounding (Bertschinger, 1985). This perturbation initially expands alongside the rest of the Universe, however its gravitational attraction gradually slows, halts, and reverses the expansion. Then a cluster forms at the centre of this fluctuation.

In reality clusters do not form spherically symmetric, and of top of that the infalling matter clumps change the gravitational potential, such that the velocity of the infalling particles are randomized according to a Maxwellian distribution. This process leads to a sort of virial stationary equilibrium where the total kinetic energy is related to the total gravitational potential energy:

$$\sum_{i=1}^N m_i \mathbf{r}_i^2 = - \sum_{i=1}^N \mathbf{F}_i \cdot \mathbf{r}_i \quad (1.14)$$

where the left hand side of the equation is twice the total kinetic energy of a system, and the right hand side is the total potential energy for the system, which in the case of a uniform sphere of radius r and $M = \sum_i m_i$, solely described by the gravitational force, takes the form GM^2/r .

The virial theorem, Eq. (1.14), produces a natural boundary for clusters, the virial radius. Numerical simulations have shown that the particles within this radius have an isotropic direction for their velocity, while outside this radius the particles are preferentially infalling.

In the spherical collapse model in a matter-dominated Universe, the virial radius is characterized by a density contrast approximated by the following relation:

$$\Delta_v = 18\pi^2 + 82[\Omega_m(z) - 1] - 39[\Omega_m(z) - 1]^2 \quad (1.15)$$

where $\Omega_m(z)$ is the matter density at the redshift of formation (Bryan and Norman, 1998), which is defined from Eq. (1.11) as $\Omega_m(z) = \Omega_m \cdot \frac{(1+z)^3}{E(z)^2}$.

This definition of the outer boundary of clusters in a matter-dominated Universe has inspired alternative definition which do not depend on cosmology. A very common radius used in the literature is the radius within which the mean matter density is $200\rho_c$ (R_{200}), where the critical density ρ_c is defined in Eq. (1.9).

1.2.3 Hydrostatic equilibrium

On the other hand the dynamic of the accreting gas differs from the dynamic of the dark matter, in fact because the gas is collisional several processes are important, not only gravity. Thus, the physics driving the infall and the successive evolution is fairly complicated, thus requiring the aid of numerical simulation to understand the exact physics which shapes the ICM.

Numerical simulation generally find that after the collapse, the baryons form an accretion shock at large radii, which, similarly to the splashback radius for the dark matter component, represents a natural boundary for the baryonic component in galaxy clusters. Shi (2016) has studied how the accretion shock is related to the splashback radius in the self-similar spherical collapse model, finding how their location depends on the mass accretion rate, how both the location of the accretion shock and of the splashback radius moves inward increasing the mass accretion rate.

Following the collapse, the baryonic matter component follows a set of quasilinear hyperbolic equations, the Euler equations. These equations represents a fluid which conserves both mass, momentum, and energy. These are a particular solution of the Navier-Stokes equations with zero viscosity and zero thermal conductivity. Recently Lau et al. (2013) and Ota et al. (2018) have shown that by using Euler equations and the Gauss's Law it is possible to split the expression for the total mass as a sum of individual contributions, such that the true mass can be expressed as:

$$M_{true} = \underbrace{\frac{-R^2}{G \langle \rho_g \rangle} \nabla \langle P \rangle}_{M_{therm}} + \underbrace{\frac{-R^2}{G \langle \rho_g \rangle} \nabla \langle \rho \rangle \sigma^2}_{M_{rand}} + \underbrace{\frac{-R^2}{G} (\langle v \rangle_\rho \cdot \nabla) \langle v \rangle_\rho}_{M_{bulk}} + \underbrace{\frac{-R^2}{G} \frac{\partial \langle u_r \rangle_\rho}{\partial t}}_{M_{accel}} \quad (1.16)$$

where $\langle \dots \rangle$ represent the spatial average. M_{therm} is the mass term representing the thermal pressure support of the gas against gravity, M_{rand} is the support from the random motions of gas which represents turbulence, M_{bulk} is the support from the bulk motion of the gas, M_{accel} is the support due to temporal variations of the mean radial gas velocities, which is physically impossible to measure in observations.

However the final baryonic configuration is generally approximately described by the hydrostatic equilibrium equation, which is just the dominating M_{therm} component, in which at each point the pressure gradient is perfectly balanced by the local gravitational potential. Assuming spherical equilibrium this takes the form:

$$\frac{1}{\rho_g} \frac{dP}{dR} = - \frac{GM_{HE}(< R)}{R^2} \quad (1.17)$$

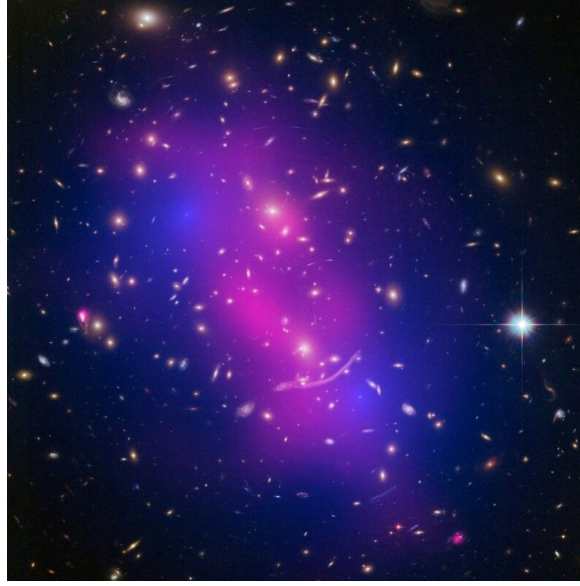


Fig. 1.4 Example of a multiwavelength observation of the galaxy cluster Abell 370. The component in luminous stars observed by *Hubble* is in yellow, with the blue the inferred distribution of dark matter through the effect of gravitational lensing, while the purple region shows the X-ray view of this cluster by *Chandra*.

where ρ_g is the gas density, and P is the gas thermal pressure. By further assuming that the gas follows the equation of an ideal gas (i.e. $P = n_e T$), the mass within a given radius can be expressed as

$$M_{HE}(< R) = -\frac{Rk_B T}{G\mu m_p} \left[\frac{d \log \rho_g}{d \log R} + \frac{d \log T}{d \log R} \right] \quad (1.18)$$

1.3 Observational properties of galaxy clusters

The study of galaxy clusters starts with Messier and Hershel, when at the end of the 17th century they found large concentration of “nebulae” in the constellation of Virgo and Coma.

The tendency of galaxy to cluster become evident once the number of known galaxies increased, and the number of clusters continued to accumulate. Definitive cluster catalogues were then compiled by G. Abell and collaborators (Abell, 1958; Abell et al., 1989), founding our modern understanding of clusters physics. Nowadays cluster catalogues account for thousands of galaxy clusters, and discoveries in the optical from concentration of galaxies in the sky, like the recent Sloan Digital Sky Survey (SDSS, Hao et al., 2010), are not the only way clusters are discovered. In fact, because the gas is heated to very high temperature, the ICM is a fully ionized plasma, thus is able to emit in X-ray via bremsstrahlung radiation,

allowing to detect directly the emission from clusters hot gas, detected first by UHURU X-ray satellite (Cavaliere et al., 1971; Forman et al., 1972; Kellogg et al., 1972), and more recently e.g. from *Rosat* (Voges et al., 1999) or from *XMM-Newton* (Snowden et al., 2008). On top of that, the CMB photons crossing galaxy clusters are subject to inverse Compton scattering off the hot ICM electrons, thus producing a spectral shift in the CMB signal, the Sunyaev-Zel'dovich (SZ) effect (Sunyaev and Zeldovich, 1972), that is detectable at microwave wavelengths.

Figure 1.4 shows an example of a multiwavelength observations of a galaxy clusters, using X-ray, optical, and lensing observations, thus probing different properties of galaxy clusters, the gas, the galaxies, and the total matter (i.e. dark matter plus baryons) respectively.

1.3.1 Galaxy clusters in optical

Identifying a cluster in optical follows the idea that in our Universe light traces mass, thus the total optical luminosity of a cluster is a probe of cluster's mass. This information is encoded in Abell's catalogue in categories of "richness", by counting the excess of galaxies brighter than a certain magnitude limit. This method is subject to projection effect, in fact presence of structure along the line of sight can mimic the effect of a cluster when projected on the plane of the sky.

An extension of Abell's method was possible with more advanced instrument which are able to observe with multiple filters. In fact galaxies inside a cluster are generally redder than the field, i.e. early-type galaxies where star formation is suppressed. Postman et al. (1996) have extended Abell's method adopting the color of galaxies as direct probe of clusters, carrying out a survey based on well-defined selection criteria which allow to produce meaningful statistical studies of the cluster population. However at very high redshift galaxies become redder due to cosmological redshift independently if they belong to a cluster or to galaxy field, therefore it is necessary to extend this technique to the near-infrared waveband in order to discover and identify galaxy clusters. The strength of this method was demonstrated by Stanford et al. (1997), finding a new galaxy cluster at $z = 1.27$.

Recently, the Sloan Digital Sky Survey (SDSS, Hao et al., 2010) have produced a very large catalog of optically selected clusters, detecting over 55.000 clusters. They have detected galaxy clusters using the clustering of member galaxies in the color-magnitude diagram in the red sequence. In fact this is unique for members galaxies, and is not present among field galaxies.

1.3.2 Galaxy clusters in X-rays

Clusters of galaxies are powerful X-ray sources because the majority of baryons are in the form of a very hot and diffuse gas embedded in a deep potential well generated and dominated by dark matter. At the temperature of $10^7 - 10^8$ K the gas is fully ionized and the free electrons emit thermal bremsstrahlung radiation produced by the deceleration of the electrons (see Rosati et al., 2002, for a complete review on the X-ray properties of galaxy clusters).

Extended X-ray emission from clusters was first observed in the Coma cluster in the 1970's (Forman et al., 1972; Gursky et al., 1971), correctly associating their emission spectra with thermal bremsstrahlung radiation. The rate at which the ICM radiates energy can be expressed in terms of a cooling function $\Lambda_c(T, Z)$ which depends on temperature T and metallicity Z , thus the emissivity is proportional to the product of the densities of the particles producing the bremsstrahlung radiation multiplied by this cooling function:

$$\epsilon_X \propto n_e n_H \Lambda_c(T, Z) \quad (1.19)$$

Therefore, because X-ray emission depends on density squared (given that the number density of hydrogen and electrons are proportional $n_H \sim n_e \cdot 1.2$), galaxy clusters stand out against less dense surrounding regions, reducing significantly any projection degeneracy.

Rosat, with its full sky coverage has produced the most complete catalogue of X-ray clusters (Voges et al., 1999), from which flux limited samples are built on (Böhringer et al., 2007). In the near future, *e-Rosita* (Borm et al., 2014; Merloni et al., 2012; Pillepich et al., 2018) is expected to increase by a factor of at least 100 the number of clusters detected in X-rays, thus opening a new perspective in the statistical studies of galaxy clusters.

1.3.3 Galaxy clusters in Microwaves

In the 70's, Sunyaev and Zeldovich predicted a specific spectral distortion in the cosmic microwave background (CMB) caused by the presence of the hot ICM gas, the so called SZ effect (Carlstrom et al., 2002; Sunyaev and Zeldovich, 1972).

A few decades later, with advanced telescopes like *Planck*, *South Pole Telescope* (SPT), and *Acatama Cosmology Telescope* (ACT), clusters are routinely observed via their thermal SZ signal, and new clusters are found using these new instruments. The surface brightness of the thermal SZ effect (tSZ) is proportional to the Compton y parameter:

$$y(r) = \frac{\sigma_T}{m_e c^2} \int P_e(l) dl \quad (1.20)$$

where the integral is computed along the line of sight, l , at the radius, r , from the centre; σ_T is the Thomson cross section, m_e the mass of the electron, and c the speed of light. The effect on the CMB temperature fluctuations is

$$\frac{\Delta T_{CMB}}{T_{CMB}} = f(v, T_e) \cdot y \quad (1.21)$$

where $f(v, T_e)$ encodes the frequency dependence, including relativistic correction depending on electron temperature Itoh et al. (1998). The thermal SZ effect depends linearly on the thermal electron pressure, thus it is a very important tool to probe the outermost parts of clusters, the outskirts. On the contrary the SZ effect has the downside of being prone to being affected by projection effects, given its linear dependency on the ICM density.

On top of this, when a galaxy cluster is moving with respect to the CMB rest frame, the CMB spectrum is Doppler shifted due to the bulk motion of the electrons in the ICM. This is the kinetic SZ effect (kSZ) which produces a change in the CMB temperature

$$\frac{\Delta T_{CMB}}{T_{CMB}} = -\frac{v_z}{c} \tau_e \quad (1.22)$$

where v_z is the cluster velocity along the line of sight, and τ_e is the total electron optical depth. However, this effect is much smaller than the thermal SZ effect, thus making it much harder to detect. Nevertheless recently there have been strong hints at the level of 4σ detection of this signal (Mroczkowski et al., 2012; Sayers et al., 2013).

1.3.4 Galaxy clusters in Radiowaves

Radio observations indicate that in galaxy clusters the presence of relativistic electrons (e.g. Willson, 1970) and large scale magnetic fields (e.g. Lazarian and Brunetti, 2011) produce extended diffuse synchrotron radiation.

Cluster mergers are thought to be the main responsible for the production of these relativistic electrons, in fact part of the energy involved within a merger is converted into turbulence, accelerating electrons to relativistic velocities, which are then visible in radio waveband as radio-halos and radio-relics (see Brunetti and Jones, 2014, for a review). Radio halos are generally connected with X-ray emission given they roundish shape centred onto the cluster centre. However radio relics are generally elongated and polarized and are found in the outer regions of galaxy clusters (Feretti et al., 2012), particularly recent studies have found their alignment with the presence of shocks, visible in X-ray, produced by the merger events, generating the observed arc shaped morphology (e.g. Akamatsu et al., 2013; Eckert et al., 2016b). The non-thermal components observed in galaxy clusters through radio

observations are therefore unique probes of the very energetic processes that are active and shape the ICM.

1.4 Mass measurement of clusters

In this section we briefly describe how the cluster mass can be estimated directly using different probes, going from optical measurements of velocity dispersion or lensing effect on background galaxies. Or how the thermodynamic properties can be used to estimate the hydrostatic mass.

1.4.1 Velocity dispersion

From observation of close galaxy clusters for which its possible to measure the radial velocities v_r of the member galaxies, then assuming a normal distribution for the galaxies in velocity space, the velocity dispersion σ_v can be estimated. From this measure, the mass of a galaxy cluster can be measured. As Zwicky (1933, 1937) have demonstrated, assuming the virial theorem, Eq. (1.14), the mass within a given radius R of a relaxed and isolated cluster is given by

$$M = \frac{3\sigma_v^2 R}{G} \quad (1.23)$$

that for the case of a $10^{14}M_\odot$ object, with a radius of 1 Mpc, produces a velocity dispersion of $\sigma_v \approx 660$ km/s. Zwicky correctly estimated that the cluster mass should be far greater than the total mass coming from the observed stars in the galaxies, first evidence of the presence of dark matter, a large amount of matter which is does not emit light.

Extensive measurements of redshift and velocities of many more galaxies allows to measure cluster masses more accurately and also as function of radius, enabling detailed studies of the dynamical state of clusters (Carlberg et al., 1997; Oegerle et al., 1995).

However galaxy cluster continue accreting material through cosmic web filaments, thus clusters are not in equilibrium and velocity dispersion with virial theorem is not sufficient to yield an exact cluster mass.

1.4.2 Lensing

In the paper of 1937 (Zwicky, 1937), Zwicky pointed out an alternative way of measuring the cluster masses: through the gravitational lensing effect that clusters have on background galaxies. However several decades passed before this method being feasible. Given the fact that gravity obeys Gauss's theorem, the lensing effect is sensitive only to the cluster mass

within a given radius, bending the trajectory of photons toward the cluster's centre. Therefore, by studying the shear distortion of a galaxy background field, is possible to measure cluster's masses within a given radius (see Bartelmann, 2010, for a complete review)

$$\hat{\alpha} = \frac{4GM}{c^2 R_{\perp}} \quad (1.24)$$

where $\hat{\alpha}$ is the deflection angle, and R_{\perp} is the impact parameter on the plane of the lens.

However this method is subject to projection effects, in fact limitations are superposition of other mass concentrations, in fact the integrated projected mass along the line of sight which is not part of the cluster can be on the order of $10^{14}M_{\odot}$, thus comparable to the cluster mass itself.

1.4.3 Thermodynamics

The mass of the ICM can be determined by knowing the thermodynamic properties, like density, temperature, and pressure, because, assuming hydrostatic equilibrium, see Eq. (1.17) and Eq. (1.18), these quantity are a direct probe of cluster masses (see Ettori et al., 2013a, for a complete review).

X-ray only observations are very powerful probe of the thermodynamical properties. In fact from surface brightness profiles extracted from images in a soft energy band, e.g. [0.5-2.0] keV typical for *Chandra* and [0.7-1.2] keV typical for *XMM-Newton* one can directly deproject and obtain the gas density profile (Eckert et al., 2016a; Ettori et al., 2010). Simultaneously, from the spectral shape observed in the detector, it is possible to estimate the gas temperature. Both density and temperature are usually extracted in several annuli around the centre of the cluster, however because density depends only on the normalization of the spectrum while temperature is sensitive to the spectral shape, the number of radial bins where temperature can be estimated is much smaller than the number of bins to extract density. SZ observations in the microwave are fully complementary to X-ray observations and provide measurement of the electron pressure. Moreover the SZ effect depends linearly on density, thus at large radii the signal drop is much smaller than the X-ray signal, therefore SZ pressure profiles can be extracted out to a very large radii, $\sim 2R_{500}$ (Planck Collaboration et al., 2013).

PHYSICS OF THE INTRACLUSTER MEDIUM

2.1 Selection effects

When deriving the statistical property of a population, of astrophysical objects for instance, from a sample which is a subset of the underlying population, one has to be certain that the sample is representative and unbiased with respect to selection effects. This means that the method used to detect or select galaxy clusters shouldn't influence any property which are of interest. Therefore, any statistical study of galaxy clusters requires a well defined selection function such that the underlying cluster population is well represented by the selected sample of clusters.

Galaxy clusters have important cosmological application (Allen et al., 2011; Burenin et al., 2007; Cunha et al., 2009; Mantz et al., 2016, 2014; Oguri and Takada, 2011; Vikhlinin et al., 2009), being very precise probe of structure formation and evolution, given the assumption that the selection applied is based on one or more parameters which are reliable proxies of their masses. However cluster masses are not a direct observable quantity, therefore one needs to exploit the various correlation between the mass of a cluster and other observable quantities.

Historically the first cluster identification and selection was made using optical observation through the definition of richness, however the relation between richness and mass is largely scattered, see Fig. 2.1 from Rettura (2017), thus a selection based on richness has limited cosmological application.

X-ray luminosity is shown to be an observable quantity tightly correlated with cluster mass, see Fig. 2.1 from Pratt et al. (2009). Thus it is easy to define flux-limited samples with well defined selection function. However some limitation arise in using X-ray luminosity to detect and build up clusters of galaxies, in fact the X-ray luminosity dims with distance, thus at high redshift the luminosity of an object will be significantly smaller than if it is nearby. Therefore, a flux-limited sample will strongly depend upon the relation between luminosity and redshift.

However since the first X-ray images of clusters, it became clear that galaxy clusters are divided in two classes, characterized by their peaked or not peaked central density (Jones and Forman, 1984). The first kind of clusters are characterized by a prominent surface brightness peak, associated with a decrease of the temperature profile in the inner region of clusters. The cooling time is shorter than the Hubble time, however the loss of heat is compensated by energy injection from the central AGN, which prevents the gas from cooling down too much and disappear from the hot phase; these clusters are classified as cool cores (CC, Molendi and Pizzolato, 2001). The second kind of clusters simply do not present these features; the surface brightness is not peaked, the cooling time is long even in the central region, and the

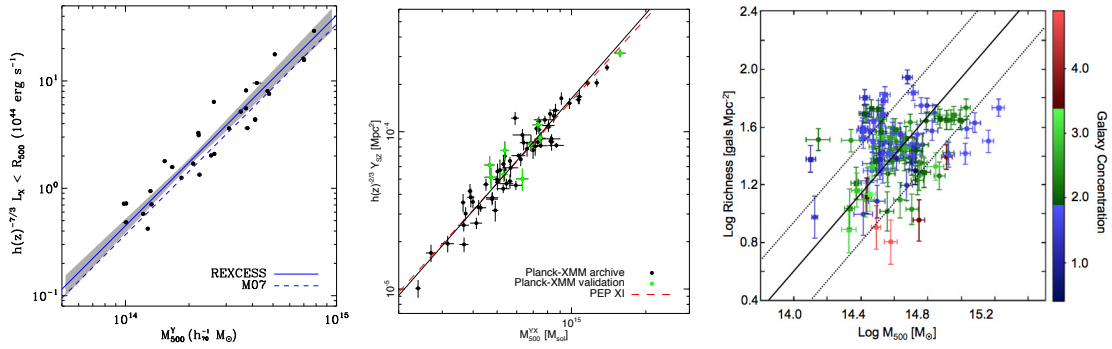


Fig. 2.1 The relation between cluster mass and observable properties. *Left*: X-ray luminosity in the REXCESS sample (Pratt et al., 2009, with M_{500}^{YX} the mass obtained by the calibrated M - Y_X scaling relation), *Centre*: SZ Compton signal (Planck Collaboration et al., 2014b, with M_{500}^{YX} the mass obtained by the calibrated M - Y_X scaling relation), *Right*: Cluster Richness (Rettura, 2017, with M_{500} measured using the calibrated M - L_X scaling relation)

central temperature does not drop; these second type of clusters are classified as non cool cores (NCC, Molendi and Pizzolato, 2001).

In the literature several indicators have been proposed to classify the two populations, based on their central properties: temperature drop (Sanderson et al., 2009, 2006), cooling time (Bauer et al., 2005) a composition of these two criteria (Dunn and Fabian, 2008; Dunn et al., 2005), the slope of the gas density profile at a given radius (Vikhlinin et al., 2007), and the core entropy (Cavagnolo et al., 2009).

The division of cluster in two categories still remains unclear. Some studies find that the observed population of clusters is bimodal (Cavagnolo et al., 2009), however other studies don't find any evidence for this bimodality (Pratt et al., 2010). Thus it is still unclear whether this is an intrinsic division into two classes or is rather caused by differences in the evolution during the history of clusters. Nevertheless X-ray selected samples are found to contain a fairly large amount of CC clusters, about 60-70% of the total.

The SZ signal instead, compared with X-ray luminosity, does not depend on the redshift of the source, thus in principle is able to detect any cluster above a given signal threshold independently of its distance. Moreover the SZ signal is less sensitive to the central morphology of clusters (CC or NCC), given the linear dependence, instead of quadratic, of the SZ signal on density. On top of that the cluster masses are tightly correlated also with SZ signal, see Fig 2.1 from Planck Collaboration et al. (2014b).

Only recently with advanced SZ observatories, *Planck*, *SPT*, *ACT*, it is possible to select clusters based on their SZ signal. However several recent works (Andrade-Santos et al., 2017; Lovisari et al., 2017; Rossetti et al., 2017) have found a significantly lower abundance of CC clusters in SZ selected samples, about 30%, confirming the scenario where X-ray

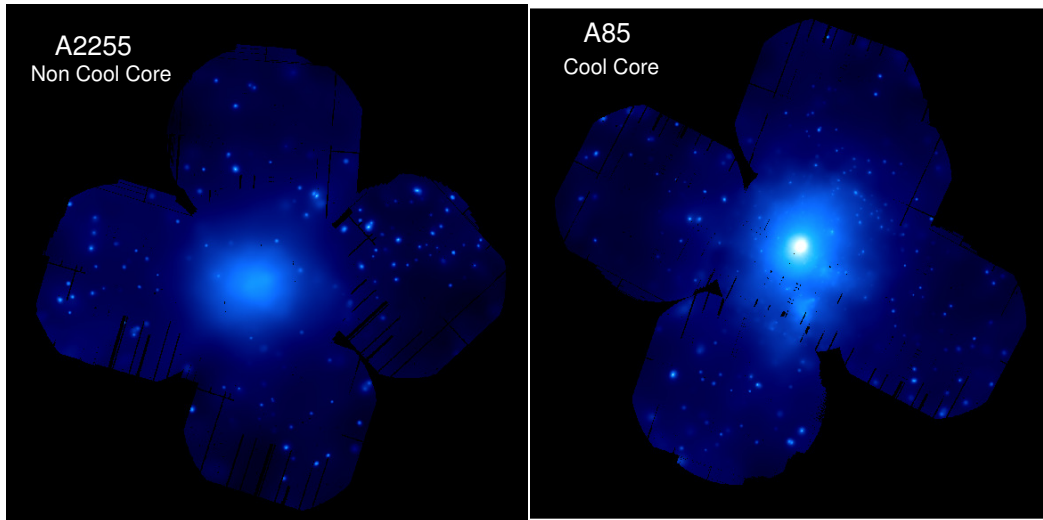


Fig. 2.2 The galaxy clusters A85 and A2255 are two nearby object which are at about the same redshift and their masses are very close (Ettori et al., 2018), however A85, being a strong cool core, is much more visible in an X-ray image.

cluster samples are affected by a “cool core bias” (Eckert et al., 2011). Indeed extended X-ray sources are detected based on their excess with respect to the background level, thus this makes easier to detect a CC cluster with a prominent peaked surface brightness profile compared to a similar cluster which is instead a NCC, thus without any surface brightness excess. This is clear in Fig. 2.2 where the X-ray images of A85 and of A2255 are displayed. In fact A85 and A2255 are at about the same redshift and have about the same mass, thus a good selection function based on cluster masses will detect equally both clusters, i.e. with the same signal, however the fact that A85 is a CC while A2255 is a NCC, makes the first much more easy to detect in an X-ray image, as one can appreciate from this figure.

This is why it is easier to detect a cluster with a prominent surface brightness peak than an object with a shallower profile, even if they have the same flux when integrated out to a physically relevant radius, like R_{500} . Thus this effect leads to a significant incompleteness in flux-limited cluster samples, indicating that the percentage of CC objects is over-estimated in X-ray selected samples.

However a few recent works (e.g. Lin et al., 2015; Sayers et al., 2013) argue that SZ selected samples could be affected by an opposite bias, i.e. SZ surveys are biased against CC. In fact the presence of radio sources, which are present mainly in CC cluster, can influence

the SZ detection. On top of this Sommer and Basu (2014) argued that in simulation the SZ signal in merging clusters is boosted for a few Gyr, thus increasing the likelihood of detecting a disturbed system.

2.2 Thermodynamic properties

The collapse of the primordial density peaks have a strong impact not only on the collisionless dark matter, but also on the thermodynamic properties of the intracluster medium. However the latter is not just affected by the gravitational potential, but astrophysical processes related to galaxy formation and evolution play an important role in shaping the ICM. These various astrophysical processes include cooling and stellar feedback (Kay et al., 2002), AGN feedback (Dubois et al., 2010; Springel et al., 2005), shocks (Vazza et al., 2012), turbulence, bulk motions (Vazza et al., 2011), cosmic rays (Pfrommer et al., 2007), and magnetic field (Dolag et al., 1999). Therefore, the thermodynamical properties of the ICM encode valuable information on the processes governing the formation and evolution of galaxy clusters.

The gas falling onto the deep gravitational potential wells of clusters, get their potential energy converted first to kinetic energy, then, via adiabatic compression and shocks, gets converted into thermal energy. Since gravity does not have a typical scale, the prediction on the thermodynamic properties from the self-similar model (Kaiser, 1986) should be respected in regions where gravity dominates. Thus since in the outskirts of galaxy cluster gravity dominate, they are expected to follow closely some self-similar model. Indeed non-radiative numerical simulations confirm this scenario, but observations in the outskirts produce controversial results (e.g. Eckert et al., 2013; Walker et al., 2012b).

High redshift preheating (Evrard and Henry, 1991; Tozzi and Norman, 2001) from astrophysical sources, i.e. AGN and stellar feedbacks, was proposed as a possible mechanism to break self-similarity. The energy required to break self-similarity at the observe degree is about 1 keV per particle, therefore Supernovae alone cannot. However preheating predict large isentropic cores and shallow pressure profiles, which is not observed in real cluster (Arnaud et al., 2010; Cavagnolo et al., 2009)

Gas cooling is another mechanism which can break self-similarity (Bryan, 2000; Voit and Bryan, 2001). In fact when a gas particle cools, it disappears from the hot ICM phase, and is replaced by a particle with higher entropy from a larger radii. This phenomena therefore removes low entropy gas and replaces it with gas with higher entropy.

2.2.1 Density

Surface brightness is a very easy observable quantity to characterize (Ettori and Molendi, 2011), nevertheless rich in physical information, given that it is proportional to the square of the density. It can be directly recovered from the analysis of images in soft energy bands, where the X-ray emissivity is almost independent on gas temperature, thus depending solely on density.

Given the assumption of hydrostatic equilibrium, Eq. (1.18), a simple model to describe the surface brightness from a gas is an isothermal sphere, known as the β -model (Cavaliere and Fusco-Femiano, 1976), which assumes that the temperature is constant from the cluster core to the cluster outermost boundary. In this model the surface brightness follows the following profile:

$$S_b \sim \left(1 + \frac{r}{r_c}\right)^{-3\beta + \frac{1}{2}} \quad (2.1)$$

where the core radius r_c measures the extension of the core, and β determines the shape. This model provides a generally good fit to observational data, however it was demonstrated that in the centre and in the outskirts of clusters the isothermal assumption breaks, thus the β -model is not able to correctly model the inner and outer parts of galaxy clusters (Jones and Forman, 1984; Vikhlinin et al., 1999, respectively). This is not something unexpected given that clusters are not isothermal.

Recent observations from *Suzaku*, thanks to its low particle background, have been consistently able to map the gas distribution in galaxy clusters from the core to the outskirts. Their studies (e.g. Akamatsu et al., 2011; Reiprich et al., 2013; Simionescu et al., 2011, 2017; Urban et al., 2014; Walker et al., 2012a,c) generally find density profiles which in the outskirts are less steep than results from other instruments, like *Chandra* (e.g. Ettori and Balestra, 2009; Morandi et al., 2015), *XMM-Newton* (Snowden et al., 2008), and ROSAT PSPC (Eckert et al., 2012; Vikhlinin et al., 1999).

The observed discrepancy can be explained by the presence of a fair amount of clumps in cluster outskirts (Roncarelli et al., 2013; Zhuravleva et al., 2013). In fact the large PSF of *Suzaku* makes any clump correction almost impossible. Gas clumping is a measure of the inhomogeneities present in the ICM. It is characterized by the clumping factor

$$C = \frac{\langle \rho_{gas}^2 \rangle}{\langle \rho_{gas} \rangle^2} \quad (2.2)$$

Simulations find that gas physics have a large impact in the distribution of the gas in the outskirts, in fact at R_{200} the presence or absence of radiative cooling changes the clumping

factor in simulations from 1.3 to 2.0 respectively (Nagai and Lau, 2011), thus leading to an overestimate of the density profile with also a flattening of the slope. Observations have access only to density square, therefore estimating directly the clumping factor is not possible, however Vazza et al. (2013, 2011) have shown that it is possible to estimate an observable quantity, the azimuthal scatter, which is related to the clumping factor. Roncarelli et al. (2013) defined the residual clumping factor as the clumping generated by large-scale accretion patterns, distinguishing from the clumping generated by individual clumps.

Zhuravleva et al. (2013) suggested that the azimuthal median of the surface brightness in each radial annulus is more representative, with respect to the mean, of the underlying distribution because it is almost insensitive to the presence of clumps. Eckert et al. (2015) tested this idea, and using ROSAT PSPC X-ray observations they find density profile which are steeper compared to the mean. Moreover they introduced a new technique to estimate the amount of clumps in their sample, which is simply taking the ratio between the mean and the median in each annulus. They measure a value of 1.1 at R_{500} and 1.2 at R_{200} , slightly smaller than the value measured in simulations (1.2 and 1.5 respectively in Vazza et al., 2013).

2.2.2 Temperature

Temperature is a very powerful probe to estimate the total mass of clusters because the mass obtained applying hydrostatic equilibrium, Eq. (1.18), is linearly dependent on temperature, with minimal dependence on temperature gradient, given that temperature profiles are generally quite flat. Thus precise temperature profile measurement are very important for an accurate mass profile reconstruction.

Chandra and *XMM-Newton* are very powerful X-ray instruments to probe the temperature of clusters in the inner regions, inside R_{500} , where the signal to noise is high (Leccardi and Molendi, 2008; Pratt et al., 2007). However beyond R_{500} systematic uncertainties on instrumental background combined with low signal to noise in these regions hampers the temperature measurement, with exceptions in the case of very bright and low temperature systems (Bonamente et al., 2013; Urban et al., 2011). *Suzaku* thanks to its stable and low particle background, have been able to study temperatures in clusters out to the boundary of clusters (Walker et al., 2012b). Recently, by combining SZ measurements of the pressure with X-ray measurements of the density it is possible to extend the measurements of the temperature out to very large radii (Eckert et al., 2013).

Generally temperature profiles are can be distinguished in the two classes discussed above, CC and NCC, characterized by different central properties, in fact CC clusters have a drop of temperature in the centre, while NCC remain with flat temperature profile in the

centre. In the outskirts however the temperature, for both classes, drops by a factor of two or more from the inner part to R_{500} and R_{200} .

2.2.3 Pressure

If temperature is the quantity which is the most directly connected to the depth of the potential well, the thermal pressure is the main source of balance with respect to the gravitational potential, see Eq. (1.17).

Simulations highlight that the accretion pattern in the outskirts is very complicated. Turbulence and shocks are frequent in unrelaxed systems, therefore influencing the pressure profile. Vazza et al. (2009) have shown that in simulations turbulence in the ICM account between 5% to 25% of the total thermal energy within the virial radius. Baryons in the outskirts bear signature of non spherical accretion, therefore pressure allows to access the level of virialization degree reached.

The Representative *XMM-Newton* Cluster Structure Survey (REXCESS Böhringer et al., 2007), a local sample selected based on X-ray luminosity, found that pressure follows a universal shape out to R_{500} (Arnaud et al., 2010), well in agreement with numerical simulations (Nagai et al., 2007). By extending the observed data within R_{500} with results from simulations, Arnaud et al. (2010) were able to construct a universal thermodynamic functional form out to the boundary of clusters, well described by a generalized NFW functional form (Nagai et al., 2007).

Recent advance in SZ studies of clusters have shown their potential, because of the linear dependency upon density of its signal and of its independence on redshift, allowing for the first time to study clusters from the core to the outskirts and beyond. Fortunately the ICM pressure, as observed by X-ray or by SZ are fully compatible, indicating that there are not any instrumental biases. SPT was the first one of these SZ probes (Plagge et al., 2010), demonstrating that it is possible to extract pressure profiles out to $2R_{500}$, with shape compatible with the universal profile obtained by Arnaud et al. (2010).

Planck Collaboration et al. (2013) made use of its full sky coverage and the 9 frequency bands used to detect clusters SZ profiles out to $3R_{500}$, i.e. out to regions where the average density contrast is about 100. They deprojected their profiles getting the pressure profiles, fully agreeing with the X-ray pressure profiles measured by *XMM-Newton* within R_{500} , however outside that radius they measured a pressure which is slightly shallower than in Arnaud et al. (2010).

However, if the agreement in the outer region of clusters between X-ray and SZ samples is evident, selection effects play an important role in the central part of clusters, in fact if

X-ray studies contain mainly CC clusters, SZ detected clusters contain mainly NCC, thus the properties of the core change depending on the selection applied.

2.2.4 Entropy

The exact physics which govern the state of the gas in the outskirts is still poorly understood. Especially regarding effects caused by gas clumping or by departure from hydrostatic equilibrium equation, measured in the form of non thermal pressure.

Entropy is probably the most important thermodynamic quantities, because it is the only thermodynamic quantity that increases when a heat flows occurs. In astrophysics, entropy is defined differently from the classical entropy:

$$K = \frac{k_B T}{n_e^{2/3}} \quad (2.3)$$

this thermodynamical property encodes information on all the non-adiabatic processes that transfer energy from external sources (like the kinetic energy of a merger) into internal thermal energy, thus leading to the thermalization of the ICM into the gravitational potential well.

Gravitational collapse models predict a stratified entropy profile, increasing steadily with radius following a power law with index ~ 1.1 (e.g. Tozzi and Norman, 2001; Voit et al., 2005, see Fig. 2.3). However, non-gravitational processes inject additional entropy, thus they can be traced through the deviation of entropy from the theoretical predictions (Chaudhuri et al., 2012).

Recently, several works, especially using the *Suzaku* observatory, have reported entropy deficit in massive clusters around the virial radius, which has been interpreted as a lack of thermalization of the ICM induced by the gas out of virial equilibrium (e.g. Bonamente et al., 2013; Ichikawa et al., 2013), or by lack of ionization equilibrium between electrons and ions (Hoshino et al., 2010). Furthermore a recent collection of *Suzaku* observation out to the virial radius have found a tendency for most entropy profiles to flatten around R_{200} (see Fig. 2.3 from Walker et al., 2012b).

Recent progress in the study of galaxy clusters using SZ measurements allows to combine X-ray density, which can be obtained out to R_{200} , and SZ pressure, measurable out to $2R_{500}$, to constrain the thermodynamic properties out to the virial radius. Surprisingly combinations of ROSAT and *Planck* (e.g. Eckert et al., 2013) find entropy profiles which are in agreement with results from simulations, highlighting the possibilities that there are systematic differences between ROSAT and *Suzaku* density profiles. As discussed above, clumping may be very

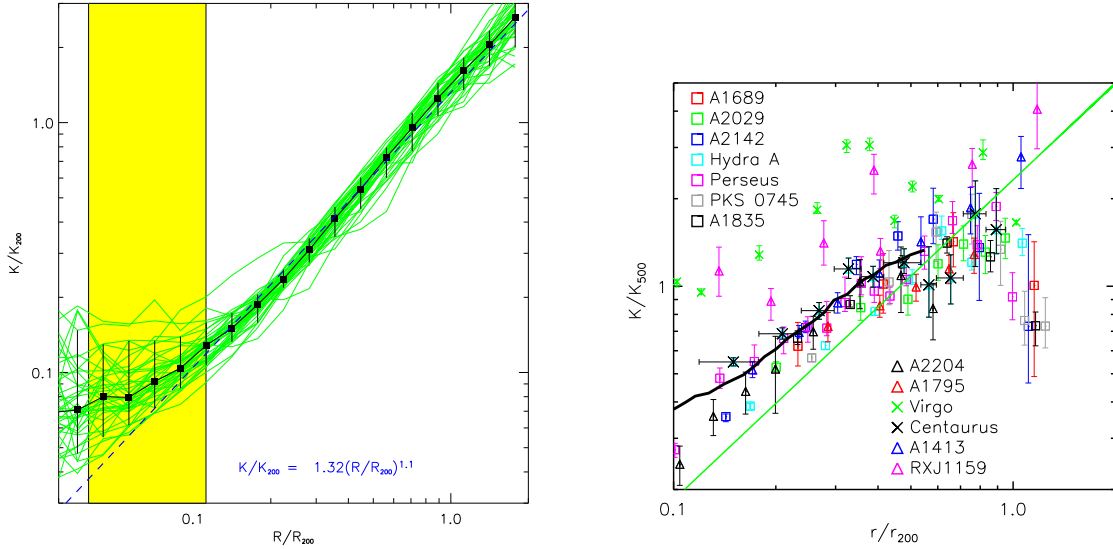


Fig. 2.3 *Left*: Stratified entropy profiles as predicted from simulations Voit et al. (2005). *Right*: Entropy profiles for 13 clusters as observed by *Suzaku* (Walker et al., 2012b).

important in cluster outskirts, and therefore the inability of *Suzaku* to remove properly substructures, due to its poor PSF, may cause these systematic differences.

2.2.5 Gas fraction

The gas mass fraction is the ratio between gas mass and total mass, therefore in general is both a global and a local function, given that it depends on both mass and radius.

In particular, the total baryon fraction of massive clusters is one of the most robust quantities derived in cosmological simulations (Ettori et al., 2006; Kravtsov et al., 2005; Mantz et al., 2014). In particular, since massive clusters originate from the collapse of large regions of the early Universe (about 30 comoving Mpc at $z = 2$, Muldrew et al., 2015), their baryon content should be representative of the entire Universe as a whole. Recent simulations confirm that the total baryonic fraction of massive clusters is almost universal (Le Brun et al., 2014; Planelles et al., 2013; Sembolini et al., 2016). Thus clusters are a fair representation of the matter content in the universe, implying that at a large enough radius, where gravity dominates, the universal baryon fraction should be recovered. Simulation support this scenario, in fact Sembolini et al. (2016) have shown that simulation of the same clusters using many different codes, produces a single gas mass fraction in the outskirts with a very small scatter.

Observations also have given some insight regarding this, Allen et al. (2008) used *Chandra* to measure the gas mass fraction at the overdensity of 2500, measuring a relatively

small dispersion. However at larger radii the measured dispersion is much larger, (e.g. at R_{200} Reiprich, 2003).

In general, the gas mass fraction depends on the underlying physical processes which govern cluster formation and evolution, however for our purpose we can describe the universal gas fraction as function of radius as

$$f_{\text{gas,univ}}(r) = Y_b(r) \frac{\Omega_b}{\Omega_m} - f_*, \quad (2.4)$$

with $Y_b(r)$ the baryon depletion factor, Ω_b/Ω_m the universal baryon fraction, and f_* the star fraction. The universal baryon fraction is determined with very high precision by the CMB power spectrum, taking the recent measurement by *Planck* of $\Omega_b/\Omega_m = 0.156 \pm 0.003$ (Planck Collaboration et al., 2016e). The baryon depletion factor encodes the fraction of the baryons that is enclosed within a given radius, and it is one of the most robust quantities predicted by numerical simulations in the regions where gravity dominates over other processes (i.e. beyond R_{500} ; Sembolini et al., 2016). They predict that its value at large cluster-centric radii depends very little on the adopted physical setup, such that the value of Y_b can be very well estimated using numerical simulations. Finally, the stellar fraction has been the subject of many studies (Chiu et al., 2018; Gonzalez et al., 2013, 2007; Laganá et al., 2013) and its value is well measured to be around 1%. On top of this some baryons seems to be missing from galaxy cluster baryon census, as Ettori (2003) pointed out this fraction should be in the range of 0-30%.

Clusters are important cosmological probes, in fact they can be used to estimate the value of several cosmological parameters (see Allen et al., 2011, for a review). Ettori et al. (2009) have studied the systematic uncertainties related to the use of the measured gas fraction to estimate the cosmological parameters, using Eq. (2.4). They point out that still a large statistical uncertainty is present, nevertheless is relatively small to a point where systematic uncertainties play an important role, being at the same order of magnitude as the statistical errors.

2.2.6 Chemistry

The chemical composition of galaxy clusters plays a very important role when studying them. In fact the emission from clusters does not contain thermal bremsstrahlung only, but also emission from charged ions. In fact ions can capture a free electron causing a free-bound (or recombination) radiation, or a bound-bound de-excitation radiation caused by an electron changing its quantum level. These two processes give rise respectively to continuum and line emission at specific energies, determined by the nature of the ion and by the quantum level

involved. Moreover considering that they require two particles to be involved, they produce an emission which is proportional to $n_e n_X$, where n_X is the number density of the ion X.

Observationally the Fe-K line emission was the first one which has been detected (Mitchell et al., 1976; Serlemitsos et al., 1977) by observing the bright nearby Perseus, Coma, and Virgo clusters. Moreover they indicate that the abundance ratio of these elements is about 0.3 the solar (calculated with respect to the solar elements abundance measurements of Anders and Grevesse, 1989). This is evidence of element pollution in the ICM caused by SNe, which elements get distributed by astrophysical phenomena such as AGN outflows, ram-pressure stripping, or galactic winds.

Recent studies with advanced telescopes like *XMM-Newton* have shown that the abundance ratio of different elements is compatible with solar. (Mernier et al., 2016a,b)

The launch of *Hitomi* was expected to yield a breakthrough in the study of the chemical composition of the ICM. In fact its first observation of the core of Perseus cluster has shown how we can measure not only each component of the Fe-K complex, but also the turbulence present in the ICM, using the line broadening (Hitomi Collaboration et al., 2016). *Hitomi* Collaboration was also able to study the abundances of a lot of different ions, obtaining that the abundance ratio in Perseus is compatible with solar (Hitomi Collaboration et al., 2017), fully in agreement with the work carried out by Mernier et al. (2016a,b), putting constraints on the origin of the observed enriched ICM, thus indicating that the percentage of SNIa is about 29-45% of the total number of SNe.

2.2.7 The polytropic state of the ICM

The polytropic equation is an assumption in which pressure depends upon density in the form

$$P_e = K n_e^\Gamma \quad (2.5)$$

where K is a constant, and Γ is the effective polytropic index. This description of the ICM is a very simple extension of the isothermal model, providing a natural gradient for the temperature.

The effective polytropic index Γ is physically different from the adiabatic index of the gas γ , the ratio between specific heat at constant pressure and the specific heat at constant volume. In fact the former is just an effective description of the global structure of the ICM, while the latter describes how the gas pressure is affected by compression or expansion.

The literature does not contain a lot of information regarding this description of the ICM, and in general the information are sparse. Simulations generally find that the polytropic equation generally provides a good description to the outer parts of galaxy clusters, with the

effective polytropic index in the range of 1.2 – 1.3 (Ascasibar et al., 2003; Capelo et al., 2012; Ostriker et al., 2005). Observations on the other hand have measured the effective polytropic index, finding values very close to the predicted one (Eckert et al., 2015; Markevitch et al., 1998; Sanderson et al., 2003, measuring 1.24, 1.24, and 1.21 respectively)

The effective polytropic index is generally measured by fitting pressure against density over a large radial range, e.g. over the radial range $[0.1 - 2]R_{500}$ in Eckert et al. (2015), thus the description of the evolution of Γ with radius or with redshift is still something unknown, perhaps related to the accretion history of clusters (Ascasibar et al., 2006).

**THE XMM CLUSTER OUTSKIRTS PROJECT
(X-COP)**

3.1 The X-COP cluster sample

The outskirts of galaxy clusters are the regions where the transition between the virialized ICM and the in-falling material takes place. Thus they are the ideal targets where study the structure formation processes. The distribution of the hot X-ray emitting gas is expected to be clumpy (Roncarelli et al., 2013; Vazza et al., 2013) and asymmetric (Eckert et al., 2012; Vazza et al., 2011), with contribution from non thermal processes playing an important role (Battaglia et al., 2012; Biffi et al., 2016; Lau et al., 2009; Nelson et al., 2014a; Shi et al., 2015; Vazza et al., 2009). In particular we have discussed in the previous chapter how the clumpiness may bias high the measured density profile, thus also biasing low the measured entropy profile. This has to be taken into account when measuring the properties of the ICM.

The *XMM-Newton* cluster outskirts project (X-COP) is a very large programme (VLP) on *XMM-Newton* that aims at advancing significantly our knowledge of the physical conditions in the outer regions of galaxy clusters ($R > R_{500}$). A sample of massive nearby objects were selected based on their high signal-to-noise ratio (S/N) in the *Planck* all-sky survey of Sunyaev-Zeldovich sources (Planck Collaboration et al., 2014a). X-COP provides a uniform *XMM-Newton* mapping of these clusters out to R_{200} , and moreover, given the recent advances in the sensitivity of SZ instruments, a *Planck* measure the pressure profile out to $3 R_{500}$. Thus by making full use of these complementary information, we aim of combining high-quality X-ray and SZ imaging throughout the entire volume of these systems.

Unlike previous studies utilizing exclusively the X-ray signal, we take advantage of the high signal-to-noise of our clusters in the *Planck* survey (Planck Collaboration et al., 2016d) to combine X-ray and SZ data to increase the precision of our measurements while keeping a good control of systematic errors. This method was already applied to reconstruct the thermodynamical properties of a few clusters (Adam et al., 2015; Basu et al., 2010; Eckert et al., 2013; Ruppin et al., 2017), and we demonstrated the ability of *XMM-Newton* and *Planck* to measure accurately the state of the gas out to the virial radius in two pilot studies (Ghirardini et al., 2018b; Tchernin et al., 2016).

The selection criteria used to select the most suitable targets are the following:

1. **S/N > 12 in the 1st *Planck* catalog (Planck Collaboration et al., 2014a):** This condition allows to target the most significant *Planck* detections, thus ensuring that the SZ effect from these clusters is detected beyond R_{500} ;
2. **Apparent size $\theta_{500} > 10$ arcmin:** This condition ensures that all clusters are well resolve by the *Planck* beam, about 7 arcmin;

3. **Redshift in the range $0.04 < z < 0.1$:** This condition allows to cover the entire azimuth of these clusters with 5 *XMM-Newton* pointings, one central and four offset, while being still well resolved by *Planck*;
4. **Galactic $N_{\text{H}} < 10^{21} \text{ cm}^{-2}$:** This condition makes sure that the X-ray signal is weakly absorbed, maximizing the sensitivity in the soft X-ray energy band, i.e. [0.7-1.2] keV.

This selection lead to a set of 16 suitable targets for our goals. We excluded two clusters (A754, and A3667) because of complicated morphologies induced by violent merging events, which could hamper the analysis of the *Planck* data given the broad *Planck* beam. One (A2256) was excluded because of its bad visibility for *XMM-Newton*, and the remaining object (A3827) for both having an apparent size very close to our cut, thus may not be properly resolved by *Planck*, and for being a merger along the line of sight (Carrasco et al., 2010).

The remaining 12 clusters selected for our study are listed in Table 3.1, together with their main properties. A uniform 25 ks mapping, which allows us to reach a limiting surface brightness of $3 \times 10^{-16} \text{ ergs cm}^{-2} \text{ s}^{-1} \text{ arcmin}^{-2}$ in the [0.5-2.0] keV band, with *XMM-Newton* was performed for 10 of these systems in the framework of the X-COP very large programme (Proposal ID 074441, PI: Eckert), which was approved during *XMM-Newton* AO-13 for a total observing time of 1.2 Ms. The remaining 2 systems (A3266 and A2142) were already mapped by *XMM-Newton*. Although the available observations of A3266 do not extend all the way out to R_{200} , they are still sufficient for some of our objectives and we include them in the present sample. Including central and archival pointings, the total observing time is about 2 Ms. The observation log, observation IDs, and observing time, after applying flare filtering, are given in Table 3.2.

Our final sample, therefore, comprises 12 clusters in the mass range $2 \times 10^{14} < M_{500} < 10^{15} M_{\odot}$ and X-ray temperature $3 < kT < 10 \text{ keV}$. In Table 3.1 we also provide the values of the central entropy K_0 from the ACCEPT catalog (Cavagnolo et al., 2009), which is an excellent indicator of a cluster's dynamical state (Hudson et al., 2010). Thus, using this indicator, four of our clusters are classified CC systems ($K_0 < 30 \text{ keV cm}^2$), while the remaining eight systems are NCC, see Table 3.1. Therefore, like other *Planck* selected samples (Andrade-Santos et al., 2017; Lovisari et al., 2017; Rossetti et al., 2017), the X-COP sample is dominated by non-cool-core systems.



Fig. 3.1 Artistic representation of the ESA satellites *XMM-Newton* (left) and *Planck* (right).

3.2 *XMM-Newton* data analysis

The European Space Agency's (ESA) X-ray Multi-Mirror Mission (*XMM-Newton*) was launched in December 1999. *XMM-Newton*, selected as part of the Horizon 2000 Science Programme, orbits around our planet since Earth's atmosphere blocks out all X-rays, which can therefore be detected only by a telescope in space. This telescope was originally scheduled to perform for just a two year mission, however after almost twenty years of operation is still in good health, and the mission duration is routinely extended.

XMM-Newton carries three European Photon Imaging Cameras (EPIC) as its primary X-ray instruments. This system is composed by two MOS-CCD cameras and a pn-CCD camera. The total field of view is about 30 arcmin, with energy sensitivity ranging from 0.15 to 15 keV (i.e. from 82.7 to 0.83 Å). The three EPIC instrument can operate independently in a variety of modes, depending on several physical factors, like the image sensitivity and the intensity of the target.

The Reflection Grating Spectrometers (RGS) are a secondary system on *XMM-Newton*, and they are built for high-resolution X-ray spectroscopy. RGS operates between 0.35 to 2.5 keV (i.e. from 35 to 5 Å)

The Optical Monitor (OM) provides with simultaneous optical/ultraviolet observation of the target between 170 and 650 nm.

Here we describe in detail the data analysis pipeline that we set up for the analysis of the *XMM-Newton* data. A flow chart describing the main steps of the analysis is presented in Fig. 3.2.

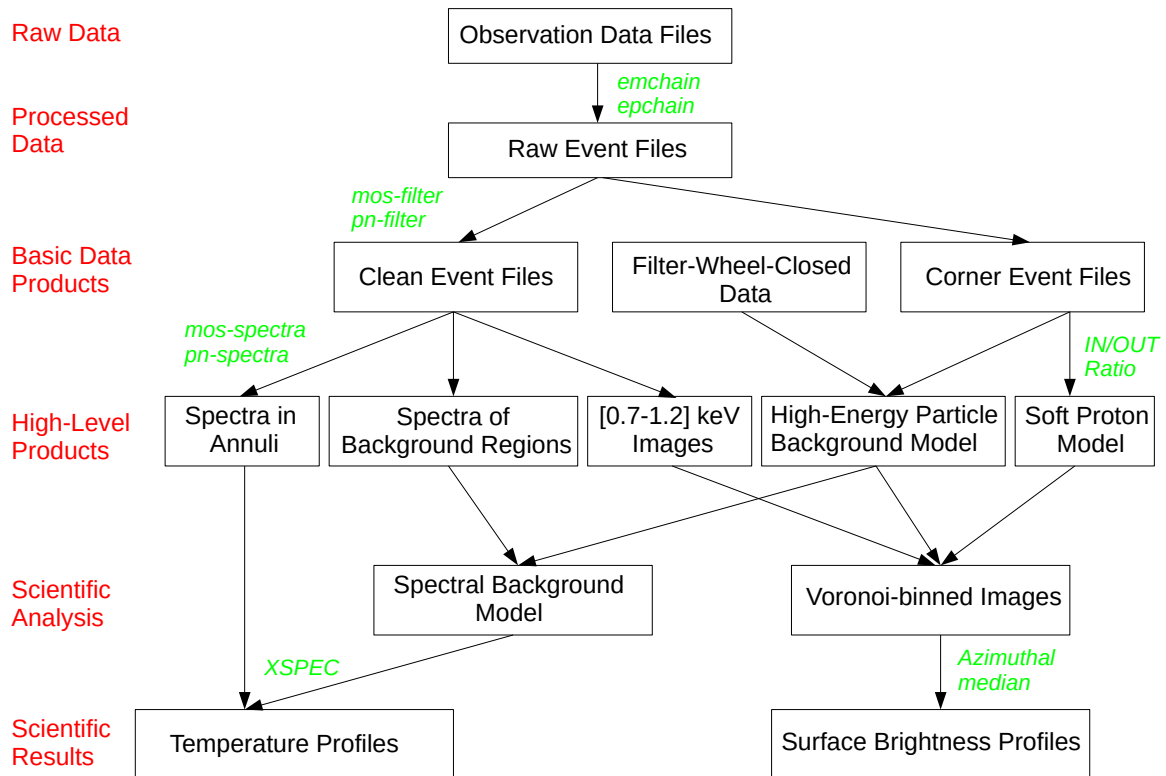


Fig. 3.2 Flow chart of the *XMM-Newton* data analysis pipeline. The steps of the analysis are shown in red, the main intermediate and final products are described in the black boxes, and the procedures are shown in green italic.

3.2.1 Data reduction

We have reduced all the data using XMM-SAS v13.5 and the Extended Source Analysis Software (ESAS) data reduction scheme (Snowden et al., 2008). To perform basic data reduction, we use the `emchain` and `epchain` pipelines to extract calibrated event files from the observations, and we rerun `epchain` in out-of-time mode to create event files for pn out-of-time events. To filter out time periods affected by soft proton flares, we run the `mos-filter` and `pn-filter` executables, which extract the light curve of each observation in the hard band and apply a sigma-clipping technique to exclude time intervals with enhanced background. We use the unexposed corners of the MOS detectors to monitor the particle background level during each observation, and measure the count rates in the high-energy band ([7.5-11.8] keV) of the MOS from the regions located inside and outside the field of view (FOV) of the telescope (hereafter IN and OUT). The comparison between IN and OUT count rates is then used to estimate the contamination of residual soft protons to the spectrum (De Luca and Molendi, 2004; Leccardi and Molendi, 2008; Salvetti et al., 2017).

3.2.2 Image extraction and preparation

We extract photon count images from the three EPIC detectors in the [0.7-1.2] keV band. This narrow band maximizes the ratio between source and background emission and is thus best suited to minimize the systematics in the subtraction of the EPIC background (Ettori et al., 2010). We use `eexppmap` to compute exposure maps taking vignetting effects into account for all three detectors independently. To create total EPIC images, we sum the count maps of the three detectors and repeat the same operation with the exposure maps, multiplying the pn exposure maps by a factor of 3.44 representing the ratio of pn to MOS effective areas in our band of interest. We use the ESAS tools `mos-spectra` and `pn-spectra` in imaging mode to compute models of the high-energy particle background. To this aim, we select the filter-wheel-closed observations recorded at the nearest possible time to the observation, and we use the spectra of the unexposed corners of the detectors to rescale the filter-wheel-closed observations. This procedure is performed individually for all CCDs, and the CCDs operating in anomalous mode are discarded. We then extract an image from the rescaled filter-wheel-closed data in the [0.7-1.2] keV band using the `mos-back` and `pn-back` executables, which we use as our model for the high-energy particle background. In the case of the pn, we repeat the operation with the out-of-time event files and create a model for the intensity and spatial distribution of out-of-time events.

Even after cleaning the light curves from soft-proton flares, it is known that a fraction of residual soft proton contamination remains within the datasets. This component can introduce systematics at the level of $\sim 20\%$ in the subtraction of the EPIC background in our band of choice (Tchernin et al., 2016). To model the contribution of residual soft protons, we follow the method outlined in Sect. 3.3 (from Ghirardini et al., 2018b), which was calibrated using a large set of ~ 500 blank-sky pointings. Namely, we measure the high-energy ([7.5-11.85] keV) MOS count rates in the exposed (IN) and unexposed (OUT) parts of the FOV, and we use the difference between IN and OUT count rates as an indicator of the contamination of each observation by residual soft protons (see Salvetti et al., 2017, for a detailed overview of this approach). We use our large blank field dataset to calibrate an empirical relation between the IN-OUT indicator and the required intensity of the soft proton component (see Sect. 3.3, or Appendix A of Ghirardini et al., 2018b) and we use this relation to create a two-dimensional soft proton model. This procedure was shown to bring the systematics in the subtraction of the EPIC background to an accuracy better than 5%.

For each cluster, we combine the resulting EPIC count maps in the [0.7-1.2] keV from each individual observation (central or offset) to create a mosaic image. We apply the same procedure to the combined EPIC exposure maps and to the background maps, summing up the non X-ray background components (quiescent particle background and residual soft

protons). We then obtain mosaicked photon maps, exposure maps and non X-ray background maps for each source. In Fig. 3.4 we show the resulting background-subtracted and exposure-corrected mosaics, which we adaptively smoothed using the `asmooth` code (Ebeling et al., 2006).

3.2.3 Point source subtraction

To detect point sources present within the field, we extract photon count maps from the three detectors in a soft ([0.5-2] keV) and a hard ([2-7] keV) band, and we use the XMMSAS tool `ewavelet` with wavelet scales in the range 1-8 pixels and signal-to-noise threshold of 5.0. We then cross-match the soft and hard band detections between the multiple (central and offset) observations of each cluster to create a global point source list per cluster. Since the vignetting and the point spread function of the *XMM-Newton* telescopes depend on off-axis angle, the sensitivity threshold for source detection depends on the position of a source on the detector. At fixed observing time, *XMM-Newton* thus detects point sources down to lower fluxes near the aim point than close to the edge of the FOV, and the fraction of the cosmic X-ray background (CXB) that is resolved by the instrument is spatially dependent. To correct for this effect, we draw the distribution of measured count rates from the detected sources and we determine the count rate at which the distribution peaks. Since the $\log N$ - $\log S$ of distant sources contributing to the CXB is a monotonically decreasing function (e.g. Luo et al., 2017; Moretti et al., 2003), the peak in the count rate distribution of our observation roughly corresponds to the threshold down to which our source detection is complete. We then excise only the sources with a measured count rate greater than our threshold and leave the fainter sources to enforce a constant flux threshold across the FOV and avoid biasing local measurements of the CXB intensity.

3.2.4 Surface brightness profiles

An important complication with the analysis of X-ray data of cluster outskirts lies in the presence of accreting structures and inhomogeneities in the gas distribution, which are expected to contribute substantially to the measured X-ray flux beyond $\sim R_{500}$ (e.g. Nagai and Lau, 2011; Roncarelli et al., 2013; Vazza et al., 2013). Since the X-ray emissivity is proportional to the square of the gas density, over-dense regions contribute predominantly to the measured X-ray flux and can bias the recovered gas density high. To alleviate this issue, we apply the azimuthal median method outlined in Eckert et al. (2015). Numerical simulations show that the median surface brightness in concentric annuli is robust against the presence of outliers in the gas density distribution (Zhuravleva et al., 2013). We thus

construct background-subtracted and exposure-corrected surface brightness maps using a Voronoi tessellation technique (Cappellari and Copin, 2003) with a target number of 20 counts per bin.

The intensity of the sky background is determined by averaging the surface brightness distribution in the regions with $R > 2R_{500}$, where we assume the cluster emission to be negligible. A systematic uncertainty of 5% of the background level (see Sect. 3.2.2) was added in quadrature to the error budget of the surface brightness profiles. This procedure was applied to all clusters except A3266, for which the current mosaic does not extend out to $2R_{500}$. In this case, we estimate the sky background intensity from the ROSAT all-sky survey background tool¹ and included a systematic error of 30% in quadrature to the full error budget.

To compute the surface brightness profiles, we draw the surface brightness distribution from the Voronoi-binned images in concentric radial bins, starting from the X-ray peak, and then choosing the annuli such that the emissivity in each bin is almost constant. The errors on the azimuthal median are estimated from 10^4 bootstrap resampling of the pixel distribution. Circular regions of 30 arcsec radius are excised around the positions of point sources selected through the procedure described in Sect. 3.2.3, corresponding to an encircled energy fraction of 90% of the point source flux.

3.2.5 Spectral extraction

We extract spectra in concentric annuli around the X-ray peak covering approximately the radial range $[0 - 1]R_{500}$, removing the point sources which contaminates the spectra, see Sect. 3.2.3, using the ESAS routines `mos-spectra` and `pn-spectra`. These tools extract source spectra from the observation and from the rescaled filter-wheel-closed data to estimate the high-energy particle background contribution. These tools also generate the appropriate response matrices and effective area files for extended sources using the observed image as an input for the photon distribution. Spectra of the pn out-of-time events are also estimated and subtracted from the measured spectra. We selected the binning such that the width of the bins increases exponentially but choosing a minimum width of 0.5 arcmin for the innermost bins such that the instrumental PSF does not contribute much to the photon in each bin. We group the output spectra with a minimum of 5 counts per bin to ensure stable fitting results, and discard the data below 0.5 keV where the EPIC calibration is uncertain. We then use XSPEC v12.9 and the C-statistic (Cash, 1979) to fit the spectra and determine the plasma parameters (see Sect. 3.2.6).

¹<https://heasarc.gsfc.nasa.gov/cgi-bin/Tools/xraybg/xraybg.pl>

3.2.6 Spectral modeling

To extract spectral diagnostics from the observed spectra (see Sect. 3.2.5), we proceeded using a full spectral modeling approach following the method described in detail in Eckert et al. (2014). Here we describe our approach to model all the individual background components and the source spectra.

- **High-energy particle background** : We use the rescaled filter-wheel-closed spectra to determine the intensity and spectral shape of the particle background. We fit the filter-wheel-closed spectra using a diagonal response matrix and a phenomenological model including a broken power law and several Gaussians to reproduce the shape of the continuum and fluorescence lines. We then apply the fitted model to the source spectrum, leaving the normalization free to vary within $\pm 10\%$ to account for possible systematics in the scaling of the filter-wheel-closed data.
- **Sky background** : We model the X-ray background and foreground emission as the sum of three components: *i*) an absorbed power law with a photon index fixed to 1.46 to describe the residual CXB (De Luca and Molendi, 2004); *ii*) an absorbed APEC thermal plasma model with a temperature allowed to vary in the range [0.15-0.6] keV to model the Galactic halo emission (McCammon et al., 2002); *iii*) an unabsorbed APEC model with a temperature fixed to 0.11 keV to represent the local hot bubble. The Galactic hydrogen column density N_H was fixed to the LAB value (Kalberla et al., 2005). Similarly to what was done for the imaging case, the parameters of the sky emission model are fitted to the spectra of background regions located at $R > 2R_{500}$ from the cluster core. Again the exception to this procedure is A3266, for which we use the *ROSAT* all-sky survey background tool to determine the sky background parameters. The best-fit model is then applied to the source spectra, rescaling the intensity of the components according to the area of each region.
- **Residual soft protons** : In cases where our IN-OUT indicator of soft proton contamination is found to be high (IN-OUT > 0.1 counts/s), we include an additional model component to the particle background model to take soft protons into account. We model the soft proton component as a broken power law with fixed spectral shape (slopes 0.4 and 0.8 and break energy 5 keV, Leccardi and Molendi, 2008) and let the normalization of this component free to vary in the overall fitting procedure.
- **Source** : We model the source emission in each annulus as an absorbed single-temperature APEC model with temperature, emission measure and metal abundance free to vary. In cases where multiple observations were available for the same regions,

we fit all the available spectra jointly, tying the source parameters between the different spectra. The Solar abundance table is set to Anders and Grevesse (1989). Since our objects are nearby and extended on scales much larger than the *XMM-Newton* PSF, we neglect the potential cross-talk between the various annuli.

All the spectra were fitted in the energy range [0.5-12] keV using XSPEC v12.9, ATOMDB v3.0.7 and the C-statistic (Cash, 1979). When several observations of the same region are available, we extract the spectra from each individual pointing and fit them jointly. We ignore the energy ranges [1.2-1.9] keV (MOS) and [1.2-1.7] keV, [7.0-9.2] keV (pn) where bright and time-variable fluorescence lines are present. We then construct projected gas temperature profiles from the best fit results. We also deproject our 2D temperature profiles using the projection matrix V and the emissivity in each annulus as weights, adopting the spectroscopic-like temperature scaling of Mazzotta et al. (2004).

3.3 Non-X-ray background modelling

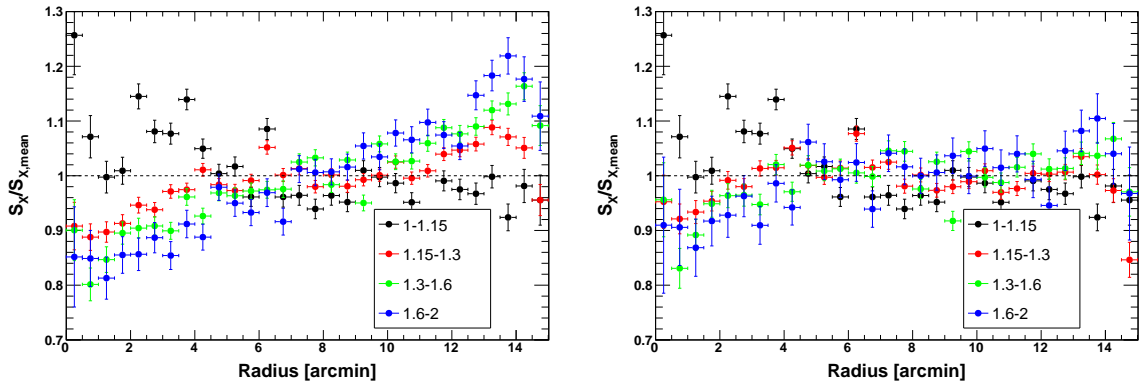


Fig. 3.3 Stacked EPIC radial profiles of 495 blank-sky pointings, sorted in bins of soft-proton contamination inFOV/outFOV. The black data points show observations with low SP contamination (inFOV/outFOV=1-1.15), whereas the blue points comprise observations that were severely affected by SP contamination (inFOV/outFOV=1.6-2.0). The left panel shows the stacked profiles obtained when subtracting only the QPB component, while in the right panel, the SP and QC components have been taken into account following Eq. 3.2.

We developed and calibrated a novel technique to model and subtract the non-X-ray background (NXB). Our approach builds upon the method devised in Tchernin et al. (2016); however, it can be more reliably applied to observations including a significant source emission above 5 keV. Here we describe the main principles of our method and validate it using a large set of blank-sky *XMM-Newton* pointings.

3.3.1 Model

It has long been known that the NXB of *XMM-Newton* is split into two main components, the quiescent particle background (QPB) and the soft protons (SP). Recently, Salvetti et al. (2017) has analysed almost the complete *XMM-Newton* archive and showed the presence of an additional stable, low-intensity component within the field of view (FOV) of the MOS2 instrument, whose origin is yet unknown. As described in Sect. 4.2, a fraction of the area of the MOS detectors is located outside the FOV of the *XMM-Newton* telescopes. The outFOV area can be used to estimate the QPB level in each observation by rescaling filter-wheel-closed data to the measured outFOV count rate. The remaining inFOV high-energy count rate can then be decomposed into a variable component (SP) and a quiescent part (QC). We can thus describe the remaining NXB as

$$\text{inFOV} - \text{outFOV} = \text{SP} + \text{QC}, \quad (3.1)$$

where inFOV and outFOV denote the [7–11.5] keV MOS2 count rates measured in the exposed and unexposed areas of the detector, respectively. We restrict the measurement to the MOS2 detector as two of the MOS1 chips have been lost throughout the mission, and the unexposed area of the pn detector is too small for our needs.

Importantly, the SP component is expected to show a different spatial signature on the detector compared to the QPB. Indeed, soft protons, which are funneled towards the detector through the telescope, are more spatially concentrated than the QPB and follow a vignetting curve $\text{SP}(r)$ that is different from the vignetting curve of the photons (Kuntz and Snowden, 2008), where r denotes the distance of each pixel from the aim point. Conversely, given that its origin is currently unclear, the spatial distribution of the QC component is unknown. Here we make the hypothesis that this component is flat over the detector.

3.3.2 Blank-sky dataset and modelling

To determine the relative contributions of the SP and QC components, we used a large set of 495 *XMM-Newton* blank-sky pointings, most of which are from the XXL survey (Pierre et al., 2016). Our dataset comprises more than 5 Ms of data. We processed the data using ESAS in the same way as for the A2319 data (see Sect. 4.2). We estimated the QPB component in each observation by measuring the outFOV count rate and rescaling filter-wheel-closed data. We also compute the high-energy inFOV and outFOV count rates for each observation. We then measured the radial profiles in the [0.7–1.2] keV band of the blank-sky pointings from the aim point to the outermost edge of the pointing in annuli of 30 arcsec width. The detected sources were masked and the QPB was subtracted from the data. As already shown

in Tchernin et al. (2016), this procedure results in radial profiles that are on average not flat, which indicates the need of modelling additional components (SP and QC).

We then describe the radial profiles $S_X(r)$ as the sum of the SP and QC components following their respective spatial distributions,

$$S_X(r) = C + N_{QC} + N_{SP}(\text{inFOV} - \text{outFOV} - \bar{Q}C)SP(r), \quad (3.2)$$

where C is the sky background intensity at the relevant location, N_{QC} the intensity of the stable QC component, N_{SP} the normalization of the variable SP, and $\bar{Q}C = 0.023$ counts/s is the mean high-energy count rate of the QC component (Salvetti et al., 2017). We then perform a joint fit on all the measured profiles and optimize for the values of N_{QC} and N_{SP} . We then used the best-fit values of N_{QC} and N_{SP} to create 2D models of these components and subtract them from the data.

In Fig. 3.3 we show the stacked radial profiles of the full sample. In the left-hand panel we show the stacked profiles obtained when subtracting the QPB component only, whereas in the right-hand panel, the SP and QC components have been modelled using the method described above and subtracted from the data. To investigate the dependence of our results on SP contamination, we grouped the data in bins of increasing SP contamination, which we trace using the inFOV/outFOV ratio (Leccardi and Molendi, 2008). Observations that were mildly affected by SP contamination exhibit an inFOV/outFOV ratio close to one, whereas heavily contaminated observations show high values of the inFOV/outFOV ratio. The effect of SP contamination is evident in the left-hand panel of Fig. 3.3, where the deviations of the stacked profiles from a straight line progressively increase with increasing SP contamination. Conversely, when applying our SP and QC modelling approach, flat profiles are found in all four bins out to the edge of the FOV, indicating that our model accurately reproduces the various NXB components. The excess scatter compared to a straight line is 5%, which we adopt as our systematic uncertainty in the subtraction of the NXB.

3.4 *Planck* data analysis

Planck was also part of ESA's Horizon 2000 Scientific Programme, however was launched in May 2009 with main scientific goal to map the anisotropies of the CMB through a few full-sky surveys with unprecedented sensitivity and angular resolution.

It is composed of 3 Low Frequency Instrument (LFI) working at 33, 44, and 70 GHz, and 6 High Frequency Instrument (HFI) at 100, 143, 217, 353, 545, and 857 GHz. *Planck* completed five full-sky surveys with all of its instruments in its 30 months of operation, thus ending its operations in October 2013.

3.4.1 Data reduction

The tSZ signal is recovered from the *Planck* survey (Planck Collaboration et al., 2016a; Tauber et al., 2010), making use of the six frequency maps provided by the High Frequency Instrument (HFI, Lamarre et al., 2010; Planck Collaboration et al., 2016b; Planck HFI Core Team et al., 2011) on board the *Planck* satellite. They are combined with the MILCA method (Modified Internal Linear Combination Algorithm, Hurier et al., 2013) to produce a Comptonisation parameter maps, i.e., y -map tracing the intensity of the SZ effect. The maps used for the X-COP project are provided with a resolution of 7 arcmin FWHM.

More specifically, we made use of the Modified Internal Linear Combination Algorithm (MILCA, Hurier et al., 2013) which offers the possibility to reconstruct the targeted signal component at various scales contributed differently by the six combined input frequency maps. We therefore reconstructed a y -map for A2319 with an angular resolution of 7 arcmin FWHM (see Fig. 4.6).

As illustrated for the cases of A2142 (Tchernin et al., 2016) and A2319 (Ghirardini et al., 2018b), we followed for the whole X-COP sample the methodology presented and used in Planck Collaboration et al. (2013). Assuming azimuthal symmetry of the cluster, we computed the y radial profile for each cluster over a regular grid scaled in units of R_{500} , with radial bins of size $\Delta\theta/\theta_{500} = 0.2$ out to $10 \times R_{500}$. The local background is assumed to be flat and constant and is computed from the area beyond $5 \times \theta_{500}$. A covariance matrix is computed for each profile to account for the correlation between points, due to the profile binning, and intrinsic noise correlation introduced from the y map construction. It cascades on the y and pressure profiles computation, hence their respective covariance matrix.

Consequently, we note that points of our y and SZ pressure profiles are correlated and that the respective error bars displayed in the figures of this thesis only represent the square root of the diagonal of the covariance matrix. Nevertheless, when pressure is used to derive other quantities we make complete use of the whole covariance matrix, and therefore we consider any impact of the *Planck* PSF in our calculations.

To extract the pressure profile we correct from the *Planck* beam redistribution through a real space deconvolution of the instrument PSF. Further assuming the spherical symmetry of the source, we reconstructed each pressure profile through a geometrical deprojection. The two steps follow the method initially presented in Croston et al. (2006). The associated covariance matrix for the pressure profile is obtained via a Monte Carlo procedure by randomising over the initial y profile covariance matrix. Throughout this thesis, we ignore the innermost three *Planck* data points because of the difficulty of deconvolving from the large *Planck* beam.

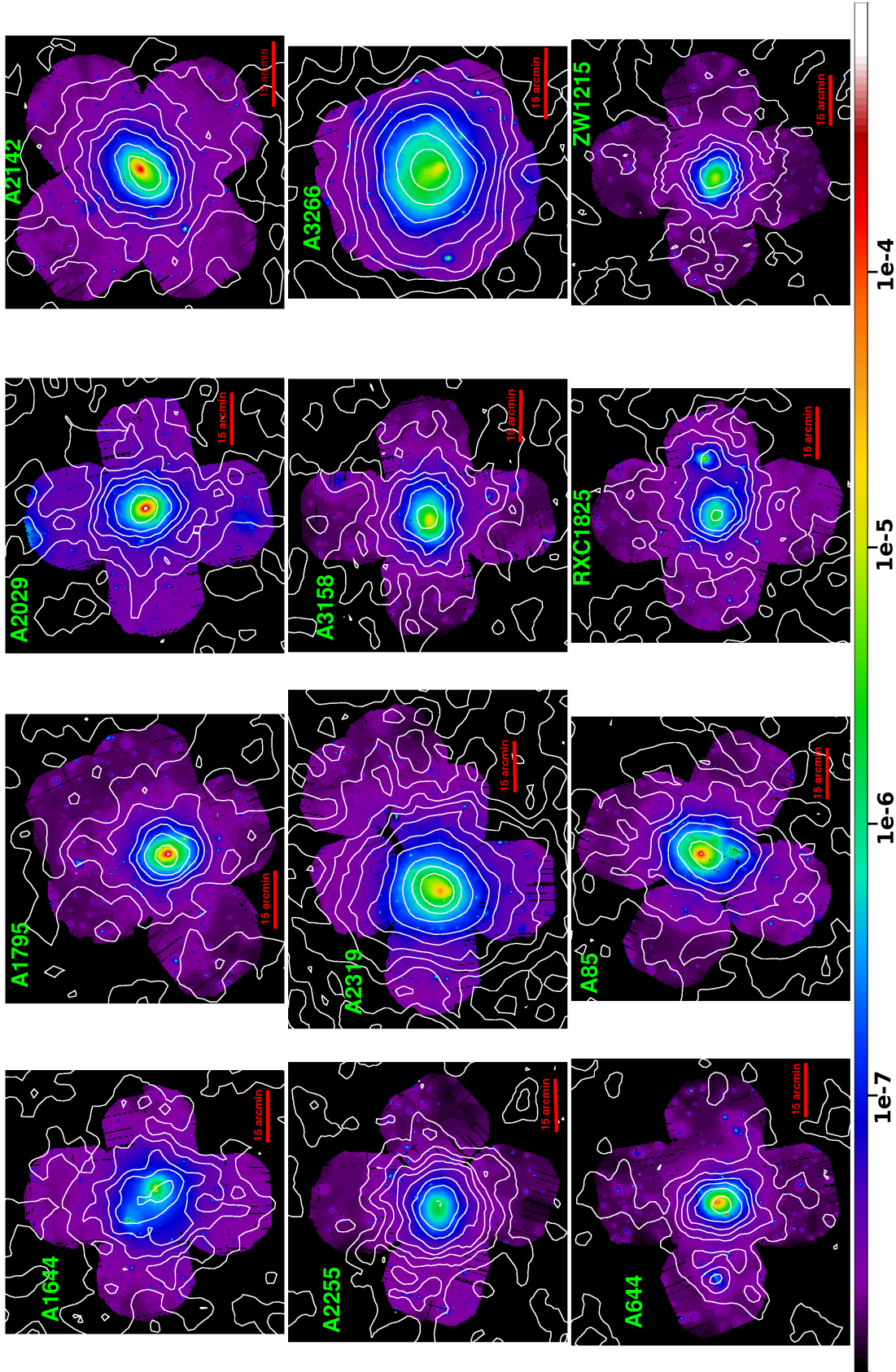


Fig. 3.4 Adaptively smoothed and exposure corrected *XMM-Newton* mosaic images in the [0.7–1.2] keV energy band for all X-COP clusters. The over-imposed white contours represents the *Planck* SZ S/N maps between 70 and 857 GHz. The contour levels correspond to 1, 3, 5, 7, 10, 15, 20, 30, 40, and 50σ . The spatial scale is given by the red thick lines, which have a common length of 15 arcmin. The color scale is given below the images, its units are $\text{cts s}^{-1} \text{pixel}^{-1}$, and it is the same for all clusters.

Table 3.1 Master table presenting the basic properties of the X-COP sample.

Name	z	S2N <i>Planck</i>	$L_{X,500}$ [10^{44} ergs s $^{-1}$]	kT_{vir} [keV]	M_{500} [$10^{14} M_{\odot}$]	R_{500} [kpc]	θ_{500} [arcmin]	K_0 [keV cm $^{-2}$]
A2319	0.0557	49.0	5.66 ± 0.02	$9.60^{+0.30}_{-0.30}$	10.56	1525	23.5	270 ± 5
A3266*	0.0589	40.0	3.35 ± 0.01	$9.45^{+0.35}_{-0.36}$	10.30	1510	22.1	72 ± 50
A2142*	0.090	28.4	8.09 ± 0.02	$8.40^{+1.01}_{-0.76}$	8.51	1403	13.9	68 ± 2
A2255	0.0809	26.5	2.08 ± 0.02	$5.81^{+0.19}_{-0.20}$	4.94	1172	12.8	529 ± 28
A2029	0.0773	23.2	6.94 ± 0.02	$8.26^{+0.09}_{-0.11}$	8.36	1399	16.1	10 ± 1
A85	0.0555	22.8	3.74 ± 0.01	$6.00^{+0.11}_{-0.11}$	5.24	1205	18.6	13 ± 1
A3158	0.059	19.8	2.01 ± 0.01	$4.99^{+0.07}_{-0.07}$	3.98	1097	16.0	166 ± 12
A1795	0.0622	19.3	4.43 ± 0.01	$6.08^{+0.07}_{-0.07}$	5.33	1209	16.8	19 ± 1
A644	0.0704	17.3	3.40 ± 0.01	$7.70^{+0.10}_{-0.10}$	7.55	1356	16.8	132 ± 9
A1644	0.0473	16.1	1.39 ± 0.01	$5.09^{+0.09}_{-0.09}$	4.12	1115	20.0	19 ± 1
RXC J1825	0.065	15.2	1.38 ± 0.01	$5.13^{+0.04}_{-0.04}$	4.13	1109	14.8	218 ± 6
ZwCl 1215	0.0766	12.8 †	2.11 ± 0.01	$6.27^{+0.32}_{-0.29}$	5.54	1220	14.0	163 ± 36

Column description: 1. Cluster name. The clusters identified with an asterisk were mapped prior to X-COP. Abbreviated names: RXC J1825.3+3026, ZwCl 1215.1+0400; 2. Redshift (from NED); 3. Signal-to-noise ratio (S2N) in the *Planck* PSZ2 catalog (*Planck* Collaboration et al., 2016d). 4. Luminosity in the [0.5–2] keV band (rest frame); 5. Virial temperature; 6. Mass within an overdensity of 500, estimated using the $M - T$ relation of Arnaud et al. (2005); 7. Corresponding value of R_{500} (in kpc); 8. Apparent size of R_{500} in arcmin; 9. Central entropy K_0 , from Cavagnolo et al. (2009);

Table 3.2 Log of X-COP observations.

Target	Obs.Id.	Obs.Date [yr/mm/dd]	N_H [10^{20}cm^{-2}]	t_{M1} [ks]	t_{M2} [ks]	t_{pn} [ks]
A1644 Center	0010420201	2001-01-08	4.2	13.5	13.6	11.9
A1644 E	0744413001	2015-01-01	4.3	15.5	17.5	10.3
A1644 N	0744412701	2014-12-29	3.9	27.5	28.4	14.8
A1644 S	0744412901	2014-12-31	4.4	10.2	11.3	4.7
A1644 W	0744412801	2015-06-30	3.8	29.2	28.7	21.7
A1795 Center	0097820101	2000-06-26	1.2	36.1	36.5	26.0
A1795 E	0744412101	2015-06-16	1.2	19.3	25.1	10.4
A1795 N	0744412001	2015-01-05	1.2	15.3	16.3	11.2
A1795 NW	0205190201	2004-01-25	1.2	22.5	22.9	21.1
A1795 S	0109070201	2003-01-13	1.2	52.6	53.5	52.1
A1795 W	0205190101	2004-01-25	1.1	29.2	28.9	27.0
A2029 Center 1	0551780201	2008-07-17	3.2	33.1	34.0	15.1
A2029 Center 2	0551780301	2008-07-19	3.2	39.0	40.9	27.4
A2029 E	0744411201	2015-01-31	3.2	26.0	26.7	20.6
A2029 N	0744410901	2015-02-08	3.0	17.5	22.3	6.6
A2029 S	0744411101	2015-02-22	3.4	11.0	16.6	4.9
A2029 W	0744411001	2015-07-27	3.2	42.6	43.3	39.2
A2142 Center	0674560201	2011-07-13	3.8	52.3	53.8	48.8
A2142 NE	0694440201	2012-07-14	3.8	33.2	33.1	29.8
A2142 NW	0694440101	2012-07-14	3.7	19.6	18.5	12.5
A2142 SE	0694440501	2012-07-16	4.0	33.2	32.5	29.8
A2142 SW	0694440601	2012-07-18	3.9	30.3	31.5	24.1
A2255 E	0744410801	2014-03-30	2.5	12.1	17.8	9.4
A2255 N	0744410501	2014-03-14	2.5	14.0	19.9	7.5
A2255 S	0744410701	2014-03-28	2.5	23.4	23.8	12.4
A2255 W	0744410601	2014-04-27	2.4	28.6	30.2	22.1
A2255 Center	0112260801	2002-12-07	2.5	7.7	8.2	2.3
A2319 E	0744410401	2014-04-08	9.1	14.5	15.9	10.9
A2319 N	0744410101	2014-03-15	8.8	23.9	24.2	21.8

Table 3.2 continued.

Target	Obs.Id.	Obs.Date [yr/mm/dd]	N_H [10^{20}cm^{-2}]	t_{M1} [ks]	t_{M2} [ks]	t_{pn} [ks]
A2319 S	0744410301	2014-04-04	8.2	13.8	14.3	8.2
A2319 W	0744410201	2014-04-09	7.7	23.8	25.4	11.1
A2319 Center 1	0302150101	2005-10-10	8.1	15.7	15.6	10.6
A2319 Center 2	0302150201	2005-11-14	8.1	16.0	15.5	12.4
A3158 Center	0300210201	2005-11-22	1.4	19.8	19.7	11.2
A3158 E	0744411601	2015-08-29	1.4	31.2	31.7	26.2
A3158 N	0744411301	2014-11-12	1.3	28.1	28.6	21.5
A3158 S	0744411501	2015-05-31	1.3	28.0	28.6	19.3
A3158 W	0744411401	2015-03-01	1.3	20.8	20.2	16.4
A3266 f1	0105260701	2000-10-01	1.5	19.1	19.5	15.5
A3266 f2	0105260801	2000-10-11	1.5	19.6	19.6	15.5
A3266 f3	0105260901	2000-10-09	1.6	23.4	23.1	17.9
A3266 f4	0105262201	2000-09-27	1.5	3.0	2.9	3.2
A3266 f5	0105262101	2000-09-25	1.8	5.8	6.1	4.1
A3266 f5b	0105261101	2000-09-25	1.8	11.3	12.3	7.1
A3266 f6	0105262001	2000-09-23	1.7	6.2	5.6	2.5
A3266 f6c	0105262501	2003-03-15	1.7	6.3	6.8	3.1
A644 Center	0744412201	2014-04-07	7.5	19.7	25.4	11.8
A644 E	0744412601	2014-05-18	6.7	20.5	24.3	8.6
A644 N	0744412301	2014-10-22	7.4	35.1	35.8	30.3
A644 S	0744412501	2014-10-24	7.0	32.3	32.2	26.2
A644 W	0744412401	2015-04-08	7.5	30.6	30.4	18.9
A85 Center	0723802201	2013-06-18	2.8	95.8	97.9	85.2
A85 E	0744411901	2014-12-11	2.8	28.2	29.0	19.5
A85 N	0744411701	2015-01-12	2.9	22.0	23.4	14.8
A85 S	0065140201	2002-01-07	2.7	12.2	12.1	9.4
A85 W	0744411801	2015-06-06	2.8	28.4	28.2	21.1
A85 NW	0744930301	2014-06-23	2.8	29.2	30.4	21.0
RXCJ1825 Center	0744413501	2014-04-11	9.4	48.1	48.2	39.1
RXCJ1825 E	0744413901	2014-04-13	10.0	31.7	32.4	16.2

Table 3.2 continued.

Target	Obs.Id.	Obs.Date [yr/mm/dd]	N_H [10^{20}cm^{-2}]	t_{M1} [ks]	t_{M2} [ks]	t_{pn} [ks]
RXCJ1825 N	0744413601	2014-04-12	8.9	20.0	20.2	14.3
RXCJ1825 S	0744413801	2014-04-14	9.5	25.5	29.5	12.4
RXCJ1825 W	0744413701	2014-10-02	9.2	41.4	40.8	36.8
ZwCl1215 Center	0300211401	2006-06-24	1.7	23.3	24.0	16.3
ZwCl1215 E	0744413401	2015-12-17	1.7	26.0	26.0	21.1
ZwCl1215 N	0744413101	2014-12-06	1.7	18.2	18.5	10.1
ZwCl1215 S	0744413301	2015-06-04	1.8	28.9	28.7	24.4
ZwCl1215 W	0744413201	2015-06-11	1.8	21.4	24.2	12.9

Column description: 1. Target name; 2. Observation identifier; 3. Observation date; 4. Equivalent hydrogen column density as estimated from 21 cm maps (Kalberla et al., 2005); 4. Exposure time for MOS1 detector after flare removal; 5. Exposure time for MOS2 detector after flare removal; 6. Exposure time for pn detector after flare removal.

**THE XMM CLUSTER OUTSKIRTS PROJECT
(X-COP): THERMODYNAMIC PROPERTIES
OF THE INTRACLUSTER MEDIUM OUT TO
 R_{200} IN ABELL 2319**

4.1 Introduction

In this chapter, we focus on Abell 2319, the most significant SZ detection in the first *Planck* catalogue, with a S/N of 49.0 in the second *Planck* catalogue (Planck Collaboration et al., 2016d). Abell 2319 is a very hot and massive cluster at low redshift ($z = 0.0557$; Struble and Rood, 1999). Its galaxy distribution indicates that this is a merger of two main components with a 3:1 mass ratio, the smaller system being located $\sim 10'$ north of the main structure (Oegerle et al., 1995). The cluster exhibits a prominent cold front SE of the main core (Ghizzardi et al., 2010) and a giant radio halo (Farnsworth et al., 2013; Storm et al., 2015).

This chapter is organized as follows: in Sect. 4.2 we describe the reduction and analysis of X-ray data, from background modelling to spatial and spectral analysis; in Sect. 4.3 we present the data reduction and analysis of the *Planck* SZ data; in Sect. 4.4, we show the reconstructed profiles of the thermodynamic quantities, describe their properties, and discuss the different methods adopted to solve the hydrostatic equilibrium equation; in Sect. 4.5 the analysis in azimuthal sectors is illustrated; the gas mass fraction and the hydrostatic bias are shown in Sect. 4.6; and the summary of our main findings and our conclusions are discussed in Sect. 4.7.

Throughout this chapter, we assume a Λ CDM cosmology with $\Omega_\Lambda = 0.7$, $\Omega_m = 0.3$ and $H_0 = 70$ km/s/Mpc. At the redshift of A2319, 1 arcmin corresponds to approximately 64.9 kpc. Uncertainties are provided at the 1σ confidence level.

In the following, we refer to and plot as reference characteristic radii, $R_{500} = 1368$ kpc and $R_{200} = 2077$ kpc, that are defined at the overdensities of $\Delta = 500$ and 200, respectively, with respect to the critical density ρ_c , see Eq. (1.9), and using the hydrostatic mass profile (see Table 4.5 in Sect. 4.4.5).

4.2 *XMM-Newton* Analysis

The procedure to reduce *XMM-Newton* data, described in detail in Sect. 3.2, is applied to all seven of the observations we use in the analysis of Abell 2319: an archival central exposure, four offset observations (done specifically for the X-COP program), and two other archival exposures pointing just outside the virial radius and used to estimate the local sky background. Table 4.1 provides some information regarding these observations, such as the OBSID, the total and the clean exposure time, and the level of soft protons contamination obtained by comparing the measured count rate in a hard spectral band in the exposed and unexposed part of the field of view (inFOV/outFOV, Leccardi and Molendi, 2008).

Table 4.1 Information on A2319’s observations

Observation	OBSID	Total [ks]	MOS1 [ks]	MOS2 [ks]	<i>pn</i> [ks]	inFOV/outFOV
Centre	0600040101	58.3	48.3	49.3	41.1	1.215
North	0744410101	36.0	23.8	24.5	19.4	1.132
South	0744410301	31.0	13.8	14.0	7.0	1.406
East	0744410401	41.9	14.4	15.4	9.5	1.346
West	0744410201	37.5	23.4	25.1	9.8	1.152
Outside	0743840201	15.0	12.1	12.3	5.7	1.261
Outside2	0763490301	18.0	12.9	12.8	9.0	1.253

Notes. Pointing name, OBSID, total exposure time, and clean exposure time for MOS1, MOS2, and *pn*, and inFOV/outFOV ratio, for the seven observations used in this work. All the observations were obtained using the medium filter, the full frame science mode for MOS, and extended full frame for *pn*.

4.2.1 Spatial analysis

The resulting Voronoi tessellated count rate map for A2319 is shown in Fig. 4.1. We chose all the pixels in the image beyond 42 arcmin from the cluster centre as the region where we estimate the local sky background (the red region in Fig. 4.1). The background level is just the mean count rate in this region: $(1.82 \pm 0.06) \times 10^{-4}$ cts s⁻¹ arcmin⁻², in the energy band [0.7–1.2] keV (or, converting in flux using a power law spectral model with photon index 1.41: $1.46 \pm 0.05 \times 10^{-15}$ erg s⁻¹ cm⁻² arcmin⁻²).

As shown in Fig. 4.2, we also evaluated the surface brightness from both the azimuthal mean and the azimuthal median of the brightness distribution. Following the analysis in hydrodynamical simulations on the effects of the densest substructures on the average gas density profile (Roncarelli et al., 2013; Zhuravleva et al., 2013), Eckert et al. (2016a) show that the median is indeed less biased than the mean—it is a more robust estimator since it is unaffected by compact X-ray substructures filling a small fraction of the total volume—and that the ratio between mean and median can be used to estimate the relative impact of the detected clumps, providing an estimate of the level of gas clumpiness.

The electron density was then recovered using two different techniques: the ‘onion-peeling’ technique (e.g. Ettori et al., 2010) and the multiscale technique (Eckert et al., 2016a). Both assume the emission to be spherically symmetric. The latter technique also requires a super-parametric functional form for the density profile, decomposing the surface brightness in a very large number of β -models which can be individually deprojected. We obtained electron density profiles that are consistent within 0.7σ , and mean relative deviation of 5% up to the virial radius (see Fig. 4.3).

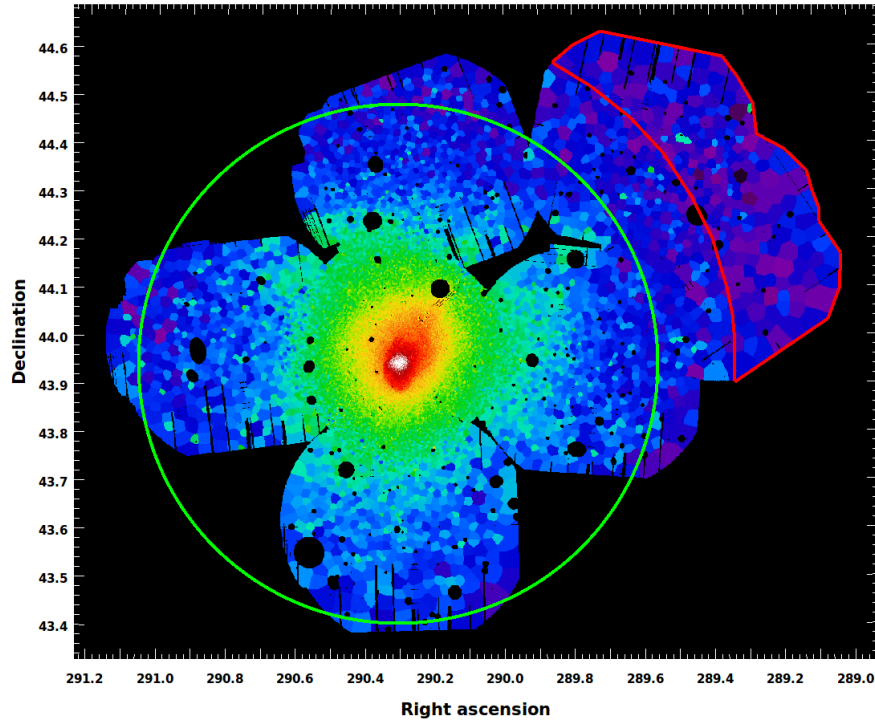


Fig. 4.1 Mosaicked and Voronoi tessellated image of A2319 in the energy band [0.7–1.2] keV corrected for the particle background. The red region is the one chosen for the estimate of the local sky background. The green circle represents the location of R_{200} .

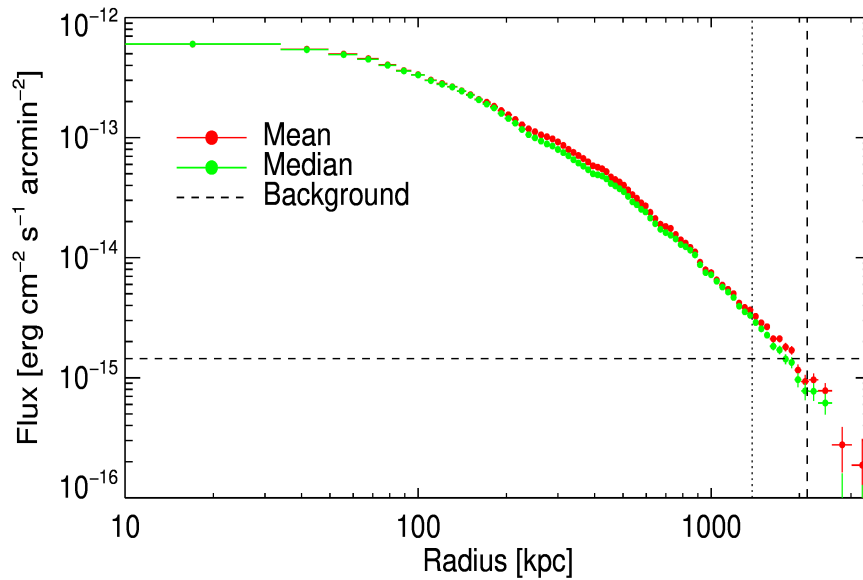


Fig. 4.2 Background-subtracted surface brightness profiles in the [0.7–1.2] keV energy band using the mean and median methods (red and green points, respectively). The sky background level is shown with a horizontal dashed line. The vertical dotted and dashed line represents the location of R_{500} and R_{200} , respectively.

4.2.2 Spectral analysis

Spectra are extracted and fitted as described in Sect. 3.3. For A2319, the number of net counts in the [0.5–11.3] keV energy band and the signal-to-background ratio are listed in Table 4.2.

All the spectra belonging to the same annulus, even if extracted from different observations, are fitted jointly using the C-statistics (Cash, 1979). The best-fit parameters are shown in Fig. 4.3 (with goodness of the fit, net counts, signal-to-background ratio, and best-fit n_H indicated in Table 4.2).

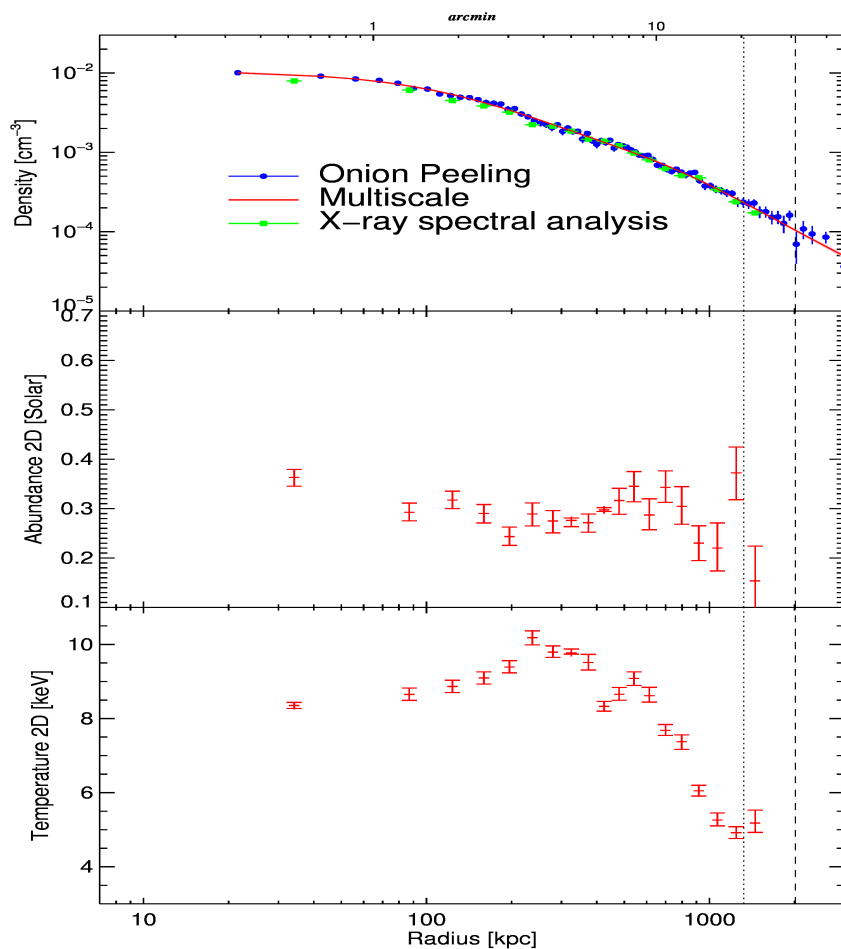


Fig. 4.3 (Top) Density profile recovered from the median surface brightness profile using the multiscale and the onion peeling technique (red line and blue points, respectively). The density coming from the spectral analysis is also shown here (green points). Abundance (Middle) and temperature (Bottom) from the fitting of the spectra in 19 annular regions. The vertical dotted and dashed line indicates the location of R_{500} and R_{200} , respectively.

4.2.3 Results of the spectral fitting

radii arcmin	C-stat.	PHA bins	C-stat. reduced	net cts 10^3	SBR	n_{H} 10^{22} cm^{-2}
-	-	-	-	-	-	-
0.00 - 1.05	2746	2603	1.05	170	85	0.075
1.05 - 1.63	2698	2591	1.04	155	58	0.078
1.63 - 2.18	2748	2552	1.08	148	42	0.081
2.18 - 2.74	2773	2575	1.08	145	32	0.077
2.74 - 3.32	2767	2484	1.11	131	24	0.078
3.32 - 3.98	2688	2573	1.05	133	17	0.081
3.98 - 4.65	2807	2582	1.09	134	14	0.079
4.65 - 5.37	2912	4005	0.73	131	11	0.075
5.37 - 6.14	2666	2387	1.13	112	8.6	0.074
6.14 - 6.95	2811	2481	1.13	101	6.8	0.077
6.95 - 7.83	3157	4949	0.64	92	5.1	0.074
7.83 - 8.85	3305	3866	0.85	89	3.6	0.073
8.85 - 10.05	3697	6052	0.61	82	2.5	0.074
10.05 - 11.51	4514	3868	1.17	80	1.7	0.076
11.51 - 13.10	4870	3583	1.36	62	1.2	0.079
13.10 - 15.18	4893	3494	1.40	46	0.9	0.077
15.18 - 17.70	2808	1844	1.52	20	0.9	0.121
17.70 - 20.63	2632	2175	1.21	19	0.6	0.101
20.63 - 24.08	2098	1916	1.09	12	0.4	0.113

Table 4.2 Statistical results of the fitting in the annular regions, with radial extension, C-statistic, number of spectral bins, reduced C-statistic indicated, net number of photons in the energy band [0.5–11.3] keV, signal-to-background ratio, and best-fit n_{H} .

In Table 4.2, we show the spectral fit results in the analysis described in Sect. 3.2, indicating the radial extension of the chosen annuli, the C-statistic, the number of the spectral bins, and the reduced C-statistic. We note that this last quantity is always of the order of 1, implying high goodness in the fit.

Since A2319 is located at low galactic latitude, $b = +13.5^\circ$, the choice to leave n_{H} free to vary is reinforced from the azimuthal variation over the cluster’s region of the dust emission as mapped at $100 \mu\text{m}$ by the InfraRed Astronomical Satellite (IRAS; see Fig. 4.4). The map shows that the sectors 5, 6, and 7 are expected to have higher Galactic absorption. Indeed the n_{H} in the eight considered sectors varies according to Table 4.3, with sector 5, 6, and 7 being $\sim 10\%$ above the other sectors.

Sector	1	2	3	4	5	6	7	8
$n_{\text{H}} [10^{20} \text{ cm}^{-2}]$	7.65	7.20	7.62	7.87	8.39	8.57	8.41	7.99

Table 4.3 Best-fit n_{H} in the eight sectors considered.

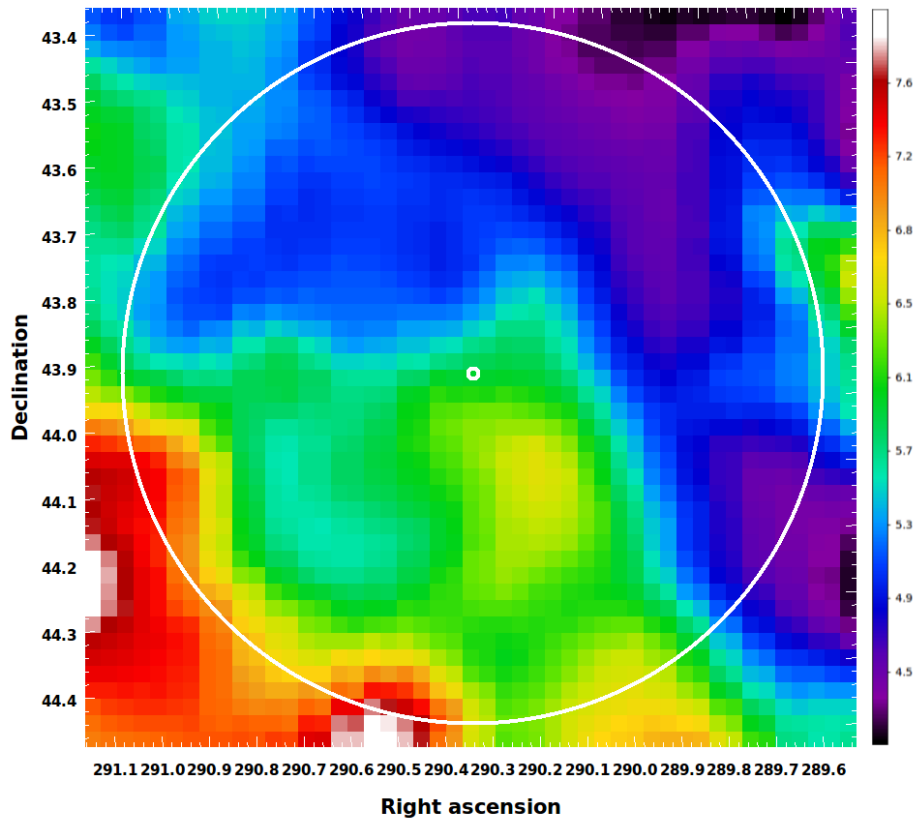


Fig. 4.4 IRAS map (minimum–maximum values in the region within R_{200} are 4.22, 7.77 MJy/sr). The white external circle represents the location of R_{200} , while the small circle represents the location of the centre of the cluster.

4.2.4 Comparison with *Chandra* data

We have analysed two archival *Chandra* observations of the inner region of A2319 (OBSID 15187, with a cleaned exposure time of 75 ksec, and OBSID 3231, with 15 ksec). We have processed the two *Chandra* ACIS-I observations of A2319 with a standard pipeline based on CIAO 4.9 (Fruscione et al., 2006) and CALDB 4.7.4 to create a new events-2 file which includes filtering for grade, status, bad pixels, and time intervals for anomalous background levels. The background is estimated through blank sky observations. We have extracted the spectra in the same annular regions as for *XMM-Newton*, and fit them in the identical way, leaving the galactic column density n_{H} free to vary within the range $7 - 13 \times 10^{20} \text{ cm}^{-2}$. The temperature profiles are compared in Fig. 4.5. We observe a good agreement among these spectral measurements, despite the claimed and still debated cross-calibration issue between *Chandra* ACIS and *XMM-Newton* EPIC (see e.g. Schellenberger et al., 2015), in particular in very hot systems ($T > 5 \text{ keV}$) as A2163. We suggest that leaving free n_{H} plays a determinant

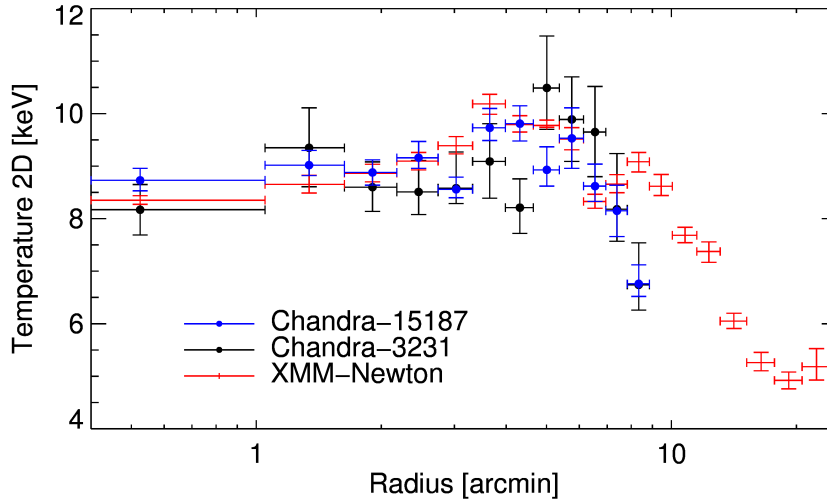


Fig. 4.5 Comparison between the spectral temperature obtained using *Chandra* and *XMM-Newton*. There is a clear excess in the temperature measured by *Chandra* of the order of 2-3 keV up to 7 arcmin.

role in adjusting the relative impact of the soft part of the spectra, where most of the observed systematic tension has been reported. In the present case, *Chandra* prefers systematically higher values of n_{H} ($\sim 1.2 - 1.3 \times 10^{21} \text{ cm}^{-2}$) than *XMM-Newton* (see Table 4.2) in all the radial bins. These higher values agree more closely with the column density corrected for molecular hydrogen as suggested in Willingale et al. (2013).

4.3 Planck analysis

The *Planck* data analysis applied in this chapter to analyze Abell 2319 is described in detail in Sect. 3.4. We reconstructed a y -map for A2319 with an angular resolution of 7 arcmin FWHM (see Fig. 4.6). We extracted the y -profile computing also the correlation matrix between data points, defined as

$$\rho_{X,Y} = \frac{\Sigma(X,Y)}{\sigma_X^2 \sigma_Y^2},$$

where Σ indicates the covariance matrix. We show the correlation matrix in Fig. 4.6.

Abell 2319 is the highest signal-to-noise ratio SZ detected cluster in the *Planck* SZ catalogues ($S/N \sim 50$; see Planck Collaboration et al., 2014a, 2016d). Its proximity and its extension makes it fully resolved even at the moderate angular resolution of the *Planck* survey, and its SZ signal extends well beyond R_{500} at high significance. We thereby were able to perform an azimuthal analysis in eight azimuthally resolved sectors (see Sect. 4.5).

The y and pressure profiles in each sector were obtained as described above after masking the y -map and its associated error map according to the sector definition.

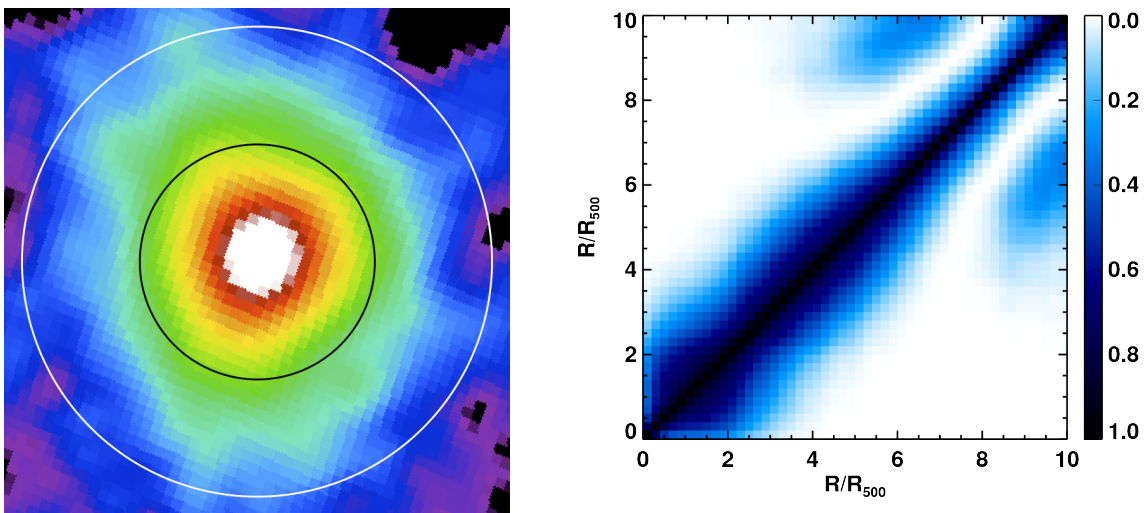


Fig. 4.6 *Left:* Comptonization map of Abell 2319 reconstructed using MILCA (Hurier et al., 2013), with an angular resolution of 7 arcmin FWHM. The black and white circles indicate the location of R_{500} and R_{200} , respectively. *Right:* *Planck* correlation matrix $\rho_{X,Y}$ for the unbinned Comptonization parameter profile.

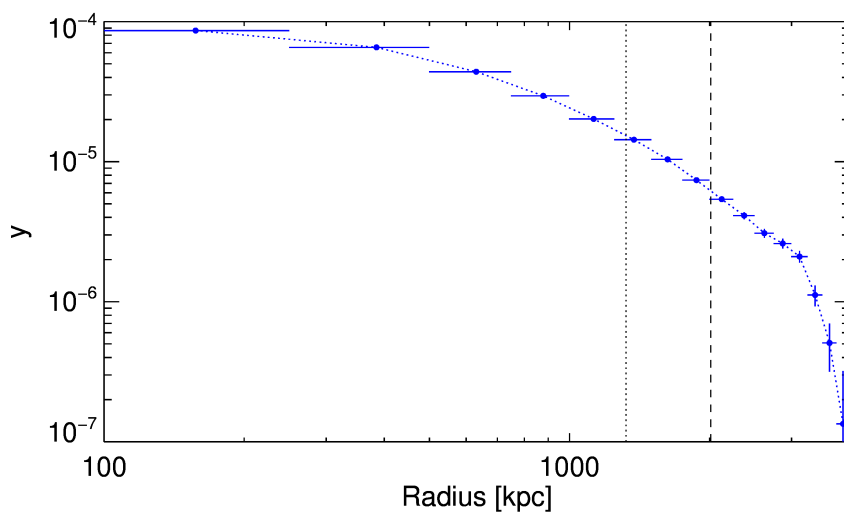


Fig. 4.7 Comptonization profile extracted from the SZ map. The vertical dotted and dashed line indicates the location of R_{500} and $2R_{500}$, respectively.

4.4 Joint X-ray–SZ analysis of the thermodynamic properties

The profiles of the electron density estimated from X-rays and of the pressure obtained through SZ can be combined to recover all the thermodynamic quantities that define the properties of the ICM:

- the gas temperature

$$T = P \cdot n_e^{-1}; \quad (4.1)$$

- the gas entropy

$$K = T \cdot n_e^{-2/3} = P \cdot n_e^{-5/3}; \quad (4.2)$$

- the gas mass

$$M_{\text{gas}}(< R) = 4\pi \int_0^R \rho_g(r') r'^2 dr', \quad (4.3)$$

where the gas mass density $\rho_g = (n_e + n_p)m_u\mu$ with m_u being the atomic mass unit and $\mu \approx 0.6$ the mean molecular weight in amu;

- the hydrostatic gravitating mass:

$$M_{\text{tot}}(< r) = -\frac{r^2}{G\rho_g(r)} \frac{dP_g(r)}{dr}, \quad (4.4)$$

where G is the gravitational constant, and the gas pressure P_g satisfies the ideal gas law $\rho_g kT / (\mu m_u) = P_g$. The gas mass fraction is then defined as $f_{\text{gas}} = M_{\text{gas}} / M_{\text{tot}}$.

4.4.1 Clumpiness profile

X-ray imaging can be directly used to estimate the level of inhomogeneities present in the ICM. The clumping factor $C = \langle n_e^2 \rangle / \langle n_e \rangle^2$ measures the bias that affects the reconstruction of the gas density from the X-ray emission, which is directly proportional to n_e^2 . Since we are considering the X-ray signal collected in a narrow energy range ([0.7–1.2] keV), which is almost insensitive to the gas temperature, we can directly use the results from the spatial analysis to estimate the gas clumping factor C .

In a first approximation, the density distribution inside a volume shell can be described by a log-normal distribution skewed by the presence of denser outliers or clumps (Roncarelli et al., 2013; Zhuravleva et al., 2013). Therefore, while the mean of this distribution tends to overestimate the gas density, the median is robust against the presence of clumps (Eckert

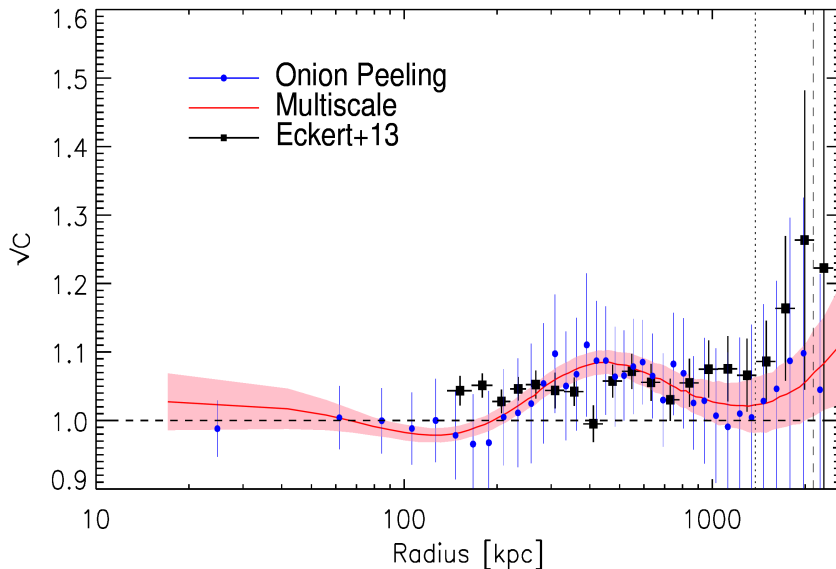


Fig. 4.8 Clumping factor radial profile for both techniques, onion peeling (blue) and multiscale (red). The pink area represents the 1σ confidence interval around the multiscale clumping factor. The black squares represent the observed value for the clumpiness in the work of Eckert et al. (2015). The vertical dotted and dashed line marks the position of R_{500} and R_{200} , respectively.

et al., 2015), and we can estimate C as the ratio of the deprojected X-ray surface brightness profiles obtained from (i) the mean of the azimuthal distribution of the counts in annuli and (ii) the median of the same distribution. The resulting profile is shown in Fig. 4.8 and indicates a \sqrt{C} of about 1.1 at R_{200} .

However, we can only detect clumps that are resolved by *XMM-Newton*, i.e. clumps on scales larger than the PSF half energy width (~ 17 arcsec ≈ 18.4 kpc, for MOS¹; see also Read et al. (2011)). This implies that clumped structures below this scale might still bias our measured thermodynamic quantities.

4.4.2 Temperature profile

Similarly to what was done for the pressure, we were able to recover the ICM temperature profiles in two different ways: (i) from the spectral analysis (T_X), as detailed in Sect. 4.2.2 and (ii) by dividing P_{SZ} by the gas density n_e recovered from the deprojection of the X-ray surface brightness (T_{SZ}). These values can be compared with the profile T_{NFW} that is obtained from the best-fit mass model (see Sect. 4.4.5) by requiring that the hydrostatic equilibrium holds between the cluster potential and the observed gas density profile. We note that T_{NFW}

¹<https://heasarc.nasa.gov/docs/xmm/uhb/onaxisxraypsf.html>

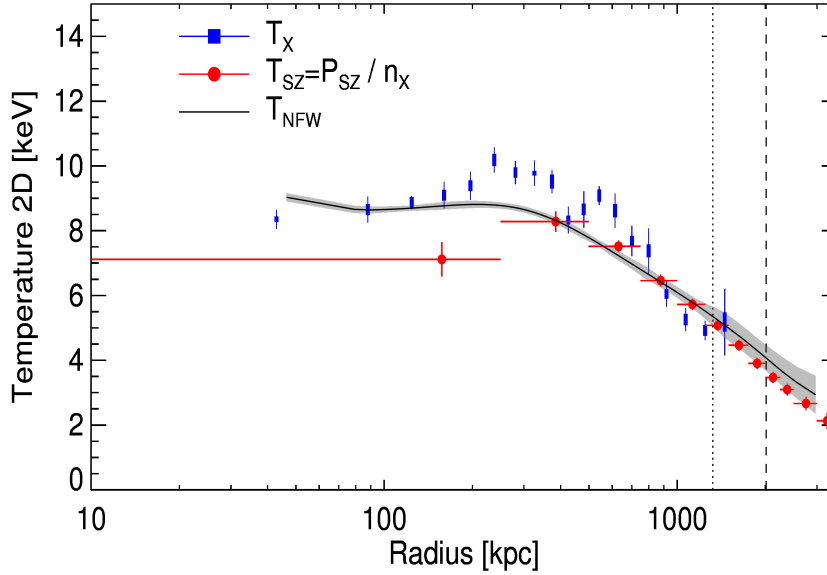


Fig. 4.9 Two-dimensional temperature profiles using X-ray spectral data (blue points; thick error bars represent the systematic uncertainty as estimated in Sect. 4.4.3, and thin error bars indicate the total uncertainties); the pressure from SZ divided by density from X-ray projected on the plane of the sky (red points); and the projection of the reconstructed temperature from the *backward* technique, which makes use of both X-ray and SZ data, on an NFW mass model (black line). The grey shaded area is the 1σ confidence region around the *backward* result. The vertical dotted and dashed line marks the position of R_{500} and R_{200} , respectively.

is not independent of the other two profiles because the best-fit mass model is obtained by fitting both the measured T_X and P_{SZ} . In order to obtain a meaningful comparison with T_X , we compute a spectroscopic projection (see Mazzotta et al., 2004; Morandi et al., 2007) of the 3D quantities T_{SZ} and T_{NFW} . The good agreement among these profiles is shown in Fig. 4.9.

Because the pressure gradient in the first point is washed out from the *Planck*'s beam of about 7 arcmin, we note that the pressure in this point is underestimated, and therefore the temperature T_{SZ} is also underestimated with respect to T_X .

4.4.3 Systematic uncertainties on the temperature profile

We constrain the projected spectroscopic temperature (see Sect. 4.2.2) with a relative statistical uncertainty ranging between 1% and 6% (median value: 2%). It is thus critical to evaluate the role of possible systematics in our measurements. In order to calculate some of the most relevant systematic uncertainties affecting our temperature measurements, we re-estimate the spectral temperature using several different methods. Our reference temper-

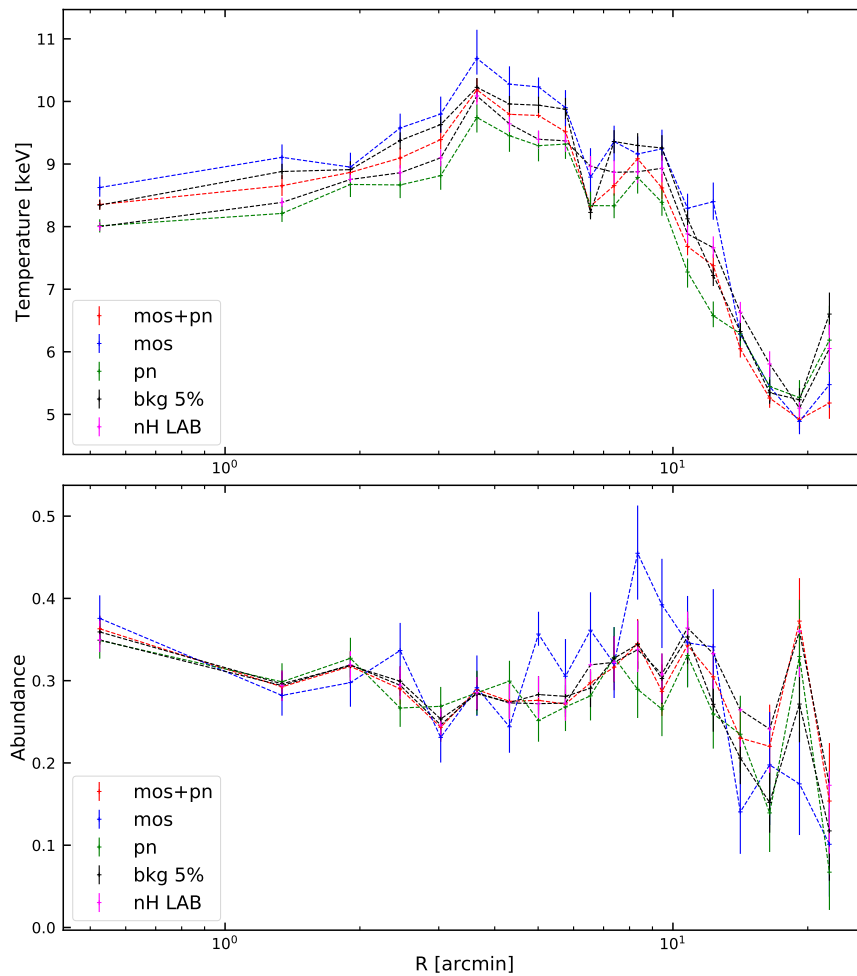


Fig. 4.10 Temperature and abundance profile adopting different techniques: using jointly MOS and pn (red), using only MOS (blue), using only pn (green), allowing the background normalizations to vary (black), and fixing the n_{H} to the LAB value (Kalberla et al., 2005); this provides an estimate of the systematic error affecting our measurement.

ature measurement is the one calculated using both MOS and *pn* data, leaving n_{H} free to vary within a defined narrow range, and fixing the parameters of the background model. By changing all these quantities one by one, we estimate the level of systematic errors that affect our measurements. In detail, we calculate the spectral temperatures in four ways: (i) only using counts collected from MOS, (ii) only using counts from *pn*, (iii) fixing n_{H} to the LAB value (Kalberla et al., 2005), and (iv) allowing the background parameters (normalizations) to vary within $\pm 5\%$ of the best-fit values. We show in Fig. 4.10 the results of this procedure. Finally, at each radial point, we estimate the systematic error using the standard deviation of the values measured with all the different methods. This error is then added, in quadrature, to the statistical error and propagated through the entire analysis. The relative systematic error

	P_0	c_{500}	γ	α	β	χ^2	d.o.f.
Arnaud et al. (2010)	8.40	1.18	0.31	1.05	5.49	-	-
Planck Collaboration et al. (2013)	6.41	1.81	0.31	1.33	4.13	-	-
SZ+X	7.7 ± 2.0	1.34 ± 0.22	0.47 ± 0.07	1.05	3.80 ± 0.22	2.62	69
SZ	9.6 ± 5.8	1.10 ± 0.35	0.23 ± 0.23	1.05	4.50 ± 0.47	3.47	9

Table 4.4 Best-fit parameters of the pressure profile using the functional form introduced by Nagai et al. (2007). ‘SZ+X’ refers to the best fit done on the best-fit mass model pressure profile (see Sec. 4.4.5), while ‘SZ’ refers to the best fit done only on the P_{SZ} .

ranges between 1.4% and 9.1%, apart from the outermost radial point where we measure a value of 19%.

4.4.4 Pressure profile

If the galaxy cluster is not affected by an ongoing merger generating shocks through the ICM, the pressure is the thermodynamic quantity that presents a smoother spatial distribution along the azimuth. It is described by a ‘universal’ form (Arnaud et al., 2010; Nagai et al., 2007),

$$\frac{P(x)}{P_{500}} = \frac{P_0}{(c_{500}x)^\gamma [1 + (c_{500}x)^\alpha]^\frac{\beta-\gamma}{\alpha}}, \quad (4.5)$$

where

$$P_{500} = 1.65 \times 10^{-3} \text{ keV cm}^{-3} \left(\frac{M_{500}}{3 \times 10^{14} M_\odot} \right)^{2/3} E(z)^{8/3} \quad (4.6)$$

and $x = R/R_{500}$; γ , α , and β are the central slope, the intermediate slope, and the outer slope defined by a scale parameter $r_s = R_{500}/c_{500}$ ($R \ll r_s$, $R \sim r_s$ and $R \gg r_s$ respectively); and P_0 is the normalization. The values of R_{500} and M_{500} adopted here are presented in Table 4.5 (see Sect. 4.4.5). We list in Table 4.4 our best-fit values, using the entire available radial range to find the best fit.

The electronic pressure can be directly recovered from the Comptonization profile (see Eq. 1.20; P_{SZ}), and from the deprojection of X-ray measurements of the temperature and density profiles of the emitting electrons (P_X). We can also estimate the pressure profile required from the best-fit mass model to satisfy the hydrostatic equilibrium (P_{NFW} , see Sect. 4.4.5). As we show in Fig. 4.11, these 3D pressure profiles agree well within their statistical errors.

We rescale the pressure profile by P_{500} and fit it with the universal functional form (Nagai et al., 2007). The best-fitting results are listed in Table 4.4. The comparison with the results of *Planck* (Planck Collaboration et al., 2013) and Arnaud et al. (2010) is shown in Fig. 4.11. We

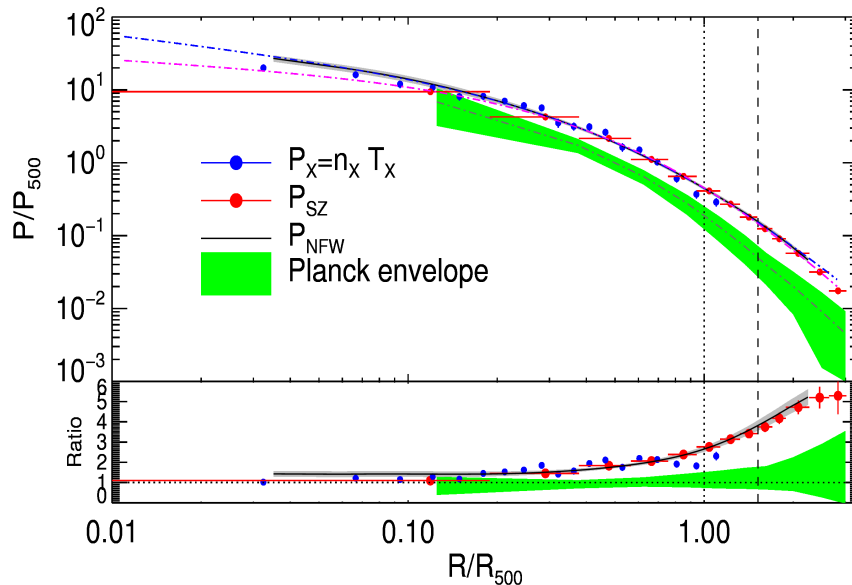


Fig. 4.11 Rescaled pressure profile in units of R_{500} . The black line with grey envelope represents the pressure profile required from the backward best-fit mass model. The blue and the pink lines represents the fit on the data using the functional form introduced by Nagai et al. (2007) on P_X and P_{SZ} , respectively. The dotted and dashed vertical line represents the position of R_{500} and R_{200} , respectively. In the bottom panel we show the ratio of P_{SZ} , P_X , and P_{NFW} with the universal pressure profile (Arnaud et al., 2010).

observe that the pressure profile in A2319 is well above the other two profiles, in particular in the outskirts, with values higher by about a factor of ~ 3.5 at R_{200} , which is $\sim 2\sigma$ away from the *Planck* envelope (Planck Collaboration et al., 2013).

We have also adopted a new technique (Bourdin et al., 2017) in order to evaluate the impact of the anisotropies in the Compton parameter detected in the outskirts of A2319 on the reconstructed pressure profile, and conclude that these anisotropies cannot explain the observed excess.

4.4.5 Hydrostatic mass

The total mass profile of the cluster is reconstructed by solving the hydrostatic equilibrium equation 4.4 (HEE, Binney and Tremaine, 1987). In this work, we use three different methods to solve this equation and recover the hydrostatic mass profile (e.g. Ettori et al., 2013a): the *backward* method, the *forward* method, and a *non-parametric* method.

The *backward* method follows the approach described in Ettori et al. (2010, 2017) and, assuming a mass model with few free parameters (generally two), minimizes a likelihood function by comparing the predicted and observed profiles of some interesting physical

Technique	Data	M_{200} ($10^{14}M_{\odot}$)	R_{200} (kpc)	M_{500} ($10^{14}M_{\odot}$)	R_{500} (kpc)
backward	$P_{SZ,NO3} + T_X$ - Median	10.7 ± 0.5	2077 ± 33	7.7 ± 0.4	1368 ± 17
backward	$P_{SZ} + T_X$ - Median	10.6 ± 0.5	2071 ± 32	7.5 ± 0.3	1357 ± 13
backward	$P_{SZ,NO3} + T_{X,SYS}$ - Median	10.3 ± 0.7	2047 ± 47	7.4 ± 0.4	1350 ± 24
backward	$P_{SZ} + T_{X,SYS}$ - Median	10.5 ± 0.5	2062 ± 34	7.3 ± 0.3	1347 ± 18
forward	P_{SZ} only - Median	9.4 ± 0.5	1984 ± 40	7.4 ± 0.4	1353 ± 25
forward	T_X only - Median	/	/	7.3 ± 0.1	1343 ± 5
forward	$P_{SZ} + T_X$ - Median	8.3 ± 0.3	1906 ± 20	7.8 ± 0.2	1375 ± 11
forward	$P_{SZ} + T_X, \beta$ fixed - Median	8.5 ± 0.6	1923 ± 48	7.7 ± 0.4	1368 ± 26
forward	$P_{SZ,NO3} + T_{X,SYS}, \beta$ fixed - Median	7.7 ± 0.7	1859 ± 59	7.4 ± 0.6	1354 ± 37
forward	$P_{SZ,NO3,SYS} + T_X$ - Median	8.3 ± 0.3	1907 ± 26	7.8 ± 0.3	1373 ± 18
non-parametric	P_{SZ} - Median	9.3 ± 1.1	1979 ± 78	6.7 ± 0.5	1307 ± 33
backward	$P_{SZ} + T_X$ - Mean	10.2 ± 0.5	2040 ± 35	7.3 ± 0.3	1346 ± 17

Table 4.5 Best-fitting results on the mass model using the techniques specified in the first column. In the second column the data used to constrain the mass are listed; P_{SZ} and T_X refer to the SZ pressure and the X-ray temperature, respectively; the subscript ‘NO3’ indicates that the first three *Planck* points were not used in the analysis; the subscript ‘SYS’ indicates that the systematic uncertainties on the X-ray temperature are added in quadrature to the statistical errors in evaluating the χ^2 (see Sec. 4.4.3); ‘Median’ or ‘Mean’ refers to how we computed the X-ray emissivity; ‘ β fixed’ indicates that the outer slope of the pressure profile is fixed to the best-fit value of the *Planck* collaboration. In the other four columns, we quote the results on M_{200} , R_{200} , M_{500} , and R_{500} , respectively. In the first row, we indicate our reference values in bold. The last two rows present the mass reconstructed using the mean density profile, and propagating the statistical error on the temperature profile only (see Sect. 4.4.3). R_{Δ} is defined as $\left(\frac{M(R)}{4/3\pi\rho_c\Delta}\right)^{1/3}$.

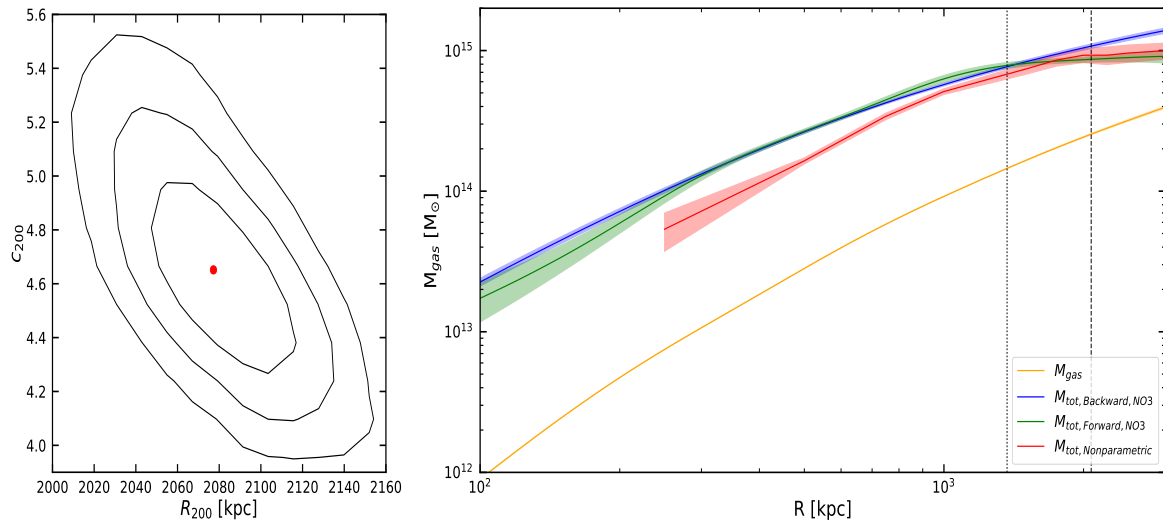


Fig. 4.12 (Left) Contour plot with confidence regions at 1, 2, and 3σ (solid lines) applying the *backward* approach to solve HEE in order to constrain the parameters of the NFW mass model; using as inputs the multiscale technique on the median emissivity profile to obtain the density, the pressure from the direct deprojection of the y -parameter radial profile, and the temperature from the spectral analysis. (Right) Gas mass and total mass profile recovered using the *backward* approach (blue and red curves, respectively). The black crosses represent the total mass profile obtained using a non-parametric method and the green cross that obtained by applying the *forward* method on temperature and density profiles. The dotted and dashed vertical line marks the position of R_{500} and R_{200} , respectively.

quantities (e.g. temperature) to constrain these parameters. In the present analysis, we assume a Navarro-Frenk-White profile (NFW, Navarro et al., 1997) for the total mass (a more extensive discussion on the best-fitting mass models will be presented in a forthcoming publication), and constrain its two parameters, concentration and scale radius (or R_{200}), using both the projected temperature profile from X-ray spectral analysis and the thermal pressure profile from the SZ analysis, and maximizing the likelihood described in Sect. 4.4.7.

In Fig. 4.12, we show the best-fit results obtained using this method to constrain the parameters of the mass model, using the median method and the multiscale technique to obtain the density profile. Very consistent results are obtained by adopting different methods to recover the input profiles of the gas temperature and density (see Table 4.5). We indicate with the subscript ‘NFW’ the thermodynamic quantities corresponding to the best-fit mass model.

In the *forward* method, functional forms are used to fit the thermodynamic quantities, density, pressure, and temperature. Then, HEE is directly applied in order to compute the total mass radial distribution. Errors are estimated through a Monte Carlo process. As mentioned in Sect. 4.2.1, we use the multiscale approach (Eckert et al., 2015) to fit the

emissivity profile which yields directly the fitted density functional form. We use a six-parameter functional form (Vikhlinin et al., 2006) to fit the temperature, and a five-parameter generalized NFW (Nagai et al., 2007) for the pressure. We combine in several ways the profiles of the thermodynamic quantities (density, pressure, and temperature), as detailed in Table 4.5, making use of a joint likelihood (see Sect. 4.4.7) when all three quantities are fitted together. It is worth noticing that, while measurements of the gas density and pressure are available up to $\sim R_{200}$, direct spectral estimates of the temperature are limited to regions below R_{500} , defining the radial range where the mass profile is more reliable in this case.

Due to the good quality data both from X-rays and SZ, we can also implement a *non-parametric* method in order to recover the total mass profile. We just insert pressure and density in the HEE, and we calculate the pressure derivative using a three-point quadratic Lagrangian interpolation. We note that the errors relative to this method are represented by a covariance matrix since we are using the SZ pressure profile, and therefore what is shown as an error bar in the plot is just the square root of the diagonal terms.

The recovered mass profiles are shown in Fig. 4.12. They are all compatible within their respective error bars at the characteristic overdensities of 500 and 200.

4.4.6 Systematic uncertainties on the hydrostatic mass

In Table 4.5, only the statistical error on M_{200} is quoted (with a relative uncertainty of about 4.7%). In this section, we evaluate the impact of some of the systematic uncertainties that affect the mass reconstruction.

The ability of the particle background model to reproduce a flat surface brightness profile when applied on blank field observations is a source of systematic uncertainty caused by the adopted procedure. As we discussed in Sect. 4.2, adopting the background model described in Sect. 3.3, we are able to reduce the systematic deviation from a flat profile below 5%. We account for this by adding 5% of the background level as an extra error in the surface brightness profile.

The results obtained by applying different methods and techniques are shown in Table 4.5. We estimate the level of the systematic uncertainties on the mass measurement at R_{500} and R_{200} of about 3.9% and 8.4%, respectively, by measuring the relative scatter around the reference value.

Another source of systematic uncertainty comes from the choice of the background region, defined in an area concentrated to the west of the cluster. Considering that A2319 has an angular extension of ~ 1 degree, cosmic variance can influence the analysis, especially in the outskirts. Using the absorbed thermal model *tbabs(apec)*, and fixing the parameters of the *apec* component, we vary the hydrogen column density alone by adopting the values of

n_H in regions located to the north, west, east, and south, as far as possible from the centre (at a distance of 33, 55, 36, and 39 *arcmin*, respectively) and remeasure the conversion factor between the count rate and the surface brightness maps. This procedure allows us to measure a relative deviation of 2% on the surface brightness, which translates into an effect of about 1.4% on the gas density and 1.1% on the mass measurement.

We therefore estimate that the total systematic uncertainties are at the level of 4.18% and 8.5% at R_{500} and R_{200} , respectively, implying that the reference values for the hydrostatic mass are, at R_{500} and R_{200} , respectively:

$$M_{500} = 7.7 \pm 0.4^{\text{stat.}} \pm 0.3^{\text{syst.}} \times 10^{14} M_{\odot}$$

$$M_{200} = 10.7 \pm 0.5^{\text{stat.}} \pm 0.9^{\text{syst.}} \times 10^{14} M_{\odot}$$

4.4.7 Likelihood for the mass reconstruction

We fit our thermodynamic quantities using the MCMC code *emcee* (Foreman-Mackey et al., 2013a), for which we define a likelihood. We included in the fitting procedure an intrinsic scatter, which is added in quadrature on the error of logarithm of pressure such that $\log P \sim \log P \pm \sigma_{int}$. By assuming a small value for σ_{int} we can write

$$\sigma_{P,int} \approx \frac{P \cdot \exp(+\sigma_{int}) - P \cdot \exp(-\sigma_{int})}{2} = P \cdot \sinh \sigma_{int}$$

and summed to the covariance matrix as

$$\Sigma_{tot} = \begin{bmatrix} \Sigma_{11} & \Sigma_{12} & \Sigma_{13} & \dots & \Sigma_{1n} \\ \Sigma_{21} & \Sigma_{22} & \Sigma_{23} & \dots & \Sigma_{2n} \\ \vdots & \vdots & \vdots & \ddots & \vdots \\ \Sigma_{n1} & \Sigma_{n2} & \Sigma_{n3} & \dots & \Sigma_{nn} \end{bmatrix} + \begin{bmatrix} \sigma_{P_1,int}^2 & 0 & 0 & \dots & 0 \\ 0 & \sigma_{P_2,int}^2 & 0 & \dots & 0 \\ \vdots & \vdots & \vdots & \ddots & \vdots \\ 0 & 0 & 0 & \dots & \sigma_{P_n,int}^2 \end{bmatrix}$$

where $\Sigma_{i,j}$ is the covariance matrix on the measured *Planck* pressure profile.

The intrinsic scatter is also propagated to the variance on temperature profile, added in quadrature to the measured errors:

$$\sigma_{tot}^2 = \sigma_T^2 + \sigma_{T,int}^2$$

with

$$\sigma_{T,int} = \frac{P_{model}}{n_{model}} \sigma_{P,int} = T_{model} \cdot \sigma_{P,int}$$

We recall that in general the likelihood is defined as

$$\mathcal{L} = \frac{1}{\sqrt{2\pi\sigma^2}} \exp(-\chi^2/2),$$

so that

$$\log \mathcal{L} = -0.5(\chi^2 + \log \sigma^2 + \log(2\pi)),$$

where the last term is a constant, and therefore is usually ignored while maximizing the likelihood, but the term with $\log \sigma^2$ is not. Finally, by using the subscript ‘m’ or ‘o’ to describe model predicted or observed quantities, respectively, we can explicitly write the logarithm of the likelihood we use to fit

$$\begin{aligned} \log \mathcal{L} = & -0.5 \left[(P - P_m) \Sigma_{tot}^{-1} (P - P_m)^T + n \log(\det(\Sigma_{tot})) \right] \\ & - 0.5 \sum_{i=1}^n \left[\frac{(T_i - T_{m,i})^2}{\sigma_{T,i}^2 + \sigma_{T,int}^2} + \log(\sigma_{T,i}^2 + \sigma_{T,int}^2) \right] \\ & - 0.5 \left[\sum_{i=1}^n \frac{(\varepsilon - \varepsilon_{m,i})^2}{\sigma_{\varepsilon,i}^2} \right] \end{aligned}$$

We point out that this method is independent of the method used to compute P_{model} and T_{model} , meaning that this kind of approach is valid both for the *forward* and *backward* methods.

4.4.8 Entropy profile

	k_0	$k_{100/500}$	α	χ^2	d.o.f.
Eq. (4.7)	75 ± 13	190 ± 12	0.82 ± 0.03	129	70
Eq. (4.10)	0.055 ± 0.010	1.17 ± 0.02	0.82 ± 0.03	124	70

Table 4.6 Best-fit results for the model of the entropy profile using the three different rescalings described in Sect. 4.4.8.

The entropy profile is recovered through the gas pressure and temperature profiles via Eq. (4.2). Entropy is a fundamental quantity that can track the thermal history of a cluster: it always rises when a heat flow occurs, and in the presence of only non-radiative processes it is expected to follow a power law with characteristic slope of 1.1 (Tozzi and Norman, 2001; Voit et al., 2005). Deviations from this power law are observed in the central regions, requiring

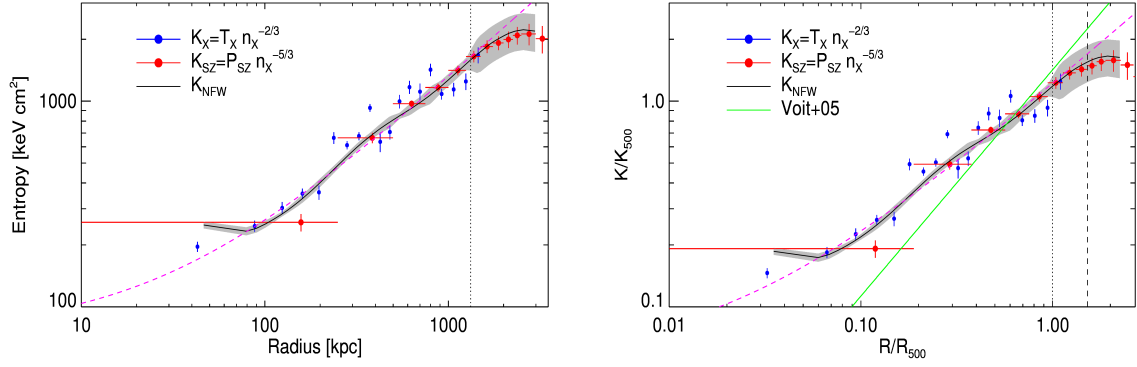


Fig. 4.13 (Left) Entropy profiles obtained from the three different methods described in Sec. 4.4.8. The dashed magenta line represents the best fit obtained on the K_{NFW} data using Eq. (4.7). (Right) Entropy profiles rescaled by K_{500} . The dashed magenta line represents the best fit obtained on the K_{NFW} data using Eq. (4.10). The green lines represents the prediction from Voit et al. (2005). The dashed pink lines are the best fit using Eqs. (4.7) and (4.10). The vertical dotted and dashed line represents the location of R_{500} and R_{200} , respectively.

an entropy ‘floor’ within ~ 100 kpc that is expressed through the formula (Cavagnolo et al., 2009)

$$K = k_0 + k_{100} \left(\frac{R}{100 \text{ kpc}} \right)^\alpha \quad (4.7)$$

The central entropy (k_0) measured with the fit in Eq. (4.7) is $75 \pm 13 \text{ keV cm}^2$ (see Table 4.6), suggesting that A2319 does not possess a relaxed, cool core (e.g. Cavagnolo et al., 2009, define a CC when $k_0 < 50 \text{ keV cm}^2$).

However, non-radiative simulations show that the self-similar behaviour is reproduced only once entropy is rescaled by a proper quantity defined with respect to the critical density (Voit et al., 2005)

$$K_{500} = 106 \text{ keV cm}^2 \left(\frac{M_{500}}{10^{14} M_\odot} \right)^{2/3} E(z)^{-2/3} f_b^{-2/3}, \quad (4.8)$$

where $f_b = 0.15$ is the universal baryon fraction. Non-radiative simulations (Voit et al., 2005) predicts that the power law describing the entropy profile is:

$$\frac{K(R)}{K_{500}} = 1.42 \left(\frac{R}{R_{500}} \right)^{1.1} \quad (4.9)$$

In order to accommodate the flattening of the entropy profile observed in many disturbed systems, we add a constant to a simple power law:

$$\frac{K(R)}{K_{500}} = k_0 + k_{500} \left(\frac{R}{R_{500}} \right)^\alpha. \quad (4.10)$$

In Fig. 4.13, we plot the measured entropy profiles, also rescaled according to Eq. 4.10. In Table 4.6, we show the best-fit results on the data using Eqs. (4.7) and (4.10). We observe that the entropy profile has a shallower slope with respect to the value predicted by the simulations (Voit et al., 2005).

4.5 Analysis in azimuthal sectors

4.5.1 Thermodynamic properties

Considering the high signal-to-noise ratio of our X-ray and SZ datasets, we can perform the analysis presented in the previous sections in each of the eight azimuthal sectors with width of 45° that we define in Fig. 4.14. The analysis performed in the sectors allows us to measure the azimuthal variance of the physical quantities and to assess which cluster regions are more relaxed. Indeed, by dividing the observed count rate map in Fig. 4.1 with a cluster model with perfect spherical symmetry and emission equal to the azimuthal median surface brightness profile, we can identify where an excess in the emission due to the ongoing merger is located. As shown in Fig. 4.14, this excess is concentrated in the NW region (sectors 1, 2, and 3, in particular).

We show the profiles of the thermodynamic properties recovered in eight angular sectors in Fig. 4.15.

In the X-ray surface brightness, we identify various features specific to each sector:

- Sector 1 has an excess in emission starting above 200 kpc with a small radial extent of about 100 kpc. This excess is due to a contamination of the merging component in this cluster, located 10 arcmin NW.
- Sector 2 also has a significant excess in the X-ray emission. This excess is located in the region where Oegerle et al. (1995) found the merging component in A2319, and has a radial extent that is quite large, from 200 to 800 kpc.
- Sector 3 has an emission slightly higher than the azimuthal average up to 1 Mpc, where a sharp transition is present reconciling the surface brightness with the azimuthally

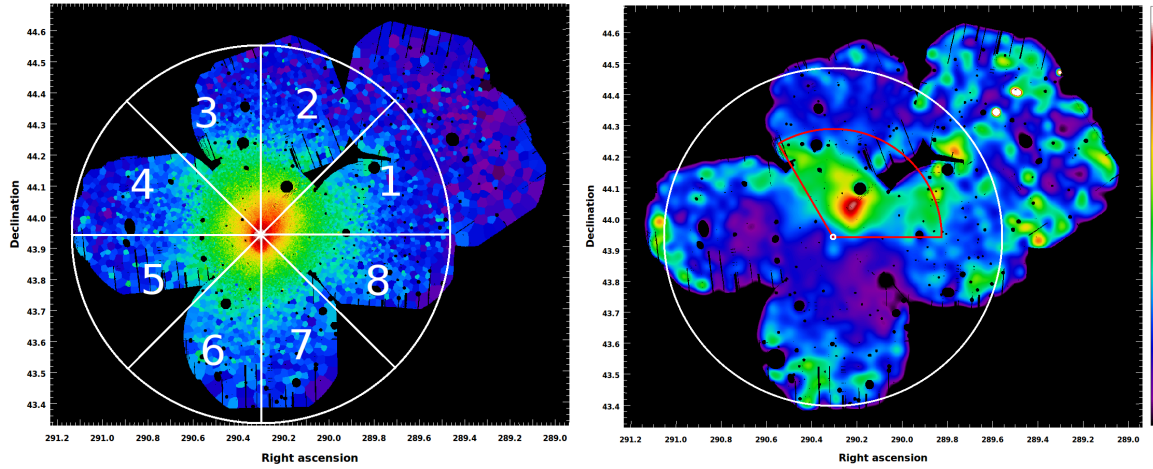


Fig. 4.14 (Left) Same as Fig. 4.1. The white sectors represents the eight regions analysed separately, each marked by a identification number. (Right) Residual image obtained by dividing the flux image by the model image reconstructed from the median method. The small white circle represents the centre of the cluster, and the big white circle represents the position of R_{200} . The red sector represents the region which shows a clear excess in the residual map.

averaged value. This sector shows evidence of a non-negligible contamination from the merger.

- Sectors 4 and 5 are quite regular, with a behaviour very similar to the azimuthally averaged profile.
- Sector 6 shows the cold front that was detected in Ghizzardi et al. (2010) and located in the SE region, about $200 \text{ kpc} \approx 3 \text{ arcmin}$ from the cluster centre.
- Sectors 7 and 8 are the most regular, and reproduce very well the combined surface brightness profile.

The pressure profile obtained from the deprojected SZ signal in each sector (see Fig. 4.15) shows clearly that this is the quantity least affected by the dynamical history of the cluster. For instance, the merging event (Oegerle et al., 1995) happening in the NW (sector 2) with mass ratio 3:1 is well resolved in the surface brightness/density profile, but it is not evident in the pressure profile (sector 3 has the highest values in the pressure profile, while sectors 1 and 2 are slightly below the azimuthally average profile), suggesting that the merger induced some shocks that have already propagated through the ICM and are at least partially thermalized, inducing a reasonably small scatter in the pressure profile at R_{200} (see Fig. 4.15).

From the spectral analysis, we observe in sector 2 that the gas temperature reaches values below those measured in the azimuthally averaged profile between 300 and 800 kpc. In sectors 1 and 3, the temperature behaves similarly, but over a narrower radial range. These radial variations can be explained by a low-temperature component contaminating sectors 1, 2, and 3 at intermediate radii. This can be associated with the accreting substructure visible in the residual map (Fig. 4.14), which is merging with the main cluster halo. Over the same region, corresponding to the merging component at about 500 kpc in sector 2, we also observe an increase in the metal abundance correlated to the gas at the lower temperature.

In Fig. 4.15, we show the entropy profiles obtained by solving the HEE with the *backward* method (a comparison between the profiles estimated with different methods is shown in Fig. 4.19). The entropy measured in sector 2 is well below the mean value estimated in the cluster, while sector 1 and 3 are just slightly below the mean value. This suggests that a substructure with a low-entropy gas is still accreting into the cluster's halo as residual of the ongoing merger.

4.5.2 Azimuthal scatter and clumpiness

The azimuthal scatter of the recovered thermodynamic quantities is defined at each radius r as

$$\sigma_Q(r) = \sqrt{\frac{1}{N} \sum_{i=1}^N \left(\frac{Q_i(r) - \bar{Q}_i(r)}{\bar{Q}_i(r)} \right)^2}, \quad (4.11)$$

with $Q = \{ n, P, T, K, M_{tot}, M_g, f_g \}$. The profiles of the azimuthal scatter are shown in Fig. 4.16.

As a general trend, we expect that $\sigma_Q(r)$ should increase monotonically with radius because as they move outward the considered radial points should be less virialized. Although this is generally observed, some other features also appear. For instance, at intermediate radii (~ 600 kpc) there is a clear increase coincidentally with the cluster centric location where the merger is taking place. Moreover, there is a particular radial location between R_{500} and R_{200} where the azimuthal scatter reaches a minimum. This point suggests the radial extension of the influence of the merger on the thermodynamic quantities.

Using this information, we can improve the characterization of the properties of the observed clumpiness in the gas density. As described in Roncarelli et al. (2013), the clumping factor of the gas (see Sect. 4.4.1) is expected to have two major contributors: some individual clumps and large-scale accretion patterns. The latter is described by the residual clumping

C_R , which, following Roncarelli et al. (2013), can be estimated as

$$C_R(r) = 1 + \frac{\sigma}{\sigma_0} + \frac{r}{r_0}, \quad (4.12)$$

where $r = R/R_{200}$; σ is the azimuthal scatter of the density n or of the Comptonization parameter y ; and σ_0 and r_0 are estimated from simulations (Roncarelli et al., 2013)

- $(\sigma_0, r_0) = (16.02, 5.87)$ for X-ray density,
- $(\sigma_0, r_0) = (2.83, 8.25)$ for SZ Comptonization parameter.

We compare the estimated clumpiness with the residual clumpiness C_R in Fig. 4.16. We observe that the measured clumping factor, both X-ray and SZ, only slightly exceeds the estimated C_R over the entire radial range, suggesting that large-scale asymmetries account for most of the clumpiness measured.

Moreover, the clumpiness profile in Fig. 4.8 shows a clear excess at intermediate radii. We interpret this excess as the presence of the merger component in the NW direction. We evaluate again the clumpiness, after masking out sectors 1, 2, and 3, which are more affected by the presence of the merger. As we show in Fig. 4.16, the excess in the clumping factor at intermediate radii disappears and the total clumpiness at R_{200} decreases to 1.05.

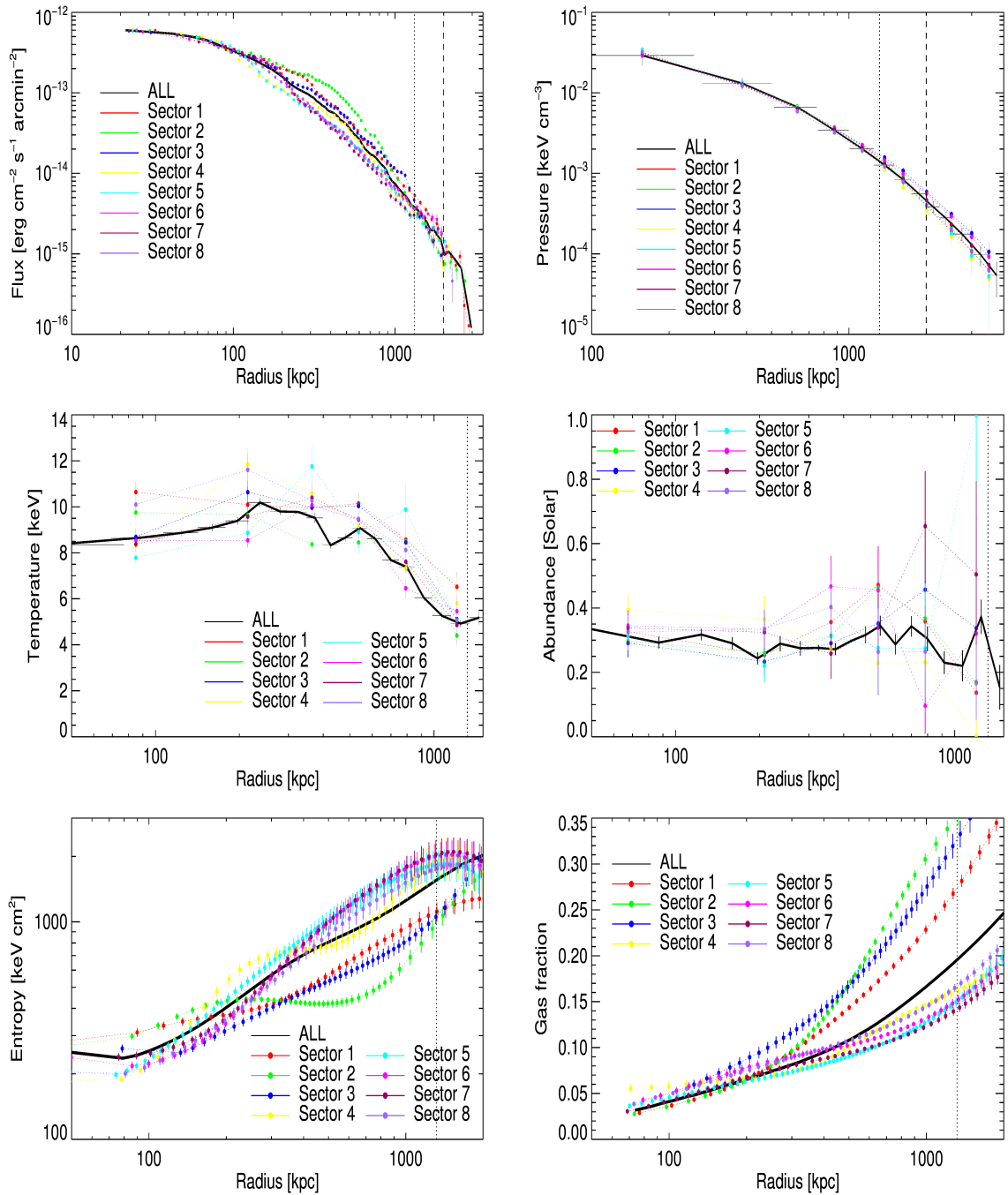


Fig. 4.15 (Top left) Surface brightness profiles for the eight sectors using the median method. The thick black line is obtained from the whole image analysis. The dotted and dashed vertical line marks the position R_{500} and R_{200} , respectively. (Top right) SZ pressure profiles for the eight sectors overplotted on top of the pressure profile for the whole cluster (black line). (Centre) Two-dimensional temperature (left) and abundance (right) profiles for the eight sectors analysed. (Bottom left) Reconstructed entropy profiles for all sectors using the *backward* method. (Bottom right) Gas fraction profiles recovered applying the *backward* technique. The thick black line is the result for the azimuthally averaged profile. The dotted and dashed vertical line marks the position R_{500} and R_{200} , respectively.

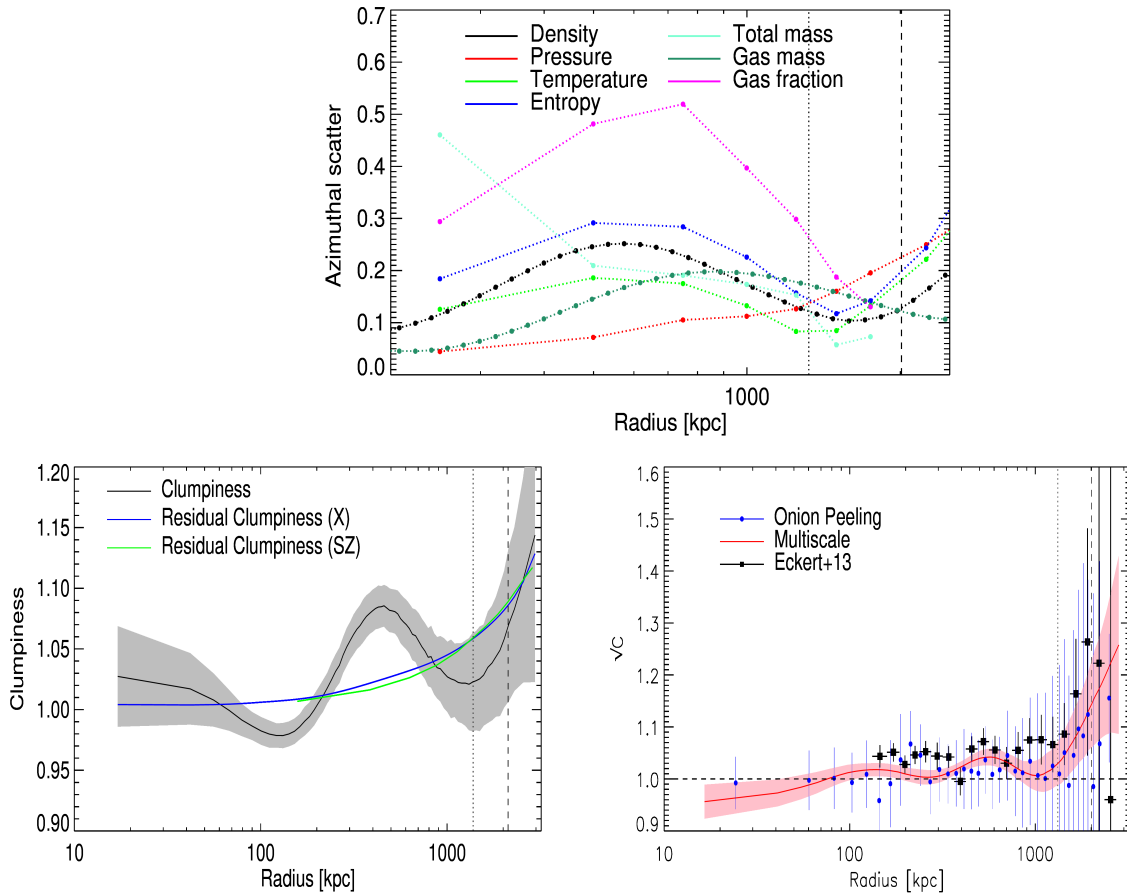


Fig. 4.16 (Top) Azimuthal scatter in the thermodynamic profiles: gas density and gas mass profiles are obtained from the X-ray spatial analysis; the pressure profile is the result of SZ data analysis; gas entropy and temperature are obtained by combining SZ pressure and X-ray density; the total mass is reconstructed by solving the hydrostatic equilibrium equation using the *forward* approach. The vertical dotted and dashed line represents the location of R_{500} and R_{200} , respectively. (Centre left) Total measured clumpiness (see Sect. 4.5.2; black line, shaded region represents 1σ uncertainty) compared with the estimated residual clumpiness using X-ray density (blue line) and the SZ Comptonization parameter (green line). (Centre right) Same as Fig. 4.8, but removing the problematic sectors (1, 2, and 3) from the analysis. The features present in the whole clumpiness profile disappear almost completely. The dotted and dashed vertical line marks the position of R_{500} and R_{200} , respectively. (Bottom left) Total measured clumpiness (see Sect. 4.5.2; black line, shaded region represents 1σ uncertainty) compared with the estimated residual clumpiness using X-ray density (blue line) and SZ Comptonization parameter (green line). (Bottom right) Same as Fig. 4.8, but after removing the merging region in the problematic sectors (1, 2, and 3) from the analysis. The features present in the whole clumpiness profile disappear almost completely. The dotted and dashed vertical line marks the position of R_{500} and R_{200} , respectively.

4.5.3 Thermodynamic quantities in azimuthal sectors

The procedures applied to study the properties of the whole clusters are applied on each azimuthal sector. In summary, we deproject surface brightness into density using the multi-scale technique on the mean profile, we deproject the Comptonization parameter to retrieve pressure, and we calculate the temperature in six spectral annuli. We then apply the *backward* approach to these thermodynamic quantities in order to find the parameters of a NFW mass model which best reproduce the observables. We compare the observed and reconstructed from the best-fit mass model pressure and temperature profiles sector by sector in Fig. 4.17 and 4.18, respectively. We observe that the only sectors with an evident discrepancy are the ones disturbed the most by the merger event, i.e. sectors 1, 2, and 3.

Similarly to what is done in Sect. 4.4.8, we compare the entropy profile reconstructed by the NFW *backward* best fit with the entropy recovered from X-ray spectroscopy ($K = kT/n_e^{2/3}$), and with the entropy recovered by combining X-ray density and SZ pressure ($K = P/n_e^{5/3}$); this sector-by-sector comparison is shown in Fig. 4.19.

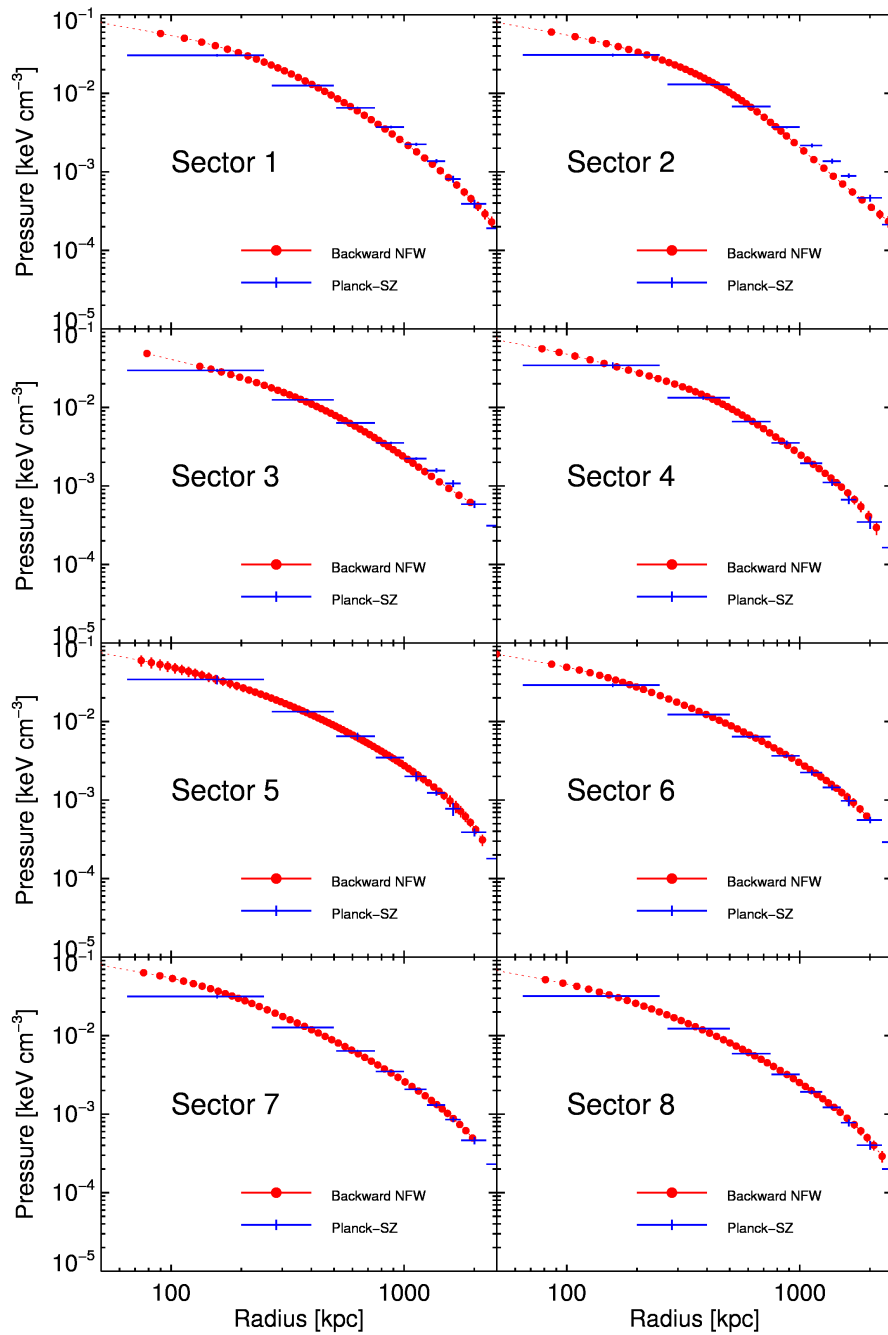


Fig. 4.17 Comparison of the observed pressure profile with that reconstructed by the NFW *backward* best fit.

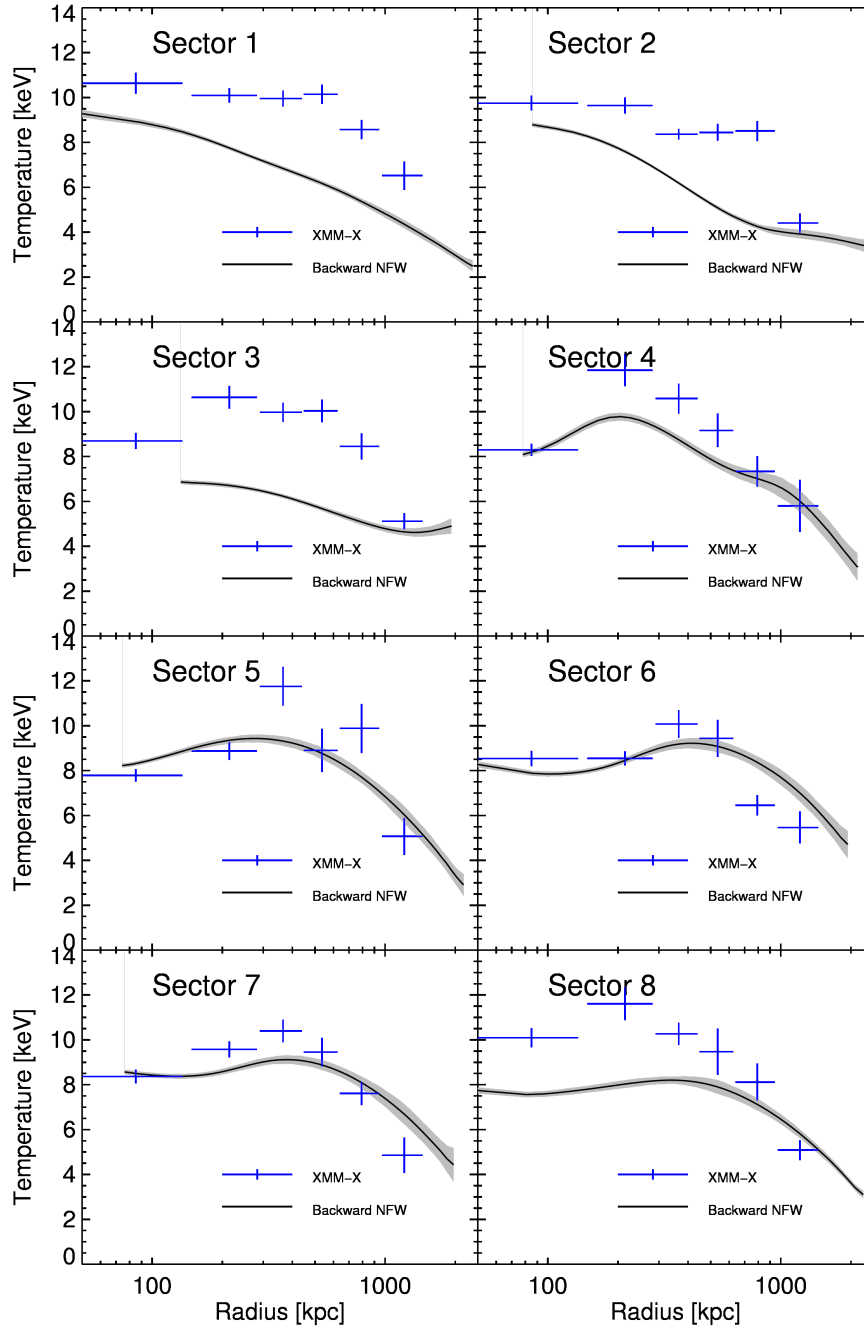


Fig. 4.18 Comparison of the observed 2D temperature profile with the one reconstructed by the NFW *backward* best fit.

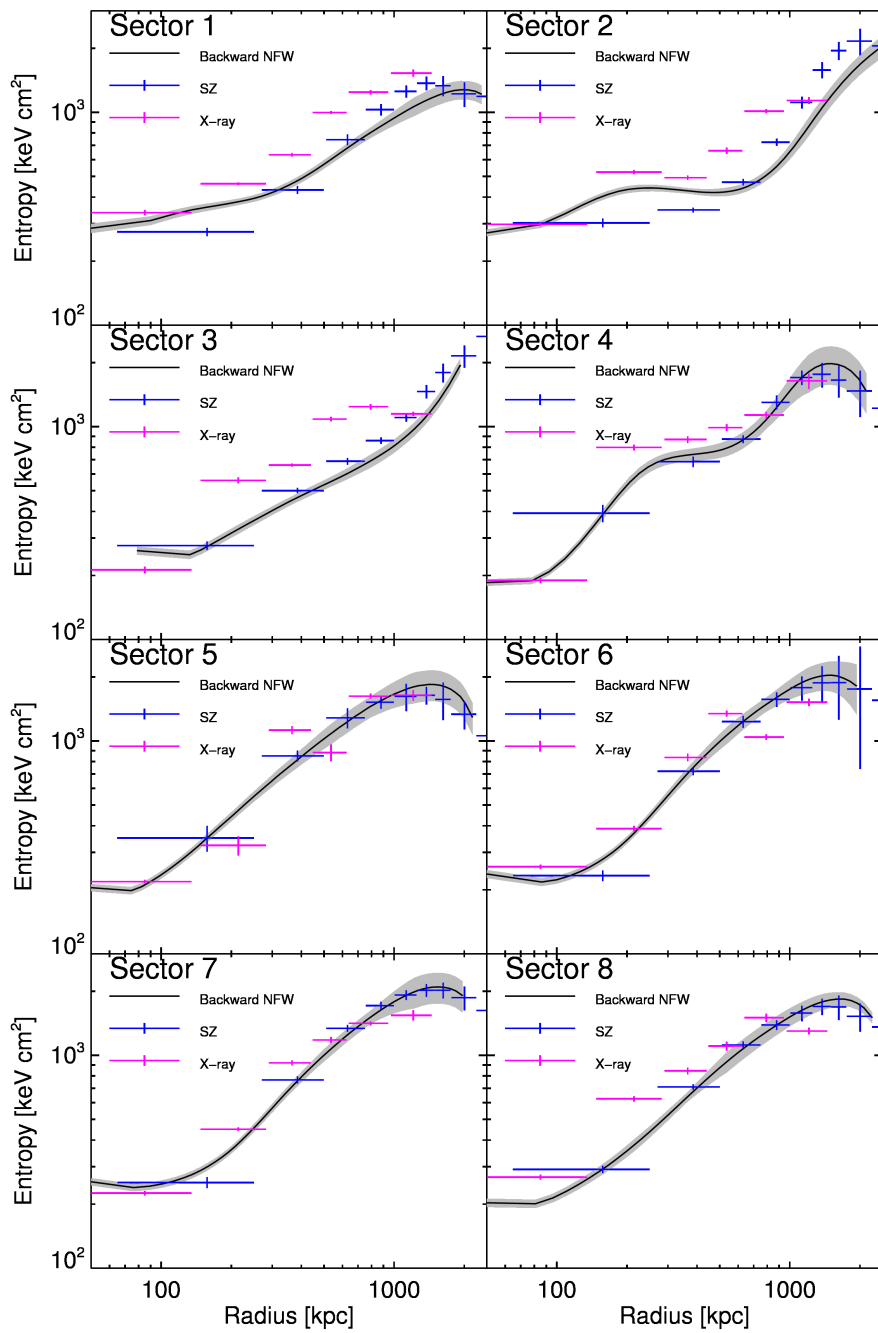


Fig. 4.19 Comparison between the entropy profile reconstructed by the NFW *backward* best fit with the entropy coming from the combination of X-ray and SZ and just using X-ray spectral results.

4.6 Characterizing the hydrostatic bias

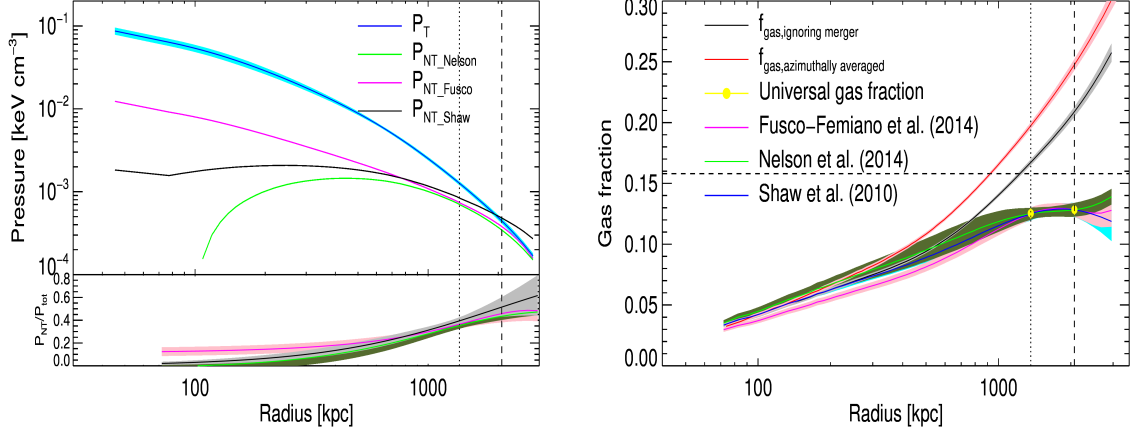


Fig. 4.20 (Left) Thermal pressure compared with non-thermal pressure using three different models (black, pink, and green lines, Fusco-Femiano and Lapi, 2014; Nelson et al., 2014a; Shaw et al., 2010, respectively). (Right) Measured gas fraction profile azimuthally averaged (red line) and ignoring the merging region (black line), and corrected accounting for the contribution of a non-thermal pressure component enabling to match the cosmic gas fraction at R_{200} and R_{500} . The horizontal line represents the universal baryon fraction (Planck Collaboration et al., 2016e), the vertical lines represents the position of R_{500} and R_{200} , and the yellow points are the universal baryon fraction depleted by the thermalized gas and by the star fraction. The pink, green, and blue lines represent the gas fraction we get by using different functional forms in order to reduce the observed gas mass fraction to the universal one.

4.6.1 Gas mass fraction and the non-thermal contribution

Since galaxy clusters originate from large regions of the primordial Universe, their baryon fraction is expected to be close to the universal fraction.

The gas mass fraction, $f_g = M_g/M_{\text{tot}}$, in massive galaxy clusters represents most of the baryons accreted in the dark matter halo and is a good proxy of the cosmic baryonic budget, which enables us to use galaxy clusters as a cosmological probe (e.g. Ettori et al., 2002, 2009),

$$\frac{\Omega_b}{\Omega_m} \cdot b = f_g + f_{\text{star}}, \quad (4.13)$$

where Ω_b and Ω_m are the cosmological baryon and matter density, b is the depletion factor that accounts for the cosmic baryons which thermalize in the cluster's potential, and f_{star} is the stellar mass fraction. Here, we adopt the cosmological parameters $\Omega_b = 0.045$

and $\Omega_m = 0.3089$ estimated from Planck Collaboration et al. (2016e); we assume from numerical simulations $b = 0.85$ and 0.87 (with a standard deviation of 0.03) at R_{500} and R_{200} , respectively (e.g. Planelles et al., 2013); and consider $M_{\text{star}}/M_{\text{gas}} = 0.069$ from optical measurements in nearby systems (Gonzalez et al., 2013). We predict, thus, a gas mass fraction f_g of 0.125 and 0.128 at R_{500} and R_{200} , respectively.

However, we measure a gas fraction, already corrected for the resolved gas clumpiness using the median profile, that reaches values well above the expected f_g at $r > R_{500}$ (see Figs. 4.15 and 4.13). We argue for the role of the non-thermal pressure contribution to the estimate of the total mass in lowering the measured gas fraction.

Indeed, Abell 2319 is in a merging state (Oegerle et al., 1995), with the presence of a giant radio halo (Farnsworth et al., 2013; Storm et al., 2015) that supports this scenario. The measured gas fraction can then be biased high as a consequence of the phenomena (like gas turbulence and bulk motion) that occur during a merger and that are not accounted for in the calculation of the hydrostatic mass, causing an underestimate of the halo mass.

Before proceeding in quantifying the amount of non-thermal pressure support, we note (from the analysis in azimuthal sectors) that the substructure that is merging with the main halo is also able to disturb the system on a much larger scale by enhancing the measured surface brightness up to ~ 1 Mpc. The net effect is to increase the gas mass by about 10% and so the relative amount of non-thermal pressure in the outskirts. To obtain an estimate of the contribution of the non-thermal pressure unbiased from any evident merger, we ignore the region where we measure this excess in the surface brightness (see red sector in Figure 4.14), and repeat our analysis. We show the comparison between the results obtained before and after masking the merging region in Table 4.7. The hydrostatic mass remains unchanged, but the gas mass decreases, implying that the gas fraction lowers by 17% at R_{200} , but it is still greater than the cosmological gas fraction predicted from numerical simulations at these radii. We note that the reconstructed gas fraction is already corrected for the resolved gas clumping using the median density profile; therefore, clumpiness cannot be responsible for the excess gas fraction (Simionescu et al., 2011).

One possibility to explain this overestimate in the gas fraction is the presence of a substantial non-thermal pressure component in the HEE which breaks the hydrostatic equilibrium assumption. We modify the HEE in Equation 4.4, by adding an extra pressure component, which we define as non-thermal pressure, and justify as being generated, for example, by unresolved gas turbulence, bulk motion, magnetic field, or asphericity. This non-thermal component can be modelled, in a first approximation, as a constant fraction of the thermal component (Loeb and Mao, 1994; Zappacosta et al., 2006). We add this non-thermal pressure term (indicated with the subscript ‘NT’) in the HEE as $P_{NT}(r) = \alpha(r)P_T(r)$, where the

Region	M_{200} ($10^{14}M_{\odot}$)	R_{200} (kpc)	$M_{gas,200}$ ($10^{14}M_{\odot}$)	$f_{gas,200}$
Azimuthal average	10.7 ± 0.5	2077 ± 33	2.54 ± 0.05	0.237 ± 0.012
Ignoring the merging region	10.7 ± 0.3	2075 ± 17	2.22 ± 0.02	0.207 ± 0.006

Table 4.7 Comparison between the mass reconstruction at R_{200} using the whole surface brightness image and ignoring the merging component. The columns show: the hydrostatic mass by solving HEE (see Eq. (4.4)), R_{200} , the gas mass obtained by integrating the gas density profile (Eq. (4.3)), and the gas mass fraction defined by $f_{gas} = M_{gas}/M_{tot}$.

Model	Functional form for $\alpha = P_{NT}/P_T$	a	b	c
Nelson et al. (2014a)	$\left[a \left(1 + \exp \left(- \left(\frac{R}{R_{200}b} \right)^c \right) \right) \right]^{-1} - 1$	0.52 ± 0.02	0.52 (fix)	1.23 ± 0.27
Fusco-Femiano and Lapi (2014)	$a \exp \left(- \left(\frac{1-R/(2R_{500})}{b} \right)^2 \right)$	0.91 ± 0.18	0.706 ± 0.09	–
Shaw et al. (2010)	$a \left(\frac{R}{R_{500}} \right)^b$	0.63 ± 0.05	1.17 ± 0.36	–

Table 4.8 Model, functional form, and best-fitting parameters for the three models which describe the ratio between non-thermal and thermal pressure support.

thermal component has the subscript ‘T’, and $\alpha(r)$ is a function of radius. The HEE is then modified as

$$\frac{1}{\rho_g} \left(\frac{dP_T}{dr} + \frac{dP_{NT}}{dr} \right) = -\frac{G}{r^2} (M_T + M_{NT}), \quad (4.14)$$

By solving the derivatives and readjusting the terms in the equation, we can then write how this propagates into the estimate of the gas mass fraction

$$f_g = \frac{M_g}{M_T + M_{NT}} = \frac{M_g}{M_T \left(1 + \frac{M_{NT}}{M_T} \right)} \frac{f_{g,T}}{1 + \alpha(r) - \frac{P_T r^2}{GM_T \mu m_p n_e} \frac{d\alpha}{dr}} \equiv \beta f_{g,T}, \quad (4.15)$$

where β is defined as the ratio between the true gas fraction and the measured thermal gas fraction. This means that in the case of $\alpha = constant$, the real gas fraction is reduced by a factor $1 + \alpha$.

By imposing that the observed cluster gas fraction should match the cosmic value in Eq. (4.13), and assuming a constant α , we require $\alpha = 0.64$ (0.32) at R_{200} (R_{500}), implying that about 39% (24%) of the total pressure is in the form of a non-thermal component.

In general, α is expected to have a radial dependence. Numerical simulations (e.g. Fusco-Femiano and Lapi, 2014; Nelson et al., 2014a; Shaw et al., 2010) predict some functional forms for P_{NT}/P_T . We can constrain the parameters of these models, if we consider the radial dependence of α in HEE, by requiring that we should be able to reproduce the expected gas mass fraction at R_{500} and R_{200} . The errors on the parameters are calculated using Monte Carlo simulations propagating the errors on the gas mass fraction profile, on the measure

of R_{200} , and on the predicted gas mass fraction points. The non-thermal pressure profiles and the corresponding gas fraction profiles obtained using the above mentioned models are shown in Fig. 4.20, and in Table 4.8 we provide the three functional forms adopted and the best-fitting parameters. We observe that already above 200-300 kpc, the non-thermal pressure support plays a very important role in flattening the gas mass fraction profile.

Finally, by imposing that the total cluster mass M_{tot} is provided from $M_T + M_{NT}$, we can estimate the amount of the hydrostatic bias factor β as

$$\beta = \frac{M_T}{M_{tot}} \Rightarrow M_{tot} = \frac{M_T}{\beta}. \quad (4.16)$$

Applying Equations (4.14), (4.15), and (4.16), the cosmological gas fraction at R_{500} and R_{200} is obtained by requiring

$$M_{500,tot} = 10.2 \pm 0.4^{\text{stat.}} \pm 0.4^{\text{syst.}} \times 10^{14} M_{\odot}$$

$$M_{200,tot} = 17.3 \pm 0.9^{\text{stat.}} \pm 1.2^{\text{syst.}} \times 10^{14} M_{\odot}$$

Using this mass estimate corrected by clumpiness and by hydrostatic bias, and the value acquired from the *Planck* catalogue (Planck Collaboration et al., 2016d) and based on scaling relations, $M_{Y_{SZ},500} = 8.74(\pm 0.12) \times 10^{14} M_{\odot}$, we infer a *Planck* bias of $1 - b = M_{Y_{SZ},500}/M_{500,tot} \approx 0.86$.

4.6.2 Effects of the hydrostatic bias on the rescaled profiles

The correction on the mass propagates to the rescaled profiles, both directly since R_{500} increases shrinking the x-axis, and indirectly since pressure and entropy, as described from Eqs. (4.6) and (4.8) respectively, follow a rescaling which is mass dependent.

In Fig. 4.21, we show the net effect on the thermodynamic rescaled profiles, that can be summarized by the following statements:

- the gas pressure profile is now in agreement with the universal pressure profile (Arnaud et al., 2010) and with the *Planck* envelope (Planck Collaboration et al., 2013);
- the gas density profile becomes compatible with the stacked density profile presented in Eckert et al. (2012);
- the gas entropy profile shows the least modification before and after this analysis; the profile becomes slightly steeper, but it is still flat in the outskirts, in agreement with the expected impact of any non-thermal pressure support (Walker et al., 2012b).

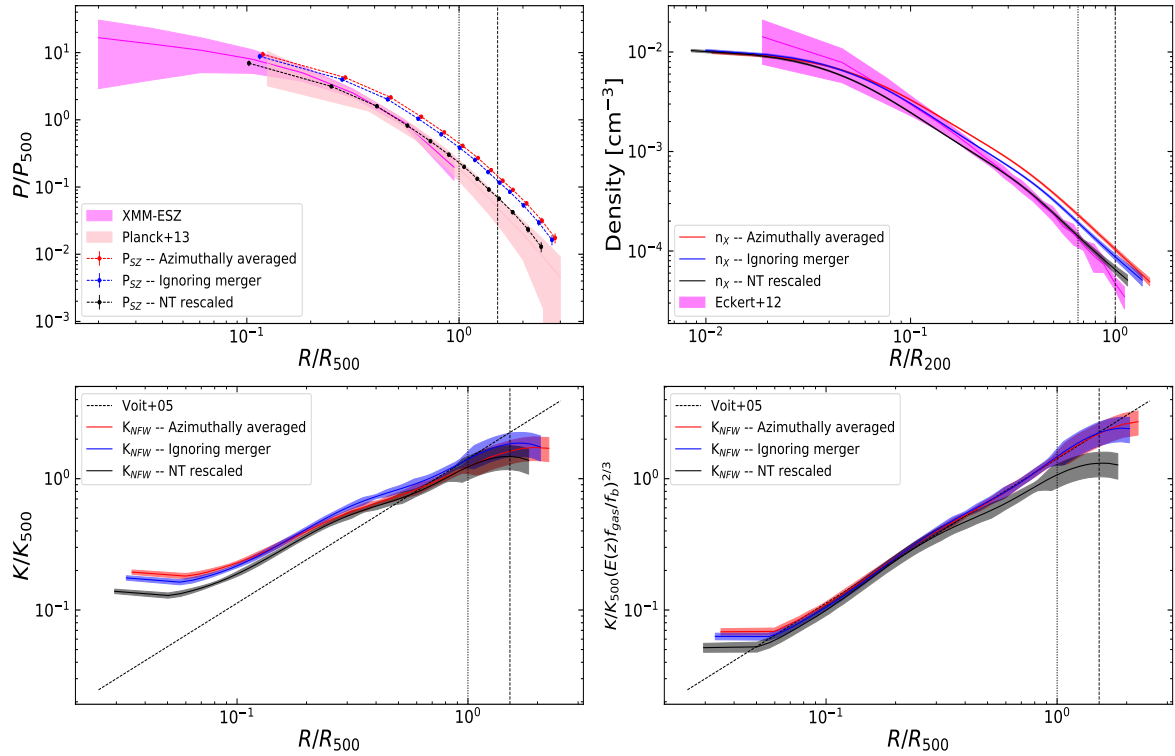


Fig. 4.21 Rescaled pressure (top left) and density (top right) profiles considering the azimuthally averaged, ignoring the merger, and ignoring the merging region and considering the $M_{200,tot}$ and $R_{200,tot}$ required to recover the cosmological gas fraction at the virial radius. We compare these profiles with the *Planck* envelope (Planck Collaboration et al., 2013) for pressure, and with the universal density profile (Eckert et al., 2012) for density. (Bottom) Rescaled entropy and rescaled entropy corrected by the gas mass fraction, before and after correcting for the true total mass.

Pratt et al. (2010) have shown that in order to reconcile entropy profile with predictions from non-radiative simulations (Voit et al., 2005), the profile has to be corrected by the gas mass fraction $K \Rightarrow K \cdot (E(z)f_{gas}/f_b)^{2/3}$. Introducing this correction in each entropy profile that we consider (i.e. the azimuthally average profile, the profile ignoring the merging region, and the profile required to recover the cosmological gas fraction at R_{200}), we obtain the results shown in Fig. 4.21. We observe that only when we include the contribution by the non-thermal pressure we obtain a corrected entropy profile that deviates from the numerical predictions, with a flattening above $0.3R_{500}$ suggesting that turbulence, or non-thermal energy at large, has not been yet converted efficiently in heat energy, not allowing the specific entropy of the ICM to rise to the value expected in systems simulated in the absence of non-gravitational processes (e.g. Voit et al., 2005).

4.7 Summary and conclusions

The very accurate background modelling of the *XMM-Newton* exposures, and the large extension of the SZ signal resolved with *Planck* have allowed us to combine X-ray and SZ data to study the thermodynamic properties of Abell 2319 over the virial region around R_{200} . Moreover, since the data quality is very high, we are able to study the properties of this cluster reaching the virial radius in eight different sectors. This enables us to study the azimuthal variance of the thermodynamic properties of the ICM in this merging system for the first time.

The measured clumpiness shows the presence of the merging component with an increase in its value at intermediate radii (~ 500 kpc). This excess disappears when we remove the merging regions from the analysis. On the other hand, in the outskirts the clumpiness measured is compatible with the estimated residual clumpiness (Roncarelli et al., 2013). This means that this cluster has no significative infalling clumps at the virial radius.

The gas density profile corrected for the resolved clumpiness is then used to recover other fundamental quantities (Eckert et al., 2015), together with the gas temperature profile that we measure, from the X-ray spectroscopic analysis, with a median relative statistical uncertainty of 2% and with a systematic error that we carefully estimate to be of the order of 4% (median value), and above 15% in the outermost radial bin alone. The exquisite quality of these complementary X-ray and SZ datasets, extending across R_{200} , enable us to constrain a NFW hydrostatic mass profile at very high precision ($M_{200} = 10.7 \pm 0.5^{\text{stat.}} \pm 0.9^{\text{syst.}} \times 10^{14} M_{\odot}$), achieving a level where systematic errors dominate over the statistical ones.

Due to the merging state of this cluster, the recovered entropy profile is flatter than the one predicted by non-radiative simulations (Voit et al., 2005). We observe the most deviations in the first and last few points: in the centre this is caused by the fact that this cluster is a non-cool core cluster (Cavagnolo et al., 2009) with a flat entropy core of ~ 75 keV cm², while some residual non-thermal energy flattens the entropy in the outskirts (Walker et al., 2012b).

The pressure profile recovered from SZ data is flatter, and above the 1σ envelope, than the universal profile measured for an ensemble of objects resolved with *Planck* (Planck Collaboration et al., 2013).

The measured gas fraction, corrected by the gas clumpiness using the median density profile, is above the value predicted from state-of-art hydrodynamical simulations for the preferred cosmological background (Gonzalez et al., 2013; Planck Collaboration et al., 2016e; Planelles et al., 2013). Analysing the azimuthal variation of the f_{gas} profile (see Fig. 4.15), we observe that it is above the average value only in the sectors most affected by the merger

(sectors 1, 2, and 3). When the region with the ongoing merger and with an estimated higher gas mass is excluded from the analysis, the gas fraction drops, but it is still higher than the expectations, indicating a non-negligible contribution from a non-thermal pressure support that we quantify as approximately 39% and 24% of the total pressure at R_{200} and R_{500} , respectively.

Once the correction induced by the non-thermal pressure support is propagated through the measurements of R_{500} , K_{500} , and P_{500} , we show that (i) the pressure profile matches the mean behaviour of objects resolved with *Planck*; (ii) the gas density profile becomes consistent with the stacked profile obtained from Rosat/PSPC observations in Eckert et al. (2012); and (iii) on the contrary, the entropy undergoes a very small change, remaining flatter than the predicted profile.

In forthcoming works, the detailed analysis presented here for A2319 will be extended to the whole X-COP sample (Eckert et al., 2017a), providing the first ensembled properties of the ICM at R_{200} and above.

**THE UNIVERSAL THERMODYNAMIC
PROPERTIES OF THE INTRACLUSTER
MEDIUM OVER TWO DECADES IN RADIUS IN
THE X-COP SAMPLE**

5.1 Introduction

In this chapter, we present the universal thermodynamical properties of the galaxy clusters in the X-COP cluster sample, see Chapter 3. Here we consider the global properties of the X-COP sample, presenting the structural properties of the ICM over more than two decades in radius ($[0.01 - 2]R_{500}$).

Throughout this chapter, we assume a flat Λ CDM cosmology with $\Omega_m = 0.3$, $\Omega_\Lambda = 0.7$ and $H_0 = 70 \text{ km s}^{-1} \text{ Mpc}^{-1}$. All our fitting is performed using the Bayesian nested sampling algorithm MultiNest (Feroz et al., 2009), if not otherwise stated.

In Sect. 5.2 we describe the available dataset and the analysis procedures. In Sect. 5.3 we present our results on the universal thermodynamic profiles, slopes and intrinsic scatter. Our findings are discussed in Sect. 5.4, we draw our conclusion in Sect. 5.5.

5.2 Dataset and analysis procedures

5.2.1 The X-COP project

The details on the cluster selection, their main properties, and the goal of the X-COP project are detailed in Chapter 3.

5.2.2 *XMM-Newton* data analysis

The detailed analysis of *XMM-Newton* data, from raw data to surface brightness profiles and spectral temperature measurements, to analyze the entire X-COP sample is described in Sect. 3.2. In the following we explore several possible way to deproject surface brightness into density.

5.2.3 Deprojection and gas density profiles

To extract gas density profiles, we take advantage of the fact that the X-ray surface brightness in our energy band of choice is proportional to the squared gas density integrated along the line of sight. To convert surface brightness profiles into emission measure, we describe the emissivity of the source with a thin-plasma model absorbed by the Galactic N_H and folded through the on-axis EPIC/MOS effective area. This approach allows us to calculate the conversion between the observed count rate in MOS units and the normalization of the APEC model, which is related to the plasma emission measure as

Table 5.1 Basic properties of the X-COP sample.

Cluster	redshift	S/N	M_{500}	R_{500}	M_{200}	R_{200}	K_0	R.A.	Dec
		<i>Planck</i>	$10^{14} M_\odot$	kpc	$10^{14} M_\odot$	kpc	keV cm ²	deg	deg
A1644	0.0473	13.2	3.48 ± 0.20	1054 ± 20	6.69 ± 0.58	1778 ± 51	19.0 (CC)	194.3015	-17.409729
A1795	0.0622	15.0	4.63 ± 0.14	1153 ± 12	6.53 ± 0.23	1755 ± 21	19.0 (CC)	207.21957	26.589602
A2029	0.0766	19.3	8.65 ± 0.29	1414 ± 16	12.25 ± 0.49	2155 ± 29	10.5 (CC)	227.73418	5.744432
A2142	0.0909	21.3	8.95 ± 0.26	1424 ± 14	13.64 ± 0.50	2224 ± 27	68.1 (NCC)	239.58615	27.229434
A2255	0.0809	19.4	5.26 ± 0.34	1196 ± 26	10.33 ± 1.23	2033 ± 81	529.1 (NCC)	258.21604	64.063058
A2319	0.0557	30.8	7.31 ± 0.28	1346 ± 17	10.18 ± 0.52	2040 ± 35	270.2 (NCC)	290.30276	43.94501
A3158	0.0597	17.2	4.26 ± 0.18	1123 ± 16	6.63 ± 0.39	1766 ± 35	166.0 (NCC)	55.717984	-53.627728
A3266	0.0589	27.0	8.80 ± 0.57	1430 ± 31	15.12 ± 1.44	2325 ± 74	72.5 (NCC)	67.843372	-61.429731
A644	0.0704	13.9	5.66 ± 0.48	1230 ± 35	7.67 ± 0.73	1847 ± 59	132.4 (NCC)	124.35736	-7.5086903
A85	0.0555	16.9	5.65 ± 0.18	1235 ± 13	8.50 ± 0.36	1921 ± 27	12.5 (CC)	10.459403	-9.3029207
RXC1825	0.0650	13.4	4.08 ± 0.13	1105 ± 12	6.15 ± 0.26	1719 ± 24	217.9 (NCC)	276.33547	30.436748
ZW1215	0.0766	12.8	7.66 ± 0.52	1358 ± 31	13.03 ± 1.23	2200 ± 69	163.2 (NCC)	184.42191	3.6557217

Notes. name, redshift, and signal-to-noise ratio from the PSZ1 catalogue (Planck Collaboration et al., 2014a). The mass information (M_{500} , R_{500} , M_{200} , R_{200}) is obtained from our own hydrostatic mass reconstruction (Ettori et al. 2018). The information on the central entropy was taken from the ACCEPT database (Cavagnolo et al., 2009), indicating the cool core clusters with $K_0 < 30$ keV cm² with CC, in the case of the non cool core with NCC. The last two columns indicate the centre of the radial profiles, in degree.

$$\text{Norm} = \frac{10^{-14}}{4\pi[d_A(1+z)]^2} \int_V n_e n_H dV, \quad (5.1)$$

where d_A is the angular diameter distance of the source and n_e, n_H are the electron and ion number densities in units of cm⁻³, with $n_e = 1.17n_H$ in a fully ionized plasma (Anders and Grevesse, 1989). Since we are using a soft energy band, the conversion between count rate and emission measure shows little dependence on the temperature as long as the temperature exceeds ~ 1.5 keV, which is the case in all X-COP systems. The resulting emission measure profiles can then be deprojected under the assumption of spherical symmetry by computing the projected volumes V of each spherical shell onto each two-dimensional annulus. To recover the three-dimensional emissivity and density profiles from the projected data, we apply two different deprojection methods that we briefly outline here.

- **L1 regularization:** This method builds on the non-parametric regularization approaches developed by Croston et al. (2006) and Ameglio et al. (2007), introducing a penalty term on the modulus of the second derivative of the 3D density profile to kill spurious small-scale fluctuations introduced by the random nature of the data (Diaz-Rodriguez et al., 2017). Given an observed 2D emission measure profile $EM = (EM_1 \dots EM_n)$ and corresponding uncertainties $\sigma_{EM} = (\sigma_{EM,1} \dots \sigma_{EM,n})$, the values of the 3D emissivity profile $\varepsilon = (\varepsilon_1 \dots \varepsilon_n)$ are obtained by maximizing the

following likelihood function

$$-2\log \mathcal{L} = \chi^2 = \sum \frac{(V\#\varepsilon - EM)^2}{\sigma_{EM}^2} + \lambda \sum \left| \frac{\partial^2 \log \varepsilon}{\partial \log r^2} \right| \quad (5.2)$$

where $V_{i,j}$ is the geometrical matrix volume of the j^{th} shell intercepted by the i^{th} annulus, $\#$ is the symbol for matrix product, and the sum is performed along all the annuli. Moreover the second derivative of the emissivity is computed as a numerical derivative of the $\varepsilon(r)$ vector. The parameter λ controls the degree of regularization of the profile. To maximize the likelihood function described in Eq. 5.2, we use the Markov chain Monte Carlo (MCMC) tool *emcee* (Foreman-Mackey et al., 2013b), leaving the value of the 3D density profile at each radius as a free parameter and setting a logarithmic prior (i.e. uniform prior in logarithmic space) on each parameter value to enforce positivity of the resulting profile. The value of the parameter λ is chosen such that the log-likelihood is about 1 per data point, to allow for typical statistical deviations of 1σ . We point out that $\lambda = 0$ is equivalent to using the onion peeling technique directly (see Etori et al., 2002, 2010; Kriss et al., 1983).

- **Multiscale fitting:** This method follows the technique developed in Eckert et al. (2016a), whereby the projected emission measure profile is decomposed into a sum of analytical multiscale functions which can be individually deprojected. Following Eckert et al. (2016a) we write the observed 2D profile as a sum of N King functions with fixed core radii and normalizations and slopes allowed to vary while fitting, choosing $N = N_{\text{points}}/4$, i.e. one model component is added for every set of 4 data points, fixing a core radius to the mean radial value of these 4 data points. Since the projection kernel is linear, each King function can be individually deprojected and the 3D profile can be analytically reconstructed from the fit to the projected data. As above, we use *emcee* to optimize for the parameters and reconstruct the error envelope around the best fitting curve.

In the top-left panel of Fig. 5.3 we compare the density profiles reconstructed with the two methods and find a remarkable agreement between them, with an average scatter $< 5\%$ at each radius. By construction, the profiles reconstructed with the L1 regularization method shows more pronounced features as the method imposes fewer constraints on the shape of the profile, whereas the profiles obtained with the multiscale method are smoother. Thus, we adopt the results of the L1 regularization when attempting to determine the exact shape of our profiles, whereas the multiscale technique is preferred when reconstructing hydrostatic mass profiles to provide better control over the gradient.

5.2.4 *Planck* data analysis

The *Planck* analysis applied in this chapter to analyze the entire X-COP sample is described in detail in Sect. 3.4.

On top of that, for the purpose of this work and to have an alternative method from which we can estimate the systematic effects associated to the pressure measurement from *Planck*, we applied an alternative method, extracting *Planck* pressure profiles using the forward-modeling approach of Bourdin et al. (2017). In this case, a spectral model for the relevant components is constructed (CMB, dust, synchrotron, and thermal SZ). The model is folded through the *Planck* response and fitted to the multi-frequency data points (see Bourdin et al., 2017, for details). In Sect. 5.2.6 we compare the results obtained with this approach to the results of the aforementioned MILCA component separation method and show their consistency. For the remainder of the chapter, we use the MILCA pressure profiles as our default choice.

5.2.5 Consistency between X-ray and SZ pressure measurements

We checked the consistency between X-ray and SZ pressure profiles, to test how our results are affected by discrepancies between the two measurements. To perform this check we introduced a parameter η_{SZ} which is the ratio between the SZ and X-ray pressure profile, and proceeded with a joint fit, allowing the scatter on X-ray and SZ data to be independent. Mathematically we can write the following system of equation:

$$\begin{cases} P_{SZ} = \eta_{SZ} P_{model} \cdot \exp[\pm \sigma_{int,SZ}] \\ P_X = P_{model} \cdot \exp[\pm \sigma_{int,X}] \end{cases} \quad (5.3)$$

where η_{SZ} , $\sigma_{int,SZ}$, and $\sigma_{int,X}$ are free parameters. For P_{model} we checked both the piecewise powerlaw fit case in the radial range where we have both X-ray and SZ measurements, and the global functional form on the entire radial range. In both cases the measured scatters are in good agreement, and compatible with the scatter shown in Fig. 5.11. More importantly the parameter η_{SZ} shows a distribution, shown in Fig. 5.1, which is consistent with unity, indicating a very good general agreement between X-ray and SZ pressure measurements.

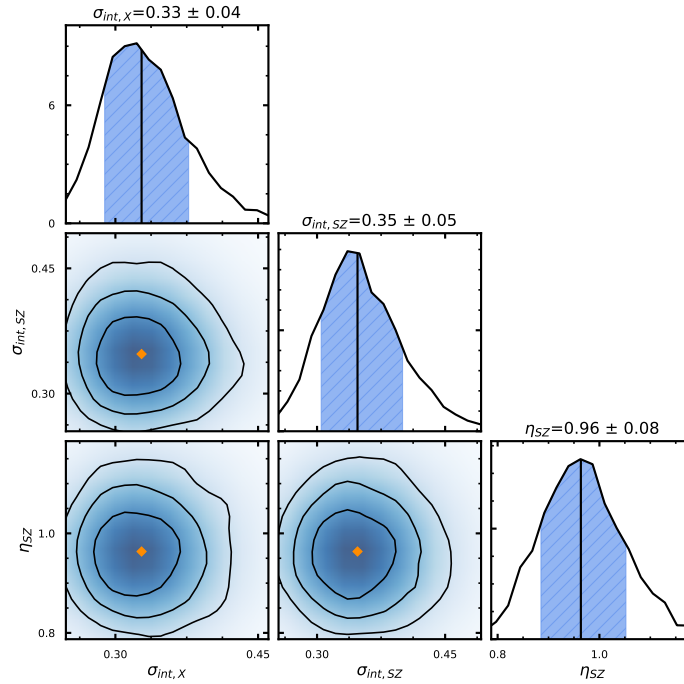


Fig. 5.1 Posterior distribution of the parameter $\eta_{SZ} \approx P_{SZ}/P_X$. The shaded blue area indicates the region containing 68% of the posterior distribution.

5.2.6 Comparison between MILCA and forward-modeling pressure profiles

To test the robustness of our pressure profile measurements, we compared the MILCA results with the pressure measured using an alternative technique (see Bourdin et al., 2017). Following this technique, *Planck*-HFI frequency maps are first wavelet cleaned for CMB and thermal dust anisotropies, a parametric pressure template (Nagai et al., 2007) is subsequently projected onto the sky plane, convolved with the frequency dependent HFI beams and fitted to the CMB and dust cleaned maps. Being fully parametric, this technique allow us to take advantage of the frequency dependent angular resolution of each HFI channel during the template fitting. This angular resolution is about 9.7 and 7.3 arcmin at 100 and 143 GHz, respectively, but reaches about 5 arcmin in the energy range [217, 857] GHz (Planck Collaboration et al., 2016c).

In Fig. 5.2 we compare the resulting best fitting pressure profile from the above procedure with the MILCA maps, see Sect. 5.2.4. The residuals are shown in the left panel, showing the nice agreement, within the statistical uncertainty, of the two different methods applied. On the right panel all the residuals are grouped together to create a distribution, which is compared with a gaussian centered in 0 and width 1, showing that the residuals follow very

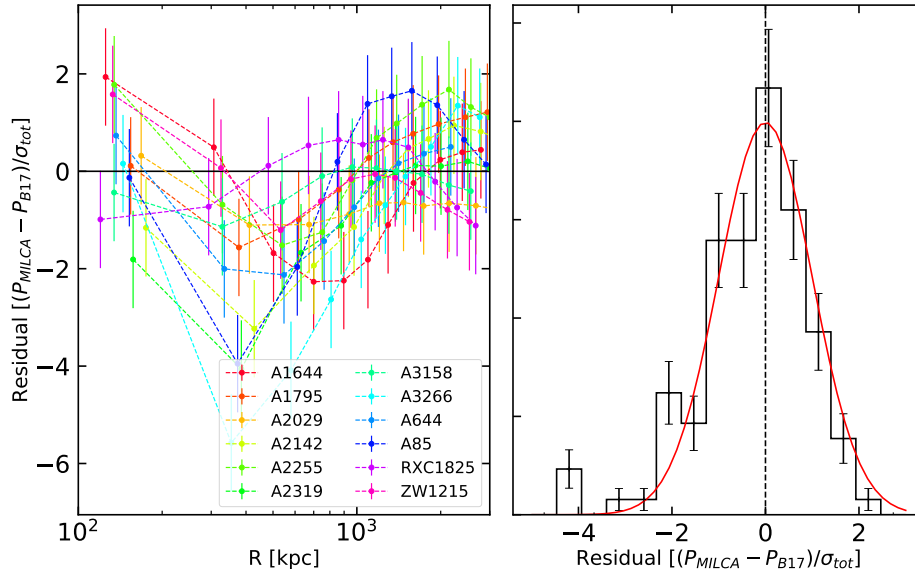


Fig. 5.2 *Left*: Residuals of the comparison of the two different methods we used to estimate the SZ pressure profile. A remarkable good agreement within the statistical uncertainties is reached at all radii, especially excluding the first 3 MILCA points which are the most affected by the *Planck* PSF. *Right*: Distribution of the residuals compared with the statistical prediction of a set of residuals: a gaussian centered in zero and width one (red line).

well this distribution, indicating that statistically the two pressure profiles are in very good agreement.

5.2.7 Mass estimates

To estimate scale radii and self-similar scaling quantities, we use the high-precision hydrostatic mass reconstructions presented in Ettori et al. (2018). The mass models were obtained by combining X-ray and SZ information for each individual system and solving the hydrostatic equilibrium equation. For the present work, we adopt as our reference mass model the *backward NFW* results, which were obtained by assuming that the mass profile follows a Navarro-Frenk-White shape (Navarro et al., 1996) with scale radius and concentration c_{200} as free parameters. This method was shown to provide the best representation of the data (Ettori et al. 2018) and at R_{500} it matches the results obtained without assuming a functional form for the mass profile with an accuracy of $\sim 5\%$. Comparison of our mass reconstruction with weak lensing and SZ estimates (Ettori et al. 2018) and convergence toward the expected universal gas fraction (Eckert et al. 2018) show that our masses and the corresponding values of R_{500} are accurate at the 10% and 3% level, respectively. For more details on the

reconstruction of hydrostatic masses and estimates of systematic uncertainties we refer to Ettori et al. (2018) and Eckert et al. (2018).

5.3 Thermodynamic properties

In the following section we describe how we derived the universal profiles, slopes and intrinsic scatter of all our thermodynamic variables. We then present our main results and provide best fitting functional forms describing the X-COP cluster population.

5.3.1 Fitting procedure

We adopt two different approaches to fit the thermodynamic properties:

- **Piecewise power law fits:** In this case, we split our data in several radial ranges as a fraction of R_{500} and we approximate the global behaviour of the population in each range as a power law with free log-normal intrinsic scatter:

$$\frac{Q(x)}{Q_{500}} = A \cdot x^B \cdot \exp(\pm \sigma_{\text{int}}) \quad (5.4)$$

with $x = R/R_{500}$, Q/Q_{500} the rescaled thermodynamic quantity at an overdensity of 500, and A , B and σ_{int} the normalization, slope and intrinsic scatter in the radial range of interest. The values of Q_{500} are computed adopting the virial theorem like in Voit et al. (2005) and are shown in Eq. (5.8), (5.10), and (5.12). The fitting procedure thus has three free parameters (A , B and σ_{int}) in each of the chosen radial ranges. We remark that this procedure provides model independent measurements of the slope and intrinsic scatter at different radii.

- **Global functional forms:** In this case, we describe the radial dependence of the thermodynamic quantity of interest throughout the entire radial range with a parametric functional form found in the literature:

$$\frac{Q(x)}{Q_{500}} = f(x) \cdot \exp[\pm \sigma_{\text{int}}(x)] \quad (5.5)$$

with Q and Q_{500} the same quantity as in Eq. (5.4), and $f(x)$ the chosen functional form for the thermodynamic quantity Q . In this case, since we model the whole radial range covered by our measurements, we allow the intrinsic scatter to vary with radius following a quadratic functional form to model the radial dependence of the intrinsic

scatter:

$$\sigma_{\text{int}}(x) = \sigma_1 \log^2 \left(\frac{x}{x_0} \right) + \sigma_0 \quad (5.6)$$

with σ_1 the width of the log-parabola, and x_0 and σ_0 are respectively the location and the intercept of the minimum of the log-parabola. A total of $n + 3$ parameters are allowed to vary during the fitting procedure, with n the number of parameters of the adopted functional form $f(x)$. Optimizing jointly for the parameters of the intrinsic scatter profile allows us to determine the shape of $\sigma_{\text{int}}(x)$.

In Fig. 5.3 through 5.9 we show our rescaled thermodynamic quantities for the gas density, pressure, temperature and entropy. The best fits with piecewise power laws and using functional forms are presented as well, together with the slopes for the parametric and non-parametric cases.

5.3.2 Density

We rescaled our density profiles by the self similar quantities, $E^2(z) = \Omega_m(1+z)^3 + \Omega_\Lambda$ and R_{500} for density and radius, respectively. In Fig. 5.3 we compare our scaled gas density profiles with the ‘universal’ density profiles from Eckert et al. (2012) from a sample of 31 clusters with available *ROSAT*/PSPC pointed data. We observe an excellent agreement with their results, A2319 is the only exception which, as shown in Ghirardini et al. (2018b), deviates at large radii because of its large non thermal pressure support.

In the top-right panel of Fig. 5.3 we show our density profiles fitted with piecewise power laws in several radial ranges, we show the best fitting parameters in Table 5.2. We parametrize the behavior of our density profiles over the whole radial range by adopting the Vikhlinin et al. (2006) functional form:

$$f^2(x) = n_e^2(x) = n_0^2 \frac{(x/r_c)^{-\alpha}}{(1+x^2/r_c^2)^{3\beta-\alpha/2}} \frac{1}{(1+x^\gamma/r_s^\gamma)^{\varepsilon/\gamma}} \quad (5.7)$$

with $x = R/R_{500}$, $\gamma = 3$ fixed. The form thus has 6 free parameters (n_0 , r_c , α , β , r_s and ε) and is able to reproduce both the core and the outer parts of the density profile. We apply flat priors in logarithmic space to n_0 , r_c and r_s and flat priors in linear space to the remaining parameters, constraining $\varepsilon < 5$ (we specify the priors adopted in Table 5.3). We show the posterior distributions of the parameters of this functional form in Fig. 5.4 as well as the covariance between them.

The resulting profile is consistent at all radii with the universal envelope computed by Eckert et al. (2012). We can appreciate from all panels how the profiles become progressively

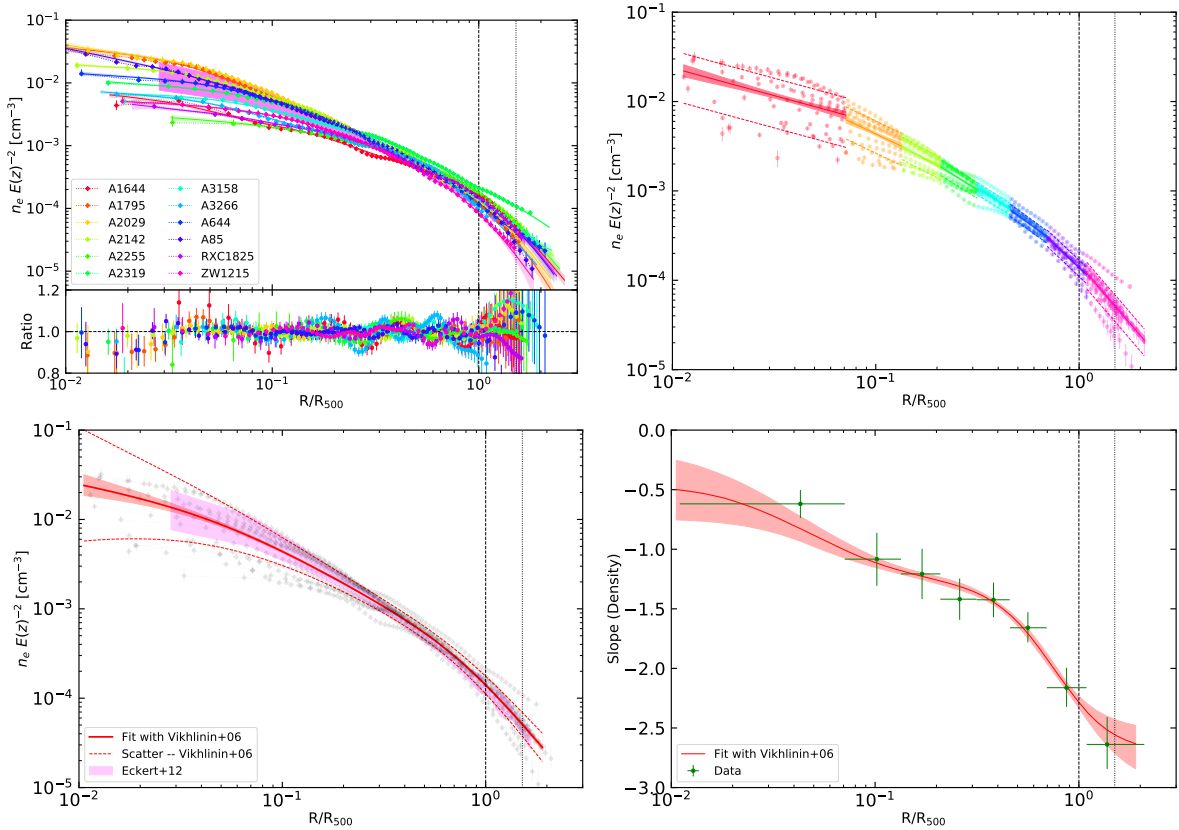


Fig. 5.3 *Top left panel:* Density profiles for all X-COP clusters obtained with two different deprojection methods: L1 regularization (data points) and multiscale fitting (solid lines). The shadow magenta area represents the scatter of the median profile in Eckert et al. (2012). The bottom panel represents the ratio between the two methods for each individual system. *Top right panel:* Joint fit to all the density profiles using piecewise power laws in several (color-coded) radial ranges. The best fits and 1σ error envelope are shown by the solid lines, while the dashed lines represent the intrinsic scatter. *Bottom left panel:* Joint fit to the density profiles using the functional form introduced by Vikhlinin et al. (2006), in red, with the shadow area indicating the 1σ error envelope around the best fit. The dashed lines represent the intrinsic scatter in the functional form as a function of radius. *Bottom right panel:* Slope of the density profiles as a function of radius. The green data points show the results of the piecewise power law fits, whereas the red curve indicates the fit to the entire radial range using the Vikhlinin et al. (2006) functional form. In all panels, the vertical dashed and dotted lines represent the location of R_{500} and R_{200} , respectively.

less scattered going toward the outskirts. While the core is affected by a large scatter likely caused by cooling, AGN feedback and different merger states, the profiles show a high degree of self-similarity in the radial range $[0.3 - 1]R_{500}$. Then in the outskirts the scatter increases again, likely caused by different accretion rates from one system to another. We note from the plot in bottom right panel in Fig. 5.3 that the slope of the density profiles steepens steadily

with radius. The slopes computed from the piecewise power law fits and from the global fit with Eq. 5.7 agree within 1σ at all points. Again, this result is in agreement with the findings of Eckert et al. (2012); Morandi et al. (2015) but at variance with the relatively flat slopes reported in several clusters observed by *Suzaku*. For instance, several papers report density slopes flatter than -2.0 , e.g. -1.7 in the outskirts of the Perseus cluster (Urban et al., 2014) or even as low as -1.2 in A1689 (Kawaharada et al., 2010) and Virgo (Simionescu et al., 2017). These measurements are clearly in tension with the slope of -2.5 at R_{200} measured here for the X-COP cluster population. It must be noted, however, that thanks to the use of the azimuthal median technique, our gas density profiles are essentially free of the clumping effect, whereas the *Suzaku* studies could not properly excise overdense regions because of the lower resolution of the instrument and/or observations performed along narrow arms.

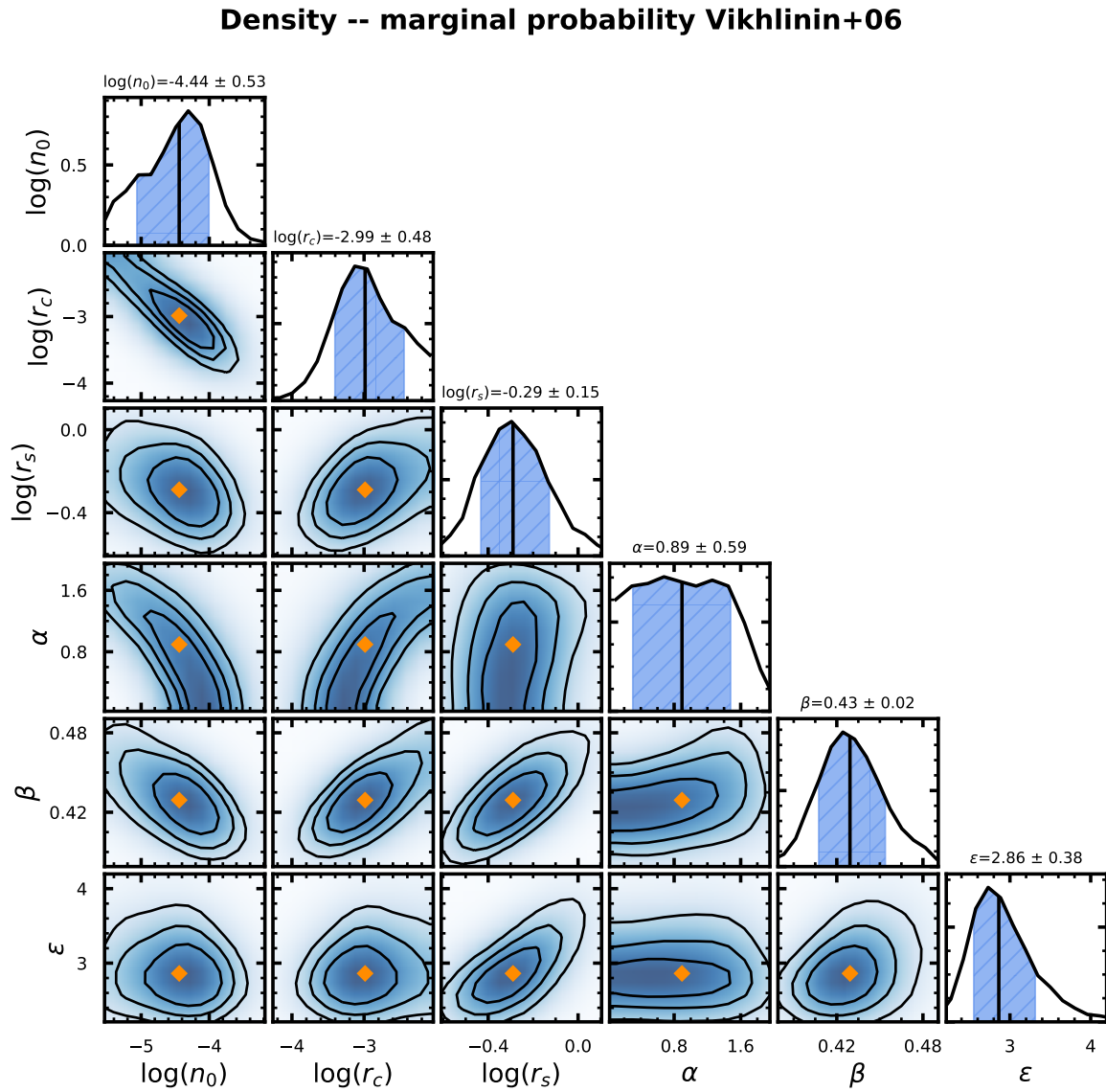


Fig. 5.4 Parameter distribution for the best fit on the density of all clusters using the Vikhlinin et al. (2006) functional form, Eq. (5.7). The priors on the parameters are shown in Table 5.3.

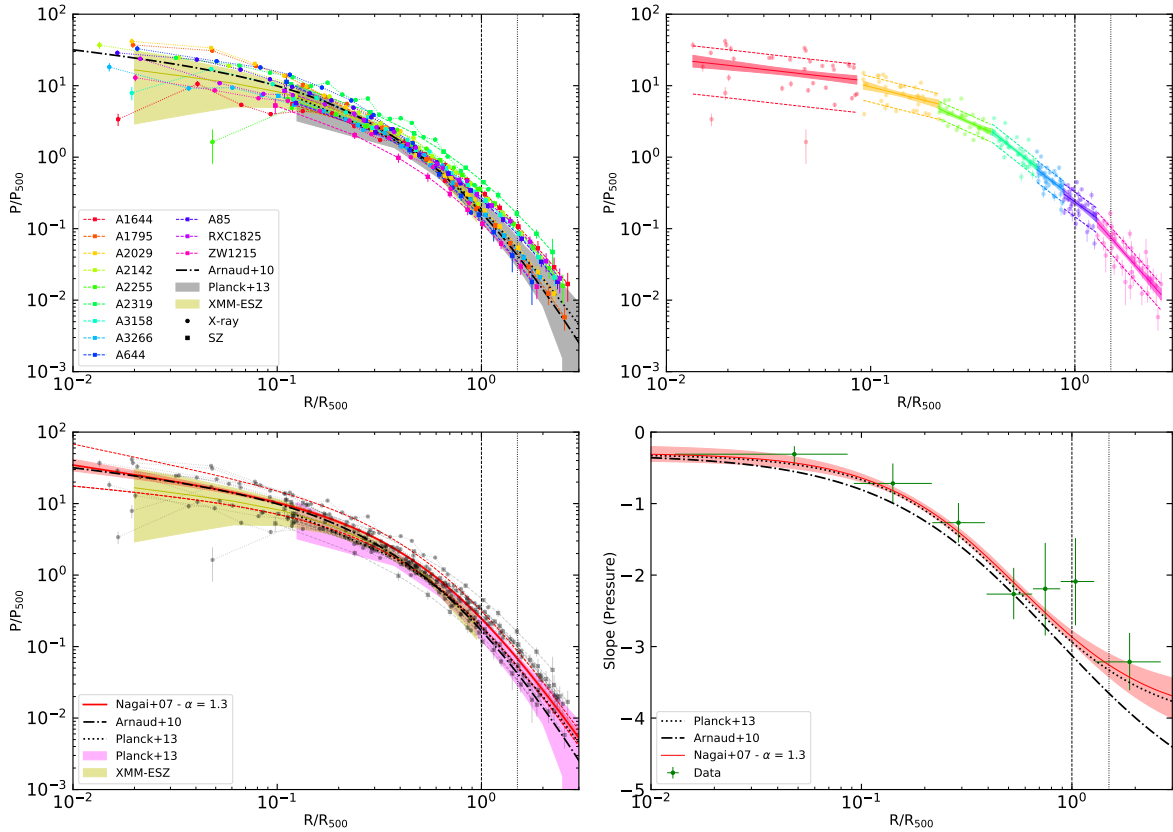


Fig. 5.5 Same as Fig. 5.3 for the pressure profiles rescaled by the self-similar quantity P_{500} (Eq. 5.8). The squares indicate data points obtained from the deprojection of the SZ signal, while the filled circles are computed by combining the X-ray gas density profiles with the spectroscopic temperature. The solid red curve in the bottom panels shows the joint best fit to the data with the generalized NFW functional form (Nagai et al., 2007, see Eq. 5.9). In all these plots the dotted and dashed-dotted lines represent the result of Planck Collaboration et al. (2013) and Arnaud et al. (2010) respectively. The shadow areas represent the envelope obtained by Planck Collaboration et al. (2013) and the Early release SZ sample (XMM-ESZ Planck Collaboration et al., 2011).

5.3.3 Pressure

Pressure in galaxy clusters is usually the smoothest thermodynamic quantity along the azimuth, if the cluster is not affected by an ongoing merger.

We recover the gas pressure both through the combination of X-ray gas density and spectral temperature and through the direct deprojection of the SZ effect. In the former case, we deproject the spectral X-ray temperature (e.g. Mazzotta et al., 2004, see Sect. 3.2.6) and combine the deprojected temperature with the gas density interpolated on the same grid to infer the pressure $P_X = k_B T_X \times n_e$. In the latter we recover the pressure directly from the

Planck data by deprojecting the measured y profiles (see Sect. 5.2.4) from which we exclude the first three points from the analysis. We thus combine the higher resolution and precision of *XMM-Newton* in the inner region with the high quality of the *Planck* data at R_{500} and beyond, which allows us to constrain the shape and intrinsic scatter of the pressure profiles in the radial range $[0.01 - 2.5]R_{500}$. We rescale our pressure profiles by the self-similar quantities at an overdensity of 500,

$$P_{500} = 3.426 \times 10^{-3} \text{ keV cm}^{-3} \left(\frac{M_{500}}{h_{70}^{-1} 10^{15} M_{\odot}} \right)^{2/3} E(z)^{8/3} \cdot \left(\frac{f_b}{0.16} \right) \left(\frac{\mu}{0.6} \right) \left(\frac{\mu_e}{1.14} \right) \quad (5.8)$$

where f_b is the Universal gas fraction, which we take to be $\Omega_b/\Omega_m = 0.16$ (Planck Collaboration et al., 2016e, rounding the number to 2 significant figures), μ and μ_e are the mean molecular weight per particle and mean molecular weight per electron for which we adopt the values measured by Anders and Grevesse (1989). In Fig. 5.5 we show the scaled pressure profiles of our 12 objects obtained through X-ray and SZ measurements of the ICM. We immediately observe that our profiles agree with the results obtained by the *Planck* Collaboration for a sample of 62 clusters (Planck Collaboration et al., 2013), falling well within the two envelopes, with the exception, as in the case of the density, of A2319 (see the discussion in Ghirardini et al., 2018b).

Similarly to the density, we fit the profiles using piecewise power laws in several radial ranges, obtaining also in this case a scatter which decreases with radius out to R_{500} and then like for the density, it increases in the outskirts, and profiles which become progressively steeper with radius, see Table 5.2. Our profiles in the outskirts are compatible with the results of the *Planck* Collaboration, both for the central value and the slope. We also fitted our data using the generalized NFW functional form introduced by Nagai et al. (2007):

$$f(x) = \frac{P(x)}{P_{500}} = \frac{P_0}{(c_{500}x)^{\gamma} [1 + (c_{500}x)^{\alpha}]^{\frac{\beta-\gamma}{\alpha}}}, \quad (5.9)$$

where $x = R/R_{500}$, with five free parameters, P_0 , c_{500} , and 3 slopes, γ , α , and β representing respectively the inner, intermediate, and outer slopes (we specify the priors adopted in Table 5.3). Since the parameters are strongly degenerate, it is advised (Arnaud et al., 2010) to fix at least one of the slopes, therefore we fixed the central slope α to the best fit value of 1.3 estimated by the *Planck* Collaboration (Planck Collaboration et al., 2013). The resulting best fit, the intrinsic scatter around the median profile, and the slope computed from the fit are

shown in Fig. 5.5. The posterior distributions of the parameters and the covariance between them are shown in Fig. 5.6.

Similar to the case of the gas density, we find that the slope of the profiles steepens steadily with radius, as expected for a gas in hydrostatic equilibrium within a NFW potential. The best fit with the generalized NFW functional form does an excellent job at reproducing the slopes estimated from the piecewise power law fits.

In the range where pressure measurements are available both from *XMM-Newton* and *Planck*, we find an excellent agreement between the two (see Sect. 5.2.5) even though the pressure profiles were obtained using completely independent probes. This shows that X-ray and SZ observations provide a consistent picture of the state of the ICM and gives us confidence that systematics in our measurements are small and under control.

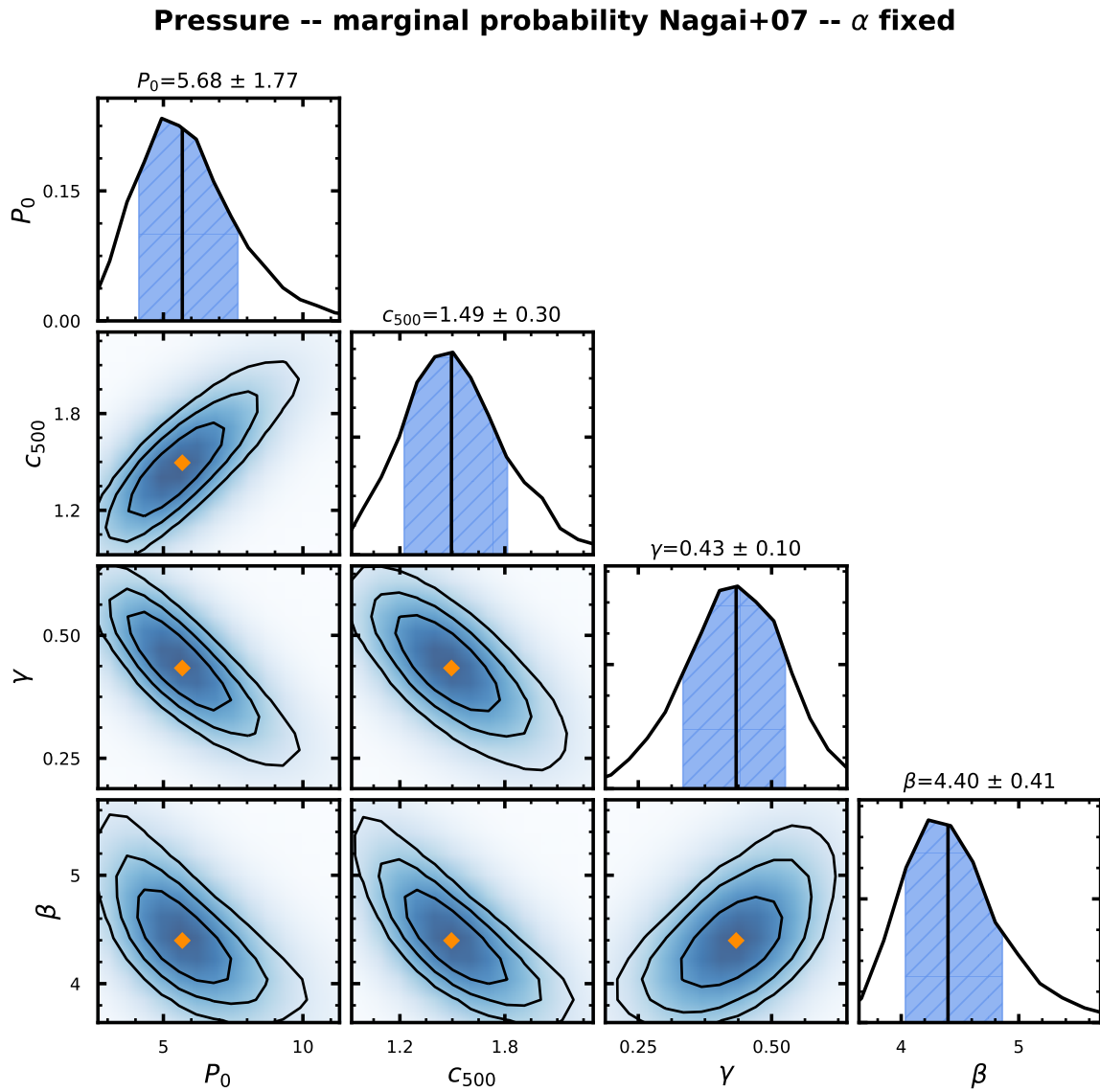


Fig. 5.6 Parameter distribution for the best fit on the pressure of all clusters using the Nagai et al. (2007) gNFW functional form, Eq. (5.9) fixing the intermediate slope α . The priors on the parameters are shown in Table 5.3.

5.3.4 Temperature

Temperature profiles in X-ray studies are usually obtained by performing spectral fitting in concentric annuli (see Sect. 3.2.6), the so called spectroscopic temperature. In addition, we also use our *Planck* SZ pressure profiles and combine them with the X-ray density profiles to obtain gas-mass-weighted temperatures $T_{gmw} = P_{SZ}/n_e$, which are then projected (using the X-ray emissivity as weight as in Mazzotta et al., 2004) on the plane of the sky and over-plotted on the spectroscopic temperatures. Our X-ray and SZ measurements of pressure and temperature cover different radial ranges. X-ray spectroscopy probes the temperature of the gas within R_{500} , while SZ probes temperatures from $0.7R_{500}$ to $2R_{500}$ (excluding the first three SZ data points), which highlights the complementarity of the two ICM diagnostics.

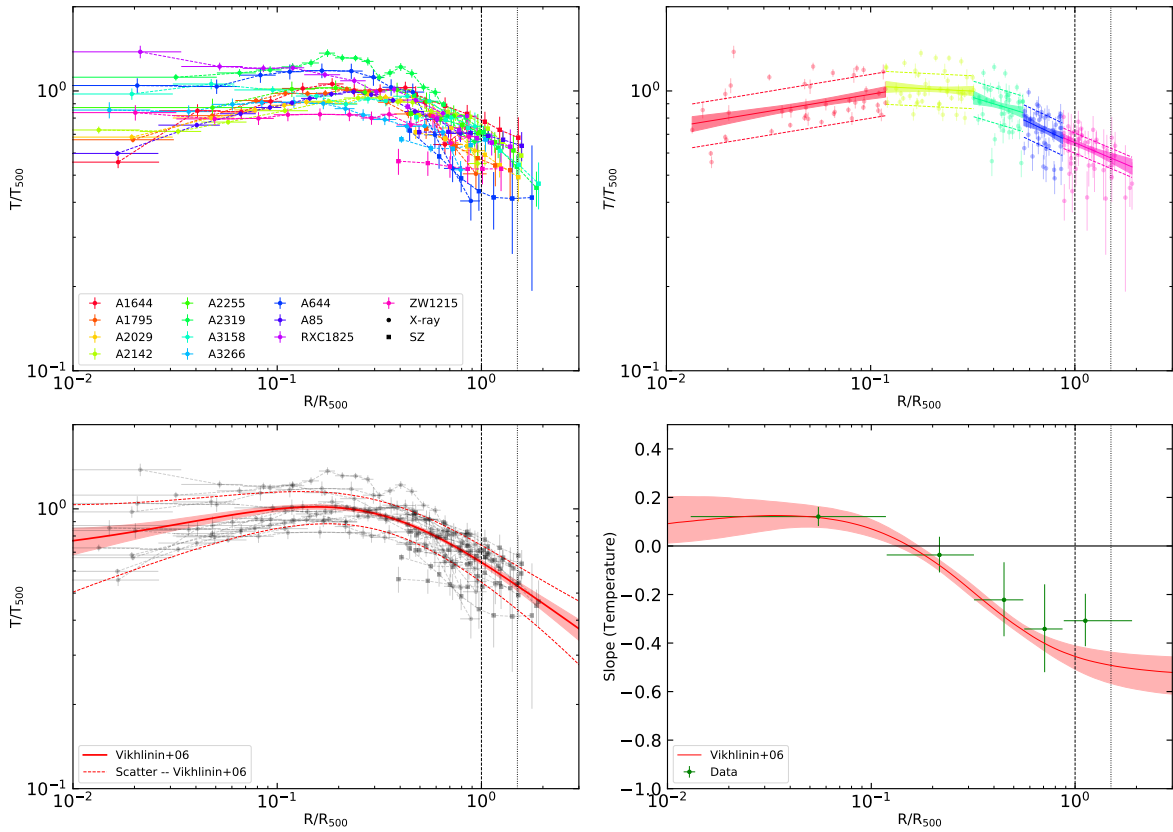


Fig. 5.7 Same as Fig. 5.3 for the projected temperature profiles rescaled by the self-similar quantity T_{500} (Eq. 5.10). The filled circles show the measurements of the X-ray spectroscopic temperature (see Sec. 3.2.6), whereas the filled squares indicate the data points obtained by combining the SZ pressure with the gas density, projected along the line of sight assuming the spectroscopic-like scaling of Mazzotta et al. (2004). The solid red curves in the two bottom panels show the best fit to the joint dataset with the functional form introduced by Vikhlinin et al. (2006) (see Eq. 5.11).

In Fig. 5.7 we show our two-dimensional spectral temperature profiles rescaled by T_{500} , defined as

$$T_{500} = 8.85 \text{ keV} \left(\frac{M_{500}}{h_{70}^{-1} 10^{15} M_{\odot}} \right)^{2/3} E(z)^{2/3} \left(\frac{\mu}{0.6} \right) \quad (5.10)$$

While density and pressure change by three to four orders of magnitude going from the centre to the outskirts of the cluster, temperature shows much milder variations. In particular, it is almost constant out to $\sim 0.5R_{500}$, and then declines beyond this point.

In Fig. 5.7 we show the results of the piecewise power law fits in several radial ranges. We perform a global fit to the temperature profiles with the functional form described in Vikhlinin et al. (2006), which is able to describe the temperature profiles both the core and the outer parts of galaxy clusters:

$$f(x) = \frac{T(x)}{T_{500}} = T_0 \frac{\frac{T_{min}}{T_0} + \left(\frac{x}{r_{cool}} \right)^{a_{cool}}}{1 + \left(\frac{x}{r_{cool}} \right)^{a_{cool}}} \frac{1}{\left(1 + \left(\frac{x}{r_t} \right)^2 \right)^{\frac{c}{2}}} \quad (5.11)$$

with $x = R/R_{500}$, and 6 free parameters: T_0 , T_{min} , r_{cool} , a_{cool} , r_t , and c (we specify the priors adopted in Table 5.3). The posterior distribution of these parameters and the covariances are shown in Fig. 5.8. This functional form provides an accurate description of the shape of the temperature profiles. The slopes estimated from the global fit follow the slopes measured from the piecewise power law fits at different radial ranges within 1σ at every radius.

The average slope of the temperature profiles is slightly positive in the central regions because of effects due to cooling, especially in cool-core clusters. Beyond $\sim 0.5R_{500}$ the slope remains relatively flat at a value of -0.3 . Such a value is consistent with the slopes measured inside R_{500} from *XMM-Newton* and *Chandra* data (Leccardi and Molendi, 2008; Pratt et al., 2007) but it is flatter than the typical slopes measured in *Suzaku* data. From a collection of a dozen clusters with published *Suzaku* temperature profiles, Reiprich et al. (2013) report that the universal shape of the profiles can be well described by the form $T/\langle T \rangle = 1.19 - 0.84(R/R_{200})$, i.e. the data are consistent with a slope of -1.0 in the outskirts, which is much steeper than the results presented here. Again, the low angular resolution of *Suzaku* may have prevented the authors from removing cool, overdense regions that could bias the measured spectroscopic temperature low. On the other hand, SZ pressure profiles are much less sensitive to gas clumping (e.g. Khedekar et al., 2013; Roncarelli et al., 2013) and our density profiles were corrected for the statistical effect of gas clumping (see Sect. 3.2.2), thus our X/SZ temperatures are closer to gas-mass-weighted temperatures (see the discussion in Adam et al., 2017).

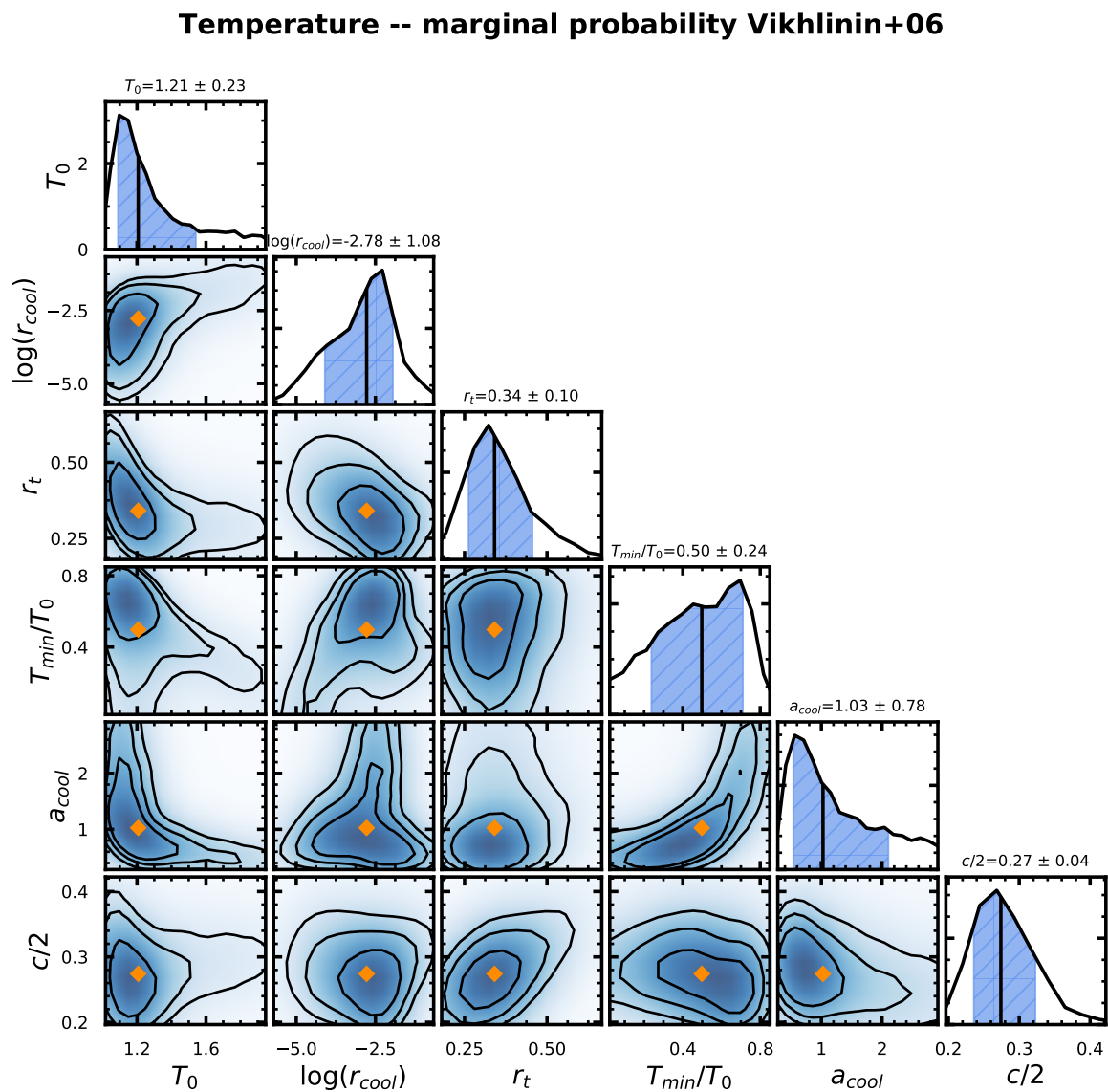


Fig. 5.8 Parameter distribution for the best fit on the temperature of all clusters using the Vikhlinin et al. (2006) functional form: Eq. (5.11). The priors on the parameters are shown in Table 5.3.

5.3.5 Entropy

Entropy traces the thermal evolution of the ICM plasma, which can be altered via cooling/heating, mixing, and convection. Simulations predict that in the presence of non-radiative processes only, entropy increases steadily with radius out to $\sim 2 \times R_{200}$, following a power law with a slope of 1.1 (Borgani et al., 2005; Lau et al., 2015; Tozzi and Norman, 2001; Voit et al., 2005). The entropy profiles of the cluster population should scale self-similarly when rescaled by the quantity

$$K_{500} = 1667 \text{ keV cm}^2 \left(\frac{M_{500}}{h_{70}^{-1} 10^{15} M_{\odot}} \right)^{2/3} E(z)^{-2/3} \cdot \left(\frac{f_b}{0.16} \right)^{-2/3} \left(\frac{\mu}{0.6} \right) \left(\frac{\mu_e}{1.14} \right)^{2/3} \quad (5.12)$$

Similarly to pressure and temperature, entropy can be recovered from X-ray-only quantities as $K = k_B T_X \times n_e^{-2/3}$ (using the deprojected temperature, see Sec. 3.2.6) or by combining SZ pressure with X-ray density as $K = P_{SZ} \times n_e^{-5/3}$ (ignoring the first 3 *Planck* points). We show our scaled entropy profiles in Fig. 5.9. Our profiles match very well with the predicted power law model beyond $0.3R_{500}$, with just A2319 showing a significant flattening not compatible within the error bars. In the central regions our profiles flatten, with non-cool-core clusters flattening more than cool-core clusters, as already noted in numerous studies (e.g Cavagnolo et al., 2009; Pratt et al., 2010, and references therein).

By fitting the profile using piecewise power laws we observe a gradual steepening of the entropy slope, which becomes consistent with the predictions of gravitational collapse (Voit et al., 2005) beyond $\sim 0.5R_{500}$, i.e. from a slope of ~ 0.6 in the core to ~ 1.1 in the outskirts. As for the previous cases, we fitted our profiles throughout the entire radial range with the functional form introduced by Cavagnolo et al. (2009), which consists of a power law with a constant entropy floor:

$$f(x) = \frac{K(x)}{K_{500}} = K_0 + K_1 \cdot x^{\alpha} \quad (5.13)$$

with $x = R/R_{500}$, and 3 free parameters K_0, K_1 and α (we specify the priors adopted in Table 5.3). The posterior distributions of the parameters and the covariances are shown in Fig. 5.10. We remark that this functional form does not provide an accurate description of the data in the outer parts of the profiles, where it is not able to follow the observed gradual change in slope throughout the radial range covered. At large radii, the best fitting slope using Eq. 5.13 reads $\alpha = 0.84 \pm 0.04$ (see Table 5.3), whereas the data prefer a slope consistent with the self-similar prediction of 1.1 beyond $0.6R_{500}$ (see Table 5.2).

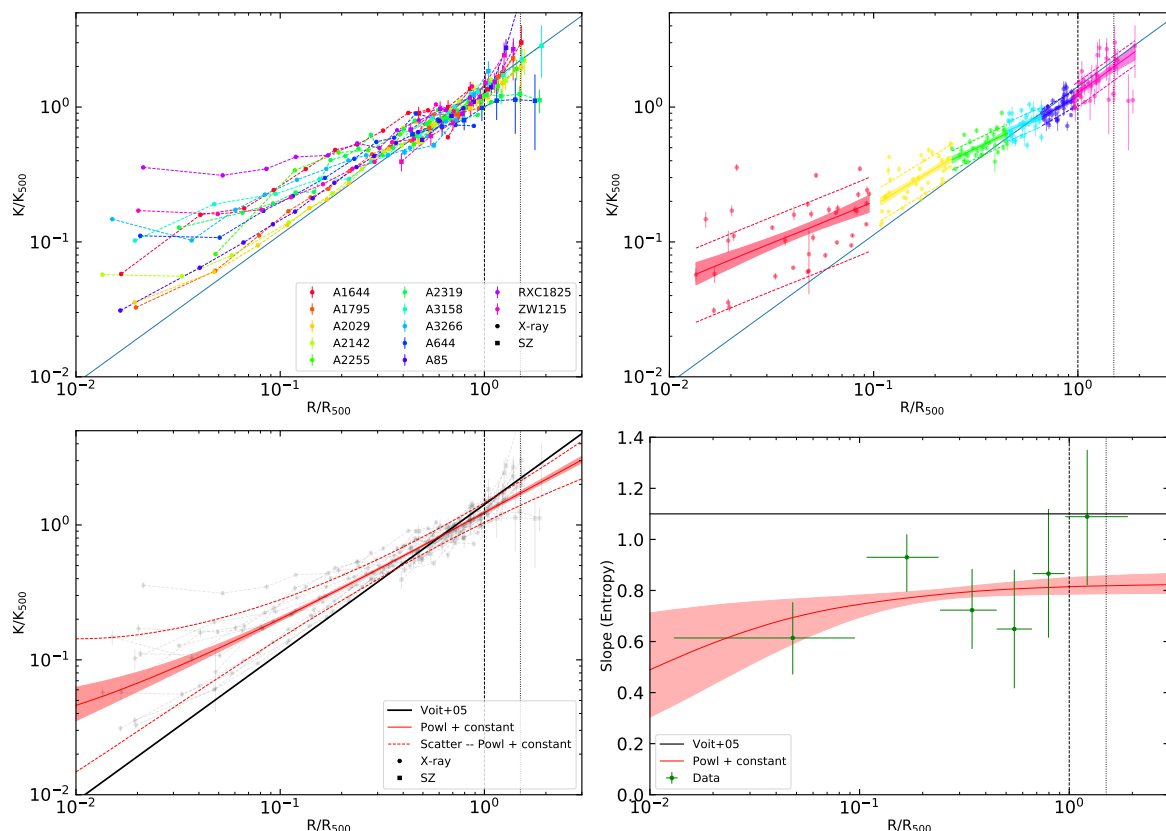


Fig. 5.9 Same as Fig. 5.3 for the entropy profiles rescaled by the self-similar quantity K_{500} (Eq. 5.12). The filled circles show the measurements obtained from the X-ray spectroscopic temperature as $K = k_B T / n_e^{2/3}$, whereas the filled squares indicate the data points obtained by combining the SZ pressure with the gas density as $K = P_e / n_e^{5/3}$. The solid red curves in the two bottom panels indicate the best fit to the entire population with the functional form presented in Eq. 5.13, whereas the solid black line shows the prediction of pure gravitational collapse (Voit et al., 2005).

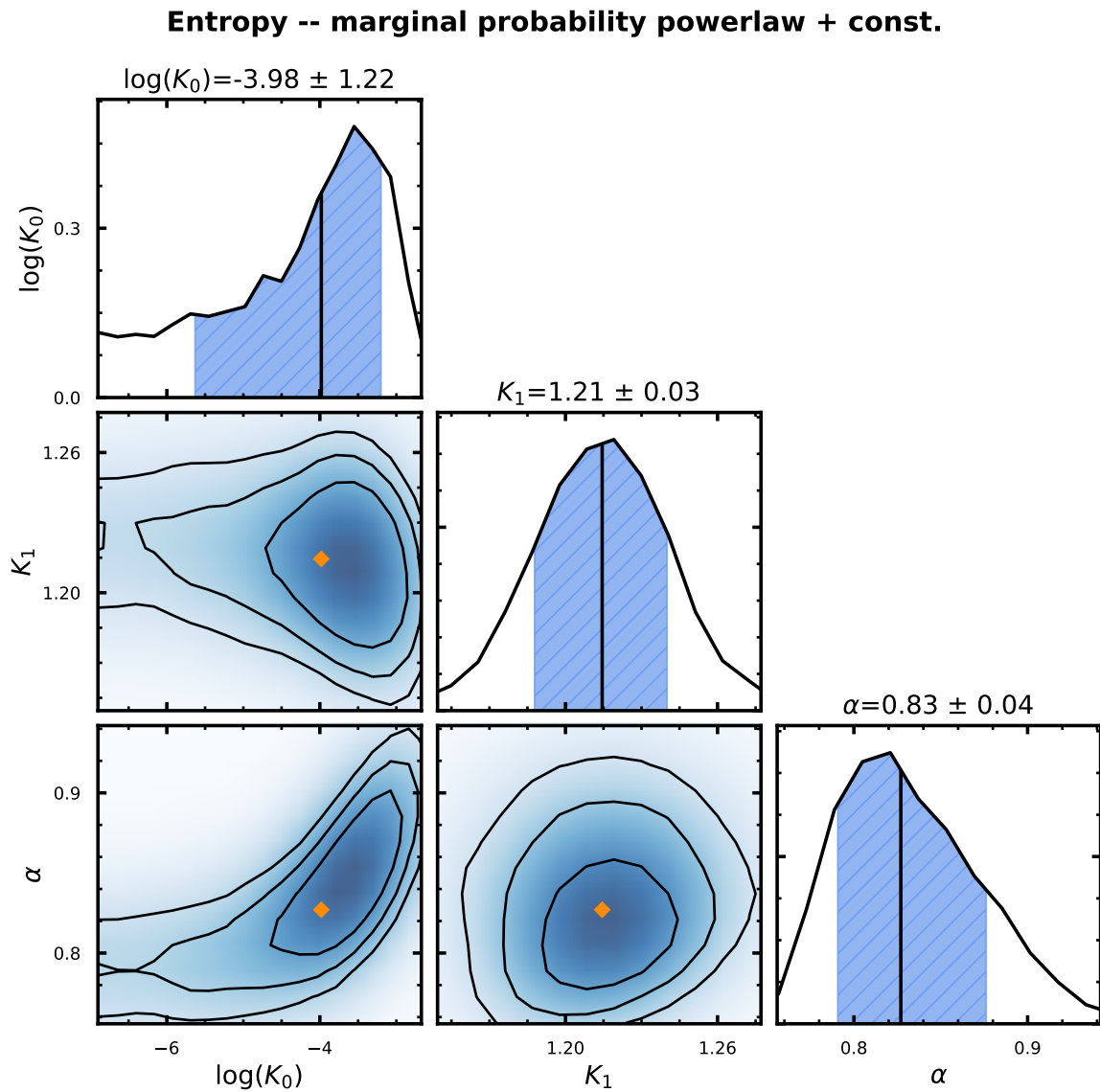


Fig. 5.10 Parameter distribution for the best fit on the entropy of all clusters using powerlaw plus constant functional form, Eq. (5.13). The priors on the parameters are shown in Table 5.3.

Table 5.2 Results of the piecewise power law fits (normalizations, slopes and intrinsic scatter, see Eq. 5.4) for the various thermodynamic quantities in several radial ranges, marked by the inner and outer rescaled radii x_{in} and x_{out} . $\rho_{A,B}$ is the correlation coefficient between A and B.

		Density			
x_{in}	x_{out}	A (10^{-4}cm^{-3})	B (slope)	σ_{int}	$\rho_{A,B}$
0.01	0.07	13.00 ± 3.83	-0.48 ± 0.10	0.38 ± 0.04	0.9884
0.07	0.13	3.44 ± 1.73	-1.04 ± 0.24	0.28 ± 0.03	0.9969
0.13	0.21	2.60 ± 0.79	-1.21 ± 0.19	0.18 ± 0.02	0.9974
0.21	0.31	2.85 ± 0.72	-1.16 ± 0.21	0.15 ± 0.01	0.9963
0.31	0.46	1.84 ± 0.31	-1.60 ± 0.20	0.15 ± 0.01	0.9938
0.46	0.72	1.63 ± 0.17	-1.80 ± 0.21	0.18 ± 0.02	0.9767
0.72	1.14	1.42 ± 0.06	-2.38 ± 0.29	0.27 ± 0.03	0.7102
1.15	2.00	1.53 ± 0.19	-2.47 ± 0.31	0.37 ± 0.04	-0.8783
		Pressure			
x_{in}	x_{out}	A	B (slope)	σ_{int}	$\rho_{A,B}$
0.01	0.09	5.75 ± 2.39	-0.31 ± 0.13	0.65 ± 0.09	0.9353
0.09	0.22	1.84 ± 1.06	-0.72 ± 0.28	0.39 ± 0.05	0.9321
0.22	0.39	0.68 ± 0.24	-1.27 ± 0.28	0.27 ± 0.04	0.9550
0.39	0.65	0.27 ± 0.07	-2.27 ± 0.36	0.29 ± 0.04	0.9636
0.65	0.88	0.26 ± 0.05	-2.19 ± 0.65	0.34 ± 0.05	0.9371
0.89	1.28	0.24 ± 0.02	-2.09 ± 0.61	0.38 ± 0.06	-0.3866
1.29	2.65	0.27 ± 0.07	-3.21 ± 0.40	0.40 ± 0.07	-0.9363
		Temperature			
x_{in}	x_{out}	A	B (slope)	σ_{int}	$\rho_{A,B}$
0.01	0.12	1.29 ± 0.16	0.12 ± 0.04	0.18 ± 0.02	0.9713
0.12	0.32	0.96 ± 0.11	-0.04 ± 0.07	0.14 ± 0.02	0.9804
0.32	0.56	0.74 ± 0.10	-0.22 ± 0.15	0.14 ± 0.02	0.9789
0.56	0.87	0.65 ± 0.04	-0.34 ± 0.18	0.13 ± 0.02	0.9388
0.88	1.90	0.65 ± 0.02	-0.31 ± 0.11	0.08 ± 0.02	-0.4798
		Entropy			
x_{in}	x_{out}	A	B (slope)	σ_{int}	$\rho_{A,B}$
0.01	0.10	0.82 ± 0.38	0.61 ± 0.14	0.56 ± 0.07	0.9394
0.11	0.24	1.57 ± 0.32	0.93 ± 0.11	0.28 ± 0.03	0.9665
0.24	0.45	1.14 ± 0.20	0.72 ± 0.16	0.16 ± 0.02	0.9783
0.45	0.66	1.11 ± 0.16	0.65 ± 0.23	0.16 ± 0.02	0.9748
0.67	0.95	1.20 ± 0.08	0.87 ± 0.25	0.14 ± 0.02	0.9057
0.96	1.90	1.27 ± 0.08	1.09 ± 0.27	0.21 ± 0.05	-0.6778

5.3.6 Scatter

The high data quality of X-COP allows us to probe the intrinsic scatter of our profiles as a function of radius. The piecewise fit using power laws allows us to measure the scatter in a nearly model independent way, whereas the global fit with functional forms and scatter described as a log-parabola provides a consistent description of both the profile shape and the intrinsic scatter throughout the entire radial range. In Fig. 5.11 we show the scatter of all our thermodynamic quantities obtained in both cases. We remind that our definition of the intrinsic scatter is relative: a value of 0.1 on the y-axis indicates that the considered quantity is intrinsically scattered by 10% of its value.

We notice that our thermodynamic profiles generally exhibit a high scatter in the central parts of the profile. The scatter decreases towards the outskirts, reaching a minimum in the range $[0.2 - 0.8]R_{500}$, and increases slightly beyond this point. We find that temperature is the least scattered thermodynamic quantity, with intrinsic scatters ranging from 10% to 20%. On the contrary, and surprisingly, pressure is the most scattered quantity at all radii (looking at the scatter reconstructed from the piecewise power law fits), ranging from 25% to 60%.

In all cases, we note that our profiles present a high degree of self-similarity in the radial range $[0.2 - 0.8]R_{500}$, with a typical intrinsic scatter less than 0.3 (~ 0.1 dex) in all the measured quantities. This radial range corresponds to the region where gravity dominates and baryonic physics (gas cooling, AGN and supernova feedback) is relatively unimportant, whereas gas accretion still plays a subdominant role. This is consistent with tightly self-regulated mechanical AGN feedback (e.g., via chaotic cold accretion Gaspari et al., 2012), which can only affect the region $< 0.1R_{500}$, with predicted moderate scatter in T/n_e as similarly retrieved here.

We note that the intrinsic scatter profiles shown in Fig. 5.11 include the scatter that is induced by uncertainties on the cluster mass, hence on the self-similar scaling quantities. In Sect. 5.3.7 we estimate numerically the residual scatter coming from uncertainties in the self-similar scaling on the various thermodynamic quantities. We found that the scaled pressure is the quantity that is most strongly affected by mass uncertainties, which introduce a scatter of $\sim 11\%$ at R_{500} , compared to 6% for the temperature, 5% for the density and 3% for the entropy. However, this effect appears insufficient to fully explain the difference in scatter between e.g. density and pressure at $0.5R_{500}$. We also checked whether the higher scatter in pressure could be explained by intrinsic differences between X-ray and SZ pressure profiles (see Sect. 5.2.5). However, we find no statistically-significant differences between the pressure profiles measured with the two methods, and the scatter in pressure remains the same when considering X-ray and SZ data separately.

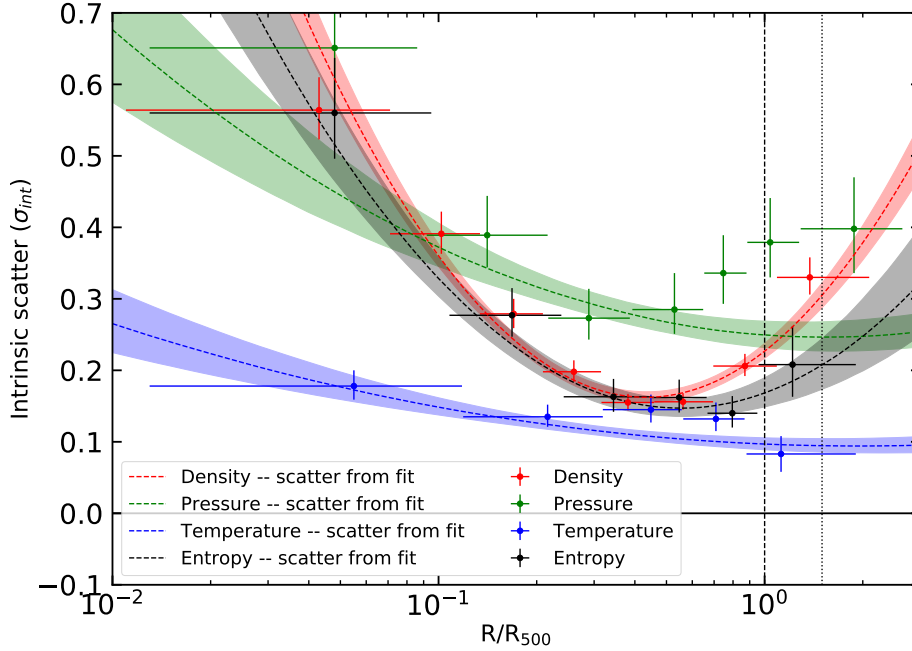


Fig. 5.11 Measured intrinsic scatter of all our thermodynamic quantities, density (red), pressure (green), temperature (blue), and entropy (black). The data points indicate the results of piecewise power law fits on several radial range, whereas the dashed lines and shaded areas show the intrinsic scatter described as a log-parabola (Eq. 5.6) around the best fitting functional forms.

5.3.7 Mass-induced scatter in thermodynamic profiles

Since the scaling of our thermodynamic quantities depends on the cluster mass both through the scale radius R_{500} and the self-similar quantities Q_{500} (see Sect. 5.3), the measured scatter profiles presented in Fig. 5.11 depend on the accuracy of the adopted masses. Both statistical and systematic fluctuations of the measured mass around the true mass will induce fluctuations of the scaling quantities, thus introducing an irreducible source of scatter originating from the limited accuracy of our mass calibration.

To take this effect into account, we estimated numerically the scatter in each quantity that is induced by uncertainties in our mass scaling. We start from scatter-free universal profiles following the measurements provided in Table 5.3, and perturb the mass scaling according to the known statistical uncertainties and biases in our mass scaling. Namely, for each X-COP cluster we randomly draw new values of the observed mass M_{obs} as

$$M_{\text{obs}} = \text{Gauss}((1 - b)M_{\text{true}}, \Delta M) \quad (5.14)$$

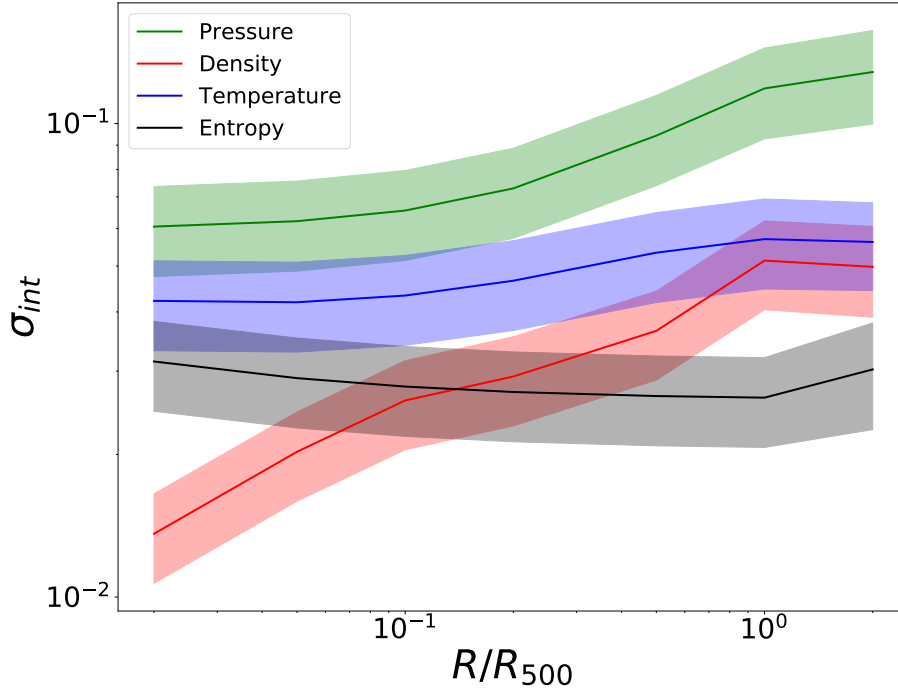


Fig. 5.12 Scatter in the various thermodynamic profiles induced by uncertainties in the mass calibration. The shaded area show the range of intrinsic scatter obtained from 1,000 simulations.

with M_{true} the assumed true mass, b the hydrostatic mass bias, and ΔM the statistical uncertainty in our hydrostatic masses (see Ettori et al. 2018 for details). For the hydrostatic mass bias, we use the distribution of non-thermal pressure values determined in Eckert et al. (2018) from the measured gas fraction. We then scale the scatter-free profiles for each quantity Q by the perturbed values of R_{500} and Q_{500} .

We apply this procedure to each X-COP cluster and compute the resulting scatter as a function of radius. We repeat this procedure 1,000 times with repetition to get an idea of the uncertainty in this procedure introduced by sample variance. In Fig. 5.12 we show the resulting mass-induced scatter for the scaled pressure, density, temperature and entropy. We can see that the effect of the mass scaling is largest on the pressure and ranges between 6% and 12% as a function of radius. Conversely, the effect on the entropy is minimal (2%-3%). The scatter in temperature and density induced by uncertainties in the mass scaling lies somewhat in between. Pressure is more affected than the other thermodynamic quantities simply because its slope is the most steep among the quantities.

Table 5.3 Best fit parameters of the functional forms describing the universal thermodynamic quantities. In all cases, we provide the results of the fit to the entire population (ALL) as well as for cool-core (CC) and non-cool-core (NCC) populations separately. σ_1 , σ_0 , and x_0 are the parameters of the log-parabola describing the behaviour of the intrinsic scatter. We indicate the priors adopted on the parameters, indicating uniform priors between a and b with $U(a, b)$.

Density: Eq. (5.7)									
Data	$\log(n_0)$	$\log(r_c)$	$\log(r_s)$	α	β	ε	σ_1	x_0	σ_0
Priors	$U(-7, -2)$	$U(-7, -2)$	$U(-2.5, 2.5)$	$U(0, 5)$	$U(0, 5)$	$U(0, 5)$	$U(0, 0.5)$	$U(0, 1)$	$U(0, 0.5)$
ALL	-4.4 ± 0.5	-3.0 ± 0.5	-0.29 ± 0.15	0.89 ± 0.59	0.43 ± 0.02	2.86 ± 0.38	0.09 ± 0.01	0.43 ± 0.02	0.16 ± 0.01
CC	-3.9 ± 0.4	-3.2 ± 0.3	0.17 ± 0.07	0.80 ± 0.61	0.49 ± 0.01	4.67 ± 0.36	0.04 ± 0.01	0.88 ± 0.10	0.13 ± 0.01
NCC	-4.9 ± 0.4	-2.7 ± 0.5	-0.51 ± 0.17	0.70 ± 0.48	0.39 ± 0.04	2.60 ± 0.27	0.10 ± 0.01	0.38 ± 0.02	0.16 ± 0.01

Pressure: Eq. (5.9)									
Data	P_0	c_{500}	γ	α	β	σ_1	x_0	σ_0	
Priors	$U(0, 14)$	$U(0, 5)$	$U(0, 0.8)$	fix	$U(2, 8)$	$U(0, 0.5)$	$U(0, 2)$	$U(0, 0.5)$	
ALL	5.68 ± 1.77	1.49 ± 0.30	0.43 ± 0.10	1.33	4.40 ± 0.41	0.02 ± 0.01	1.63 ± 0.36	0.25 ± 0.02	
CC	6.03 ± 1.61	1.68 ± 0.23	0.51 ± 0.10	1.33	4.37 ± 0.26	0.03 ± 0.01	1.52 ± 0.33	0.00 ± 0.00	
NCC	7.96 ± 2.54	1.79 ± 0.38	0.29 ± 0.11	1.33	4.05 ± 0.41	0.01 ± 0.01	1.28 ± 0.52	0.30 ± 0.03	

Temperature: Eq. (5.11)									
Data	T_0	$\log(r_{cool})$	r_t	$\frac{T_{min}}{T_0}$	a_{cool}	$c/2$	σ_1	x_0	σ_0
Priors	$U(0, 2)$	$U(-7, 0)$	$U(0, 1)$	$U(0, 1.5)$	$U(0, 3)$	$U(0, 1)$	$U(0, 0.5)$	$U(0, 3)$	$U(0, 0.5)$
ALL	1.21 ± 0.23	-2.8 ± 1.1	0.34 ± 0.10	0.50 ± 0.24	1.03 ± 0.78	0.27 ± 0.04	0.01 ± 0.01	2.13 ± 0.67	0.09 ± 0.01
CC	1.32 ± 0.25	-2.8 ± 0.7	0.40 ± 0.10	0.22 ± 0.17	0.74 ± 0.30	0.33 ± 0.06	0.01 ± 0.01	0.08 ± 0.04	0.03 ± 0.01
NCC	1.09 ± 0.10	-4.4 ± 1.8	0.45 ± 0.14	0.66 ± 0.32	1.33 ± 0.89	0.30 ± 0.07	0.01 ± 0.01	2.22 ± 0.63	0.11 ± 0.01

Entropy: Eq. (5.13)							
Data	$\log(K_0)$	K_1	α	σ_1	x_0	σ_0	
Priors	$U(-7, 0)$	$U(1, 2)$	$U(0, 2)$	$U(0, 0.5)$	$U(0, 1)$	$U(0, 0.5)$	
ALL	-3.98 ± 1.22	1.21 ± 0.03	0.83 ± 0.04	0.06 ± 0.02	0.56 ± 0.11	0.14 ± 0.01	
CC	-5.50 ± 1.10	1.35 ± 0.06	0.93 ± 0.04	0.03 ± 0.02	0.60 ± 0.22	0.17 ± 0.03	
NCC	-2.77 ± 0.55	1.14 ± 0.03	0.84 ± 0.07	0.05 ± 0.02	0.57 ± 0.16	0.14 ± 0.01	

5.3.8 CC vs NCC

We divide our cluster sample into two populations based on the central entropy value, shown as the last column in Table 5.1. We use as an indicator of dynamical state the central entropy of our clusters as measured by *Chandra* (Cavagnolo et al., 2009), which has a better spatial resolution than *XMM-Newton*, and therefore is able to trace more accurately the behaviour of the entropy profiles in the inner regions. Using this indicator we identify 4 clusters as cool-core (CC) and 8 as non-cool-core (NCC) using the value of $K_0 = 30 \text{ keVcm}^2$ as discerning value.

In Fig. 5.13 we show the data split into the CC and NCC populations, together with the fit using the functional forms used above, Eq. (5.7) for density, Eq. (5.9) for pressure, Eq. (5.11) for temperature, and Eq. (5.13) for entropy. The best fitting functional forms for the CC and NCC classes separately are provided in Table 5.3, and the results of piecewise power law fits to the two populations individually are given in Table 5.4 and Fig 5.14. We immediately

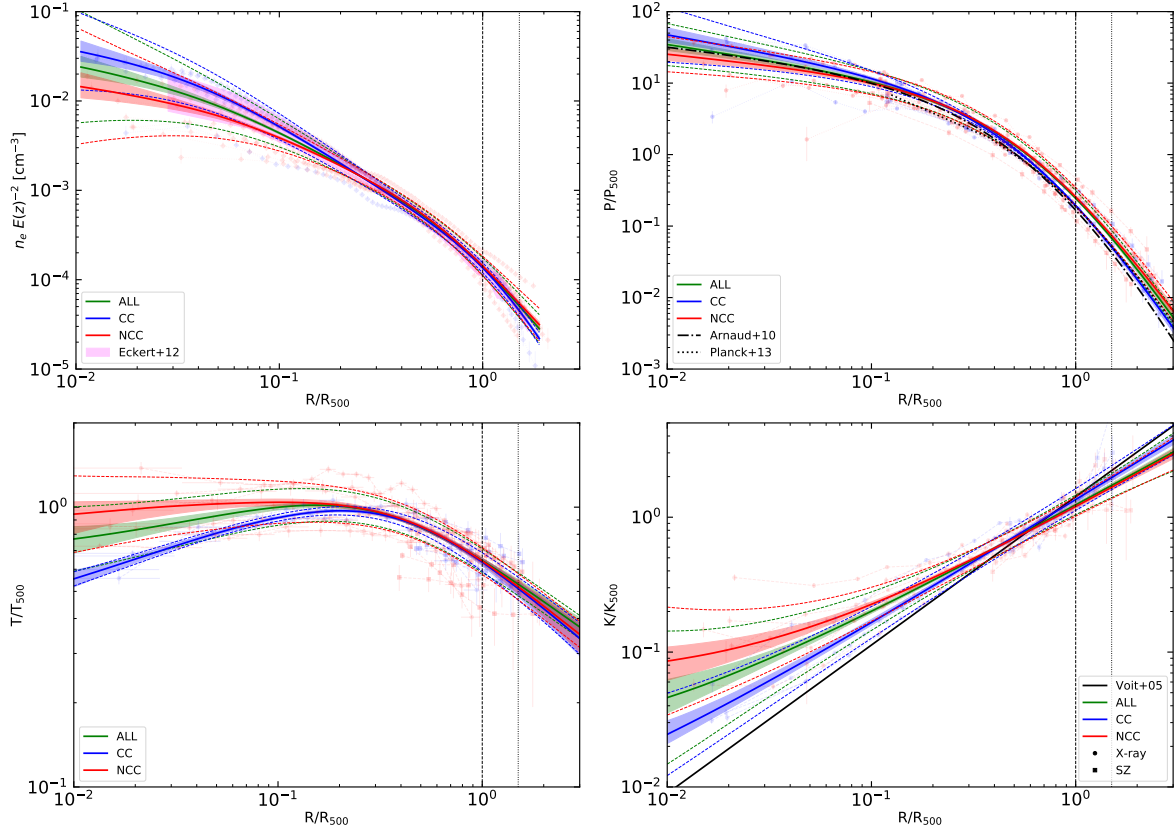


Fig. 5.13 Thermodynamic quantities of the X-COP clusters dividing the clusters in the two populations of cool-core (CC, in blue) and non-cool-core clusters (NCC, in red), compared with the entire population (ALL, in green). *Top left:* Density profiles fitted using the functional form presented in Eq. (5.7), over-plotted on the data and on the ‘universal’ density profile of Eckert et al. (2012, pink shaded area). *Top right:* Pressure profiles fitted using the functional form presented in Eq. (5.9), over-plotted on the data and compared to the *Planck* results (Planck Collaboration et al., 2013, dotted black line) and the universal pressure profile of Arnaud et al. (2010, dash-dotted black line). *Bottom left:* Temperature profiles fitted using the functional form presented in Eq. (5.7) and over-plotted on the data. *Bottom right:* Entropy profiles fitted using the functional form presented in Eq. (5.13), over-plotted on the data and on the gravitational collapse predictions (Voit et al., 2005, solid black line).

notice that in the core CC and NCC systems separate out. However, we do not observe any significant differences between CC and NCC systems outside of the core: the properties of our SZ selected clusters beyond $0.3R_{500}$ are not influenced by the properties of the core. We remark that in the case of the temperature there is a slight difference between the two best fits, with NCC having steeper temperature profiles, however well within the 1σ error envelope. The only marginally significant difference is found in the entropy profiles, which appear slightly flatter in the outskirts of NCC clusters. As shown in Table 5.3, we measure an outer slope $\alpha_{CC} = 0.95 \pm 0.03$ for the CC populations, as opposed to $\alpha_{NCC} = 0.85 \pm 0.07$. However, we note that this difference can be an artefact of the poor fit to the data obtained with a simple power law with an entropy floor, Eq. (5.13). Indeed, similar to the case of the fit to the overall population, we find a steeper slope at large radii when fitting the data points for the two populations with a piecewise power law ($\alpha_{CC} = 1.23 \pm 0.14$, $\alpha_{NCC} = 0.94 \pm 0.14$, see Table 5.4), which is consistent with the self-similar slope of 1.1 within 1σ . Thus, the evidence for a flatter entropy slope beyond R_{500} in the NCC population is marginal.

In Fig. 5.15 we also show the best fit scatter of the populations as a function of radius, splitting into CC and NCC clusters and comparing with the full population. In this case, we caution that the number of systems in each category is small (4 CC and 8 NCC systems) and the measurements of the scatter may be unreliable.

Table 5.4 Same as Table 5.2 but discerning between cool-core and non-cool-core clusters.

Density									
cool-cores (CC)					Non-cool-cores (NCC)				
x_{in}	x_{out}	A (10^{-4} cm^{-3})	B (slope)	σ_{int}	x_{in}	x_{out}	A	B (slope)	σ_{int}
0.01	0.09	10.16 ± 3.26	-0.80 ± 0.10	0.42 ± 0.04	0.01	0.16	8.33 ± 1.27	-0.66 ± 0.06	0.40 ± 0.03
0.09	0.25	2.46 ± 0.64	-1.32 ± 0.14	0.31 ± 0.03	0.16	0.34	2.66 ± 0.29	-1.21 ± 0.08	0.19 ± 0.01
0.25	0.65	1.68 ± 0.13	-1.56 ± 0.08	0.18 ± 0.02	0.35	0.72	1.75 ± 0.08	-1.64 ± 0.07	0.16 ± 0.01
0.67	1.81	1.31 ± 0.03	-2.47 ± 0.09	0.15 ± 0.02	0.72	2.09	1.39 ± 0.04	-2.23 ± 0.10	0.30 ± 0.02

Pressure									
cool-cores (CC)					Non-cool-cores (NCC)				
x_{in}	x_{out}	A	B (slope)	σ_{int}	x_{in}	x_{out}	A	B (slope)	σ_{int}
0.02	0.11	6.23 ± 2.63	-0.31 ± 0.15	0.76 ± 0.13	0.01	0.15	3.85 ± 1.51	-0.40 ± 0.13	0.48 ± 0.07
0.12	0.29	1.12 ± 0.48	-0.97 ± 0.25	0.26 ± 0.06	0.16	0.37	0.77 ± 0.23	-1.18 ± 0.21	0.33 ± 0.04
0.32	0.66	0.30 ± 0.05	-1.98 ± 0.23	0.20 ± 0.05	0.39	0.71	0.26 ± 0.06	-2.36 ± 0.37	0.36 ± 0.05
0.69	1.17	0.22 ± 0.02	-2.52 ± 0.35	0.19 ± 0.05	0.71	1.08	0.26 ± 0.03	-2.07 ± 0.58	0.39 ± 0.06
1.23	2.65	0.30 ± 0.07	-3.54 ± 0.39	0.31 ± 0.10	1.12	2.50	0.27 ± 0.05	-3.03 ± 0.36	0.43 ± 0.08

Temperature									
cool-cores (CC)					Non-cool-cores (NCC)				
x_{in}	x_{out}	A	B (slope)	σ_{int}	x_{in}	x_{out}	A	B (slope)	σ_{int}
0.02	0.19	1.40 ± 0.05	0.19 ± 0.01	0.04 ± 0.01	0.01	0.27	1.13 ± 0.09	0.05 ± 0.03	0.17 ± 0.02
0.22	0.66	0.72 ± 0.04	-0.23 ± 0.05	0.07 ± 0.02	0.28	0.68	0.68 ± 0.05	-0.31 ± 0.09	0.15 ± 0.02
0.66	1.57	0.66 ± 0.02	-0.22 ± 0.10	0.08 ± 0.03	0.69	1.90	0.64 ± 0.02	-0.31 ± 0.10	0.13 ± 0.02

Entropy									
cool-cores (CC)					Non-cool-cores (NCC)				
x_{in}	x_{out}	A	B (slope)	σ_{int}	x_{in}	x_{out}	A	B (slope)	σ_{int}
0.02	0.19	1.30 ± 0.29	0.90 ± 0.08	0.33 ± 0.05	0.01	0.27	0.83 ± 0.14	0.54 ± 0.06	0.37 ± 0.04
0.22	0.66	1.26 ± 0.16	0.81 ± 0.12	0.19 ± 0.03	0.28	0.68	1.19 ± 0.09	0.78 ± 0.09	0.15 ± 0.02
0.66	1.57	1.37 ± 0.06	1.32 ± 0.17	0.12 ± 0.04	0.69	1.90	1.22 ± 0.04	0.92 ± 0.13	0.17 ± 0.03

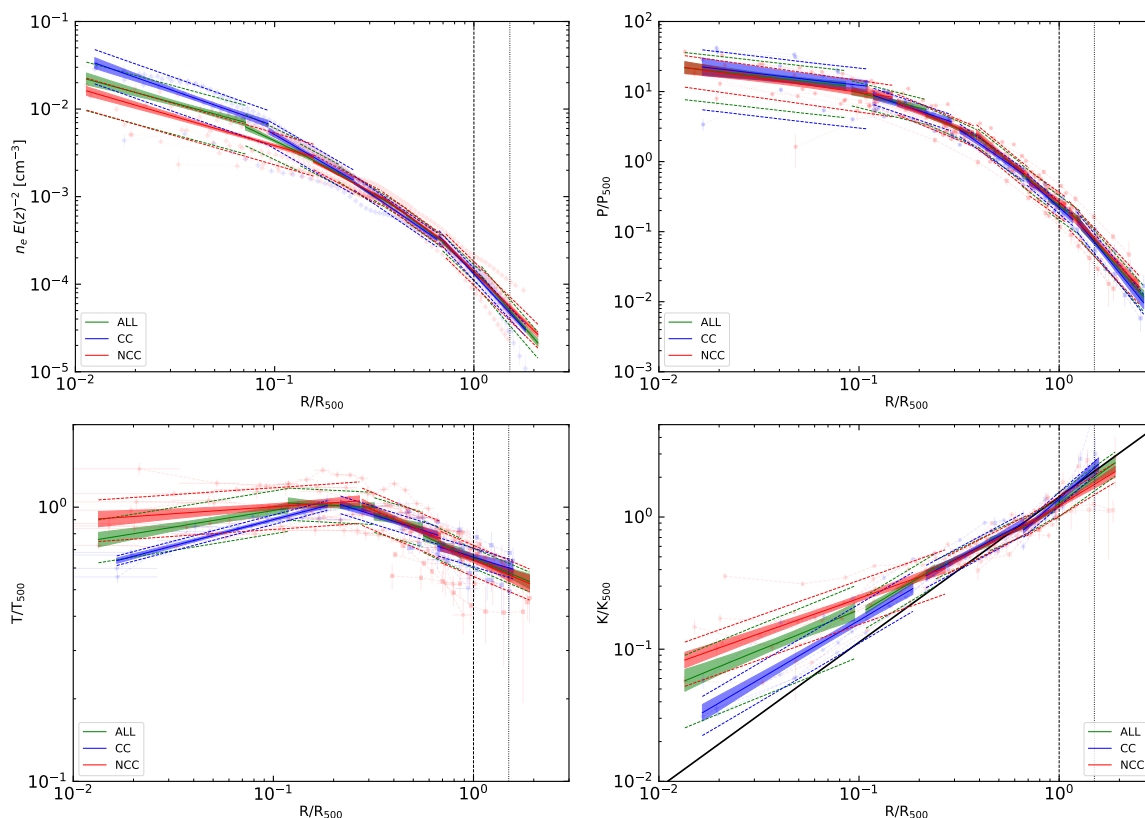


Fig. 5.14 Same as Fig. 5.13 but using the piecewise fit instead of global functional form. The cluster population of X-COP is divided in cool-core (CC, in blue) and non-cool-core clusters (NCC, in red), compared with the entire population (ALL, in green).

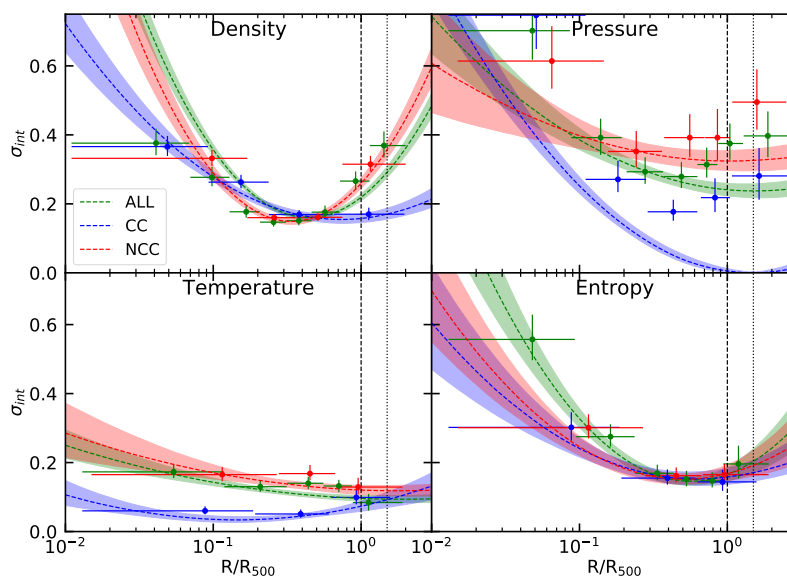


Fig. 5.15 Scatter of our thermodynamic quantities dividing our cluster sample in CC and NCC

Table 5.5 Stacked thermodynamic profiles. N_X and N_{SZ} indicates respectively the number of objects reaching the indicated radius. We indicate the median of the 12 cluster profile, and with the subscripts *low* and *high* we indicate the values which contain 68% of the objects.

$\frac{R}{R_{500}}$	$n_e E(z)^{-2}$	Density		N_X
-	cm^{-3}	$(n_e E(z)^{-2})_{low}$	$(n_e E(z)^{-2})_{high}$	-
		cm^{-3}	cm^{-3}	
1.058e-02	8.814e-03	6.543e-03	1.503e-02	12
1.179e-02	8.751e-03	6.224e-03	1.416e-02	12
1.313e-02	8.684e-03	6.018e-03	1.457e-02	12
1.463e-02	8.712e-03	5.929e-03	1.421e-02	12
1.630e-02	8.409e-03	5.839e-03	1.324e-02	12
1.816e-02	8.110e-03	5.666e-03	1.269e-02	12
2.024e-02	8.007e-03	5.560e-03	1.314e-02	12
2.255e-02	7.720e-03	5.432e-03	1.100e-02	12
2.513e-02	7.627e-03	5.440e-03	1.167e-02	12
2.799e-02	7.593e-03	5.445e-03	1.165e-02	12
3.119e-02	7.513e-03	5.503e-03	1.133e-02	12
3.475e-02	7.334e-03	5.534e-03	1.089e-02	12
3.872e-02	7.086e-03	5.271e-03	1.058e-02	12
4.314e-02	6.889e-03	5.086e-03	1.000e-02	12
4.807e-02	6.675e-03	4.839e-03	9.519e-03	12
5.356e-02	6.408e-03	4.531e-03	8.860e-03	12
5.967e-02	6.161e-03	4.246e-03	8.219e-03	12
6.649e-02	5.628e-03	3.817e-03	7.509e-03	12
7.408e-02	5.255e-03	3.550e-03	6.841e-03	12
8.254e-02	4.875e-03	3.359e-03	6.049e-03	12
9.197e-02	4.473e-03	3.196e-03	5.461e-03	12
1.025e-01	4.141e-03	2.992e-03	4.983e-03	12
1.142e-01	3.813e-03	2.728e-03	4.495e-03	12
1.272e-01	3.429e-03	2.527e-03	4.023e-03	12
1.417e-01	3.011e-03	2.327e-03	3.565e-03	12
1.579e-01	2.678e-03	2.123e-03	3.089e-03	12
1.759e-01	2.385e-03	1.854e-03	2.676e-03	12
1.960e-01	2.142e-03	1.650e-03	2.296e-03	12
2.184e-01	1.892e-03	1.478e-03	1.992e-03	12
2.434e-01	1.675e-03	1.328e-03	1.723e-03	12
2.712e-01	1.444e-03	1.159e-03	1.475e-03	12
3.021e-01	1.193e-03	1.038e-03	1.238e-03	12
3.366e-01	1.013e-03	9.677e-04	1.039e-03	12
3.751e-01	8.583e-04	8.375e-04	8.741e-04	12
4.179e-01	7.145e-04	6.885e-04	7.349e-04	12
4.656e-01	5.997e-04	5.689e-04	6.211e-04	12
5.188e-01	4.926e-04	4.631e-04	5.208e-04	12
5.780e-01	4.043e-04	3.744e-04	4.390e-04	12
6.440e-01	3.391e-04	3.190e-04	3.530e-04	12
7.176e-01	2.742e-04	2.657e-04	2.832e-04	12
7.995e-01	2.199e-04	2.106e-04	2.277e-04	12
8.908e-01	1.783e-04	1.691e-04	1.843e-04	12
9.925e-01	1.423e-04	1.312e-04	1.493e-04	12
1.106e+00	1.142e-04	1.051e-04	1.213e-04	11
1.232e+00	8.635e-05	7.469e-05	9.571e-05	11
1.373e+00	6.274e-05	5.512e-05	6.934e-05	11
1.530e+00	4.767e-05	4.269e-05	5.336e-05	10
1.704e+00	3.720e-05	3.132e-05	4.402e-05	5
1.899e+00	2.769e-05	2.355e-05	3.228e-05	2

Continued on next page

Table 5.5 continued.

Pressure								
$\frac{R}{R_{500}}$	$\left(\frac{P}{P_{500}}\right)_X$	$\left(\frac{P}{P_{500}}\right)_{X,low}$	$\left(\frac{P}{P_{500}}\right)_{X,high}$	N_X	$\left(\frac{P}{P_{500}}\right)_{SZ}$	$\left(\frac{P}{P_{500}}\right)_{SZ,low}$	$\left(\frac{P}{P_{500}}\right)_{SZ,high}$	N_{SZ}
2.283e-02	2.396e+01	1.380e+01	2.829e+01	10	-	-	-	-
2.909e-02	2.110e+01	1.243e+01	2.603e+01	10	-	-	-	-
3.706e-02	2.198e+01	1.420e+01	2.376e+01	11	-	-	-	-
4.723e-02	1.995e+01	1.447e+01	2.123e+01	11	-	-	-	-
6.018e-02	1.569e+01	1.025e+01	1.847e+01	12	-	-	-	-
7.669e-02	1.318e+01	8.647e+00	1.557e+01	12	-	-	-	-
9.772e-02	1.086e+01	7.665e+00	1.283e+01	12	-	-	-	-
1.245e-01	8.800e+00	7.024e+00	1.022e+01	12	-	-	-	-
1.587e-01	6.847e+00	5.763e+00	7.680e+00	12	-	-	-	-
2.022e-01	5.144e+00	4.492e+00	5.694e+00	12	-	-	-	-
2.577e-01	3.896e+00	3.390e+00	4.181e+00	12	-	-	-	-
3.283e-01	2.702e+00	2.537e+00	2.837e+00	12	-	-	-	-
4.184e-01	1.834e+00	1.748e+00	1.921e+00	12	-	-	-	-
5.331e-01	1.093e+00	1.059e+00	1.152e+00	12	9.885e-01	9.060e-01	1.077e+00	11
6.794e-01	6.140e-01	5.636e-01	6.594e-01	12	6.075e-01	5.461e-01	6.765e-01	12
8.657e-01	3.260e-01	2.643e-01	3.803e-01	8	3.571e-01	3.031e-01	4.056e-01	12
1.103e+00	-	-	-	-	1.939e-01	1.562e-01	2.242e-01	12
1.406e+00	-	-	-	-	9.760e-02	7.288e-02	1.132e-01	12
1.791e+00	-	-	-	-	4.649e-02	3.710e-02	5.343e-02	11
Temperature								
$\frac{R}{R_{500}}$	$\left(\frac{T}{T_{500}}\right)_X$	$\left(\frac{T}{T_{500}}\right)_{X,low}$	$\left(\frac{T}{T_{500}}\right)_{X,high}$	N_X	$\left(\frac{T}{T_{500}}\right)_{SZ}$	$\left(\frac{T}{T_{500}}\right)_{SZ,low}$	$\left(\frac{T}{T_{500}}\right)_{SZ,high}$	N_{SZ}
2.283e-02	7.606e-01	7.049e-01	8.741e-01	10	-	-	-	-
2.909e-02	7.776e-01	7.338e-01	8.823e-01	10	-	-	-	-
3.706e-02	8.259e-01	7.814e-01	9.534e-01	11	-	-	-	-
4.723e-02	8.485e-01	8.086e-01	9.598e-01	11	-	-	-	-
6.018e-02	8.759e-01	8.434e-01	9.510e-01	12	-	-	-	-
7.669e-02	9.102e-01	8.705e-01	9.650e-01	12	-	-	-	-
9.772e-02	9.460e-01	9.028e-01	9.913e-01	12	-	-	-	-
1.245e-01	9.669e-01	9.314e-01	1.011e+00	12	-	-	-	-
1.587e-01	9.717e-01	9.425e-01	1.021e+00	12	-	-	-	-
2.022e-01	9.816e-01	9.354e-01	1.024e+00	12	-	-	-	-
2.577e-01	9.751e-01	9.518e-01	1.005e+00	12	-	-	-	-
3.283e-01	9.540e-01	9.347e-01	9.794e-01	12	-	-	-	-
4.184e-01	9.317e-01	8.946e-01	9.662e-01	12	-	-	-	-
5.331e-01	8.714e-01	8.409e-01	8.970e-01	12	7.616e-01	7.053e-01	8.134e-01	11
6.794e-01	7.529e-01	7.093e-01	7.937e-01	12	7.253e-01	6.779e-01	7.748e-01	12
8.657e-01	6.540e-01	6.061e-01	6.917e-01	8	6.872e-01	6.461e-01	7.280e-01	12
1.103e+00	-	-	-	-	6.381e-01	6.001e-01	6.673e-01	12
1.406e+00	-	-	-	-	5.664e-01	5.317e-01	6.012e-01	11
1.791e+00	-	-	-	-	4.852e-01	4.380e-01	5.406e-01	6
Entropy								
$\frac{R}{R_{500}}$	$\left(\frac{K}{K_{500}}\right)_X$	$\left(\frac{K}{K_{500}}\right)_{X,low}$	$\left(\frac{K}{K_{500}}\right)_{X,high}$	N_X	$\left(\frac{K}{K_{500}}\right)_{SZ}$	$\left(\frac{K}{K_{500}}\right)_{SZ,low}$	$\left(\frac{K}{K_{500}}\right)_{SZ,high}$	N_{SZ}
2.283e-02	9.245e-02	5.696e-02	1.159e-01	10	-	-	-	-
2.909e-02	1.058e-01	5.736e-02	1.192e-01	10	-	-	-	-
3.706e-02	1.116e-01	7.998e-02	1.377e-01	11	-	-	-	-
4.723e-02	1.303e-01	8.800e-02	1.516e-01	11	-	-	-	-
6.018e-02	1.455e-01	1.059e-01	1.643e-01	12	-	-	-	-
7.669e-02	1.701e-01	1.403e-01	1.863e-01	12	-	-	-	-
9.772e-02	2.024e-01	1.745e-01	2.263e-01	12	-	-	-	-
1.245e-01	2.367e-01	2.107e-01	2.637e-01	12	-	-	-	-
1.587e-01	2.879e-01	2.584e-01	3.121e-01	12	-	-	-	-
2.022e-01	3.412e-01	3.060e-01	3.960e-01	12	-	-	-	-
2.577e-01	4.147e-01	3.895e-01	4.615e-01	12	-	-	-	-
3.283e-01	4.881e-01	4.737e-01	5.074e-01	12	-	-	-	-
4.184e-01	6.452e-01	5.985e-01	6.999e-01	12	-	-	-	-
5.331e-01	7.886e-01	7.595e-01	8.156e-01	12	6.631e-01	6.304e-01	6.973e-01	11
6.794e-01	8.852e-01	8.467e-01	9.227e-01	12	8.607e-01	8.225e-01	8.982e-01	12
8.657e-01	1.027e+00	9.461e-01	1.104e+00	8	1.107e+00	1.046e+00	1.168e+00	12
1.103e+00	-	-	-	-	1.460e+00	1.360e+00	1.569e+00	12
1.406e+00	-	-	-	-	2.060e+00	1.779e+00	2.389e+00	11
1.791e+00	-	-	-	-	2.774e+00	1.658e+00	4.491e+00	6

5.4 Discussion

5.4.1 Systematic uncertainties

In this section we describe the potential systematic errors affecting our analysis.

- **Gas density:** As described in Sect. 3.2.2, we paid special attention to the minimization of the systematics in the subtraction of the *XMM-Newton* background. The method that we used to model the contribution of each individual background component was calibrated using a large set of ~ 500 blank-sky pointings and leads to residual systematics of the order of 3% on the subtraction of the local background (see Appendix A of Ghirardini et al., 2018b). For the present work, we conservatively increased the level of systematics to 5% to include potential uncertainties associated with the application of the method to a cluster field instead of a blank field. A systematic error of 5% of the background value was thus added in quadrature to all our surface brightness measurements. We note that the systematic uncertainty becomes comparable to the statistical errors only beyond $\sim 2 \times R_{500}$. At R_{200} the systematic uncertainty is typically 20% or less of the measured signal. Further improvements in the modelling of the *XMM-Newton* background could allow us in the future to provide information beyond the current limiting radii, since in many cases our SZ pressure profiles extend beyond $2 \times R_{500}$.
- **Pressure profiles:** A possible source of systematics on the reconstruction of SZ pressure profiles is the relativistic corrections to the SZ effect (Itoh et al., 1998), which reduce the amplitude of the SZ increment in the high-frequency part of the CMB spectrum. Several recent works claimed a detection of the relativistic SZ corrections on stacked *Planck* data (Erler et al., 2018; Hurier, 2016). In particular, Erler et al. (2018) noted that the relativistic corrections could lead to an underestimate of the integrated SZ signal up to 15% for the hottest clusters, which could thus affect our pressure profiles too. However, we note that the gas temperature decreases by a factor 2 – 2.5 from the core to the outskirts, such that the impact of SZ corrections should be limited to the central regions, where spectroscopic X-ray measurements are preferred because of their higher signal-to-noise and resolution. For typical temperatures of ~ 5 keV at R_{500} and beyond, the expected effect is less than 5% (Erler et al., 2018). For more discussion on the impact of systematic uncertainties we refer to Planck Collaboration et al. (2013).

- **Spectroscopic temperatures:** Although our modelling of the *XMM-Newton* spectra is fairly sophisticated (see Sect. 3.2.6), uncertainties in the subtraction of the *XMM-Newton* background can lead to systematics in our spectral measurements in the outermost regions considered. Following Leccardi and Molendi (2008) we do not attempt to perform spectral measurements in the regions where our signal is less than 60% of the background intensity to avoid introducing biases. Another potential source of systematics is the calibration of the telescope’s effective area. Schellenberger et al. (2015) reported systematic differences at the level of 15% between *XMM-Newton* and *Chandra* temperature measurements for the same regions, *Chandra* returning systematically higher temperatures than *XMM-Newton*. As shown in Fig. 5.5 and demonstrated in Sect. 5.2.5, we observe a very good agreement between *XMM-Newton* and *Planck* pressure profiles, the only exception being ZwCl 1215, for which the pressure measured by *XMM-Newton* actually *exceeds* the SZ pressure by $\sim 20\%$, which could be explained by orientation effects since the X-ray and SZ signals have different line-of-sight dependencies. Since our X-ray and SZ pressure profiles are obtained in an independent way from different instruments and different techniques, we conclude that our spectral measurements are robust.
- **Self-similar scaling:** Given that the scaling quantities depend on the measured mass, and that we use as our reference mass model the *backward NFW* mass model (Ettori et al., 2010; Ghirardini et al., 2018b), uncertainties on the mass measurements should be taken into account. In Ettori et al. (2018) we discuss the accuracy of our mass models by testing our mass measurements using various methods (forward fitting, Gaussian processes and several functional forms for the mass model). We find that all the methods agree with the NFW mass reconstruction, with the mass profiles scattered by less than 5% at a fixed radius of 1.5 Mpc. The uncertainty in our scaling is therefore less than 3% on P_{500} and K_{500} , and less than 2% on R_{500} . In Eckert et al. (2018) we also assess the level of non-thermal pressure support by comparing the X-COP gas fraction profiles with the expected universal gas fraction. We find that the bias in our mass measurements at R_{500} is just 6% on average, again resulting in very small corrections in the self similar quantities.

5.4.2 Regular outskirts

The wide radial range accessible with the X-COP data allows us to study the properties of the gas at R_{500} and beyond and to constrain the shape of the universal thermodynamic profiles throughout the entire cluster volume for the first time. Compared to previous works

addressing the state of the gas in cluster outskirts (e.g. with *Suzaku* data), the study presented here constitutes a substantial improvement in several ways: *i*) the ability of our azimuthal median method to excise overdense regions down to scales of 10-20 kpc depending on the cluster redshift (Eckert et al., 2015), which allows us to measure gas density profiles that are free of the effects of gas clumping on the scales we are able to resolve (typically 30 kpc); *ii*) a nearly uniform azimuthal coverage for all our clusters out to R_{200} , which guarantees that our measurements are representative of the global behaviour and were not obtained along preferential directions; *iii*) an exquisite control of systematic uncertainties even in the faint cluster outskirts regime (see above).

As described in Sect. 5.3, our reconstruction of clumping-free thermodynamic quantities leads to results that differ substantially from the typical results obtained with *Suzaku*. We recall that several studies found relatively flat density profiles, steep temperature profiles and entropy profiles that fall below the prediction of gravitational collapse and sometimes even roll over (e.g. Kawaharada et al., 2010; Simionescu et al., 2017; Urban et al., 2014; Walker et al., 2012a,c). Conversely, our clumping-corrected reconstruction yields density and pressure profiles that steepen steadily with radius (see Fig. 5.3 and 5.5), temperature profile decreasing with a mild slope of -0.3 that is consistent with the slopes observed inside R_{500} by *XMM-Newton* and *Chandra* (Leccardi and Molendi, 2008; Pratt et al., 2007; Vikhlinin et al., 2006), and entropy profiles rising with a slope that is consistent with the self-similar slope of 1.1 beyond $0.6R_{500}$ and all the way out to the largest radii considered ($2 \times R_{500}$).

All the results presented here point to gas clumping as the primary origin for the deviations from the predictions reported so far by *Suzaku*, in agreement with the results presented in Tchernin et al. (2016) for the case of Abell 2142. Indeed, the low resolution of *Suzaku* (~ 2 arcmin) prevented the authors from excising cool, overdense structures that would bias at the same time the gas density towards high values and the spectroscopic temperature towards low values, resulting in underestimated values for the entropy that are not representative of the bulk of the ICM. If the gas in such infalling structures is in pressure equilibrium with its environment, as usually predicted (e.g. Planelles et al., 2017; Roncarelli et al., 2013), pressure profiles reconstructed from the SZ effect are mildly affected by such inhomogeneities and the combination of SZ pressure and clumping-free gas density is representative of the state of the ICM well beyond R_{500} .

The only exception to this scenario is the case of Abell 2319 (Ghirardini et al., 2018b), which deviates systematically from the measured universal profiles even when the profiles are corrected for clumping. In Ghirardini et al. (2018b) we showed that the deviations from self-similarity cannot be explained by azimuthal variations, but rather that the ongoing merging activity causes a high level of non-thermal pressure support. This conclusion is

supported by the high hydrostatic gas fraction of this system and a clear deficit of entropy beyond R_{500} , even after excising clumps. Abell 2319 is the only system within the X-COP sample that exhibits such a behaviour (see also Eckert et al. 2018), which suggests that this system is currently experiencing a transient phase of high non-thermal pressure induced by a violent merger with a mass ratio of 3 to 1 (Oegerle et al., 1995).

Overall, the results presented here establish that in the majority of cases, the bulk of the ICM is virialized and follows the predictions of gravitational collapse out to $2 \times R_{500} \approx R_{100}$. Accretion shocks that are expected to raise the entropy level of the smooth infalling gas should be located approximately at $3 - 4 \times R_{500}$ (Lau et al., 2015), and one would expect the entropy of the ICM to turn over around this radius. Such radii should also correspond to the approximate location of the splashback radius (Diemer and Kravtsov, 2014; Diemer et al., 2017), which represents a natural boundary of dark matter halos. Future X-ray and SZ facilities such as *ATHENA* (Nandra et al., 2013a) and CMB-S4 (Abazajian et al., 2016) will attempt to detect the ICM at the cluster boundary to constrain the location of accretion shocks and the accretion rate. The results presented here highlight the need for relatively high angular resolution experiments with a low and highly reproducible background to reach these goals.

5.4.3 Self-similarity of the profiles

Our analysis shows that the thermodynamic profiles exhibit a high level of similarity once the profiles are rescaled according to the self-similar model (Kaiser, 1986). The level of self-similarity is particularly remarkable beyond the core ($R > 0.3R_{500}$) and it reaches a maximum in the radial range $[0.2 - 0.8]R_{500}$. As already discussed in Sect. 5.3.6, the region of minimum scatter observed in this study corresponds to the region where the gas is highly virialized and baryonic effects are negligible. In the central regions ($R < 0.3R_{500}$) baryonic effects (cooling, AGN feedback) lead to a substantial scatter within the cluster population. Beyond $\sim R_{500}$, we again observe an increase in the measured scatter, which might be explained by different accretion rates from one system to another. Importantly, our study shows that the properties of the X-COP cluster population beyond $0.3R_{500}$ are not correlated with the core state (CC or NCC). While the core state probably retains memory of past major mergers, it does not trace the accretion rate on large scales at the present epoch. This result agrees with the predictions of Planelles et al. (2017), which did not find differences in the accretion rate of simulated CC and NCC systems. For instance, the case of A2029 is striking. This cluster hosts a strong cool-core and it is one of the most regular in our sample. However, our large-scale mosaic reveals that it is located within a chain of at least 3 X-ray detected structures (see Fig. 3.4)

with overlapping R_{200} , and the optical information shows that this system is part of a larger filamentary structure extending over ~ 20 Mpc (Smith et al., 2012).

Another important result of our study is that beyond the central regions pressure is the most scattered thermodynamic quantity (see Fig. 5.11). The scatter in $P_e = T_X \times n_e$ is about 50% larger than the scatter in either T_X or n_e , which is expected in case fluctuations in temperature and density are uncorrelated. This result is opposite to the widely accepted view that temperature and density variations are anti-correlated, which has led people to postulate that the quantity $Y_X = M_{\text{gas}} \times T_X$ has the lowest scatter at fixed mass (Kravtsov et al., 2006). Our results disagree with this conclusion and imply that the scatter in M_{gas} is less than the scatter in Y_X at fixed mass. These results are consistent with the recent predictions of Truong et al. (2018), which found that in the simulation runs including gas cooling and sub-grid thermal AGN feedback, temperature and density are essentially uncorrelated (see their Fig. 10), implying that the scatter in M_{gas} and T_X is less than that in Y_X . Beyond the core, X-ray observables appear to behave self similarly to a high level of precision. In case a selection based on the integrated gas mass or the core-excised X-ray luminosity can be achieved, future X-ray surveys such as *eROSITA* (Predehl et al., 2010) will yield large cluster catalogues and low-scatter mass proxies, even in comparison to SZ surveys (Mantz et al., 2018).

5.5 Conclusion

In this chapter, we presented the universal thermodynamic properties of the intracluster medium for 12 SZ-selected galaxy clusters observed with *XMM-Newton* and *Planck*. Our observational strategy allowed us to construct radial profiles of gas density, pressure, temperature and entropy over an unprecedentedly wide radial range from $0.01R_{500}$ to $2 \times R_{500}$, i.e. covering the entire cluster volume. We fitted our self-similar scaled profiles with universal functional forms and provided estimates of the radial dependence of the slope and intrinsic scatter. Our findings can be summarized as follows:

- Our gas density and pressure profiles are in excellent agreement with previous determinations of the universal density (Eckert et al., 2012) and pressure profiles (Planck Collaboration et al., 2013). The typical uncertainties in the gas density and pressure at R_{200} are at the level of 10%, allowing us to perform a detailed analysis of the shape and intrinsic scatter.
- The logarithmic slope of the density and pressure profiles steepens steadily with radius, reaching a value of -2.5 and -3.0 at R_{200} for density and pressure, respectively. These

results are consistent with the expectations for an ideal gas in hydrostatic equilibrium within a NFW potential well.

- Beyond $\sim 0.3R_{500}$ the temperature profiles decrease steadily with radius with a logarithmic slope of -0.3 , which is somewhat shallower than the slope of ~ -1.0 observed in the outer regions of several systems with *Suzaku* (Reiprich et al., 2013).
- With the exception of one system, beyond $\sim 0.5R_{500}$ all clusters follow the gravitational collapse prediction for entropy generation in galaxy clusters (Voit et al., 2005) out to the largest radii considered ($2 \times R_{500}$). This result is at odds with the conclusions usually reached from *Suzaku* observation, which often show a deficit of entropy beyond R_{500} . The difference is explained by the steep slope of the *Suzaku* temperature profiles compared to ours and by our treatment of gas clumping. We postulate that the impossibility of properly excising clumps in low-resolution *Suzaku* data is responsible for biasing the observed temperatures low and gas densities high.
- The outer regions of galaxy clusters exhibit a high level of self-similarity. Beyond $\sim 0.3R_{500}$ we find no significant difference between the cool-core and non-cool-core cluster populations in any of the quantities of interest. This result implies that the core properties are determined by the merging history of a system but do not trace efficiently the current accretion rate, which determines the state of the gas in the outskirts.
- We determined for the first time the scatter of each thermodynamical quantity within the cluster population as a function of radius. The scatter of all quantities is maximum in the core and reaches a minimum in the radial range $[0.2 - 0.8]R_{500}$, see Table 5.2 and Fig. 5.11. We find that the gas temperature is the least scattered quantity at nearly all radii.

A recently accepted *XMM-Newton* program will extend the X-COP sample to objects that were initially excluded (A754, A3667, and A3827), which will allow us to perform a similar analysis on a statistically complete SZ-selected sample. Furthermore, since pressure profiles extend beyond $2 \times R_{500}$, a further reduction of the systematics on the surface brightness profile would be useful to extend the thermodynamic profiles beyond the current limits, provided that observations with higher statistical quality can be performed.

**HYDROSTATIC MASS PROFILES IN X-COP
GALAXY CLUSTERS**

6.1 Introduction

In this chapter we present the reconstruction of the hydrostatic mass profiles in the *XMM-Newton* cluster outskirts project (X-COP, Eckert et al., 2017a, see Chapter 3) using thermodynamic profiles of the gas temperature, density, and pressure that have been spatially resolved out to (median value) $0.9R_{500}$, $1.8R_{500}$, and $2.3R_{500}$.

The hydrostatic masses are recovered with a relative (statistical) median error of 3 % at R_{500} and 6% at R_{200} . The unprecedented accuracy of these hydrostatic mass profiles out to R_{200} allows us (i) to assess the level of systematic errors in the hydrostatic mass reconstruction method, (ii) to evaluate the intrinsic scatter in the NFW $c - M$ relation, (iii) to quantify robustly differences among different mass models, different mass proxies and different gravity scenarios.

For the purpose of this Chapter only, to the original X-COP list of 12 clusters, Chapter 3, we added HydraA (Abell 780) due to the availability of a high-quality *XMM-Newton* mapping (De Grandi et al., 2016). The X-ray signal for this cluster extends out to R_{200} and therefore it is possible to recover its hydrostatic mass with very high precision, even though the *Planck* signal for this cluster is contaminated by a bright central radio source.

The chapter is organized as follows. We describe in Sect. 6.2 the different techniques adopted to recover the hydrostatic masses. In Sect. 6.3, we compare these dark matter profiles with the ones recovered from scaling laws, weak lensing and galaxy dynamics. A comparison with predictions from the modified Newtonian dynamics and the ‘‘Emergent Gravity’’ scenario is discussed in Sect. 6.4. We summarize our main findings in Sect. 6.5.

Throughout the chapter, we assume a Λ CDM cosmology with $\Omega_m = 0.3$, $\Omega_\Lambda = 0.7$ and $H_0 = 70$ km/s/Mpc. Note that since our clusters are local ($z < 0.1$) the results have a very mild dependence on the adopted cosmology.

6.2 The total gravitating mass with the Hydrostatic Equilibrium Equation

Under the assumption that the intracluster medium has a spherically-symmetric distribution and follows the equation of state for a perfect gas, $P_{\text{gas}} = kT_{\text{gas}}n_{\text{gas}}$, where k is the Boltzmann’s constant, the combination of the gas density n_{gas} , as the sum of the electron and proton densities $n_e + n_p \approx 1.83n_e$, with the X-ray spectral measurements of the gas temperature and/or the SZ derived gas pressure, allows to evaluate the total mass within a radius r through

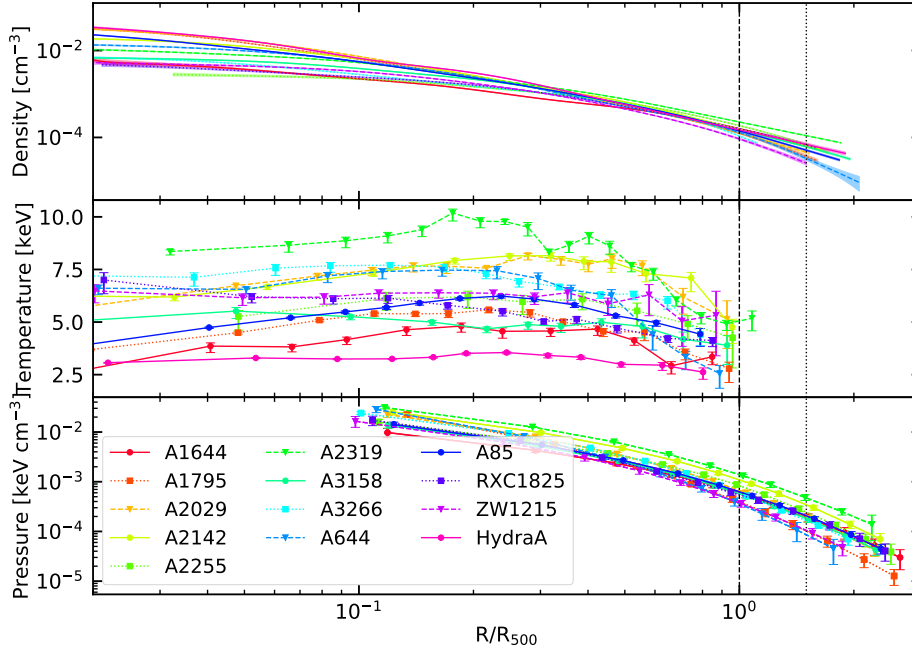


Fig. 6.1 (From top to bottom panel) Reconstructed electron density, projected temperature and SZ pressure profiles, with the statistical error bars overplotted against the radius in scale units of R_{500} . The two vertical lines indicate R_{500} and R_{200} .

the hydrostatic equilibrium equation (see e.g. Ettori et al., 2013a)

$$M_{\text{tot}}(< r) = -\frac{r P_{\text{gas}}}{\mu m_{\text{u}} G n_{\text{gas}}} \frac{d \log P_{\text{gas}}}{d \log r}, \quad (6.1)$$

where G is the gravitational constant, $m_{\text{u}} = 1.66 \times 10^{-24}$ g is the atomic mass unit, and $\mu = \rho_{\text{gas}} / (m_{\text{u}} n_{\text{gas}}) \approx (2X + 0.75Y + 0.56Z)^{-1} \approx 0.6$ is the mean molecular weight in atomic mass unit for ionized plasma, with X , Y and Z being the mass fraction for hydrogen, helium and other elements, respectively ($X + Y + Z = 1$, with $X \approx 0.716$ and $Y \approx 0.278$ for a typical metallicity of 0.3 times the Solar abundance from Anders and Grevesse, 1989).

In the present analysis, we apply both the *backward* and the *forward* method (see e.g. Ettori et al., 2013a), as discussed and illustrated in our pilot study on A2319 (Ghirardini et al., 2018b). We combine all the information available (measured pressure P_{m} , temperature

T_m , and emissivity, ε_m) to build a joint likelihood \mathcal{L} :

$$\begin{aligned} \log \mathcal{L} = & -0.5 [(P - P_m) \Sigma_{tot}^{-1} (P - P_m)^T + n \log (\det (\Sigma_{tot}))] \\ & - 0.5 \sum_{i=1}^{n_T} \left[\frac{(T_i - T_{m,i})^2}{\sigma_{T,i}^2 + \sigma_{T,int}^2} + \log (\sigma_{T,i}^2 + \sigma_{T,int}^2) \right] \\ & - 0.5 \left[\sum_{j=1}^{n_\varepsilon} \frac{(\varepsilon - \varepsilon_{m,j})^2}{\sigma_{\varepsilon,j}^2} \right], \end{aligned} \quad (6.2)$$

that includes in the fitting procedure both an intrinsic scatter $\sigma_{T,int}$ to account for any tensing between X-ray and SZ measurements, and the covariance matrix Σ_{tot} among the data in the *Planck* pressure profile (see for details Appendix D in Ghirardini et al., 2018b).

The emissivity ε is obtained from the Multiscale fitting (Eckert et al., 2016a, ; see also Sect. 2.2.5 in Ghirardini et al. 2018) of the observed X-ray surface brightness. In the *backward* method, a parametric mass model is assumed and combined with the gas density profile to predict a gas temperature profile T that is then compared with the one measured T_m in the spectral analysis and the one estimated from SZ as P/n_{gas} (losing the spatial resolution in the inner regions because of the modest 7 arcmin FWHM angular resolution of our *Planck* SZ maps, but gaining in radial extension due to the *Planck* spatial coverage; Planck Collaboration et al., 2013) to constrain the mass model parameters. In the *forward* method, some functional forms are fitted to the deprojected gas temperature and pressure profiles, as detailed in Ghirardini et al. (2018b), with, on reverse, no assumptions on the form of the gravitational potential. Note that we neglect the 3 innermost *Planck* points for the analysis to avoid possible biases induced by the *Planck* beam. The hydrostatic equilibrium equation (Eq. 6.1) is then directly applied to evaluate the radial distribution of the mass.

The profiles are fitted using an MCMC approach based on the code *emcee* (Foreman-Mackey et al., 2013a) with 10000 steps, about 100 walkers, and throwing away the first 5000 points because of ‘burnt-in’ time. From the resulting posterior distribution on our parameters we estimate the reference values using the median of the distributions, and the errors as half the difference between the 84th and 16th percentiles. In the present analysis, we investigate different mass models (Sect. 6.2.1), and adopt as reference model a NFW mass model with two free parameters, the mass concentration and R_{200} (see Sect. 6.2.2).

6.2.1 Comparison among different mass models with the *backward* method

We apply the *backward* method with the following set of different mass models and estimate their maximum likelihood in reproducing the observed profiles of gas density, temperature and SZ pressure.

The mass profile is parametrized through the expression

$$\begin{aligned}
 M(< r) &= n_0 r_s^3 f_c F(x) \\
 n_0 &= \frac{4}{3} \pi \Delta \rho_{c,z} = 1.14 \times 10^{14} h_z^2 M_\odot \text{Mpc}^{-3} \\
 f_c &= \frac{c^3}{\log(1+c) - c/(1+c)}
 \end{aligned} \tag{6.3}$$

where $\Delta = 200$, $h_z = H_z/H_0$ and $x = r/r_s$, with the scale radius r_s and the "concentration" c being the two free parameters of the fit. The function $F(x)$ characterizes each mass model and is defined as follows:

NFW $F(x) = \log(1+x) - x/(1+x)$ (Navarro et al., 1997);

EIN $F(x) = a^{1-a_1}/2^{a_1} e^{a_0} \gamma(a_1, a_0 x^{1/a})$ with $a = 5$, $a_0 = 2n$, $a_1 = 3n$ and $\gamma(a, y)$ being the incomplete gamma function equal to $\int_0^y t^{a-1} \exp(-t) dt$ (from eq. A2 in Mamon and Lokas, 2005);

ISO $F(x) = \log(x + \sqrt{1+x^2}) - \frac{x}{\sqrt{1+x^2}}$, that is the King approximation to the isothermal sphere (King, 1962);

BUR $F(x) = \log(1+x^2) + 2\log(1+x) - 2\arctan(x)$ (Salucci and Burkert, 2000);

HER $F(x) = \frac{x^2}{(x+1)^2}$ (Hernquist, 1990).

We note that our observed profiles can not provide any robust constraint on the third parameter a of the Einasto profile that is therefore fixed to the value of 5 as observed for massive halos (e.g. Dutton and Macciò, 2014). Moreover, the parameter c is defined as the "concentration" in the NFW profile, whereas it represents a way to constrain the normalization for the other mass models. In our MCMC approach, we adopt for c an uniform a-prior distribution in the linear space in the range 0.1-15. The a-prior distributions on the scale radius (or $R_{200} = c \times r_s$ for the NFW case) are still defined as uniform in the linear space in the following ranges: 1-3 Mpc (NFW); 0.1-2.8 Mpc (EIN); 0.02-0.8 Mpc (ISO); 0.02-0.8 Mpc (BUR); 0.2-3 Mpc (HER).

In Table 6.1, we quote all the best-fit parameters, and the relative Bayesian Evidence E estimated, for each mass model, as the integral of the likelihood function \mathcal{L} (equation 6.2) over the a-prior distributions $P(\theta)$ of the parameters θ ($E = \int \mathcal{L}(\theta) P(\theta) d\theta$; as implemented in e.g. MultiNest, Feroz et al., 2009).

In Fig. 6.2, we present the Bayes factor estimated for each object as the difference between the logarithm of the Bayesian Evidence of the mass model with the highest Evidence

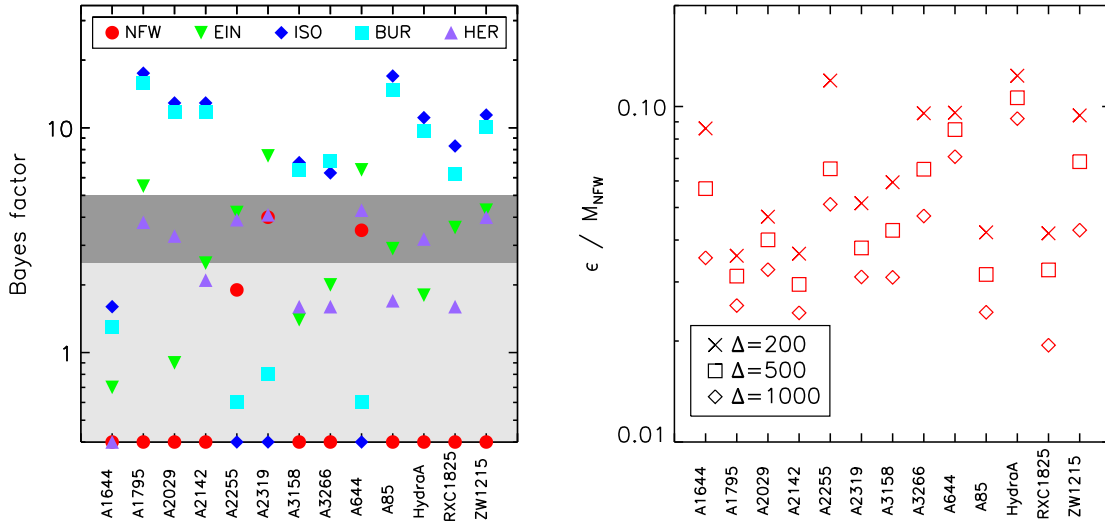


Fig. 6.2 *Left*: Bayes factor of the mass models investigated with respect to the one with the highest Evidence (see Table 6.1). Shaded regions identify values of the Bayes factor where the tension between the models is either weak (< 2.5) or strong (> 5) according to the Jeffreys’s scale (Jeffreys, 1961). *Right*: Relative error (at 1σ) on the hydrostatic mass recovered with the *backward* method and a NFW model (see Table 6.2).

with respect to the others. Nine, out of 13, objects prefer a NFW model fit and have data that are significantly inconsistent (Bayes factor > 5) with an isothermal/Burkert mass model. The remaining four objects prefer different mass models (ISO for A2255 and A2319, HER for A1644, and BUR for A644) but do not show any statistically significant (Bayes factor < 5) tension with NFW.

6.2.2 Reference mass model: *backward* method with NFW mass model

We present the results of our analysis with a *backward* method and a NFW mass model in Table 6.2. We measure mean relative (statistical only) errors lower than 8% (median, mean and dispersion at $\Delta = 1000, 500$, and 200 , respectively: 3, 4, 2%; 4, 5, 2%; 6, 7, 3%; see Fig. 6.2).

In the Cold Dark Matter scenario, the structure formation is hierarchical and allows the build-up of the most massive gravitationally-bound halos, like galaxy clusters, only at later cosmic times. Considering that the central density of halos reflects the mean density of the Universe at the time of formation, halos with increasing mass are expected to have lower mass concentration at given redshift (e.g. Bullock et al., 2001; Diemer and Kravtsov, 2015; Dolag et al., 2004; Navarro et al., 1997).

We can investigate how our best-fit results on NFW concentration and M_{200} (quoted in Table 6.2) reproduce the predictions from numerical simulations. We can also assess the level of the intrinsic scatter in the $c_{200} - M_{200}$ relation in this mass range. Simulations suggest that this scatter is related to the variation in formation time and is expected to be lower in more massive halos that form more recently (e.g. Neto et al., 2007).

We model the relation with a standard power law,

$$c_{200} = 10^\alpha \left(\frac{M_{200}}{M_{\text{pivot}}} \right)^\beta. \quad (6.4)$$

The intrinsic scatter $\sigma_{c|M}$ of the concentration around a given mass, $c_{200}(M_{200})$, is taken to be lognormal.

We fit the data with a linear relation in decimal logarithmic (log) variables with the R-package LIRA¹. LIRA is based on a Bayesian hierarchical analysis which can deal with heteroscedastic and correlated measurements uncertainties, intrinsic scatter, scattered mass proxies and time-evolving mass distributions (Sereno, 2016).

The mass distribution of the fitted clusters has to be properly modelled to address Malmquist/Eddington biases (Kelly, 2007). The Gaussian distribution can provide an adequate modelling (Sereno and Ettori, 2015). The parameters of the distribution are found within the regression procedure. This scheme is fully effective in modelling both selection effects at low masses and the steepness of the cosmological halo mass function at large masses.

Performing an unbiased analysis of the c - M relation requires to properly address uncertainties connected to the correlations and intrinsic scatter. Indeed, measured mass and concentration are strongly anti-correlated, causing the c - M relation to appear steeper (Auger et al., 2013; Du and Fan, 2014; Dutton and Macciò, 2014; Sereno et al., 2015). By correcting for this effect, it is possible to obtain a more precise, significantly flatter, relation (Sereno et al., 2015). On the other hand, the intrinsic scatter of the measurable mass with respect to the true mass can bias the estimated slope towards flatter values (Rasia et al., 2013; Sereno and Ettori, 2015). To correct for this effect, we measure the mass-concentration uncertainty covariance matrix for each cluster from the MCMC chains whereas we model the intrinsic scatter as a free fit parameter to be found in the regression procedure.

Adopting non-informative priors (Sereno et al., 2017a), we find $\alpha = 0.89 \pm 0.90$, $\beta = -0.42 \pm 0.98$ in agreement with theoretical predictions for slope and normalization (see

¹LIRA (LInear Regression in Astronomy) is available from the Comprehensive R Archive Network at <https://cran.r-project.org/web/packages/lira/index.html>.

Fig. 6.3) Statistical uncertainties are very large and we cannot discriminate between the different theoretical predictions.

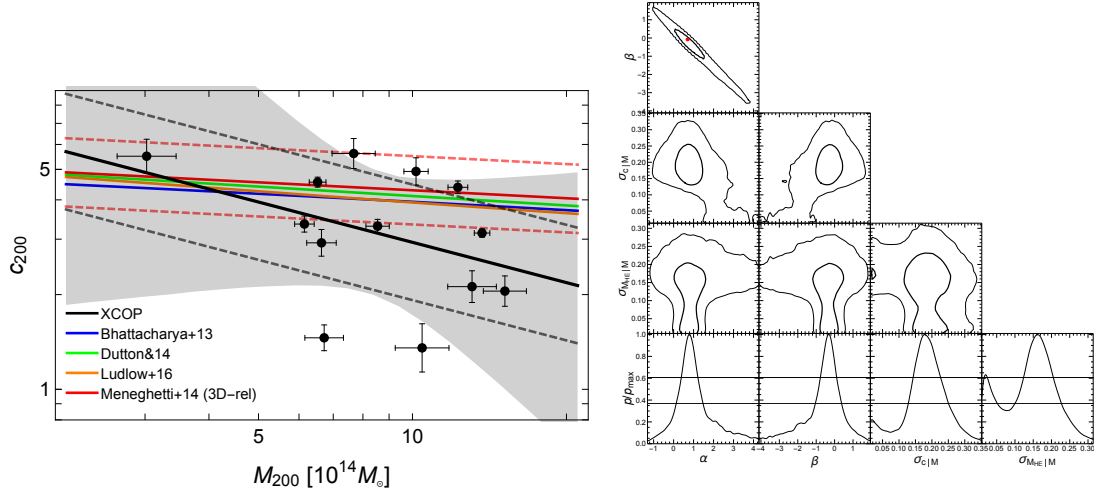


Fig. 6.3 (Left) The mass–concentration relation of the X-COP clusters. The dashed black lines show the median scaling relation (full black line) plus or minus the intrinsic scatter at redshift $z = 0.06$. The shaded grey region encloses the 68.3 per cent confidence region around the median relation due to uncertainties on the scaling parameters. As reference, we plot the mass–concentration relations of Bhattacharya et al. (2013, blue line), Dutton and Macciò (2014, green line), Ludlow et al. (2016, orange line), and Meneghetti et al. (2014, solid and dashed red lines). The dashed red lines enclose the $1\text{-}\sigma$ scatter region in the theoretical mass–concentration relation from the MUSIC-2 N -body/hydrodynamical simulations. (Right) Probability distributions of the parameters of the mass–concentration relation. The thick and thin black contours include the 1 -, $2\text{-}\sigma$ confidence regions in two dimensions, here defined as the regions within which the probability is larger than $\exp(-2.3/2)$, or $\exp(-6.17/2)$ of the maximum, respectively. The red disk represents the parameters found by Meneghetti et al. (2014) for the relaxed sample. The bottom row plots the marginalised 1D distributions, renormalised to the maximum probability. The thick and thin black levels denote the confidence limits in one dimension, i.e. $\exp(-1/2)$ and $\exp(-4/2)$ of the maximum.

On the other hand, mass measurement uncertainties are very small and we can estimate the intrinsic scatter of the hydrostatic masses, $\sigma_{M_{\text{HE}}|M} = 0.15 \pm 0.08$. Even though the marginalized posterior distribution of $\sigma_{M_{\text{HE}}|M}$ is peaked at ~ 0.15 (see Fig. 6.3), smaller values are fully consistent. The (posterior) probability that $\sigma_{M_{\text{HE}}|M}$ is less than 10 per cent (i.e. $\sigma_{M_{\text{HE}}|M} < 0.043$) is 15 per cent. Our estimate of hydrostatic mass scatter is in agreement with results from higher- z samples (Sereno and Ettori, 2015) and larger, even though compatible within uncertainties, with results from numerical simulations (Rasia et al., 2012).

The intrinsic scatter of the c - M relation, $\sigma_{c|M} = 0.18 \pm 0.06$, is compatible with theoretical predictions (Bhattacharya et al., 2013; Meneghetti et al., 2014, $\sigma_{c|M} \sim 0.15$) and previous

observational constraints (e.g. Ettori et al., 2010; Mantz et al., 2016). The relation between mass and concentration for subsamples can differ from the general relation due to selection effects. Intrinsically over-concentrated clusters may be overrepresented in a sample of clusters selected according to their large Einstein radii or to the apparent X-ray morphology (Meneghetti et al., 2014; Sereno et al., 2015). Intrinsic scatter of the c - M relation for relaxed samples is expected to be smaller than for the full population of mass selected halos. However, given the statistical uncertainty on the measured $\sigma_{c|M}$, we cannot draw any firm conclusion on the equilibrium status of the clusters.

6.2.3 Comparison among different methods and systematic errors

To evaluate some of the systematic uncertainties affecting our measurements of the hydrostatic mass, we estimate the mass at some fixed physical radii (500, 1000 and 1500 kpc) and at two overdensities (R_{500} and R_{200}) using the *forward* method and the other mass models described in Sect. 6.2.1, and compare them to the results obtained from our model of reference (*backward* NFW). We summarize the results of this comparison in Table 6.3.

We observe that the use of the *forward* method (with or without SZ profiles) introduces a systematic error of few percent at any radius, with a median difference of about 4% at R_{500} , and $<2\%$ (1st-3rd quartile: -5.4 / +8.1 %) at R_{200} .

Any other mass model constrained with the *backward* method introduces some systematic uncertainties that depends mainly on the shape characteristic of the model and on the fact that all the models have 2 only parameters, implying not so large flexibility to accommodate the distribution in the observed profiles. For instance, we note that cored profiles, like ISO and BUR, present larger positive (negative) deviations in the core (outskirts), up to about 25%.

We notice that this budget of the systematic uncertainties does not include other sources of error, such as any non-thermal contribution to the total gas pressure (e.g. Nelson et al., 2014a; Sereno et al., 2017b), and terms that account for either departures from the hydrostatic equilibrium (e.g. Biffi et al., 2016; Nelson et al., 2014b) or the violation of the assumed sphericity of the gas distribution (e.g. Sereno et al., 2017b). All these contributions have been shown to affect more significantly the clusters' outskirts and tend to bias higher (by 10-30%) the total mass estimates at $r > R_{500}$, with smaller effects in the inner regions. In particular, by imposing the distribution of the cluster mass baryon fraction estimated in the state-of-art hydrodynamical cosmological simulations, we evaluate in Eckert et al. (2018) a median value of about 6% and 10% at R_{500} and R_{200} , respectively, for the relative amount of non-thermal pressure support in the X-COP objects.

NFW					EIN				
Name	kpc	c	$\sigma_{T,int}$	$\ln E$	Name	kpc	c	$\sigma_{T,int}$	$\ln E$
A1644	1778 ⁺⁵⁵ ₋₄₈	1.46 ^{+0.14} _{-0.14}	0.001 ^{+0.000} _{-0.000}	-2.5	A1644	1119 ⁺¹⁰⁷ ₋₂₀₇	0.66 ^{+0.15} _{-0.06}	0.005 ^{+0.047} _{-0.003}	-3.1
A1795	1755 ⁺²² ₋₂₁	4.55 ^{+0.16} _{-0.14}	0.009 ^{+0.012} _{-0.007}	9.0	A1795	480 ⁺²³ ₋₂₁	1.92 ^{+0.08} _{-0.07}	0.009 ^{+0.007} _{-0.006}	3.5
A2029	2173 ⁺³⁵ ₋₃₃	4.26 ^{+0.19} _{-0.17}	0.023 ^{+0.006} _{-0.005}	-2.5	A2029	571 ⁺²⁹ ₋₃₈	1.95 ^{+0.13} _{-0.08}	0.020 ^{+0.010} _{-0.008}	-3.4
A2142	2224 ⁺²⁹ ₋₂₅	3.14 ^{+0.10} _{-0.10}	0.001 ^{+0.000} _{-0.000}	-0.6	A2142	866 ⁺⁴² ₋₃₉	1.27 ^{+0.05} _{-0.05}	0.001 ^{+0.000} _{-0.000}	-3.1
A2255	2033 ⁺⁸⁸ ₋₇₄	1.37 ^{+0.24} _{-0.23}	0.002 ^{+0.006} _{-0.001}	-4.2	A2255	959 ⁺⁹⁷ ₋₁₂₄	0.88 ^{+0.14} _{-0.09}	0.002 ^{+0.009} _{-0.001}	-6.5
A2319	2040 ⁺³⁴ ₋₃₀	4.86 ^{+0.51} _{-0.37}	0.055 ^{+0.009} _{-0.008}	-12.4	A2319	403 ⁺⁴⁶ ₋₄₇	2.64 ^{+0.34} _{-0.26}	0.067 ^{+0.017} _{-0.013}	-15.9
A3158	1766 ⁺³⁴ ₋₃₇	2.88 ^{+0.26} _{-0.17}	0.002 ^{+0.015} _{-0.001}	1.2	A3158	530 ⁺³⁴ ₋₅₂	1.57 ^{+0.16} _{-0.09}	0.004 ^{+0.028} _{-0.003}	-0.2
A3266	2325 ⁺⁷⁴ ₋₇₅	2.04 ^{+0.25} _{-0.20}	0.036 ^{+0.008} _{-0.009}	-7.1	A3266	765 ⁺⁶¹ ₋₉₁	1.34 ^{+0.18} _{-0.10}	0.057 ^{+0.015} _{-0.013}	-9.1
A644	1847 ⁺⁶¹ ₋₅₈	5.58 ^{+0.65} _{-0.51}	0.063 ^{+0.017} _{-0.016}	-9.7	A644	325 ⁺⁶⁰ ₋₅₃	2.99 ^{+0.52} _{-0.42}	0.062 ^{+0.017} _{-0.012}	-12.7
A85	1921 ⁺³⁰ ₋₂₄	3.31 ^{+0.13} _{-0.13}	0.019 ^{+0.012} _{-0.005}	7.5	A85	636 ⁺⁴⁰ ₋₇₃	1.49 ^{+0.18} _{-0.08}	0.026 ^{+0.021} _{-0.008}	4.6
HydraA	1360 ⁺⁵⁸ ₋₅₅	5.51 ^{+0.67} _{-0.61}	0.079 ^{+0.020} _{-0.016}	698.1	HydraA	299 ⁺³³ ₋₂₉	2.45 ^{+0.21} _{-0.21}	0.046 ^{+0.009} _{-0.006}	696.3
RXC1825	1719 ⁺²⁴ ₋₂₅	3.35 ^{+0.20} _{-0.19}	0.001 ^{+0.001} _{-0.000}	1.7	RXC1825	495 ⁺²⁶ ₋₆₆	1.71 ^{+0.25} _{-0.08}	0.002 ^{+0.011} _{-0.001}	-1.9
ZW1215	2200 ⁺⁷⁴ ₋₆₄	2.11 ^{+0.22} _{-0.18}	0.003 ^{+0.006} _{-0.002}	5.4	ZW1215	1341 ⁺¹⁴⁵ ₋₁₆₁	0.75 ^{+0.10} _{-0.07}	0.004 ^{+0.008} _{-0.002}	1.1
ISO					BUR				
Name	kpc	c	$\sigma_{T,int}$	$\ln E$	Name	kpc	c	$\sigma_{T,int}$	$\ln E$
A1644	298 ⁺¹⁹ ₋₁₃	4.50 ^{+0.16} _{-0.19}	0.001 ^{+0.000} _{-0.000}	-4.0	A1644	294 ⁺¹⁷ ₋₁₆	2.74 ^{+0.13} _{-0.11}	0.001 ^{+0.000} _{-0.000}	-3.7
A1795	144 ⁺⁸ ₋₆	9.45 ^{+0.32} _{-0.39}	0.055 ^{+0.012} _{-0.008}	-8.5	A1795	146 ⁺⁷ ₋₆	5.86 ^{+0.22} _{-0.22}	0.047 ^{+0.012} _{-0.009}	-6.8
A2029	195 ⁺¹³ ₋₁₀	8.81 ^{+0.37} _{-0.39}	0.078 ^{+0.015} _{-0.012}	-15.4	A2029	186 ⁺⁹ ₋₁₀	5.73 ^{+0.25} _{-0.21}	0.064 ^{+0.010} _{-0.009}	-14.2
A2142	240 ⁺¹³ ₋₁₁	7.35 ^{+0.27} _{-0.26}	0.060 ^{+0.011} _{-0.008}	-13.5	A2142	237 ⁺¹¹ ₋₁₁	4.59 ^{+0.19} _{-0.16}	0.060 ^{+0.014} _{-0.010}	-12.4
A2255	444 ⁺⁴² ₋₄₁	3.62 ^{+0.28} _{-0.22}	0.001 ^{+0.001} _{-0.000}	-2.3	A2255	409 ⁺²⁸ ₋₂₈	2.31 ^{+0.14} _{-0.12}	0.002 ^{+0.002} _{-0.001}	-2.9
A2319	241 ⁺¹⁴ ₋₉	7.22 ^{+0.23} _{-0.32}	0.041 ^{+0.018} _{-0.009}	-8.4	A2319	229 ⁺¹¹ ₋₁₃	4.68 ^{+0.23} _{-0.18}	0.042 ^{+0.013} _{-0.012}	-9.2
A3158	223 ⁺¹⁵ ₋₁₃	6.19 ^{+0.33} _{-0.29}	0.030 ^{+0.009} _{-0.011}	-5.8	A3158	217 ⁺¹² ₋₁₃	3.90 ^{+0.21} _{-0.17}	0.026 ^{+0.013} _{-0.022}	-5.3
A3266	312 ⁺³⁰ ₋₂₁	5.61 ^{+0.31} _{-0.30}	0.076 ^{+0.015} _{-0.013}	-13.4	A3266	313 ⁺³⁰ ₋₂₆	3.44 ^{+0.26} _{-0.21}	0.074 ^{+0.015} _{-0.013}	-14.2
A644	168 ⁺⁹ ₋₁₂	9.03 ^{+0.39} _{-0.35}	0.029 ^{+0.028} _{-0.027}	-6.2	A644	172 ⁺⁶ ₋₇	5.64 ^{+0.16} _{-0.15}	0.001 ^{+0.000} _{-0.000}	-6.8
A85	190 ⁺⁹ ₋₉	7.71 ^{+0.35} _{-0.28}	0.057 ^{+0.011} _{-0.008}	-9.5	A85	188 ⁺⁹ ₋₁₁	4.87 ^{+0.21} _{-0.19}	0.060 ^{+0.013} _{-0.009}	-7.3
HydraA	221 ⁺⁶³ ₋₃₁	6.22 ^{+0.45} _{-0.42}	0.324 ^{+0.029} _{-0.028}	687.0	HydraA	96 ⁺¹⁵ ₋₁₁	7.01 ^{+0.53} _{-0.57}	0.097 ^{+0.019} _{-0.013}	688.4
RXC1825	233 ⁺¹⁰ ₋₉	5.98 ^{+0.19} _{-0.18}	0.001 ^{+0.001} _{-0.000}	-6.6	RXC1825	220 ⁺¹⁰ ₋₁₀	3.86 ^{+0.15} _{-0.14}	0.001 ^{+0.000} _{-0.000}	-4.5
ZW1215	313 ⁺¹⁸ ₋₁₆	5.25 ^{+0.19} _{-0.17}	0.001 ^{+0.000} _{-0.000}	-6.0	ZW1215	303 ⁺²⁰ ₋₁₉	3.30 ^{+0.15} _{-0.14}	0.002 ^{+0.002} _{-0.001}	-4.7
HER									
Name	kpc	c	$\sigma_{T,int}$	$\ln E$					
A1644	2026 ⁺²³⁰ ₋₁₈₈	0.72 ^{+0.07} _{-0.06}	0.001 ^{+0.001} _{-0.000}	-2.4					
A1795	721 ⁺³¹ ₋₃₇	2.37 ^{+0.12} _{-0.09}	0.017 ^{+0.016} _{-0.007}	5.2					
A2029	925 ⁺⁶⁹ ₋₄₂	2.27 ^{+0.10} _{-0.13}	0.028 ^{+0.008} _{-0.007}	-5.8					
A2142	1262 ⁺⁴⁶ ₋₄₉	1.63 ^{+0.06} _{-0.05}	0.006 ^{+0.011} _{-0.004}	-2.7					
A2255	2235 ⁺²⁰³ ₋₂₈₉	0.73 ^{+0.11} _{-0.05}	0.001 ^{+0.001} _{-0.000}	-6.2					
A2319	674 ⁺⁵⁵ ₋₇₇	2.99 ^{+0.41} _{-0.22}	0.068 ^{+0.014} _{-0.010}	-12.5					
A3158	1203 ⁺¹³⁷ ₋₈₀	1.36 ^{+0.09} _{-0.12}	0.001 ^{+0.001} _{-0.000}	-0.4					
A3266	1952 ⁺²⁸⁵ ₋₁₈₉	1.03 ^{+0.10} _{-0.12}	0.036 ^{+0.008} _{-0.008}	-8.7					
A644	478 ⁺⁷³ ₋₇₄	3.73 ^{+0.67} _{-0.45}	0.090 ^{+0.027} _{-0.022}	-10.5					
A85	914 ⁺⁵⁵ ₋₁₀₉	1.92 ^{+0.26} _{-0.09}	0.027 ^{+0.019} _{-0.010}	5.8					
HydraA	473 ⁺⁶⁴ ₋₄₃	2.86 ^{+0.24} _{-0.26}	0.055 ^{+0.010} _{-0.007}	694.9					
RXC1825	913 ⁺⁴⁹ ₋₆₉	1.76 ^{+0.14} _{-0.09}	0.002 ^{+0.007} _{-0.001}	0.1					
ZW1215	1325 ⁺⁸⁶ ₋₁₁₃	1.38 ^{+0.12} _{-0.07}	0.004 ^{+0.020} _{-0.002}	1.4					

Table 6.1 We list the best-fit parameters (scale radius r_s - R_{200} in the case of NFW- and the "concentration" -or normalization- as defined in equation 6.3), the intrinsic scatter $\sigma_{T,int}$ of equation 6.2, and the logarithmic value of the evidence E for the mass models discussed in Sect. 6.2.1.

Name	z	c_{200}	0.5 Mpc $10^{14}M_{\odot}$	1 Mpc $10^{14}M_{\odot}$	1.5 Mpc $10^{14}M_{\odot}$	R_{500} Mpc	M_{500} $10^{14}M_{\odot}$	R_{200} Mpc	M_{200} $10^{14}M_{\odot}$
A1644	0.0473	$1.46^{+0.14}_{-0.14}$	1.15 ± 0.02	3.24 ± 0.10	5.47 ± 0.26	1.054 ± 0.020	3.48 ± 0.20	1.778 ± 0.051	6.69 ± 0.58
A1795	0.0622	$4.55^{+0.16}_{-0.14}$	1.95 ± 0.02	4.06 ± 0.08	5.77 ± 0.15	1.153 ± 0.012	4.63 ± 0.14	1.755 ± 0.021	6.53 ± 0.23
A2029	0.0773	$4.26^{+0.19}_{-0.17}$	2.78 ± 0.03	6.25 ± 0.13	9.24 ± 0.26	1.423 ± 0.019	8.82 ± 0.35	2.173 ± 0.034	12.57 ± 0.59
A2142	0.0909	$3.14^{+0.10}_{-0.10}$	2.48 ± 0.02	6.08 ± 0.09	9.44 ± 0.19	1.424 ± 0.014	8.95 ± 0.26	2.224 ± 0.027	13.64 ± 0.50
A2255	0.0809	$1.37^{+0.24}_{-0.23}$	1.39 ± 0.06	4.08 ± 0.11	7.10 ± 0.36	1.196 ± 0.026	5.26 ± 0.34	2.033 ± 0.081	10.33 ± 1.23
A2319	0.0557	$4.86^{+0.51}_{-0.37}$	2.61 ± 0.08	5.58 ± 0.12	8.01 ± 0.25	1.346 ± 0.017	7.31 ± 0.28	2.040 ± 0.035	10.18 ± 0.52
A3158	0.0597	$2.88^{+0.26}_{-0.17}$	1.59 ± 0.02	3.76 ± 0.09	5.70 ± 0.21	1.123 ± 0.016	4.26 ± 0.18	1.766 ± 0.035	6.63 ± 0.39
A3266	0.0589	$2.04^{+0.25}_{-0.20}$	2.02 ± 0.05	5.57 ± 0.15	9.32 ± 0.39	1.430 ± 0.031	8.80 ± 0.57	2.325 ± 0.074	15.12 ± 1.44
A644	0.0704	$5.58^{+0.65}_{-0.51}$	2.36 ± 0.09	4.74 ± 0.26	6.59 ± 0.45	1.230 ± 0.035	5.66 ± 0.48	1.847 ± 0.059	7.67 ± 0.73
A85	0.0555	$3.31^{+0.13}_{-0.13}$	1.94 ± 0.02	4.53 ± 0.08	6.81 ± 0.18	1.235 ± 0.013	5.65 ± 0.18	1.921 ± 0.027	8.50 ± 0.36
HydraA	0.0538	$5.51^{+0.67}_{-0.61}$	1.28 ± 0.07	2.40 ± 0.20	3.22 ± 0.32	0.904 ± 0.032	2.21 ± 0.23	1.360 ± 0.056	3.01 ± 0.37
RXC1825	0.0650	$3.35^{+0.20}_{-0.19}$	1.64 ± 0.02	3.69 ± 0.07	5.46 ± 0.15	1.105 ± 0.012	4.08 ± 0.13	1.719 ± 0.024	6.15 ± 0.26
ZW1215	0.0766	$2.11^{+0.22}_{-0.18}$	1.93 ± 0.03	5.22 ± 0.15	8.61 ± 0.39	1.358 ± 0.031	7.66 ± 0.52	2.200 ± 0.069	13.03 ± 1.23

Table 6.2 Values of the total gravitating mass as estimated with the *backward* method and a NFW model at some radii of reference (0.5, 1, 1.5 Mpc) and at the overdensities of 500 and 200 with respect to the critical density of the universe at the cluster's redshift.

M_i	B (inter-quartile range) %				
	0.5 Mpc	1 Mpc	1.5 Mpc	R_{500}	R_{200}
Forw	$+0.6(-1.1/+3.3)$	$-2.0(-5.9/+1.4)$	$-4.6(-7.9/+1.3)$	$-4.7(-10.9/-0.5)$	$+1.2(-5.4/+8.1)$
Forw (no SZ)	$-1.5(-3.4/+4.1)$	$-1.9(-8.0/+0.6)$	$-1.3(-5.4/+4.5)$	$-4.2(-9.0/+1.8)$	$+1.3(-11.9/+8.0)$
EIN	$-0.3(-1.7/+1.3)$	$-1.7(-6.5/-0.2)$	$-1.0(-9.7/+1.5)$	$-0.8(-7.6/+1.0)$	$-0.8(-10.3/+4.3)$
ISO	$+14.1(+11.8/+21.0)$	$-3.0(-3.5/+5.4)$	$-13.3(-19.0/-9.7)$	$-8.2(-13.0/-5.3)$	$-23.5(-28.7/-16.5)$
BUR	$+11.4(+10.4/+15.1)$	$-3.1(-5.8/+4.0)$	$-13.7(-19.2/-8.3)$	$-8.3(-12.9/-5.2)$	$-20.8(-24.2/-17.9)$
HER	$+1.6(+0.9/+2.1)$	$-0.7(-5.6/+0.2)$	$-5.5(-11.4/-2.4)$	$-3.7(-5.3/-1.9)$	$-9.3(-13.5/-6.8)$

Table 6.3 Systematic differences between the *forward* method ("Forw") and the other mass models described in Sect. 6.2.1 with respect to the model of reference defined as *backward* NFW. These differences are quoted as the median (1st-3rd quartiles, in parenthesis) of the quantity $B = (M_i/\text{NFW} - 1) \times 100 \%$, where M_i is listed in the first column.

6.3 Comparison with mass estimates from scaling laws, weak lensing and galaxy dynamics

We compare our estimates of the hydrostatic mass with constraints obtained from (i) X-ray based scaling relations applied to $Y_X = M_{\text{gas}} \times T$ (Vikhlinin et al., 2009), gas mass fraction (Mantz et al., 2010, also including a correction factor of 0.9 for *Chandra* calibration updates -see caption of their Table 4), SZ signal (the *Planck* mass proxy M_{Y_z} in Planck Collaboration et al., 2016f), (ii) weak lensing signal associated to the coherent distortion in the observed shape of background galaxies (as measured in the Multi Epoch Nearby Cluster Survey - MENeCS, Herbonnet et al. in prep.) and (iii) galaxy dynamics either through the estimate of the velocity dispersion (Zhang et al., 2017) or via the Caustic method (Rines et al., 2016), that calculates the mass from the escape velocity profile which is defined from the edges (i.e. the "caustics") of the distribution in the redshift-projected radius diagram. The comparison is done by evaluating the hydrostatic M_{NFW} at the radius defined by the other methods at given overdensity ($\Delta = 500$ for X-ray and SZ scaling laws, galaxy dynamics and WL; $\Delta = 200$ for WL and Caustics).

Mass estimates based on X-ray scaling laws provide a very reassuring agreement: we measure a median ratio M/M_{NFW} of 1.06 and 1.03 for the 9 and 6 objects in common with Vikhlinin et al. (2009) and Mantz et al. (2010), respectively. For the 11 objects in common with *Planck*-SZ catalog (Hydra-A and Zw1215 are not included there), we measure a median (1st-3rd quartile) of 0.98 (0.92–1.01) and an error-weighted mean of 0.96 (r.m.s. 0.08).

Similar good agreement is obtained with the 6 WL measurements in common: the error-weighted means are $1.18 (\pm 0.12; \text{r.m.s. } 0.26; \text{median: } 1.16)$ and $1.14 (\pm 0.12; \text{r.m.s. } 0.32; \text{median: } 1.17)$ at R_{500} and R_{200} , respectively.

Considering the eight clusters in common with Zhang et al. (2017), we measure a median of 0.96, with 1st-3rd quartiles of 0.78–1.10. On the other hand, a clear tension is measured with respect to the 6 mass values obtained from Caustics: $M_{\text{Cau}}/M_{\text{NFW}}$ has an error-weighted mean of $0.59 (\pm 0.02; \text{r.m.s. } 0.06)$, with ratios smaller than 0.5 in 3 objects (A85, A2142, ZW1215). Simulations in e.g. Serra and Diaferio (2013) show this might be the case when an insufficient number of spectroscopic member galaxies are adopted to constrain the caustic amplitude.

We plot the medians and weighted-means of the ratios M/M_{NFW} in Fig. 6.4.

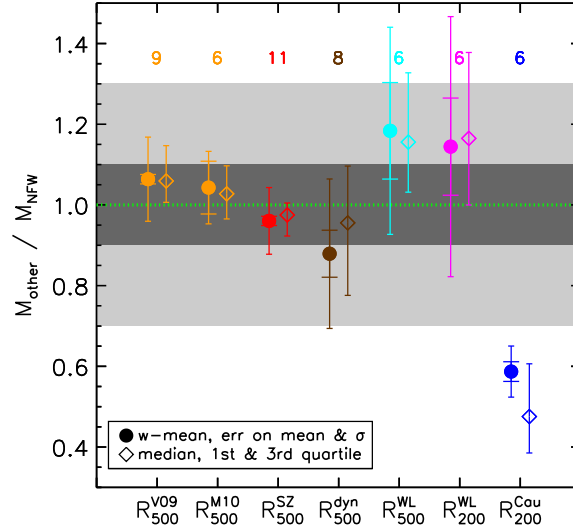


Fig. 6.4 Comparison between the *backward* NFW model and estimates of the mass from X-ray scaling relations (Y_X from Vikhlinin et al. (2009)) and f_{gas} from Mantz et al. (2010)), dynamical analysis for the HIFLUGCS sample (Zhang et al., 2017), *Planck* PSZ2 catalog (Planck Collaboration et al., 2016f), lensing (Herbonnet et al. 2018 in prep.), caustics (Rines et al., 2016). The number of objects in common is shown. Shaded regions indicate the <10% (darkest) and <30% differences.

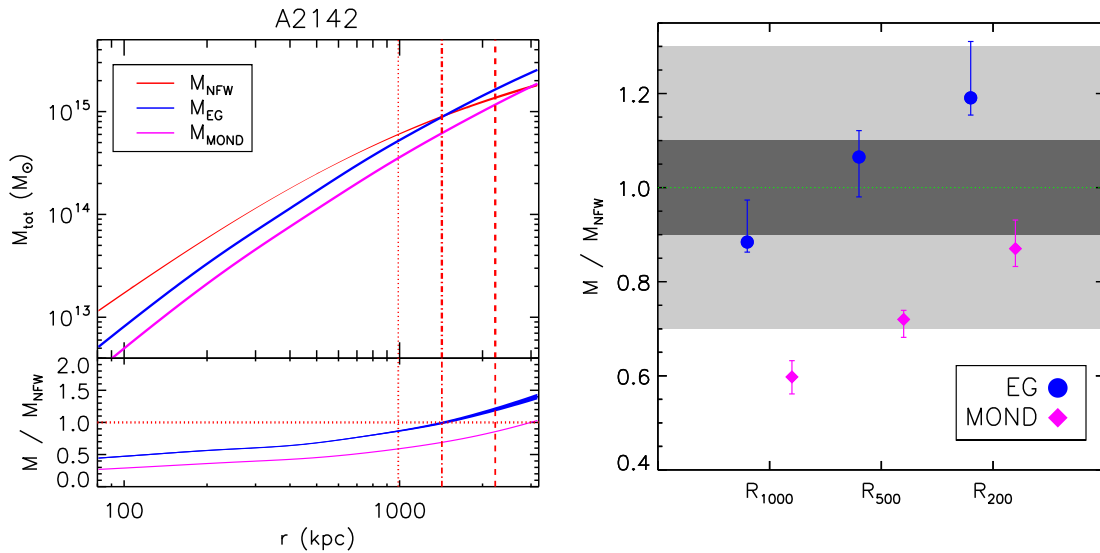


Fig. 6.5 (Left) Typical hydrostatic, EG and MOND radial mass profiles (here for A2142; see Ettori et al., 2018, for the remaining 12 objects). Vertical lines indicate R_{1000} (dotted line), R_{500} (dash-dotted line) and R_{200} (dashed line). (Right) Medians (and 1st and 3rd quartiles) of the ratio between the hydrostatic mass and the value predicted from EG and MOND for the whole X-COP sample. Shaded regions indicate the <10% (darkest) and <30% differences.

6.4 Comparison with predictions from the Emergent Gravity scenario and MOND

The lack of a valuable candidate particle for the Cold Dark Matter has induced part of the community to search for alternative paradigms on how gravity works at galactic and larger scales. In galaxy clusters, the largest gravitationally bound structures in the universe, visible matter can account for only a fraction of the total gravitational mass. These systems represent thus a valid and robust test for models that want to explain this missing mass problem. Among these rivals of the current cosmological paradigm, we consider here two models, one that introduces modifications in the Newtonian dynamical laws (MOND, Milgrom, 1983), the other that compensates for the required extra gravitational force by an “Emergent Gravity” (Verlinde, 2016). They both can be described by similar equations, are able to describe the behaviour of the gravity on galactic scales, but are also known to be in trouble when applied on larger scales (the so-called “upscaling problem” in Massimi, 2018), where for instance MOND predicts a gravitational acceleration that is too weak, suggesting that it can be an incomplete theory, to say the least.

In the “Emergent Gravity”, dark matter can appear as manifestation of an additional gravitational force describing the “elastic” response due to the displacement of the entropy that can be associated to the thermal excitations carrying the positive dark energy, and with a strength that can be described in terms of the Hubble constant and of the baryonic mass distribution. For a spherically symmetric, static and isolated astronomical system, Verlinde (2016) provides a relation between the emergent dark matter and the baryonic mass (see his equation 7.40) that can be rearranged to isolate the dark matter component M_{DM} . Following Ettori et al. (2017), we can write

$$M_{\text{DM,EG}}^2(r) = \frac{cH_0}{6G} r^2 M_{\text{B}}(r) (1 + 3\delta_{\text{B}}), \quad (6.5)$$

where $M_{\text{B}}(r) = \int_0^r 4\pi\rho_{\text{B}}r'^2 dr' = M_{\text{gas}}(r) + M_{\text{star}}(r)$ is the baryonic mass equal to the sum of the gas and stellar masses, and δ_{B} is equal to $\rho_{\text{B}}(r)/\bar{\rho}_{\text{B}}$, with $\bar{\rho}_{\text{B}} = M_{\text{B}}(r)/V(< r)$ representing the mean baryon density within the spherical volume $V(< r)$. In our case, the gas mass has been obtained from the integral over the cluster’s volume of the gas density (Fig. 6.1). The stellar mass has been estimated using a Navarro-Frenk-White (NFW, Navarro et al., 1997) profile with a concentration of 2.9 (see e.g. Lin et al., 2004) and by requiring the $M_{\text{star}}(< R_{500})/M_{\text{gas}}(< R_{500}) = 0.39 (M_{500}/10^{14}M_{\odot})^{-0.84}$ (Gonzalez et al., 2013). For the X-COP objects, we measure a median $M_{\text{star}}/M_{\text{gas}}$ of 0.09 (0.07–0.12 as 1st and 3rd quartile) at R_{500} .

As we discuss in Ettori et al. (2017), Equation 6.5 can be expressed as an acceleration g_{EG} depending on the acceleration g_{B} induced from the baryonic mass

$$g_{\text{EG}} = g_{\text{B}} \left(1 + y^{-1/2} \right), \quad (6.6)$$

where $y = 6/(cH_0) \times g_{\text{B}}/(1 + 3\delta_{\text{B}})$.

Equation 6.6 takes a form very similar to the one implemented in MOND (e.g. Milgrom and Sanders, 2016) with a characteristic acceleration $a_0 = cH_0(1 + 3\delta_{\text{B}})/6$. MOND is another theory that accounts for the mass in galaxies and galaxy clusters without any dark component and by modifying Newtonian dynamics, and requires an acceleration $g_{\text{MOND}} = g_{\text{B}} \left(1 + y^{-1/2} \right)$, with $y = g_{\text{B}}/a_0$ and $a_0 = 10^{-8} \text{ cm/s}^2$. For sake of completeness, we have also estimated a gravitating mass associated to a MOND acceleration.

The results of our comparison are shown in Fig. 6.5 (where we present as an example the case of A2142; the other mass profiles are shown in the Appendix of Ettori et al. (2018)). Although in the inner cluster's regions the mismatch is indeed significant, with mass values from modified gravities that underestimate the hydrostatic quantities by a factor of few, over the radial interval between R_{1000} and R_{200} , the medians of the distribution of the ratios between the mass estimates obtained from modified accelerations and from the hydrostatic equilibrium equation are in the range 0.6 – 0.87 for the MOND (consistent with previous studies; e.g., Pointecouteau and Silk, 2005) and between 0.88 and 1.19 for EG, with the latter that indicates a nice consistency at R_{500} where $M_{\text{EG}}/M_{\text{Hyd}} \approx 1.07$ (0.99 – 1.12 as 1st and 3rd quartiles).

6.5 Conclusions

We have investigated the hydrostatic mass profiles in the X-COP sample of 13 massive X-ray luminous galaxy clusters for which the gas density and temperature (from *XMM-Newton* X-ray data) and SZ pressure profiles (from *Planck*) are recovered at very high accuracy up to about R_{500} for the temperature and at R_{200} for density and pressure.

We constrain the total mass distribution by applying the hydrostatic equilibrium equation on these profiles, reconstructed under the assumption that the ICM follows a spherically symmetric distribution and using two different methods and five mass models. By adopting as reference model a NFW mass profile constrained with the *backward* method, we estimate the radial mass distribution up to R_{200} with a mean statistical relative error lower than 8%. A *forward* method, that is independent from any assumption on the shape of the gravitational potential, provides consistent results within 5% both at R_{500} and R_{200} .

Other sources of systematic uncertainties, like any non-thermal contribution to the total gas pressure that we discuss in a companion X-COP paper (Eckert et al. 2018), or departures from the hydrostatic equilibrium (e.g. Biffi et al., 2016; Nelson et al., 2014b), or the violation of the assumed sphericity of the gas distribution (e.g. Sereno et al., 2017b), could push our mass estimates to higher values by a further 10-20%, in particular at $r > R_{500}$.

A NFW mass profile represents the best-fit model for nine objects, where we measure a statistically significant tension with any cored mass profile. The remaining four clusters prefer different mass models but are also consistent with a NFW. The latter systems are also the ones that deviate more in the NFW $c_{200} - M_{200}$ plane with respect to the theoretical predictions from numerical simulations. Overall, we measure a scatter of 0.18 in the $c - M$ relation and of 0.15 ± 0.08 (with a-posteriori probability of 15 per cent to be below 10%) in the hydrostatic mass measurements. The latter is in agreement with results from literature (Sereno and Ettori, 2015) and larger, but still compatible within uncertainties, with those obtained from numerical simulations (Rasia et al., 2012).

For a subsample of X-COP objects, we can quantify the average discrepancy between hydrostatic masses and estimates obtained from (i) scaling relations based on X-ray data and applied to the SZ signal, (ii) weak-lensing, and (iii) galaxy dynamics. Overall, we obtain a remarkably good agreement (with an error-weighted mean and median of the ratios between hydrostatic and other masses around 1 ± 0.2), apart from the caustic method that underestimates severely the hydrostatic values in this massive local relaxed systems by more than 40 per cent on average.

Then, we compare these mass estimates to predictions from scenarios in which the gravitational acceleration is modified. We note that both the traditional MOND acceleration and the one produced as manifestation of apparent dark matter in the ‘‘Emergent Gravity’’ theory predict masses that are a factor of few below the hydrostatic values in the inner 1 Mpc, with EG providing less significant tension in particular at R_{500} as estimated from M_{Hyd} , where we measure $M_{\text{EG}}/M_{\text{Hyd}} \approx (0.9 - 1.1)$.

We conclude that these estimates of the hydrostatic masses represent the best constraints ever measured, with a statistical error budget that is in the order of the systematic uncertainties we measure, and both within 10 per cent out to R_{200} . Future extension of the X-COP sample, with comparable coverage of the X-ray and SZ emission out to R_{200} , to dynamically non-relaxed systems, even at higher redshifts, will permit to build a proper collection of hydrostatic masses that will provide the reference to study in details the robustness of the assumption of the hydrostatic equilibrium. A complete census of any residual kinetic energy in the gas bulk motions and turbulence as major bias in the estimates of the hydrostatic mass requires direct measurements of the Doppler broadening and shifts of the emission lines in the ICM over

the entire cluster's volume. *Hitomi* has provided the first significant results in the field, but limited to the inner parts of the core of the Perseus cluster (Hitomi Collaboration et al., 2016, 2018, 2017; ZuHone et al., 2018). The next generation of X-ray observatories equipped with high-resolution spectrometers, like *XARM* (Ota et al., 2018) and *Athena* (Ettori et al., 2013b; Nandra et al., 2013b), will deepen our knowledge on the state of the ICM enlarging the sample and the regions of study.

**NON-THERMAL PRESSURE SUPPORT IN
X-COP GALAXY CLUSTERS**

7.1 Introduction

In this chapter, we use high-precision hydrostatic masses obtained from the *XMM-Newton* cluster outskirts project (X-COP, Eckert et al., 2017a, see Chapter 3) out to R_{200} to estimate the level of non-thermal pressure. We present a high-confidence estimate of the universal gas fraction of galaxy clusters and use our assessment of the universal gas fraction to probe the level of systematics in our hydrostatic mass measurements. We apply the same technique to examine potential systematics in the mass calibration adopted by the *Planck* team to derive cosmological parameters from Sunyaev-Zeldovich (SZ) cluster counts, which has resulted in the well-known tension between cosmic microwave background (CMB) and cluster counts (Planck Collaboration et al., 2014b).

The chapter is organized as follows. In Sect. 7.2 we present the dataset and the methods used to derive gas fraction profiles. In Sect. 7.3 we estimate the universal gas fraction and describe our method to derive the non-thermal pressure fraction. Our results are presented in Sect. 7.4 and discussed in Sect. 7.5.

Throughout the chapter, we assume a Λ CDM cosmology with $\Omega_m = 0.3$, $\Omega_\Lambda = 0.7$ and $H_0 = 70$ km/s/Mpc. Note that since our clusters are local ($z < 0.1$) the results have a very mild dependence on the adopted cosmology.

7.2 Data analysis

7.2.1 Hydrostatic masses and gas fraction

Our hydrostatic mass measurements and the procedure to obtain them are described in detail in Chapt. 6. In short, we adopt as our reference mass model the *backward NFW* model (Ettori et al., 2010), which describes the mass profile using a Navarro-Frenk-White (NFW, Navarro et al., 1996) mass model, we assume that the ICM is in hydrostatic equilibrium (HSE) within the gravitational potential well, and that the kinetic energy has been fully converted into thermal energy, in which case the HSE equation reads like in Eq. (1.17).

To determine, at each radius, the enclosed gas mass, we integrate the gas density profiles:

$$M_{\text{gas}}(< r) = \int_0^r 4\pi r^2 \rho_{\text{gas}}(r) dr \quad (7.1)$$

where $\rho_{\text{gas}} = \mu m_p (n_e + n_p)$, with $n_e \approx 1.17 n_p$ the number densities of electron and proton in a fully ionized gas, $\mu \approx 0.6$ the mean molecular weight, and m_p the mass of the proton. The hydrostatic gas fraction profiles are then computed as $f_{\text{gas,HSE}}(r) = M_{\text{gas}}(< r) / M_{\text{HSE}}(< r)$. In

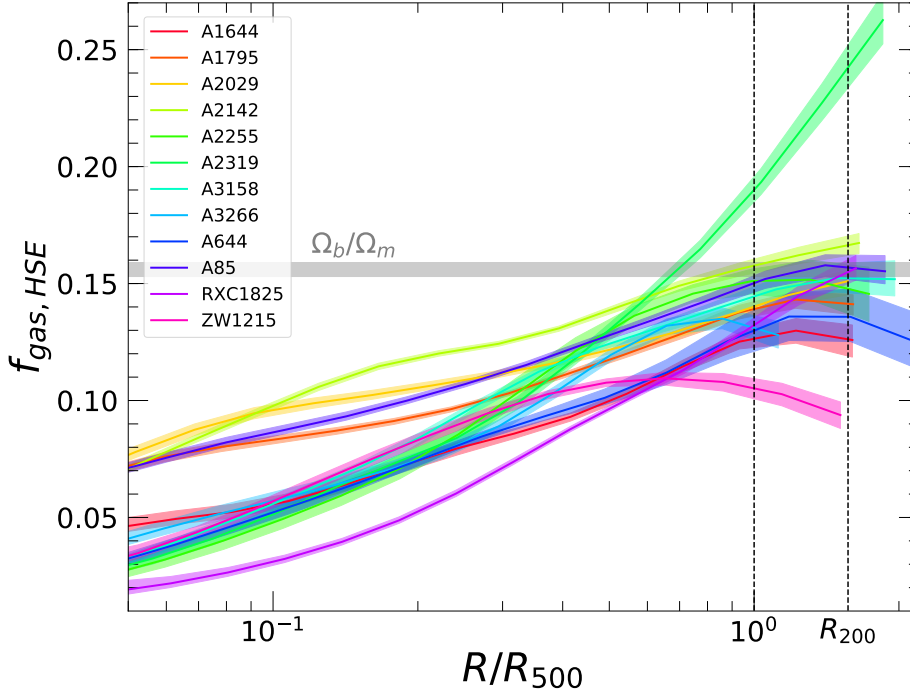


Fig. 7.1 Hydrostatic gas fraction profiles $f_{\text{gas,HSE}}(R) = M_{\text{gas}}(< R)/M_{\text{HSE}}(< R)$ as a function of scale radius R/R_{500} for the X-COP clusters; in particular we observe that all the profiles flattens at about 0.15 at R_{500} , with the exception of A2319 which is the only one going much above the average. The gray shaded area shows the *Planck* universal baryon fraction Ω_b/Ω_m (Planck Collaboration et al., 2016e).

Fig. 7.1 we show the hydrostatic gas fraction profiles as a function of the scale radius $R_{500,HSE}$ for the 12 X-COP clusters. The radial range of each profile corresponds to the regions for which information on both the density and the pressure are available. For 10 objects out of 12 our gas fraction profiles extend out to R_{200} without requiring any extrapolation. The typical statistical uncertainties in $f_{\text{gas,HSE}}$ are $\sim 5\%$ at R_{500} and $\sim 10\%$ at R_{200} . In the case for which our measurements do not extend all the way out to R_{200} (A3266), the NFW mass model is extrapolated out to R_{200} to estimate the values of $f_{\text{gas,HSE}}$.

7.3 Methodology

7.3.1 Parameters of the universal gas fraction

The gas mass fraction can be calculated as in Eq. (2.4), here we add details to the various components which make up the formula, Y_b , Ω_b , Ω_m , and f_\star .

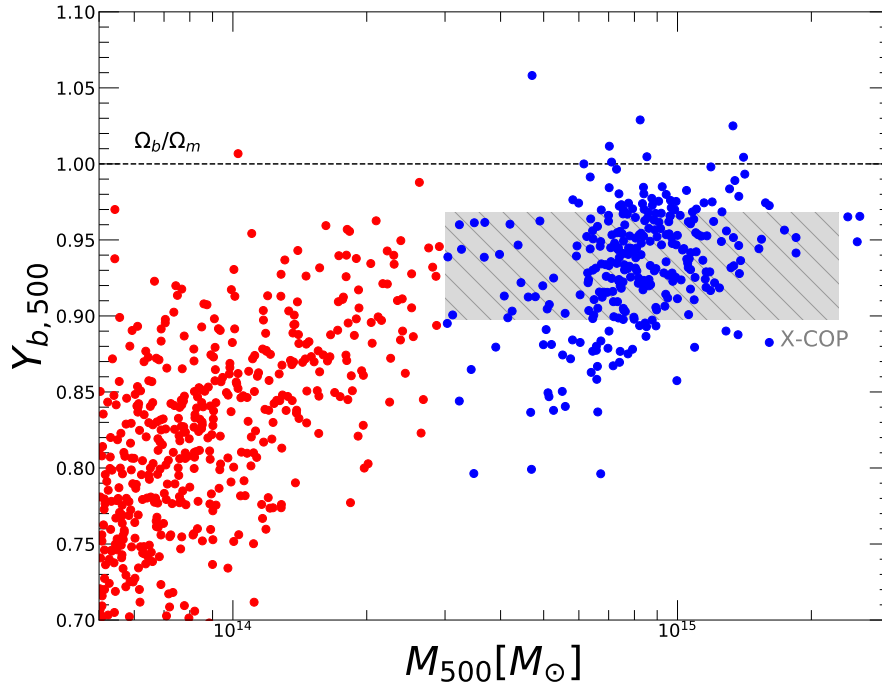


Fig. 7.2 Baryon depletion factor Y_b at R_{500} for the clusters in the300 simulation (filled circles). The blue points show the objects with a mass $M_{500} > 3 \times 10^{14} M_{\odot}$. The hashed grey shaded area shows the mass range covered by X-COP clusters and our determination of the universal baryon depletion factor and its scatter.

7.3.2 Baryon depletion factor

For the purpose of this chapter, we utilize simulated clusters with masses in the X-COP range extracted from The Three Hundred Project simulations (hereafter the300, Cui et al. in preparation) to estimate the baryon depletion factor Y_b . the300 is a project which is comprised of zoom-in re-simulations of more than three hundred Lagrangian regions, of $15\text{--}20 h^{-1} \text{Mpc}$ radius, centered on the most massive cluster-size haloes selected from one of the dark matter only MultiDark Simulations run carried out with Planck cosmology (Planck Collaboration et al., 2016e).

All the regions have been re-simulated at higher resolution (with dark-matter particle mass around $2 \times 10^9 M_{\odot}$) using a modified version of the Smoothed-Particle-Hydrodynamics (SPH) GADGET-3 code (Springel et al., 2005). The re-simulations include the treatment of a large variety of physical processes to describe the baryonic component, such as gas cooling, star formation, chemical enrichment, stellar and Active Galactic Nuclei (AGN) feedback (see Rasia et al. 2015 and references therein). For a more detailed description of the hydrodynamical code used, and Cui et al, in prep., for details on the resimulation technique).

Table 7.1 Baryon depletion factor in the simulated clusters from the clusters in the300 project with $M_{500} > 3 \times 10^{14} M_{\odot}$.

Δ	Median	16th	84th	Min	Max
500	0.938	0.897	0.966	0.794	1.026
200	0.951	0.923	0.982	0.875	1.024

Column description: Overdensity Δ ; Median value of Y_b in the sample; 16th and 84th percentiles of the values; minimum and maximum values.

Thanks to the large statistics afforded by these simulations, we can constrain the value of Y_b and its scatter with good precision. In Fig. 7.2 we show the measurements of Y_b at R_{500} for the whole sample of simulated clusters. As previous studies pointed out (e.g. Planelles et al., 2013), the value of Y_b at large radii is typically about 0.9-0.95. For masses $M_{500} \geq 3 \times 10^{14} M_{\odot}$, corresponding to the X-COP mass range, the baryon depletion factor is approximately constant albeit with a large scatter. The median, 1σ percentiles, and extreme values of Y_b at R_{500} and R_{200} , in X-COP mass range, are provided in Table 7.1. Smaller systems are instead largely influenced by the AGN activity that on one side pushes outside the hot gas and on the other quenches star formation, consequentially reducing both baryonic components.

7.3.3 Stellar fraction

While the ICM contains the vast majority of the baryons in galaxy clusters, a fraction of the baryons are locked into stars, both inside galaxies and in the form of intracluster light (ICL, Budzynski et al., 2014; Montes and Trujillo, 2014; Zibetti et al., 2005a). Predicting the exact amount of stars in numerical simulations is a quite difficult, because star formation rate and its evolution depend critically on the adopted physical setup describing gas cooling and feedback from supernovae and AGN (e.g. Kravtsov et al., 2005). However, the stellar content of galaxy clusters has been extensively studied in the literature (Andreon, 2010; Chiu et al., 2018; Giodini et al., 2009; Gonzalez et al., 2013, 2007; Laganá et al., 2013) and the stellar fraction can be robustly set by its observed value.

In Fig. 7.3 we present a compilation of recent results on the stellar fraction of dark-matter halos as a function of their mass. Results obtained by directly integrating the stellar mass of member galaxies (Andreon, 2010; Chiu et al., 2018; Giodini et al., 2009; Gonzalez et al., 2013; Laganá et al., 2013) and from the halo occupation distribution (Coupon et al., 2015; Eckert et al., 2016a; Leauthaud et al., 2012; Zu and Mandelbaum, 2015a) are compared. While the results obtained with the two methods differ substantially in the galaxy group

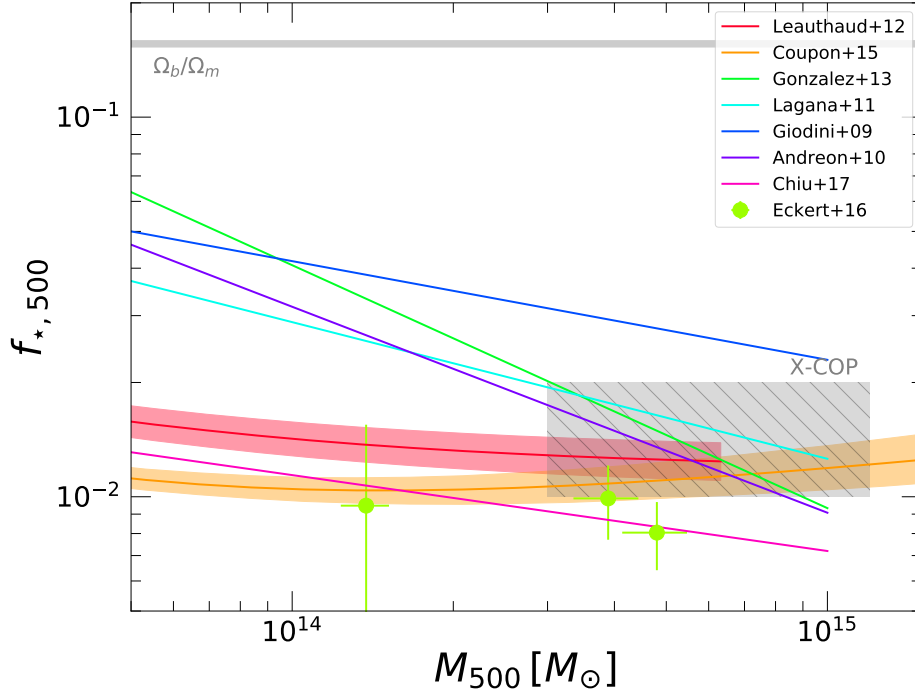


Fig. 7.3 Stellar fraction within R_{500} estimated in several works from the literature. The hashed grey area represents the mass range of X-COP clusters and the range of f_* adopted in this work.

regime ($M_{500} \lesssim 10^{14} M_{\odot}$). However in the mass range covered by X-COP clusters, i.e. $3 \times 10^{14} < M_{500} < 1.2 \times 10^{15} M_{\odot}$, all studies are broadly consistent and converge to a median stellar fraction of about 1.2%. The contribution of ICL was included in some, but not all cases; measurements indicate that ICL can account for $\sim 20 - 30\%$ (Lin and Mohr, 2004; Zibetti et al., 2005b) of the total stellar mass. To encompass the uncertainty associated with the ICL fraction and with the various studies shown in Fig. 7.3, for the present study we conservatively set the value of the stellar fraction to be

$$f_{*,500} = 0.015 \pm 0.005. \quad (7.2)$$

Beyond the central regions the stellar fraction has been shown to be nearly constant (van der Burg et al., 2015), thus we adopt the same value for $f_{*,200}$.

7.3.4 Cosmological parameters and estimated universal gas fraction

The cosmological parameters Ω_b , Ω_m , and their ratio, are measured by CMB probes, as WMAP or *Planck*. In the present work we take the most recent measurement from the *Planck*

probe, therefore $\Omega_b/\Omega_m = 0.156 \pm 0.003$ (Planck Collaboration et al., 2016e), slightly lower but consistent compared with the WMAP9 measurement (0.166 ± 0.009 , Hinshaw et al., 2013).

Combining the results from the previous sections, from Sect. 7.3.4 to 7.3.3, and through Eq. 2.4 we estimate the following values for the universal gas fraction:

$$f_{\text{gas},500} = 0.131 \pm 0.009 \quad , \quad f_{\text{gas},200} = 0.134 \pm 0.007. \quad (7.3)$$

The errors reported here include both the actual uncertainties in Ω_b/Ω_m , f_* , and on the measured scatter in Y_b in the300 simulation.

7.3.5 Non-thermal pressure fraction

The non-thermal pressure support contaminating this sample is computed similarly as in the case of A2319, see Sect. 4.6. The idea is that since our X-ray emissivity profiles are corrected for the effects of gas clumping (Eckert et al., 2015) down to the limiting resolution of our observations (10-20 kpc), we expect that any residual deviation of the gas mass fraction with respect to the universal gas fraction should be caused by an additional non-thermal pressure component. In absence of hydrostatic equilibrium, the state of the gas in the presence of a gravitational potential is described by the Euler equation, see Eq. (1.16), where the extra terms compared with HEE, Eq. (1.17), can be described like in the following equation by a non-thermal component

$$\frac{d}{dr}(P_{th}(r) + P_{NT}(r)) = -\rho_{\text{gas}} \frac{GM_{\text{tot}}(< r)}{r^2} \quad (7.4)$$

where the subscript “*NT*” indicates the non-thermal component, while the subscript “*th*” indicates the thermal part. Setting $\alpha(r) = P_{NT}(r)/P_{\text{tot}}(r)$, the non-thermal pressure fraction, i.e. $P_{NT} = \alpha P_{\text{tot}} = \frac{\alpha}{1-\alpha} P_{th}$, we rewrite Eq. (7.4) as

$$M_{\text{tot}}(< r) = M_{\text{HSE}}(< r) + \alpha(r)M_{\text{tot}}(< r) - \frac{P_{th}r^2}{(1-\alpha)\rho_{\text{gas}}G} \frac{d\alpha}{dr} \quad (7.5)$$

with $M_{\text{HSE}}(< r) = -\frac{r^2}{\rho_{\text{gas}}G} \frac{dP_{th}}{dr}$ is the mass from hydrostatic equilibrium, see Eq. (1.17). Therefore the gas mass fraction as a function of radius can be written as

$$f_{\text{gas}}(r) = \frac{M_{\text{gas}}(< r)}{M_{\text{tot}}(< r)} = f_{\text{gas,HSE}}(r)(1-\alpha) \left(1 - \frac{P_{th}r^2}{(1-\alpha)\rho_{\text{gas}}GM_{\text{HSE}}} \frac{d\alpha}{dr} \right)^{-1} \quad (7.6)$$

Thus, if the true gas fraction is known, the non-thermal pressure fraction $\alpha(r)$ can be estimated by comparing the measured $f_{\text{gas,HSE}}$ with the universal value (Ghirardini et al., 2018b). For $\alpha(r)$ we use the functional form introduced by Nelson et al. (2014a),

$$\alpha(r) = \frac{P_{NT}}{P_{\text{tot}}}(r) = 1 - A \left(1 + \exp \left\{ - \left[\frac{r}{Br_{200}} \right]^\gamma \right\} \right) \quad (7.7)$$

with A , B , and γ being free parameters. This functional form was shown to reproduce the behavior of the non-thermal pressure fraction in the simulations of Nelson et al. (2014a) and should be approximately valid in the range $[0.3 - 2]R_{200}$. For the present work, we fix $B = 1.7$ to the best fitting value in the300 simulation. Note that in case $\alpha(r)$ is constant this quantity is simply equal to the usual hydrostatic bias $b = 1 - M_{\text{HSE}}/M_{\text{tot}}$.

As already discussed, the gas fraction predicted by various simulations was found to be consistent (Sembolini et al., 2016). The predictions however diverge in the inner regions (see their Fig. 10). Thus, we focus on the gas fraction at large radii to compare $f_{\text{gas,HSE}}$ to $f_{\text{gas,univ}}$ and determine the parameters of $\alpha(r)$. We set the universal gas fraction at R_{500} and R_{200} to the values derived in previous Sect. 7.3.4, and solve numerically Eq. (7.6) for the parameters A and γ . Since this procedure results in a corrected estimate for M_{500} and M_{200} , we iteratively repeat the procedure with the revised mass estimates until it converges.

We use the output MCMC chains of our mass models to propagate the uncertainties in $f_{\text{gas,HSE}}$ into our estimate of $\alpha(r)$. We also propagate the dispersion and uncertainties in the universal gas fraction (see Sect. 2.2.5) by randomizing the value of f_{gas} in Eq. 7.6. The best-fit curves for $\alpha(r)$ are then computed from the posterior distributions of the parameters.

7.4 Results

7.4.1 Non-thermal pressure fraction in X-COP clusters

In Fig. 7.4 we show the values of $f_{\text{gas,HSE}}$ for the 12 X-COP clusters at $R_{500,\text{HSE}}$ and $R_{200,\text{HSE}}$ compared to the universal baryon fraction (Planck Collaboration et al., 2016e) and the universal gas fraction predicted from the300 simulation. With the exception of A2319 (Ghirardini et al., 2018b), for which a substantial non-thermal pressure support was clearly detected, at R_{500} our measurements of $f_{\text{gas,HSE}}$ lie very close to the universal gas fraction, albeit $\sim 7\%$ higher on average (median $f_{\text{gas},500} = 0.141 \pm 0.005$, with 12% scatter), implying a mild contribution of non-thermal pressure. Conversely, at R_{200} , the majority of the measurements (9 out of 12) slightly exceed the universal gas fraction (median

Table 7.2 Hydrostatic gas fraction, non-thermal pressure fraction, and total (bias-corrected) masses at R_{500} and R_{200} in X-COP clusters.

Cluster	$M_{\text{HSE},500}$ [$10^{14}M_{\odot}$]	$M_{\text{HSE},200}$ [$10^{14}M_{\odot}$]	$f_{\text{gas},500}$	$f_{\text{gas},200}$	$\alpha(R_{500})$ [%]	$\alpha(R_{200})$ [%]	$M_{\text{tot},500}$ [$10^{14}M_{\odot}$]	$M_{\text{tot},200}$ [$10^{14}M_{\odot}$]
A1644	3.48 ± 0.20	6.69 ± 0.58	0.128 ± 0.008	0.126 ± 0.011	< 10.5	< 14.8	$3.52^{+0.20}_{-0.22}$	$6.58^{+0.72}_{-0.59}$
A1795	4.63 ± 0.14	6.53 ± 0.23	0.139 ± 0.005	0.144 ± 0.005	$2.2^{+5.6}_{-2.2}$	$6.7^{+6.0}_{-4.5}$	$4.77^{+0.35}_{-0.31}$	$6.76^{+0.37}_{-0.35}$
A2029	8.65 ± 0.29	12.25 ± 0.49	0.141 ± 0.005	0.152 ± 0.006	$6.0^{+5.8}_{-5.7}$	$10.4^{+9.0}_{-10.4}$	$8.98^{+0.84}_{-0.83}$	$13.29^{+0.78}_{-0.60}$
A2142	8.95 ± 0.26	13.64 ± 0.50	0.158 ± 0.005	0.168 ± 0.006	$15.8^{+4.5}_{-4.8}$	$18.6^{+7.1}_{-8.8}$	$10.50^{+0.57}_{-0.89}$	$16.37^{+0.95}_{-0.82}$
A2255	5.26 ± 0.34	10.33 ± 1.23	0.153 ± 0.011	0.146 ± 0.018	$5.6^{+6.8}_{-5.6}$	$6.1^{+6.3}_{-6.1}$	$5.87^{+0.47}_{-0.45}$	$10.70^{+0.77}_{-0.58}$
A2319	7.31 ± 0.28	10.18 ± 0.52	0.189 ± 0.008	0.237 ± 0.012	$43.6^{+3.5}_{-3.6}$	$52.3^{+3.4}_{-4.6}$	$11.44^{+1.06}_{-1.11}$	$20.11^{+1.14}_{-1.31}$
A3158	4.26 ± 0.18	6.63 ± 0.39	0.145 ± 0.007	0.155 ± 0.010	$8.5^{+5.7}_{-5.8}$	$12.5^{+8.9}_{-11.6}$	$4.53^{+0.38}_{-0.37}$	$7.34^{+0.46}_{-0.35}$
A3266	8.80 ± 0.57	15.12 ± 1.44	0.132 ± 0.009	0.108 ± 0.018	< 11.2	< 15.9	$8.94^{+0.60}_{-0.53}$	$14.49^{+3.01}_{-2.39}$
A644	5.66 ± 0.48	7.67 ± 0.73	0.132 ± 0.012	0.139 ± 0.015	$3.2^{+6.4}_{-3.2}$	$5.6^{+6.4}_{-5.6}$	$6.03^{+0.62}_{-0.69}$	$8.35^{+0.70}_{-0.52}$
A85	5.65 ± 0.18	8.50 ± 0.36	0.150 ± 0.005	0.159 ± 0.007	$10.2^{+4.9}_{-5.6}$	$11.5^{+8.9}_{-9.5}$	$6.22^{+0.54}_{-0.44}$	$9.56^{+0.53}_{-0.46}$
RXC1825	4.08 ± 0.13	6.15 ± 0.26	0.133 ± 0.005	0.155 ± 0.007	$5.1^{+5.1}_{-5.1}$	$15.2^{+6.4}_{-7.8}$	$3.94^{+0.36}_{-0.28}$	$6.87^{+0.40}_{-0.37}$
ZwCl1215	7.66 ± 0.52	13.03 ± 1.23	0.106 ± 0.008	0.092 ± 0.009	< 11.9	< 15.7	$7.67^{+0.59}_{-0.47}$	$13.03^{+1.37}_{-1.12}$
Median			$0.141^{+0.006}_{-0.005}$	$0.149^{+0.009}_{-0.008}$	$5.9^{+2.9}_{-3.3}$	$10.5^{+4.3}_{-5.5}$		

Column description: Cluster name; masses reconstructed using hydrostatic equilibrium (see Ettori et al. 2018); hydrostatic gas fractions; non-thermal pressure ratio $\alpha = P_{\text{NT}}/P_{\text{tot}}$; total masses corrected for non-thermal pressure. Upper limits are at the 90% confidence level.

$f_{\text{gas},200} = 0.149^{+0.006}_{-0.008}$). With just two exceptions (A3266 and ZwCl 1215), the gas fraction of all systems is at least as large as our determination of the Universal gas fraction.

To investigate any dependence of the measured gas fraction on the core state, we split our sample into cool core (CC) and non cool core (NCC) classes based on their central entropy K_0 as measured by *Chandra* (Cavagnolo et al., 2009), as in Chapter 3. At R_{500} , we estimate median values $f_{\text{gas,CC}} = 0.142 \pm 0.006$ and $f_{\text{gas,NCC}} = 0.141 \pm 0.008$, i.e. there is no difference in the hydrostatic gas fraction of the two sub-populations. The values of $f_{\text{gas,HSE}}$ in the NCC population appear to be more scattered than in the CC population (15% versus $< 7\%$). However, the small number of objects in our sample makes it difficult to make any strong statistical claim about the scatter of the two populations.

We used the distribution of output values for the parameters of the non-thermal pressure fraction (Eq. 7.7) to determine the non-thermal pressure fraction at R_{500} and R_{200} . The normalization of the non-thermal pressure term A in Eq. 7.7 is usually well determined and lies in the range 0.4 – 0.8 (median 0.65). The slope γ is however poorly constrained, given that we are constraining it using only two anchor points (R_{500} , R_{200}). In the cases where no modification to the gas fraction was required we computed upper limits at the 90% confidence level. In Table 7.2 we provide our measurements of the hydrostatic gas fraction, of the non-thermal pressure ratio, and of the total cluster masses after applying the method

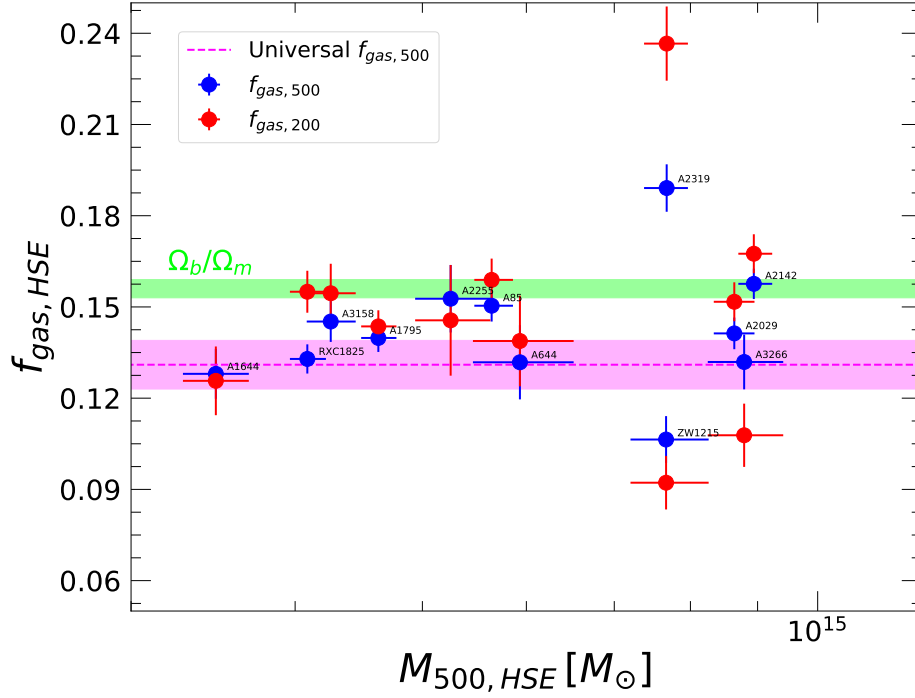


Fig. 7.4 Hydrostatic gas fractions at $R_{500,HSE}$ (blue points) and $R_{200,HSE}$ (red points) obtained from our reference hydrostatic mass model as a function of cluster mass. The dashed magenta line and shaded area represent the universal gas fraction at R_{500} estimated in Sect. 2.2.5 and its uncertainty. The green shaded area indicates the cosmic baryon fraction (Planck Collaboration et al., 2016e).

described in Sect. 7.3.5 (labelled as M_{tot} hereafter). In the cases for which no evidence for non-thermal pressure was found, M_{tot} is just equal to M_{HSE} .

In Fig. 7.5 we show the non-thermal pressure fractions at R_{500} and R_{200} for the entire X-COP sample. We immediately see that in the vast majority of cases non-thermal support in X-COP clusters is mild. We use a bootstrap method to compute the median of the distribution and the uncertainties on the median. We find a median non-thermal pressure of $5.9^{+2.9}_{-3.3}\%$ and $10.5^{+4.3}_{-5.5}\%$ at R_{500} and R_{200} , respectively. For comparison, in Fig. 7.5 we show the average non-thermal pressure ratio in two sets of numerical simulations (Ω_{500} , Nelson et al. (2014a); the300, Rasia et al. in prep.), with the scatter of the population indicated as the shaded areas. Assuming that the non-thermal pressure support is due to random gas motions, the level of non-thermal pressure in numerical simulations was defined as the ratio of the pressure induced by random motions $P_{rand} = \frac{1}{3}\rho\sigma_{gas}^2$ to the sum of random and thermal pressure (Biffi

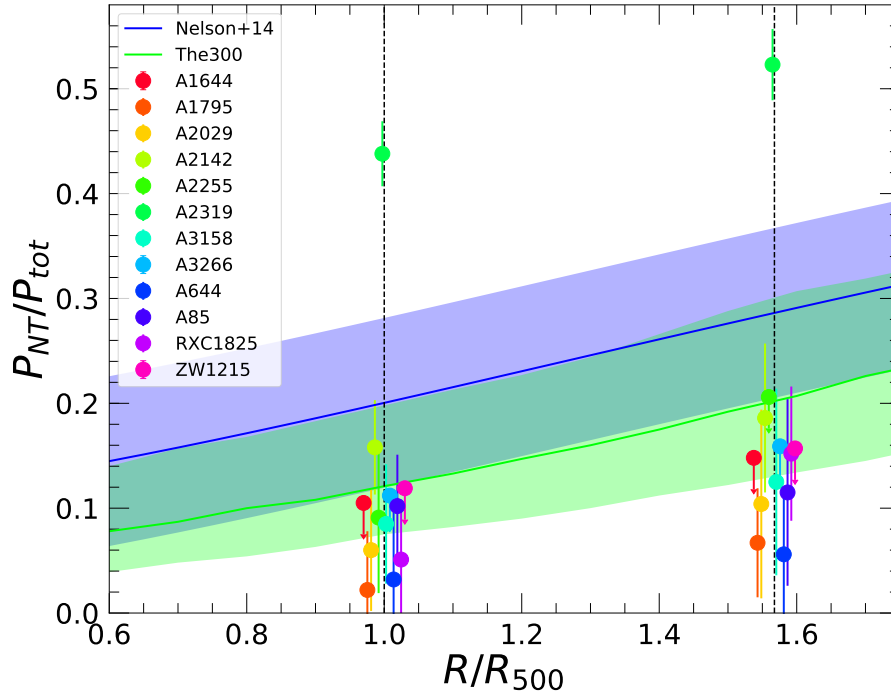


Fig. 7.5 Non-thermal pressure fraction in X-COP clusters at R_{500} and R_{200} . The positions on the X axis are slightly shifted for clarity. The blue and green curves and shaded areas show the mean non-thermal pressure ratio predicted from the numerical simulations of Nelson et al. (2014a) and Rasia et al., respectively.

et al., 2016; Nelson et al., 2014a),

$$\frac{P_{NT}}{P_{tot}} = \frac{\sigma_{\text{gas}}^2}{\sigma_{\text{gas}}^2 + (3kT/\mu m_p)}, \quad (7.8)$$

with σ_{gas} the velocity dispersion of gas particles in spherical shells, k the Boltzmann constant, μ the mean molecular weight and m_p the proton mass. Interestingly, most of our measurements lie substantially below the Nelson et al. (2014a) curve, possibly indicating a higher level of thermalization in the real population compared to the simulations. A somewhat lower level of non-thermal pressure is predicted in the300 simulation, in better agreement with our results. We discuss this comparison in further detail in Sect. 7.5.2.

While the selection of the X-COP sample was designed to be fairly clean (see Chapter 3), our original selection excluded 4 systems for which we were unsure whether the strategy adopted for the project could be applied. This includes clusters with obvious substructures, aspherical morphology, bad visibility for *XMM-Newton*, or an apparent size barely larger than the *Planck* beam (see Sect. 2.1 of Ghirardini et al. 2018). Two of these systems (A754 and

A3667) are extreme mergers which may deviate substantially from hydrostatic equilibrium in a way similar to A2319, thus the average level of non-thermal pressure support in our sample may be biased by the exclusion of these objects. To investigate the potential impact of these systems on our results, we assumed that these two missing objects show a level of non-thermal pressure similar to that of A2319 and that the remaining two are representative of the population. Such a choice has no influence on the median non-thermal pressure fraction, but increases the mean value from 9% to 13% at R_{500} . We can thus conclude that our analysis sets an upper limit of 13% to the mean level of non-thermal pressure in the *Planck* cluster population.

7.4.2 Comparison with *Planck* SZ masses

Following the discovery of the tension between *Planck* CMB cosmology and SZ number counts (Planck Collaboration et al., 2014b), considerable effort has been devoted to evaluating the accuracy of the mass calibration adopted by the *Planck* collaboration. *Planck* SZ masses were derived from a relation between SZ flux Y_{SZ} and total mass that was calibrated using *XMM-Newton* HSE masses. Biases in the estimation of the mass might arise from the potential impact of non-thermal pressure in the calibration sample and/or from the measurement of the total SZ flux from *Planck* data. Cosmological constraints from *Planck* CMB and cluster counts could be reconciled in case the $Y_{SZ} - M_{500}$ relation adopted by the *Planck* team is biased low by a factor $1 - b = M_{SZ}/M_{\text{true}} = 0.58 \pm 0.04$, presumably because of strong non-thermal pressure support (Nagai et al., 2007; Rasia et al., 2006). Numerous studies have addressed this issue by directly comparing masses derived using X-ray and weak lensing techniques (e.g. Hoekstra et al., 2015; Smith et al., 2016; von der Linden et al., 2014), resulting in somewhat divergent values for the *Planck* mass bias ($1 - b$ in the range 0.7-1.0, Sereno and Ettori, 2015). Here we take a different route and combine our high-quality measurements of hydrostatic masses with our robust assessment of the universal gas fraction to probe the reliability of *Planck* SZ masses. Indeed, in case SZ masses are incorrect we expect the corresponding gas fractions to deviate from the universal gas fraction, which can be easily tested with our data.

We retrieved the masses of X-COP clusters from the PSZ2 catalog (Planck Collaboration et al., 2016d) and determined the value of $R_{500,SZ}$ accordingly. We recall that the PSZ2 masses were determined by applying a relation between SZ signal Y_{500} and total mass $M_{500,SZ}$ calibrated using HSE masses. ZwCl 1215 does not have an associated mass in PSZ2 because of an updated point-source mask, thus in this case we use the mass provided in PSZ1 (Planck Collaboration et al., 2014a). We integrated our gas masses out to $R_{500,SZ}$ and computed the corresponding values of $f_{\text{gas},SZ}$. We repeated the exercise by correcting the

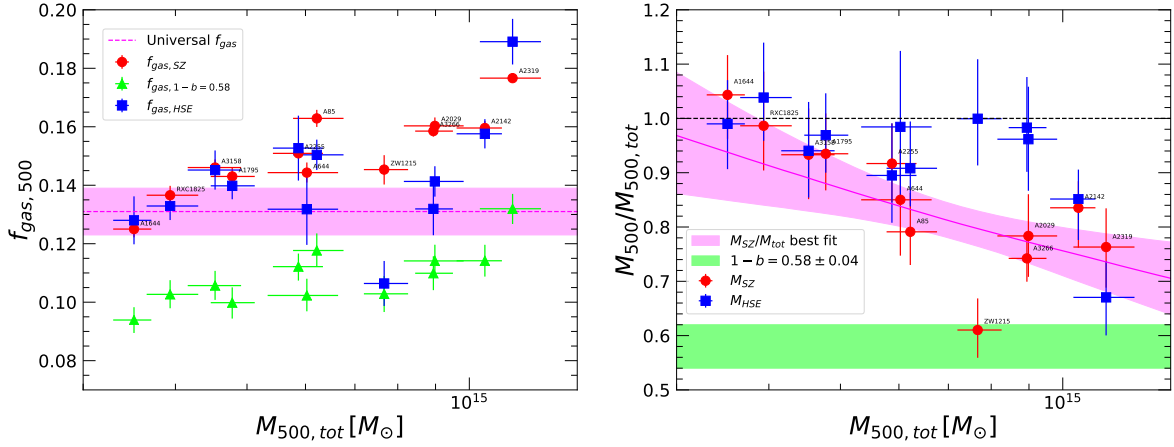


Fig. 7.6 *Left:* ICM gas fraction at R_{500} obtained from our reference hydrostatic-based mass model (blue squares) as a function of the total mass corrected for non-thermal pressure support (see Sect. 7.4.2). The red points show the gas fraction obtained using the *Planck* PSZ2 masses estimated from the $Y_{\text{SZ}} - M_{500}$ relation, whereas the green triangles show the gas fraction one would get by correcting the PSZ2 masses with a uniform mass bias $1 - b = 0.58 \pm 0.04$ (Planck Collaboration et al., 2014b). The dashed magenta line and shaded area represent the universal gas fraction estimated in Sect. 2.2.5. *Right:* Comparison between HSE (blue squares)/SZ (red dots) and total masses corrected for non-thermal pressure as a function of mass. The magenta line and shaded area show our best fit to the SZ data with a power law, whereas the green area displays the expectation for a constant mass bias $1 - b = 0.58 \pm 0.04$.

PSZ2 masses assuming a mass bias $1 - b = 0.58 \pm 0.04$, and derived the corresponding gas fractions. In Fig. 7.6 we show the gas fractions determined using the hydrostatic equilibrium assumption (see Table 7.2) as a function of total cluster masses corrected for non-thermal pressure support. We also show the gas fractions $f_{\text{gas},\text{SZ}}$ measured from the PSZ2 masses and from the masses corrected to reconcile CMB and SZ number count cosmology.

In Fig. 7.6 we can clearly see that the gas fraction of X-COP clusters exceeds the expected value in case the *Planck* masses are assumed to be correct. The median gas fraction is $f_{\text{gas},\text{SZ}} = 0.150^{+0.006}_{-0.004}$, i.e. $\sim 15\%$ higher than the universal gas fraction. We also notice a trend of increasing gas fraction with cluster mass, which may indicate a mass-dependent bias. Conversely, when correcting the SZ masses by a factor $1 - b = 0.58$ the gas fraction is substantially lower than expected, with a median value $f_{\text{gas},1-b=0.58} = 0.108 \pm 0.006$. All objects but one would lie outside of the allowed range for $f_{\text{gas,univ}}$. Reconciling CMB and SZ cosmology would thus imply that the most massive local clusters are missing about a third of their baryons.

As shown in Fig. 7.6, measurements of $f_{\text{gas},500}$ are very sensitive to the adopted mass calibration and thus they can be used to assess systematics in the *Planck* mass calibration.

We compared our masses corrected for non-thermal pressure support under the assumption of a universal gas fraction (see Table 7.2) to the *Planck* SZ-derived masses. In Fig. 7.6 we show the ratio of SZ masses to total masses. We measure a median value $1 - b = M_{500,\text{SZ}}/M_{500,\text{tot}} = 0.85 \pm 0.05$ for the *Planck* mass bias in our systems. As noted in several previous studies (Ettori, 2015; von der Linden et al., 2014), we observe a substantial mass dependence of the SZ mass bias, with the most massive objects ($M_{500} \sim 10^{15} M_{\odot}$) being biased at the $\sim 25\%$ level, while for $M_{500} \sim 4 \times 10^{14} M_{\odot}$ SZ masses appear to be unbiased. For comparison, in Fig. 7.6 we also show the ratio between our direct HSE measurements and the masses corrected for non-thermal pressure support. In the latter case we find that with the notable exception of A2319 our masses require little correction, with a median bias $M_{500,\text{HSE}}/M_{500,\text{tot}} = 0.94 \pm 0.04$.

To assess the dependence of the *Planck* bias on the mass, we describe the relation between SZ mass and total mass as a power law and use the Bayesian mixture model code `linmix_err` (Kelly, 2007) to fit the data. The resulting parameters read

$$\frac{M_{\text{SZ}}}{M_{\text{tot}}} = (0.87 \pm 0.05) \left(\frac{M_{\text{tot}}}{5 \times 10^{14} M_{\odot}} \right)^{-0.21 \pm 0.12} \quad (7.9)$$

i.e. a mass dependence is detected at $\sim 2\sigma$. The best-fitting curve and error envelope are displayed in Fig. 7.6. A high, constant bias $1 - b = 0.58 \pm 0.04$ is rejected at the 4.4σ level.

7.5 Discussion

7.5.1 Systematic uncertainties

Beyond uncertainties associated with the determination of the universal gas fraction (see Sect. 2.2.5), our results can also be affected by potential systematics in our measurements of $f_{\text{gas,HSE}}$. Here we review potential sources of systematic uncertainties.

- **Reconstruction of M_{HSE} :** As described in Sect. 7.2.1, we adopt as our reference mass reconstruction method the *backward NFW* method (Ettori et al., 2010), which assumes that the mass profile can be accurately described by a NFW parametric form. However, this method may be inaccurate if the true mass distribution differs substantially from NFW. In Ettori et al. (2018) we compare the results obtained with our reference *backward NFW* method with the results obtained with methods that do not make any assumption on the shape of the dark matter halo (forward fitting, Gaussian processes). We find that the results obtained with the various methods agree within $\sim 5\%$ at a radius of 1.5 Mpc, with the NFW method returning on average slightly higher masses.

This propagates to a systematic uncertainty of $\sim 5\%$ on the hydrostatic gas fraction, and thus on the non-thermal pressure fraction.

- **Gas mass measurements:** The gas mass of local clusters is one of the quantities that can be most robustly computed from X-ray observations. Studies on mock X-ray observations of simulated clusters have shown that measurements of M_{gas} are accurate down to the level of a few percent and exhibit very little scatter, even in situations of violent mergers (Eckert et al., 2016a; Nagai et al., 2007). The measured gas densities tend to be biased high in cluster outskirts by the presence of accreting substructures and large-scale asymmetries (Nagai and Lau, 2011; Roncarelli et al., 2013), which introduces a systematic uncertainty of 5-10% on the true gas mass at R_{200} . However, thanks to the use of the azimuthal median as a robust estimator of the surface brightness (Eckert et al., 2015), the bias introduced by infalling substructures has been taken into account in our study. Residual clumping on scales smaller than the resolution of our study ($\lesssim 20$ kpc) can still introduce a slight positive bias in our estimates of M_{gas} , however we expect the residual effect to be less than a few percent.
- **Calibration uncertainties:** Temperature measurements are known to be affected by systematics of the order of $\sim 15\%$ in the high-temperature regime because of uncertainties in the calibration of the effective area of the instrument (Nevalainen et al., 2010; Schellenberger et al., 2015), with *Chandra* returning systematically higher gas temperatures than *XMM-Newton*. If *Chandra* temperatures are correct, our masses should be underestimated by $\sim 15\%$, meaning that our estimates of the non-thermal pressure should be overestimated. However, we note that our mass reconstruction makes use of joint *XMM-Newton* and *Planck* data. In the radial range where data from both instruments are available, we do not observe a systematic offset between X-ray and SZ pressure (see also Adam et al., 2017). While effective area calibration introduces some uncertainty in the recovered temperature, its effect on the gas density and gas mass is mild. Bartalucci et al. (2017) compared *XMM-Newton* and *Chandra* reconstructions of gas density profiles and gas masses and found an exquisite agreement between the two missions at the level of 2.5%.

7.5.2 Implications on the thermalization of the ICM

As described in Sect. 7.4.1, our gas fraction data imply a low level of non-thermal pressure in our population, $\alpha = P_{NT}/P_{\text{tot}} = 6\%$ and 10% at R_{500} and R_{200} , respectively. If we ascribe the excess gas fraction entirely to residual isotropic gas motions (Eq. 7.8), we can relate the

measured non-thermal pressure to the velocity dispersion by rewriting Eq. 7.8 as

$$\frac{\sigma_{\text{gas}}^2}{c_s^2} = \mathcal{M}_{3\text{D}}^2(r) = \frac{3}{\gamma} \frac{\alpha(r)}{1 - \alpha(r)}, \quad (7.10)$$

with $c_s = (\gamma kT / \mu m_p)^{1/2}$ the sound speed in the medium, $\mathcal{M}_{3\text{D}}$ the Mach number of residual gas motions, $\gamma = 5/3$ the polytropic index, and $\alpha(r)$ the functional form for $P_{\text{NT}}/P_{\text{tot}}(r)$ following the definition of Eq. 7.7. The values estimated here thus imply an average Mach number at R_{500}

$$\mathcal{M}_{3\text{D},500} = 0.33_{-0.12}^{+0.08}, \quad (7.11)$$

i.e. isotropic gas motions in the X-COP cluster population are clearly subsonic. This value broadly agrees with the Mach numbers estimated from the amplitude of relative ICM fluctuations (Eckert et al., 2017b; Hofmann et al., 2016; Zu and Mandelbaum, 2015b).

As shown in Fig. 7.5, our values are somewhat smaller than the predictions of non-radiative adaptive mesh refinement (AMR) simulations by Nelson et al. (2014a) and closer to the curves extracted from the the300 simulation with the smoothed particle hydrodynamics (SPH) code GADGET-3. While in the past legacy SPH codes (employing a typically large artificial viscosity to handle shocks) tended to predict a more clumped and inhomogeneous ICM than grid codes (Rasia et al., 2014), we observe the opposite here.

A few possible reasons can be given for this difference. First, to better reproduce standard hydrodynamics tests, the300 simulation incorporates a number of advanced features compared to previous SPH codes, including a higher-order Wendland C^4 kernel function, the implementation of a time-dependent artificial viscosity scheme, and artificial conduction (Beck et al., 2016). Compared to previous SPH codes, the SPH scheme included in the300 leads to a more efficient mixing of the gas phases with different entropies. This promotes a faster thermalization of the accreting gas and of small merging substructures, thus reducing the non-thermal pressure fraction. On top of that, the300 simulation implements a wide range of baryonic processes (including radiative cooling, star formation, and AGN and supernova feedback) whereas the predictions of Nelson et al. (2014a) are extracted from non-radiative simulations. The balance of cooling and AGN feedback implemented in these simulations substantially changes the appearance of galaxy- and group-scale halos by removing the most structured phase of the ICM from the X-ray emitting phase and by increasing their gas entropy, which leads to smoother and flatter density profiles compared to simulations without powerful feedback mechanisms. The AGN activity provides extra energy to the gas residing in the shallow potential well of small systems, further enhancing its mixing with the cluster ICM during, or immediately after, a merger. The subsequent clumping factor is thus reduced

compared to the non-radiative case (Planelles et al., 2017) where the entropy difference between the medium and the denser and colder substructure is substantially larger. As a result, infalling motions get virialized on shorter timescales and the non-thermal pressure fraction is reduced.

It should be stressed that the estimate of the non-thermal pressure support in the simulated ICM is by itself non-trivial, owing to the complexity of gas motions in the stratified cluster atmosphere. While all modern simulations overall agree on the predicted radial trend of turbulent motions moving from the cluster centers to the periphery (e.g. Biffi et al., 2016; Nelson et al., 2014a; Vazza et al., 2011), their quantitative answer may change depending on the adopted filtering techniques to disentangle the various velocity components of the ICM (e.g. bulk motions, shock jumps and small-scale chaotic motions), which is particularly crucial in cluster outskirts (e.g. Vazza et al., 2017). For example, if motions along the radial direction are predominantly directed inwards, the missing pressure estimated with radial averages in simulations may overestimate the non-thermal pressure recovered here using the method devised in Sect. 7.3.5. More detailed comparisons using exactly the same technique as used here are necessary to test this hypothesis.

7.5.3 Implications for cosmology

The results presented in Sect. 7.4.2 have important implications for the use of galaxy clusters as cosmological probes. They imply that galaxy cluster masses derived under the assumption of hydrostatic equilibrium in a fully thermalized ICM require little correction from non-thermal pressure support. This conclusion is further supported by our direct comparison of hydrostatic and weak lensing masses when available (see Sect. 4 of Ettori et al. 2018), which finds a median ratio $M_{500,\text{HSE}}/M_{500,\text{WL}} = 0.87 \pm 0.10$ and $M_{200,\text{HSE}}/M_{r_{m200},\text{WL}} = 0.86 \pm 0.13$ for the 6 X-COP clusters with available weak lensing measurements, fully consistent with the non-thermal pressure and the mass ratio $M_{500,\text{HSE}}/M_{500,\text{tot}} = 0.94 \pm 0.04$ estimated from the universal gas fraction method used here.

At face value, our results strongly disfavor a large hydrostatic bias as the origin of the tension in the $\Omega_m - \sigma_8$ plane between SZ cluster counts and primary CMB. As shown in Fig. 7.6, our hydrostatic gas fraction measurements are very close to the values obtained with the *Planck* mass calibration, although we note a mildly significant trend of increasing bias in the *Planck* calibration with cluster mass. However, the median mass of the systems in the *Planck* cosmological sample is $\sim 5 \times 10^{14} M_\odot$, where our analysis shows that the SZ masses are biased only at the 10% level. Although quantifying the exact impact of our results on the cosmological parameters is beyond the scope of this chapter, it is fair to say that our study favors lower values of σ_8 compared to primary CMB, similar to what was obtained from

essentially all cluster count (de Haan et al., 2016; Vikhlinin et al., 2009) and weak lensing tomography studies (Heymans et al., 2013; Hildebrandt et al., 2017).

Obviously, the conclusions reached here rest on the premise that our determination of the universal gas fraction is accurate. As shown in Fig. 7.6, a large, constant hydrostatic bias would imply that the most massive galaxy clusters are missing about a third of their baryons. We also note that our estimate of the stellar fraction (Sect. 7.3.3) lies on the high side of the published measurements (see Fig. 7.3), thus our estimate of f_{gas} is probably on the low side. Extreme AGN feedback would be required to push a substantial fraction of the baryons outside of R_{200} , which would lead to high-entropy cores and large offsets from the observed scaling relations (e.g. Le Brun et al., 2014). High-resolution hydrodynamic simulations testing different AGN feedback models have shown that the feedback must be gentle and tightly self-regulated (e.g. Gaspari et al., 2014), thus affecting only the regions within $\sim 0.1R_{500}$. An extreme thermal/Sedov blast ($\sim 10^{62}$ erg) would be required to evacuate a substantial fraction of the gas away from R_{500} , which would transform any CC cluster into a NCC cluster, with cooling times well above the Hubble time. The gentle preservation of many cool cores up to redshift ~ 2 (e.g. McDonald et al., 2017) rules out the strong and impulsive AGN feedback scenario. In the absence of evidence for such extreme phenomena, we conclude for the time being that our estimate of the universal gas fraction does not need to be revised.

7.6 Conclusion

In this chapter, we presented high-precision measurements of the hydrostatic gas fraction from the X-COP project, a sample of 12 clusters with high-quality X-ray and SZ data from *XMM-Newton* and *Planck*. The statistical uncertainties in $f_{\text{gas,HSE}}$ are less than 10% in all cases and measurements at R_{200} are achieved for 10 out of 12 objects without requiring any extrapolation. We used our measurements to estimate the level of non-thermal pressure in our sample. Our results can be summarized as follows.

- Combining a large set of clusters simulated with a state-of-the-art SPH code with literature measurements of the stellar fraction in observed clusters, we robustly estimate the universal gas fraction of massive clusters to be $f_{\text{gas},500} = 0.131 \pm 0.009$ and $f_{\text{gas},200} = 0.134 \pm 0.007$ at R_{500} and R_{200} , respectively. The uncertainties quoted here include both statistical uncertainties and scatter in the simulated cluster population.
- Our hydrostatic gas fractions are on average consistent with the estimated universal gas fraction, lying just 7% and 11% above the universal value at R_{500} and R_{200} , respectively.

- To determine the integrated level of non-thermal pressure support, we modified the hydrostatic equilibrium equation to incorporate the contribution of a non-thermal pressure term, which we describe using the parametric function of Nelson et al. (2014a) (see Sect. 7.3.5). The parameters of the non-thermal pressure component were then determined by comparing the measured hydrostatic gas fraction profiles with the universal gas fraction. Our procedure leads to revised mass measurements that incorporate the contribution of non-thermal pressure.
- With the notable exception of A2319 (Ghirardini et al., 2018b), the required levels of non-thermal pressure are mild, with median values $P_{\text{NT}}/P_{\text{tot}}(R_{500}) \sim 6\%$ and $P_{\text{NT}}/P_{\text{tot}}(R_{200}) \sim 10\%$. These values are lower than the predictions of numerical simulations (Biffi et al., 2016; Nelson et al., 2014a), possibly implying a faster thermalization of the kinetic energy in the real population compared to hydrodynamical simulations.
- Assuming that the residual non-thermal pressure can be entirely ascribed to random gas motions, we infer an average Mach number $\mathcal{M}_{3D} = 0.33^{+0.08}_{-0.12}$, implying that residual kinetic motions are clearly subsonic.
- We used our masses corrected for the effects of non-thermal pressure to test the accuracy of *Planck* SZ masses in our systems. We find that PSZ2 masses lead to an average gas fraction $f_{\text{gas,SZ}} = 0.150 \pm 0.005$ at R_{500} , indicating that SZ masses are slightly underestimated. Comparing PSZ2 masses with our masses corrected for non-thermal pressure support, we infer a median bias $1 - b = 0.85 \pm 0.05$. As noted in previous studies (Ettori, 2015; von der Linden et al., 2014), the bias appears to depend slightly on cluster mass, $M_{\text{SZ}}/M_{\text{tot}} \propto M_{\text{tot}}^{-0.21 \pm 0.12}$.
- If instead we assume that the PSZ2 masses are biased low by a constant factor $M_{\text{SZ}}/M_{\text{true}} = 0.58 \pm 0.04$ to reconcile *Planck* primary CMB and SZ cluster counts, the gas fraction of X-COP clusters would fall short of the universal baryon fraction (median $f_{\text{gas},1-b=0.58} = 0.108 \pm 0.006$), implying that the most massive local clusters would be missing about a third of their baryons. This would pose a serious challenge to our understanding of cluster formation processes and feedback energetics.

**THE POLYTROPIC STATE OF THE
INTRACLUSTER MEDIUM IN THE X-COP
SAMPLE**

8.1 Introduction

In this chapter we study the relation between pressure and density from the core out to the outskirts in the X-COP cluster sample. We constrain the effective polytropic index, its radial dependence, its implication regarding applications on mass reconstruction, and how it can be used to build new universal functional form for the thermodynamic quantities. The chapter is organized as follows. In Sect. 8.2 we study the relation between pressure and density, as function of density and as function of radius. In Sect. 8.3 we introduce the NFW polytropic model showing how it provides a very good description for clusters outside the core, and we show how the polytropic approximation can provide a very tight mass probe. Finally we draw our conclusions in Sect. 8.4. Throughout the chapter, if not otherwise stated, we assume a flat Λ CDM cosmology with $\Omega_m = 0.3$, $\Omega_\Lambda = 0.7$ and $H_0 = 70 \text{ km s}^{-1} \text{ Mpc}^{-1}$, and use the Bayesian nested sampling algorithm MultiNest (Feroz et al., 2009) to constrain the best-fit parameters.

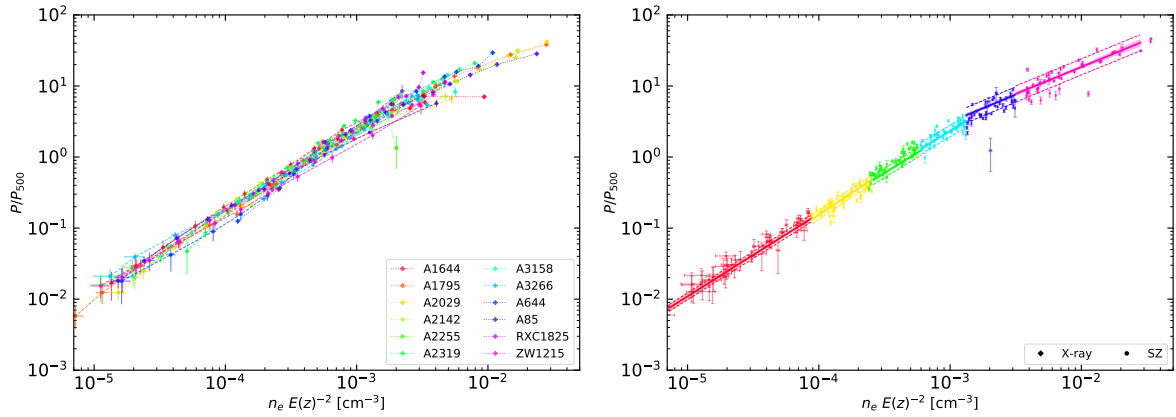


Fig. 8.1 *Left*: Rescaled pressure profile for the X-COP objects compared with density corrected by redshift evolution, a clear trend with very small scatter over several orders of magnitude is evident. *Right*: Piecewise power law fit of the density against density. Solid lines and contour indicate the best fitting result with statistical uncertainties, dashed lines indicate the intrinsic scatter in the distribution around the best fit.

8.2 The polytropic equation

The hydrostatic equilibrium equation (HEE) relates the thermodynamic quantities on one side, and the gravitational potential on the other side:

$$\frac{1}{\mu m_p n_e} \frac{dP_e}{dR} = -\frac{GM(< r)}{r^2}. \quad (8.1)$$

The polytropic equation reads the following relation between the gas pressure and density

$$P_e = K n_e^\Gamma \quad (8.2)$$

where K is a constant, and Γ is the effective polytropic index. Combining Eq. (1.17) and (8.2) with a functional form which describes the gravitational potential allows to construct a functional form of the thermodynamic profiles, i.e. how density, pressure, temperature, and entropy vary with radius (e.g. as shown in Bulbul et al., 2010, using a generalized NFW to describe the gravitational potential).

In Ettori et al. (2018), we have shown that the NFW (Navarro et al., 1997) is the best representation for the gravitational potential in the X-COP objects, as evaluated by computing the Bayesian evidence for several possible mass models, with or without a core and with different slopes in the external parts. Also in the few cases where NFW is not the best fitting mass model, it does not show any statistically significant tension with the best fitting mass model.

As discussed in Bulbul et al. (2010), a NFW mass model, $M(< r) \propto \log(1+x) - \frac{x}{1+x}$, where $x = r/r_s = c_{500} r/R_{500}$ and r_s and c_{500} are the NFW scale radius and concentration, respectively, permits to recover analytically a profile for the thermodynamic quantities, once the HEE is assumed (Eq. 1.17) with a polytropic gas (Eq. 8.2):

$$n_e(x)^{\Gamma-1} \propto \frac{\log(1+x)}{x}. \quad (8.3)$$

However, in order to introduce a physically motivated analytic model to describe the average behaviour of the thermodynamic quantities, we have to verify whether gas pressure and density are correlated, at which degree, and ultimately if this relation is a polytrope.

8.2.1 Relations between gas pressure, gas density and radius

We start our analysis by studying how the pressure depends on density, and how the slope of this relation depends on both density and radius. We have indeed three quantities $n_e E(z)^{-2}$, $\frac{P_e}{P_{500}}$, and $\frac{R}{R_{500}}$ that correlate among them, allowing us to study, for instance, how the effective index Γ depends on the measured quantities and on radius.

We refer to Ghirardini et al. (2018a) for a detailed description on the measurements of the gas density and pressure in the X-COP clusters out to $2 \times R_{500}$. In Fig. 8.1, we show these estimates for all the data of our sample. A tight power-law-like relation between the rescaled thermodynamic quantities is evident, with just a mild change in slope in the high density regime.

Table 8.1 Results of the piecewise power-law fits on pressure against density, also in several radial intervals, using the function described in Eq. (8.4).

$n_{in}E(z)^{-2}$	$n_{out}E(z)^{-2}$	A	Γ	σ_{int}
7.22e-06	8.75e-05	8.87 ± 0.47	1.16 ± 0.05	0.11 ± 0.02
8.88e-05	2.54e-04	9.43 ± 0.66	1.23 ± 0.08	0.15 ± 0.02
2.60e-04	6.04e-04	8.67 ± 0.65	1.14 ± 0.08	0.15 ± 0.02
6.06e-04	1.32e-03	8.60 ± 0.67	1.12 ± 0.10	0.19 ± 0.02
1.33e-03	3.11e-03	6.47 ± 0.34	0.77 ± 0.06	0.25 ± 0.03
3.16e-03	2.81e-02	6.42 ± 0.33	0.76 ± 0.06	0.26 ± 0.03

x_{in}	x_{out}	$x_{average}$	Γ	σ_{int}
0.013	0.112	0.058	0.764 ± 0.058	0.26 ± 0.03
0.113	0.251	0.168	0.848 ± 0.075	0.20 ± 0.03
0.263	0.451	0.327	1.078 ± 0.093	0.17 ± 0.02
0.451	0.712	0.565	1.322 ± 0.068	0.14 ± 0.02
0.720	1.148	0.885	1.204 ± 0.078	0.16 ± 0.02
1.162	2.645	1.729	1.200 ± 0.045	0.11 ± 0.03

To constrain the significant parameters of this relation, and compute the effective polytropic index Γ , we implement a method similar to the piecewise power-law fitting procedure described in Ghirardini et al. (2018a). We define 6 intervals in density (see Table 8.1) and fit the following functional form:

$$\frac{P_e}{P_{500}} = A [n_e E(z)^{-2}]^\Gamma \exp(\pm \sigma_{int}) \quad (8.4)$$

with A being the normalization, Γ the effective polytropic index, and σ_{int} the intrinsic scatter in the relation.

We find that the relation between pressure and density is pretty tight, with small scatter of about 0.15 on average. We show the resulting best fitting function in Fig. 8.1, and the resulting best-fit parameters in Table 8.1.

We notice that there are two different regimes: one where Γ is about 0.8, and the other where Γ is about 1.2. This suggests a transition in the slope of the temperature profile ($\Gamma < 1$ and > 1 indicate positive and negative radial gradient in the temperature profile, respectively)

To constrain the value of the density where this transition occurs, we proceed with another fit

$$\frac{P_e}{P_{500}} = \begin{cases} A_0 [n_e E(z)^{-2}]^{\Gamma_0} \exp(\pm \sigma_{int,0}), & \text{if } Y \geq Y_0 \\ A_1 [n_e E(z)^{-2}]^{\Gamma_1} \exp(\pm \sigma_{int,1}), & \text{if } Y \leq Y_0, \end{cases} \quad (8.5)$$

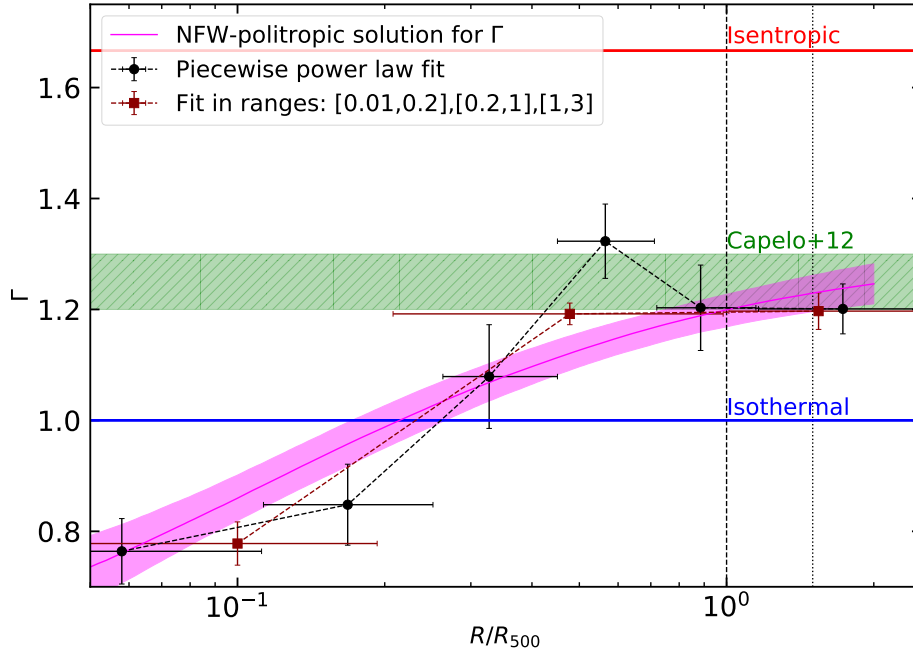


Fig. 8.2 Effective polytropic index as function of radius, as fitted with the NFW polytropic analytic solution (Eq. 8.13). The horizontal blue and red lines indicate the location of the isothermal and isentropic limits respectively. The horizontal green stripe indicates the predicted values from Capelo et al. (2012).

where $Y = n_e E(z)^{-2}$ and allowing $Y_0 = n_0$ to be a free parameter indicating the “transition” density. We impose continuity by forcing $A_1 = A_0 \cdot n_0^{\Gamma_0 - \Gamma_1}$. We find $n_0 = (2.45 \pm 0.46) \cdot 10^{-3} \text{cm}^{-3}$, $\Gamma_0 = 1.17 \pm 0.01$ and $\Gamma_1 = 0.79 \pm 0.07$.

Then, we study the dependence upon the radius. We divide our profiles in 6 radial bins, fitting Eq. (8.4) in each of them to estimate the effective polytropic index. The best-fit values are shown in Fig. 8.2. We notice how Γ increases from the center to the outskirts, flattening in the outermost bins to values around 1.2, as expected from hydrodynamical simulations (Capelo et al., 2012). Similarly to the case above, we notice two regimes in Γ . Hence, we fit equation 8.5 again, where we define $Y = r/R_{500}$ and $Y_0 = r_0$. We measure $r_0 = 0.19 \pm 0.04$, $\Gamma_0 = 1.17 \pm 0.01$, and $\Gamma_1 = 0.78 \pm 0.04$.

We have thus demonstrated that it is possible to define well distinct regions associated to a “core”, where $n_e E(z)^{-2} > (2.45 \pm 0.46) \cdot 10^{-3} \text{cm}^{-3}$ and $r/R_{500} < 0.19(\pm 0.04)$, and to the outskirts of galaxy clusters. In the latter region, the scatter in the relation between pressure and density is very small (0.10–0.15) and the relation follows an almost precise power-law where the effective polytropic index is almost constant to the value of ~ 1.2 .

8.2.2 Functional form for pressure against density

It is convenient to describe the relation between pressure and density using a single function such that it is continuous with also continuous first derivative, i.e. a C^1 function for mathematicians. The simplest function we think of is very similar to the one defined in Eq. (8.5) where the transition at Y_0 between the “core” and the outskirts is smooth. To make the transition smooth we use the Gauss error function $\text{erf}(x)$ defined as

$$\text{erf}(x) = \int_{-x}^x e^{-t^2} dt$$

which is simply a step function which has the property of being C^1 . Therefore we adopt the following constraints

$$\begin{cases} A_1 = A_0 \cdot x_0^{(\Gamma_0 - \Gamma_1)} \\ A(x) = (A_1 - A_0) \cdot \frac{\text{erf}(\log(x) - x_0) + 1}{2} + A_0 \\ \Gamma(x) = (\Gamma_1 - \Gamma_0) \cdot \frac{\text{erf}(\log(x) - x_0) + 1}{2} + \Gamma_0 \\ \sigma_{int}(x) = (\sigma_{int,1} - \sigma_{int,0}) \cdot \frac{\text{erf}(\log(x) - x_0) + 1}{2} + \sigma_{int,0} \end{cases} \quad (8.6)$$

Thus the simple modified broken power law that describes the dependence of pressure upon density can be described by the following function:

$$y = A(x)x^{\Gamma(x)} \exp(\pm \sigma_{int}(x)) \quad (8.7)$$

where $x = n_e E(z)^{-2}$, $y = \frac{P_e}{P_{500}}$, and $A(x)$, $\Gamma(x)$, and $\sigma_{int}(x)$ defined by Eq. (8.6). $x_0 = \log(n_0)$, $\Gamma_0, \Gamma_1, A_0, \sigma_{int,0}$, and $\sigma_{int,1}$ the parameters of this functional form.

The resulting best fitting parameters are $x_0 = -6.38 \pm 0.16$, thus $n_0 = (1.70 \pm 0.27) \cdot 10^{-3} \text{cm}^{-3}$, $\Gamma_0 = 1.16 \pm 0.01$ and $\Gamma_1 = 0.81 \pm 0.04$, $A_0 = 0.90 \pm 0.10$, $\sigma_{int,0} = 0.14 \pm 0.01$, and $\sigma_{int,1} = 0.25 \pm 0.02$. The representation of this functional form, and the posterior distribution on the best fitting parameters are shown in Fig. 8.3.

8.2.3 Application of the functional form $\mathbf{P(n)}$ in mass reconstruction

The tightness of the relation between pressure and density can be exploited in order to solve HEE using only one thermodynamic quantity. In fact if by modeling the relation between rescaled pressure and rescaled density using a function f

$$\frac{P_e}{P_{500}} = \mathcal{F}(n_e E(z)^{-2})$$

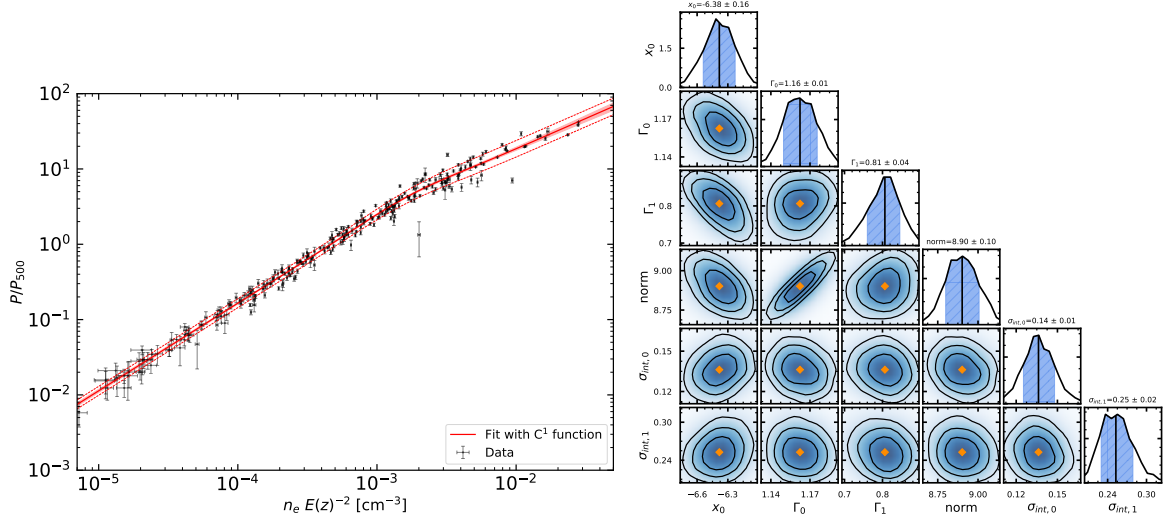


Fig. 8.3 *Left:* Pressure against density plot fitted using the functional form Eq. 8.7. *Right:* Posterior distribution of the fitting parameters of the functional form Eq. 8.7.

then HEE Eq. (1.17) is re-casted as

$$\frac{d\mathcal{F}(n_e E(z)^{-2})}{d(n_e E(z)^{-2})} \frac{d \log(n_e E(z)^{-2})}{d \log(R)} E(z)^{-2} = -\frac{\mu m_p G M(< R)}{P_{500} R} \quad (8.8)$$

therefore, by knowing this function \mathcal{F} , we just need to measure its derivative to get the mass profile. In fact, from the definition of P_{500} from Ghirardini et al. (2018a), we can simplify previous equation.

$$P_{500} = T_{e,500} \cdot n_{e,500} = \frac{\mu m_p G M_{500}}{2R_{500}} \cdot \frac{500 f_b \rho_c}{\mu_e m_p} \quad (8.9)$$

using μ and μ_e from Anders and Grevesse (1989), and f_b from Planck Collaboration et al. (2016e).

Therefore HEE can be rewritten as:

$$\frac{d\mathcal{F}(n_e E(z)^{-2})}{d(n_e E(z)^{-2})} \frac{d \log(n_e E(z)^{-2})}{d \log(R)} E(z)^{-2} \frac{500 f_b \rho_c}{2\mu_e m_p} = -\frac{M(< R) R_{500}}{M_{500} R} \quad (8.10)$$

which can be solved using only the density profile at $R = R_{500}$:

$$-\frac{d\mathcal{F}(n_e E(z)^{-2})}{d(n_e E(z)^{-2})} \frac{d \log(n_e E(z)^{-2})}{d \log(R)} E(z)^{-2} \frac{500 f_b \rho_c}{2\mu_e m_p} = 1 \quad (8.11)$$

and finally by substituting the physical constants:

$$-\frac{d\mathcal{F}(n_e E(z)^{-2})}{d(n_e E(z)^{-2})} \frac{d \log(n_e E(z)^{-2})}{d \log(R)} \cdot 1.93 \cdot 10^{-4} \text{cm}^{-3} \frac{f_b}{0.16} \left(\frac{\mu_e}{1.14} \right)^{-1} = 1 \quad (8.12)$$

This equation can be directly solved for R_{500} , which then can be reintroduced in the Eq. (8.10) to obtain the entire total mass profile, given only the slope of the density profile.

A possible functional form $\mathcal{F}(n_e E(z)^{-2})$ is the one introduced in Eq. 8.7, with best fitting parameters and shape shown in Sect. 8.2.2.

8.3 A polytropic NFW model for the gas

The tight correlation between gas density and pressure, combined with the observational evidence that the NFW is the best fitting mass model in our sample (Ettori et al., 2018), allows us to use the NFW-polytropic profile described in Sect. 8.2 (see also Bulbul et al., 2010), and properly re-written as function of $x = r/R_{500}$, to model the stratification of the gas:

$$E(z)^{-2} n_e(x) = n_0 f(x)^{\frac{1}{\Gamma-1}}, \quad (8.13)$$

where $f(x) = \log(1 + c_{500}x)/x$ and the correlated relations, $P(x)/P_{500} = P_0 f(x)^{\Gamma/(\Gamma-1)}$, $T(x)/T_{500} = T_0 f(x)$, $K(x)/K_{500} = K_0 f(x)^{(\Gamma-5/3)/(\Gamma-1)}$ hold, with n_0 , P_0 , T_0 , and K_0 being the normalization factors, c_{500} the NFW concentration, and Γ the effective polytropic index.

In principle, if these were just generic universal functional forms, the parameters do not have any physical sense, meaning that their values are not expected to be the same in different forms. However, if the physical assumption behind this model is true and robust, then the values of c_{500} and Γ should be the same for all the thermodynamic quantities.

Since the assumption of constant Γ is strictly valid only beyond $\sim 0.2R_{500}$, we evaluate in this radial range the performance of the NFW-polytropic functional form with other functional forms (see Ghirardini et al., 2018a).

First, we fit each thermodynamic quantities independently. We show the results of the fit in Table 8.2. We notice that c_{500} and Γ from the fits are compatible at the 1σ level. This indicates that the NFW-polytropic model is a very good model to characterize the outer regions of galaxy clusters.

Then, we proceed with a joint-fit, i.e. forcing c_{500} and Γ to be the same for all thermodynamic quantities, showing the best fitting results in the last row of Table 8.2, and the posterior distribution of the parameters in Fig. 8.5. We show the best fitting results in Fig. 8.4, comparing with the functional forms described in Ghirardini et al. (2018a). We observe that

Table 8.2 Best fitting parameters for the functional form described in Sec. 8.3. We define the following priors: $(-13, -9)$ on $\log(n_0)$; $(-5, -1)$ on $\log(P_0)$; $(-2, 2)$ on $\log(T_0)$; $(-4, 4)$ on $\log(K_0)$; $(0.73, 0.52)$ on $\log(c_{500})$; $(1, 1.5)$ on Γ .

Density	$\log(n_0)$	$\log(c_{500})$	Γ
	-10.3 ± 0.4	0.99 ± 0.16	1.20 ± 0.01
Pressure	$\log(P_0)$	$\log(c_{500})$	Γ
	-2.94 ± 0.61	0.96 ± 0.21	1.19 ± 0.02
Temperature	$\log(T_0)$	$\log(c_{500})$	
	-0.60 ± 0.10	0.85 ± 0.15	
Entropy	$\log(K_0)$	$\log(c_{500})$	Γ
	0.92 ± 0.34	1.07 ± 0.35	1.21 ± 0.02
Joint fit	$\log(n_0)$	$\log(P_0)$	$\log(T_0)$
	-10.2 ± 0.2	-2.99 ± 0.26	-0.68 ± 0.06
	$\log(K_0)$	$\log(c_{500})$	Γ
	0.87 ± 0.08	0.97 ± 0.09	1.19 ± 0.02

the NFW-polytropic is a very good fit to the data, with a Bayesian Evidence just slightly larger than the one obtained from other functional forms available in the literature (Vikhlinin et al. (2006) for density and temperature; Nagai et al. (2007) for pressure; Cavagnolo et al. (2009) for entropy). On the other hand, the improvement is dramatic for what concerns both the physical interpretation of the best-fit parameters, and the simplification of the fitting procedure, considering the limited number of parameters in this new functional forms and the lack of any degeneracy among the parameters.

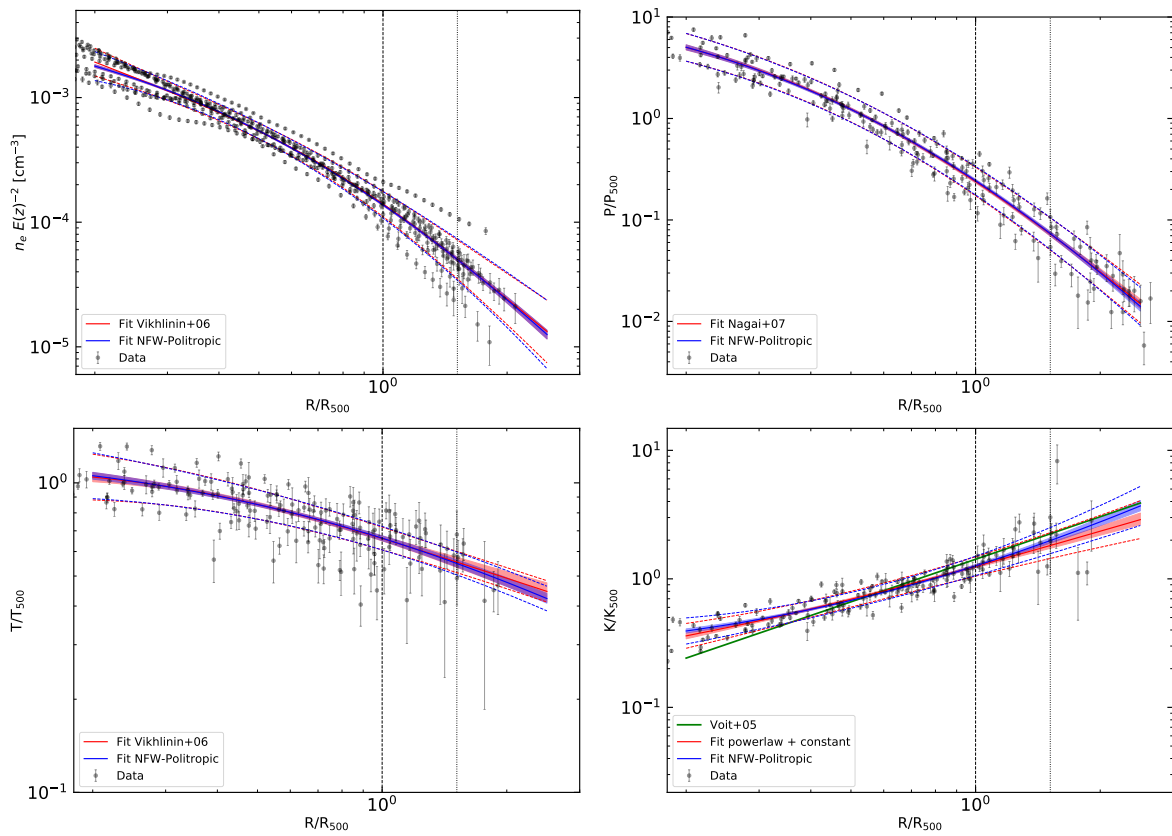


Fig. 8.4 Fit on the thermodynamic quantities using NFW-polytropic functional form, and the functional form used in (Ghirardini et al., 2018a)

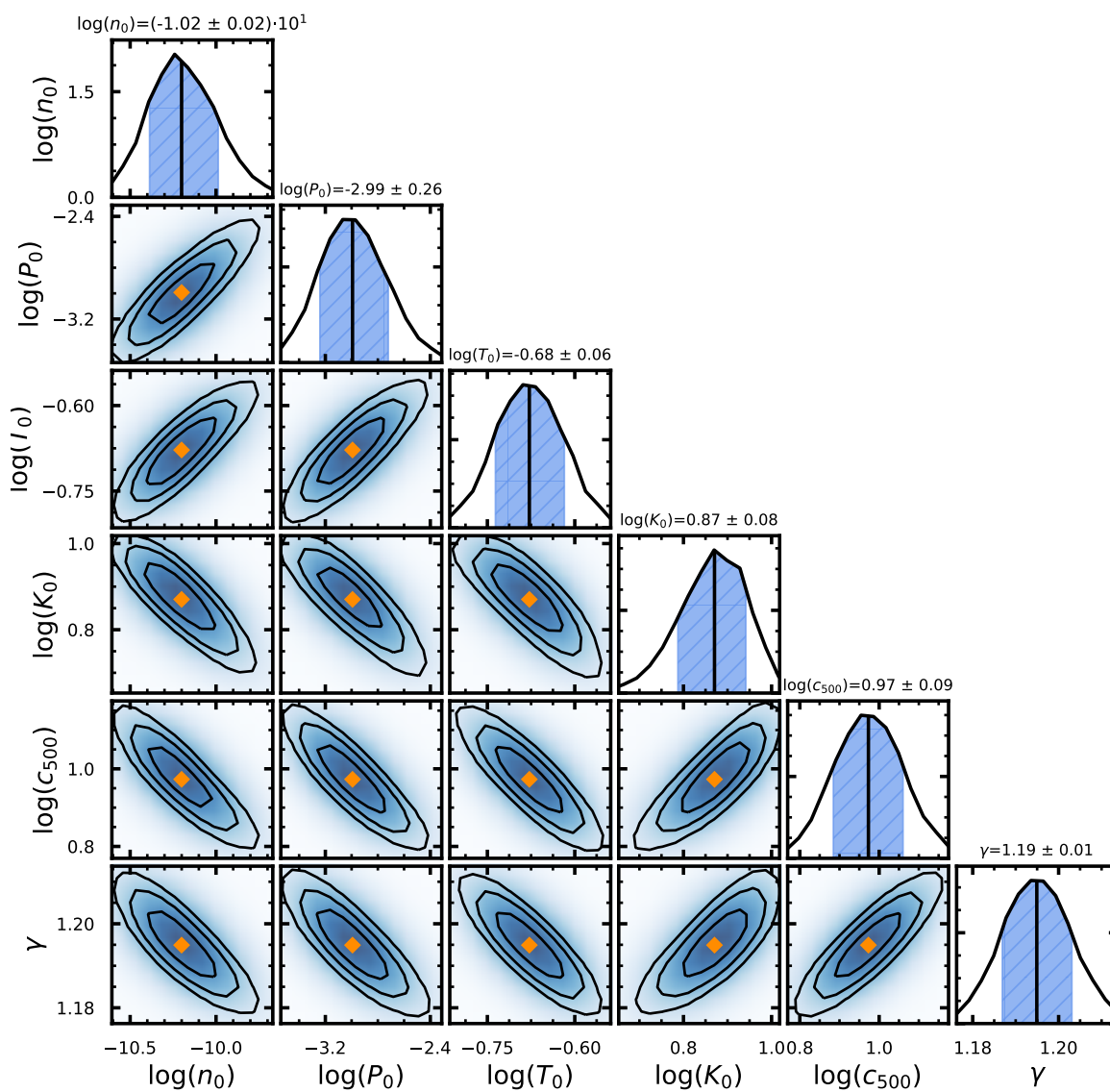


Fig. 8.5 Posteriors on the parameters of the thermodynamic profiles by performing a joint fit and using the functional forms introduced in Sect. 8.3

8.3.1 NFW polytropic model with $\Gamma(r)$

The functional forms presented in Sect. 8.3 can be also generalized by assuming that Γ is a function of radius. From the equation of the hydrostatic equilibrium (Eq. 1.17) with a NFW potential, we can write

$$\frac{1}{\rho} \frac{d\rho^\Gamma}{dx} = \rho^{\Gamma-1} \frac{d}{dx}(\Gamma \log \rho) = -\frac{GM(< r)}{r^2} = K \frac{d}{dx} \left(\frac{\log(1+x)}{x} \right). \quad (8.14)$$

Adopting the NFW polytropic modelling of the gas (Eq. 8.3; $\rho_{\text{gas}}^{\Gamma-1} = A \log(1+x)/x$), we can expand the first term of the above equation:

$$\rho^{\Gamma-1} \frac{d}{dx}(\Gamma \log \rho) = A \frac{\log(1+x)}{x} \frac{d}{dx} \left[\frac{\Gamma}{\Gamma-1} \log \left(A \frac{\log(1+x)}{x} \right) \right]. \quad (8.15)$$

By using this expansion in Eq. 8.14, and moving the terms with $y = \log(1+x)/x$ on the same side, we can write:

$$\frac{K}{A} \frac{dy}{y} = \frac{d}{dx} \left[\frac{\Gamma}{\Gamma-1} \log(Ay) \right]. \quad (8.16)$$

Finally, converting from $\frac{1}{y} \frac{dy}{dx}$ to $\frac{d \log(y)}{dx}$, integrating both side of the equation and adding an integration constant C , we have:

$$\frac{K}{A} \log y + \log(C) = \left[\frac{\Gamma}{\Gamma-1} \log(Ay) \right]. \quad (8.17)$$

Moving all the Γ terms to one side and rearranging them, we obtain a functional form for the radial dependence of Γ :

$$\Gamma(r) = \left(1 - \frac{A \log(Ay)}{K \log(Cy)} \right)^{-1} \quad (8.18)$$

The fit with this functional form on the measured Γ 's is shown in Fig. 8.2. This functional form allows for a global fit for all thermodynamics considering the dependence of Γ in Eq. (8.18).

Therefore we fit density and pressure jointly as function of radius, but also considering the dependence of Γ in Eq. (8.18).

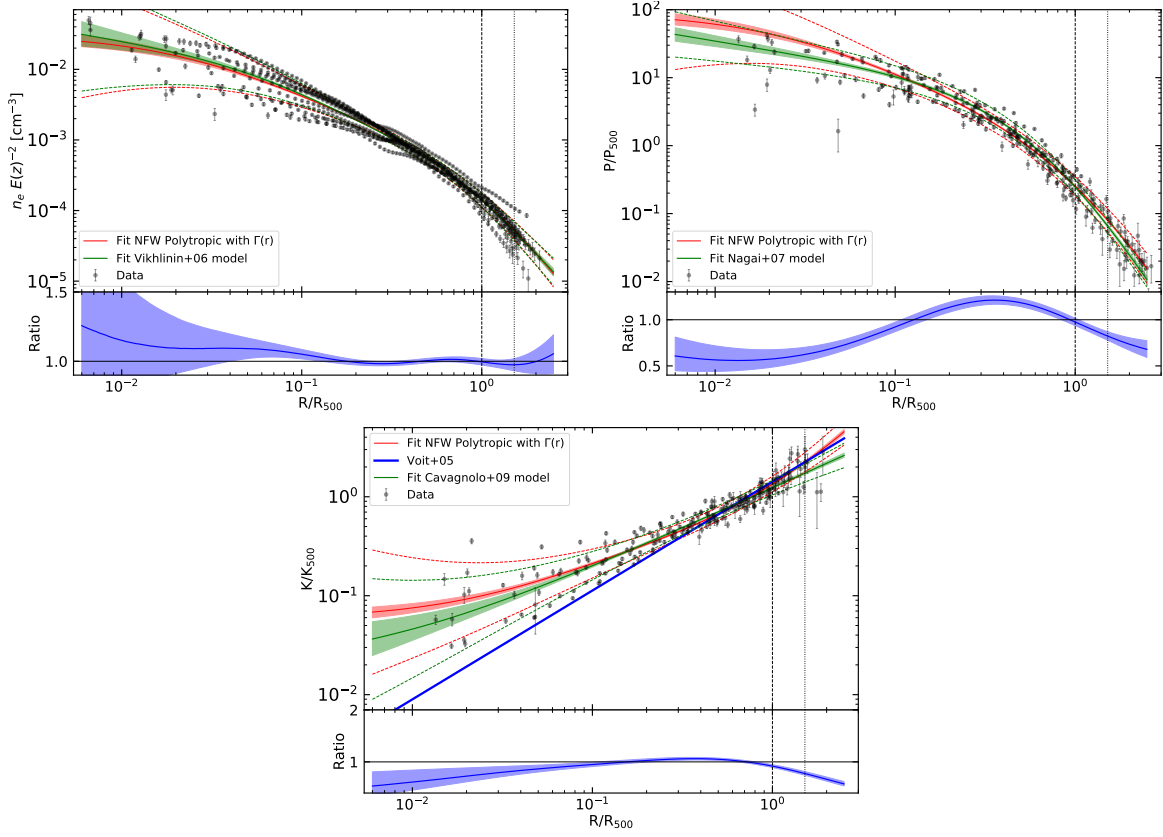


Fig. 8.6 Density (*top left*), pressure (*top right*), and entropy (*bottom*) with the fit as in Ghirardini et al. (2018a) in green, and using the new NFW polytropic with $\Gamma(r)$ in red. The bottom panels show the ratio between the the two best fitting results.

8.3.2 Derivation of $\Gamma(r)$

We know that density should be written in the form:

$$\rho = \left(A \frac{\log(1+x)}{x} \right)^{\frac{1}{\Gamma-1}} \quad (8.19)$$

In the same way hydrostatic equilibrium equation (with an NFW potential) can be recasted by absorbing all constant term in a constant ‘ K ’, which does not just include physical constants but also the ‘ k ’ in the polytropic equation of state $P = k\rho^\Gamma$

$$K \frac{d}{dx} \left(\frac{\log(1+x)}{x} \right) = \frac{1}{\rho} \frac{d\rho^\Gamma}{dx} = \rho^{\Gamma-1} \frac{d}{dx} (\Gamma \log \rho) \quad (8.20)$$

As we have already seen, introducing Eq. 8.19 of Bulbul et al. (2010) we have an exact solution to HEE. However we insert it back but allowing Γ to be a function of x :

$$K \frac{d}{dx} \left(\frac{\log(1+x)}{x} \right) = A \frac{\log(1+x)}{x} \frac{d}{dx} \left[\frac{\Gamma}{\Gamma-1} \log \left(A \frac{\log(1+x)}{x} \right) \right] \quad (8.21)$$

By moving the term in front of the right derivative to the left:

$$\frac{K \frac{d}{dx} \left(\frac{\log(1+x)}{x} \right)}{A \frac{\log(1+x)}{x}} = \frac{d}{dx} \left[\frac{\Gamma}{\Gamma-1} \log \left(A \frac{\log(1+x)}{x} \right) \right] \quad (8.22)$$

and remembering that $\frac{1}{f} \frac{df}{dx} = \frac{d \log(f)}{dx}$

$$\frac{K}{A} \frac{d}{dx} \left[\log \left(\frac{\log(1+x)}{x} \right) \right] = \frac{d}{dx} \left[\frac{\Gamma}{\Gamma-1} \log \left(A \frac{\log(1+x)}{x} \right) \right] \quad (8.23)$$

therefore by integrating both left and right this equation and adding an integration constant we have:

$$\frac{K}{A} \left[\log \left(\frac{\log(1+x)}{x} \right) \right] + \log(C) = \left[\frac{\Gamma}{\Gamma-1} \log \left(A \frac{\log(1+x)}{x} \right) \right] \quad (8.24)$$

and moving all the Γ terms to one side we have:

$$\frac{\Gamma}{\Gamma-1} = \frac{K \log \left(C \frac{\log(1+x)}{x} \right)}{A \log \left(A \frac{\log(1+x)}{x} \right)} \quad (8.25)$$

which can be rearranged into:

$$\Gamma = \frac{1}{1 - \frac{A \log \left(A \frac{\log(1+x)}{x} \right)}{K \log \left(C \frac{\log(1+x)}{x} \right)}} \quad (8.26)$$

We notice that without introducing the integration constant $\log(C)$, the final solution for Γ would have just been a constant value:

$$\Gamma = \frac{1}{1 - \frac{A}{K}}. \quad (8.27)$$

8.4 Conclusions

We present the relation between the ICM pressure and density in the outskirts of 12 SZ-selected galaxy clusters observed with *XMM-Newton* and *Planck* for the *XMM-Newton* Cluster Outskirt Project (X-COP, Eckert et al., 2017a). We use their radial profiles as recovered in Ghirardini et al. (2018a), and investigate the polytropic relation between them, $P \propto n^\Gamma$, and the dependence of the slope on the radius.

Our main results are:

- we identify a core region by identifying the transition where the slope of the effective polytropic index Γ changes from the inner value of ~ 0.8 to the outer value of ~ 1.2 , both in gas density and in radius; this core is defined by the region where the gas density is larger than $(2.45 \pm 0.46) \cdot 10^{-3} \text{cm}^{-3}$, or the radius is $< 0.19(\pm 0.04)R_{500}$;
- pressure and density are tightly correlated; beyond the core, they are well represented by a single power-law with index $\Gamma = 1.17 \pm 0.01$;
- relying on the tight single power-law relation between pressure and density in the outskirts of the X-COP clusters, and using the NFW mass model (Navarro et al., 1997), which is the one which best reproduces the observed thermodynamic quantities assumed to be in hydrostatic equilibrium (see Ettori et al., 2018), we adopt the model introduced by (Bulbul et al., 2010) to fit the thermodynamic quantities; we find that this model fits the observed quantities slightly better than the models found in the literature, with the advantage of being physically motivated and with parameters with important physical interpretations;
- having demonstrated that the relation between gas pressure and density is tight and is well described by a functional form, see Eq. 8.7, we can also reduce the application of the hydrostatic equilibrium equation to recover a gravitational mass profile to the more simple exercise to measure the density gradient at some specific radius; indeed, from equation 1.17, we can write

$$\frac{dP_e}{d\rho_e} \frac{d \log n_e}{d \log(r)} = - \frac{GM(< r)}{r}, \quad (8.28)$$

where $dP_e/d\rho_e$ is obtained from our functional form and what is missing is the gradient of the gas density.

**ENTROPY AND PRESSURE PROFILES IN
X-RAY GALAXY CLUSTERS AT $z > 0.4$**

9.1 Introduction

In this chapter, we use the results of the analysis of the mass distribution in a sample of 47 galaxy clusters in the redshift range 0.405–1.235 presented in Amodeo et al. (2016) in order to study the radial shape of some thermodynamic properties, in particular pressure and entropy, at different redshifts, looking for deviations from the self-similar behaviour (Voit et al. (2005) and Arnaud et al. (2010)), and in particular looking for a possible evolution with cosmic time.

The chapter is organized as follow: in Sect. 9.2, we present the method we applied to reconstruct the entropy and pressure profiles, and how we model their radial dependence. The data analysis is detailed in Sect. 9.3, with an exhaustive discussion of our results presented in Sect. 9.4. We draw our Conclusions in Sect. 9.5.

In the present study, we assume a flat Λ CDM cosmology, with matter density parameter $\Omega_M = 0.3$ and an Hubble constant of $H_0 = 70 \text{ km s}^{-1} \text{ Mpc}^{-1}$. All the quoted statistical uncertainties are at 1σ level of confidence.

9.2 The method to reconstruct $K(r)$ and $P(r)$

In Figure 9.1, we show the redshift and mass distributions of the objects in our sample, with 9 systems at $z > 0.8$ and 8 with an estimated M_{500} larger than $2 \times 10^{15} M_\odot$. Being massive objects, the relatively long *Chandra* exposure time ($t_{exp} > 75 \text{ ksec}$) considered for each cluster permits to extract at least 4 independent spectra over the cluster's emission which allows to make a complete X-ray analysis as it is usually done for low redshift clusters (see Amodeo et al., 2016, for details on the sample selection and X-ray analysis).

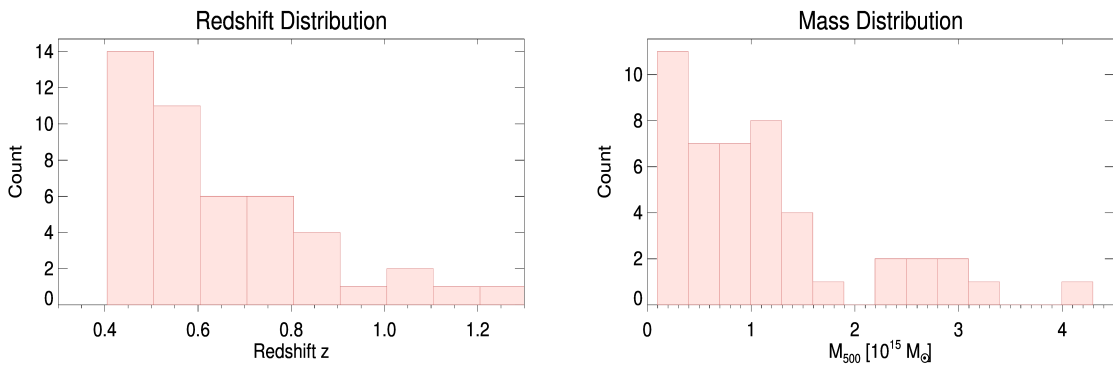


Fig. 9.1 Redshift (left) and total mass (right) distribution of the clusters in our sample.

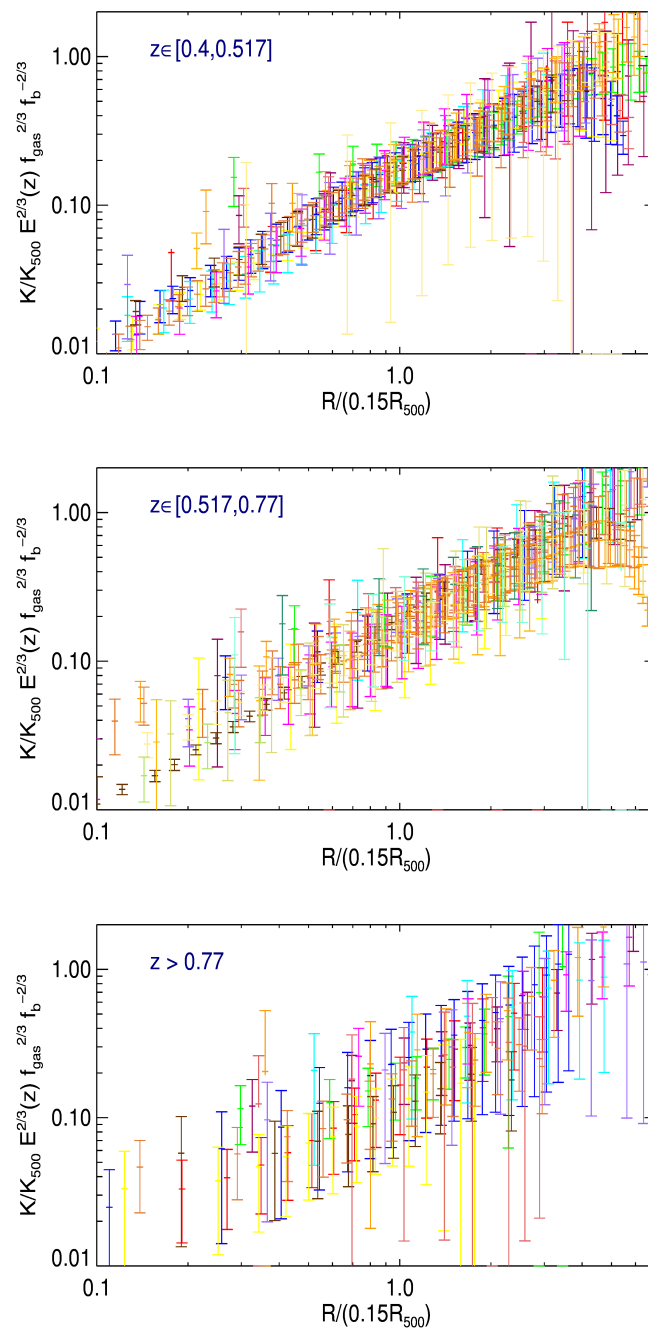


Fig. 9.2 Entropy profiles measured in the three redshift bins considered. Each color represents data from a single cluster.

In Amodeo et al. (2016), we present the method applied to constrain the mass distribution of the galaxy clusters in our sample under the assumption that a spherically symmetric ICM is in hydrostatic equilibrium with the underlying dark matter potential. The backward method

adopted (see Ettori et al., 2013a) allows to constrain the parameters of a mass model, i.e. the concentration and the scale radius for a NFW model (Navarro et al., 1997), using both the gas density profile, obtained from the geometrical deprojection of the X-ray surface brightness profile, and the spatially resolved spectroscopic measurements of the gas temperature. As by-product of the best-fit mass model, we obtain the 3D temperature profile associated to the gas density measured in each radial bin. In other words, we obtain an estimates of the ICM temperature in each volume's shell where a gas density is measured from the geometrical deprojection of the X-ray surface brightness profile in such a way that, inserting the temperature and density profiles into the hydrostatic equilibrium equation, the best-fit mass model is reproduced. From the combination of these profiles, the thermodynamical properties, like pressure and entropy, are recovered.

In our study, we consider also a rescaling dependent on the halo's mass. To apply this, we measure the quantities of interest over the cluster's regions defined as overdensity Δ with respect to the critical density of the universe $\rho_c \equiv \frac{3H^2(z)}{8\pi G} = \frac{3H_0^2}{8\pi G} E^2(z) \approx 136 \frac{M_\odot}{\text{kpc}^3} E^2(z)$, where $E(z) \equiv H(z)/H_0 = [\Omega_M(1+z)^3 + \Omega_\Lambda]^{1/2}$. In the following analysis, we choose $\Delta = 500$, considering that our profiles do not extend much further than R_{500} . By definition, M_{500} is then equal to $4/3\pi 500\rho_c R_{500}^3$. Following Voit et al. (2005), temperature, entropy and pressure associated to this halo's overdensity are, respectively:

$$\begin{aligned}
 k_B T_{500} &= 10.3 \text{ keV} \left(\frac{M_{500}}{10^{15} h^{-1} M_\odot} \right)^{2/3} E(z)^{2/3} \\
 P_{500} &= 1.65 \cdot 10^{-3} \text{ keV cm}^{-3} \left(\frac{M_{500}}{3 \cdot 10^{14} M_\odot} \right)^{2/3} E(z)^{8/3} \\
 K_{500} &= 103.4 \text{ keV cm}^2 \left(\frac{M_{500}}{10^{14} M_\odot} \right)^{2/3} E(z)^{-2/3} f_b^{-2/3} \\
 K(R)/K_{500} &= 1.42 \left(\frac{R}{R_{500}} \right)^{1.1},
 \end{aligned} \tag{9.1}$$

where the radial dependence of K has been here rescaled from $\Delta = 200$ to 500 using the ratio $\frac{R_{500}}{R_{200}} \approx 0.66$ as predicted from a NFW for massive systems.

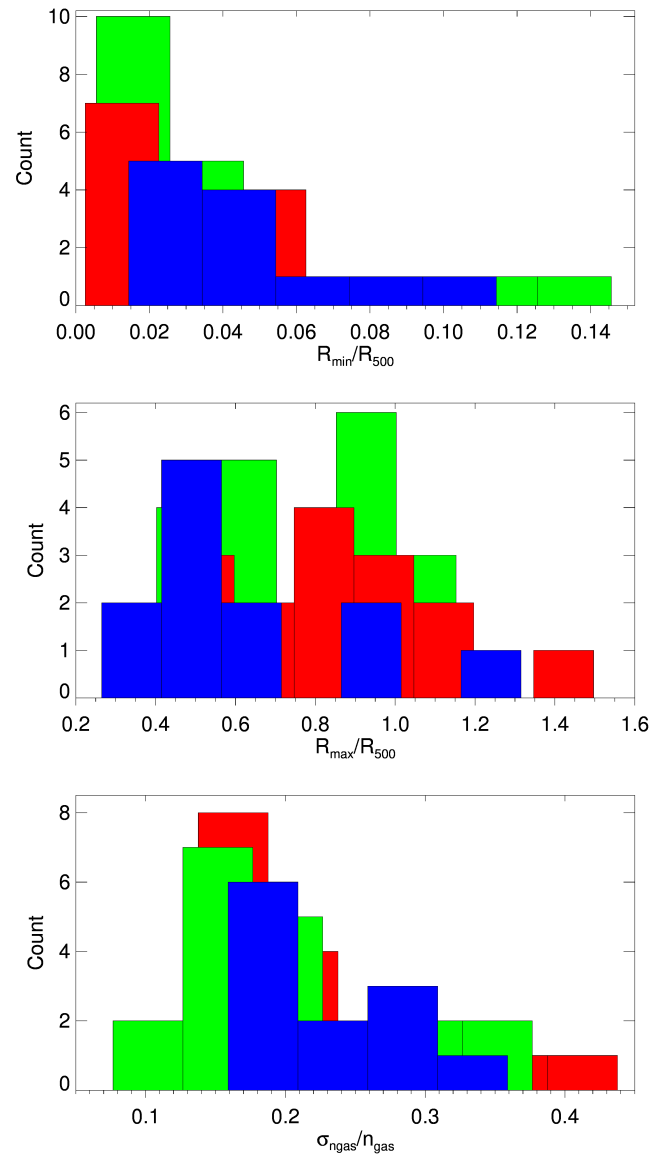


Fig. 9.3 Distribution of the rescaled innermost (Top) and outermost (Middle) radial spatial bin color coded with redshift. (Bottom) Distribution of the median relative error on gas density.

9.3 Data Analysis

The gas density profiles in our sample cover the median radial range of $[0.04 R_{500} - 0.76 R_{500}]$, with a mean relative error of 21%; for the complete distribution of minimum radius, maximum radius and relative error we refer to Fig. 9.3. We point out that half of the clusters have a radial extent which stops before reaching $0.77 R_{500}$.

Because of the poor statistic of each single profile, we combined them. First, we have extrapolated the data using the best-fit power law plus a constant for the entropy profile, and the functional introduced by Nagai et al. (2007) for the pressure profile, in order to have at least one point in each radial bin, chosen logarithmically with an increment of 1.14¹, over the range $[0.015R_{500}, R_{500}]$. We have then calculated the value of the thermodynamical quantities in the extrapolated radial points. The error associated to each radial point is the sum of the fitting error plus the mean error on the data.²

Furthermore, to investigate the average behaviour of these profiles as function of redshift, we divided the dataset into 3 redshift bins, chosen in order to have approximatively the same number of clusters: 15 objects with $z \in [0.4, 0.52]$; 20 clusters with $z \in [0.52, 0.77]$; 12 systems with $z > 0.77$. In each redshift bin, the profiles are stacked using the inverse of the $1 - \sigma$ error as weights, meaning that at each radial point the weighted mean is:

$$\langle x \rangle = \frac{\sum w_i x_i}{\sum w_i} \text{ with } w_i = \sigma_i^{-2}$$

where x refers to the logarithm of the considered thermodynamic quantities, which in our case can be pressure or entropy. This ‘‘stacking’’ procedure ensures an higher statistical significance of the measured entropy and an higher precision associated to the best-fit parameters of the functional forms adopted.

9.3.1 Fitting procedure for the entropy profile

In Figure 9.2, we show the reconstructed entropy profiles, rescaled as described below, of the 47 clusters in our sample.

A power law, with a constant to reproduce the inner value representing the net effect of the combined action of the central cooling and heating feedbacks (see Cavagnolo et al. (2009)), has been widely used to describe the radial behaviour of the entropy distribution:

$$K = K_0 + K_{100} \left(\frac{R}{100 \text{ kpc}} \right)^\alpha \quad (9.2)$$

This functional form has an underlying physical sense when we rescale with 100 kpc, since typically deviations from non-radiative simulations are seen below this radius, where cool core clusters and not cool core clusters actually differ. K_0 has the meaning of central entropy, which has been used in several work (i.e. Cavagnolo et al. (2009) Voit et al. (2005),

¹The increment of 1.14 has been chosen to guarantee a proper radial coverage

²The mean error on the data is just the mean value of the errors associated to the data points.

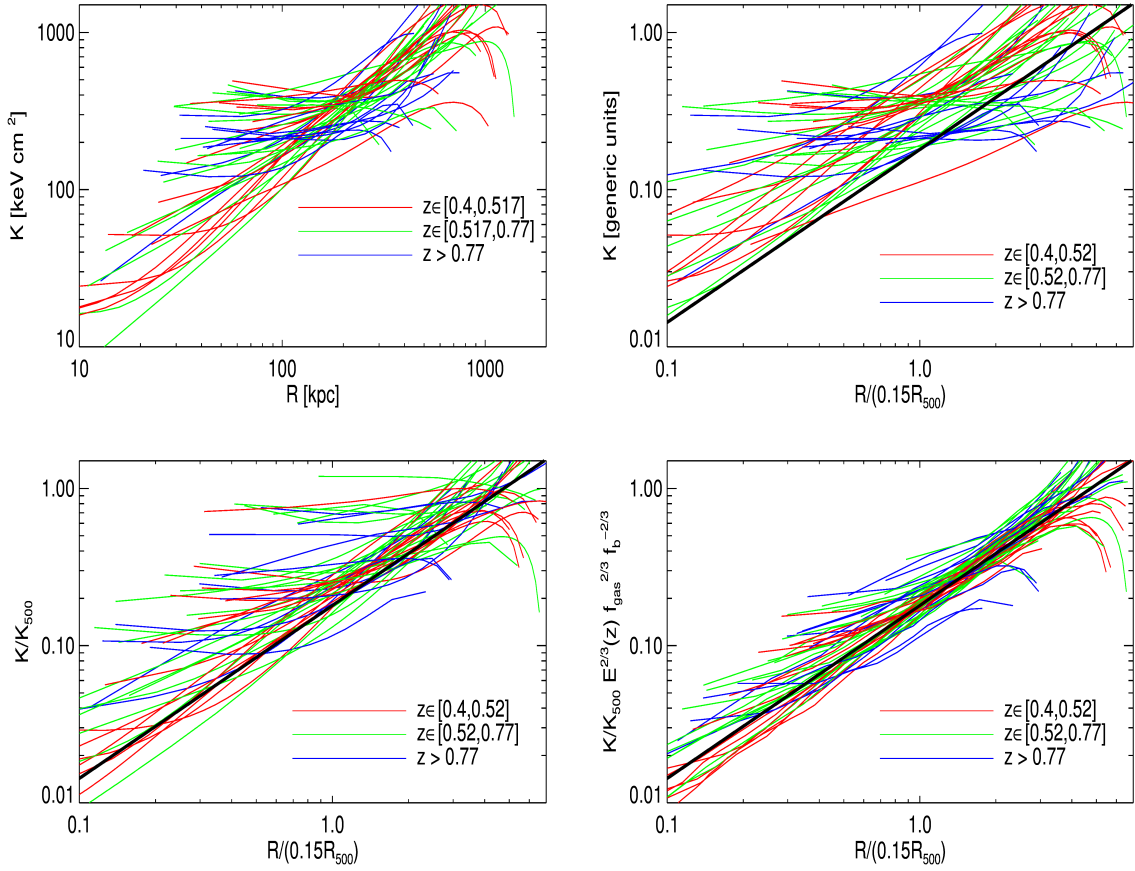


Fig. 9.4 The complete sample of our data has been plotted color coded with respect to redshift. We can see the effect of rescaling from top to bottom, from largely scattered data to coherent ones. No error bars are drawn for sake of clarity.

McDonald et al. (2013)) to discriminate between relaxed Cool-Core clusters, with $K_0 \sim 30$ keV cm², and disturbed non-CC systems, with $K_0 > 70$ keV cm².

We have also considered a functional form where the inner properties refers to $0.15R_{500}$ to rescale more properly the dimension of the core in systems at different mass and redshift:

$$\frac{K}{K_{500}} = K'_0 + K'_{0.15} \left(\frac{R}{0.15R_{500}} \right)^{\alpha'} . \quad (9.3)$$

As shown in Pratt et al. (2010), we expect the scatter among clusters' entropy profiles to be suppressed even more when the renormalization includes both the global and the radial

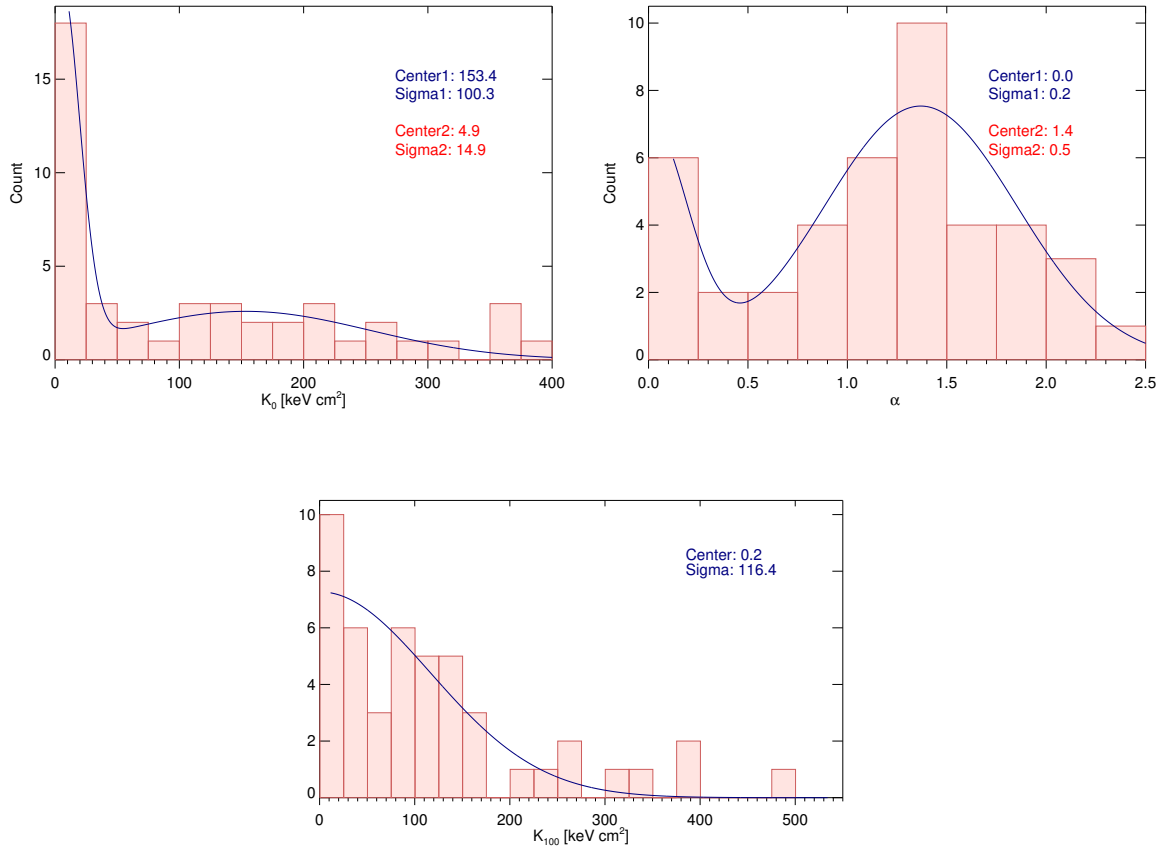


Fig. 9.5 Here we see the distributions of the fitting parameters of Eq.(9.2) for all clusters.

dependence on the gas mass fraction:

$$E(z)^{2/3} \frac{K}{K_{500}} \left(\frac{f_{gas}}{f_b} \right)^{2/3} = K_0'' + K_{0.15}'' \left(\frac{R}{0.15R_{500}} \right)^{\alpha''}, \quad (9.4)$$

where f_b is fixed to 0.15.

In Figure 9.4 we show how our refinement in the rescaling procedure of the entropy profiles, from “no rescaling” at all to the inclusion of the dependence upon the gas fraction (see Equation 9.4), reduces the scatter among the profiles, improving the agreement with the self-similar prediction (Voit et al., 2005).

9.3.2 No rescaling

In the first panel of Figure 9.4 we plot all the entropy profiles without applying any rescaling, meaning that on the x-axis we see the actual physical size in kpc and on the y-axis the entropy

in keV cm^2 . We call this kind of data “raw data”, because the physical values are reported without any rescaling. We point out that the clusters in our dataset had many different thermodynamic histories because they have very different shape for the entropy profiles which do not indicate any presence of self-similarity.

We fit all the entropy profiles using Equation 9.2, in order to look at the occupation of the parameter space in our sample. For each cluster we obtain a value for each one of the parameters K_0 , K_{100} and α and we plot all those values in Figure 9.5. For each one of the three histograms we tried to look for a best fit in the form of a single or a double gaussian. In this Figure we show only the fit with the lowest value of the χ^2 .

Regarding the parameter K_0 the best fit is obtained using two gaussians, with $\chi_{red}^2 = 2.5$. The best fit may indicate the presence of a bimodality, like Cavagnolo et al. (2009) found in their study, with a peak at 5 keV cm^2 and one at 160 keV cm^2 . However, as we are going to show in a following subsection, this bimodality is barely significant from a statistical point of view.

The distribution of the parameter K_{100} is better fitted by a single gaussian with $\chi_{red}^2 = 2.1$. The distribution of this parameter shows that renormalizing with respect to 100 kpc is a choice which makes sense considering the fact that the distribution of this parameter spans less than one order of magnitude.

Finally, in the last panel, we plot the distribution of the power law index α . We fit it with a double gaussian with $\chi_{red}^2 = 1.6$. The presence of two peaks is evident. One peak is at measured at 1.4, with a dispersion of 0.5, which is compatible with the non-radiative prediction (Voit et al., 2005).

9.3.3 Rescaling using K_{500}

Galaxy clusters have the same entropy profiles, in general all the thermodynamical properties, once we rescale them using a proper quantity. Non-radiative simulations (see Voit et al., 2005) have shown that we should rescale using quantities defined with respect to the critical density in order to achieve this. As it was stated above, we use an overdensity of 500, and rescale the entropy profile using K_{500} , defined in Eq. 9.1. We can observe the effect of the scaling in the third panel of Figure 9.4. The profiles we get are less scattered, even though the scatter is still quite high, about one order of magnitude. Nevertheless we observe that above $0.15R_{500}$ most of the clusters have a self similar behaviour. It is due to the fact that non gravitational processes are less relevant in the outskirts of galaxy clusters (Voit, 2005).

As described above, we rebin radially the data and we fit using Eq. (9.3). We show the rebinned data and the fitting results with their errors bars in Figure 9.6 and in top part of Table 9.1.

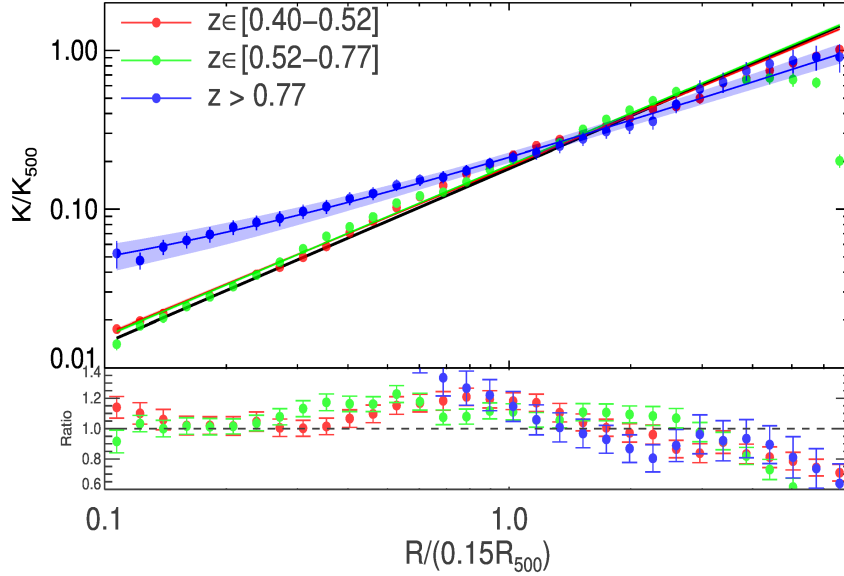


Fig. 9.6 Fits in the different redshift bins, the shaded area represents the errors on the fit. The colors of the points are representative of the redshift bin considered, blue for $z > 0.77$, green for $z \in [0.52 - 0.77]$ and red for $z \in [0.4 - 0.52]$.

As we can observe from the ratio between the data and the predicted profile, self-similarity is present below $0.5R_{500}$ for the two low redshift bins while it is reached only between $0.15R_{500}$ and $0.5R_{500}$ at high redshift ($z > 0.77$). Moreover the high redshift stacked profile is quite flatter than the others, with a slope of 0.85 ± 0.07 .

9.3.4 Rescaling using the gas fraction

The entropy distribution depends on baryon fraction with a mass (or equivalently, temperature) dependence. Consequently entropy has both a radial and global dependence in the gas fraction (Pratt et al., 2010). Correcting by this effect, data becomes compatible with the non-radiative prediction (Voit et al., 2005) and the dispersion drops dramatically.

A practical way to quantify the deviation from the self-similar prediction is shown in Figure 9.7. Here we see the behaviour of the entropy profiles at some specific radii ($0.15R_{500}$, R_{2500} and R_{1000}) with respect to the mass. It's clear that when the mass decreases the deviation from the self-similar prediction increases. Modelling this dependence with a simple power law we obtain a slope value which becomes smaller (in modulus) for large radii. We particularly point out that at the higher radius considered (R_{1000}), the profile is compatible with a flat profile, even though the influence of just 2 or 3 points makes the best fit slope of the fit slightly negative.

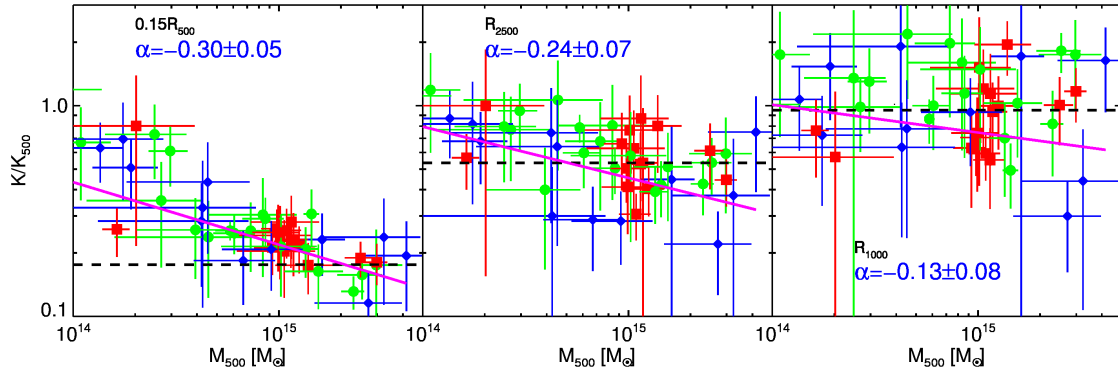


Fig. 9.7 Dimensionless entropy K/K_{500} as a function of mass M_{500} at different radii. Here the radii of $0.15R_{500}$, R_{2500} and R_{1000} have been used since we can measure directly this data point by interpolating the surrounding point to the specific radii. Whether radii as big as R_{500} are mostly extrapolated and therefore would not yield robust results and are therefore not shown. The black dashed curve is the prediction from self-similarity, and the magenta line is the best fit using a power law with index $-\alpha$

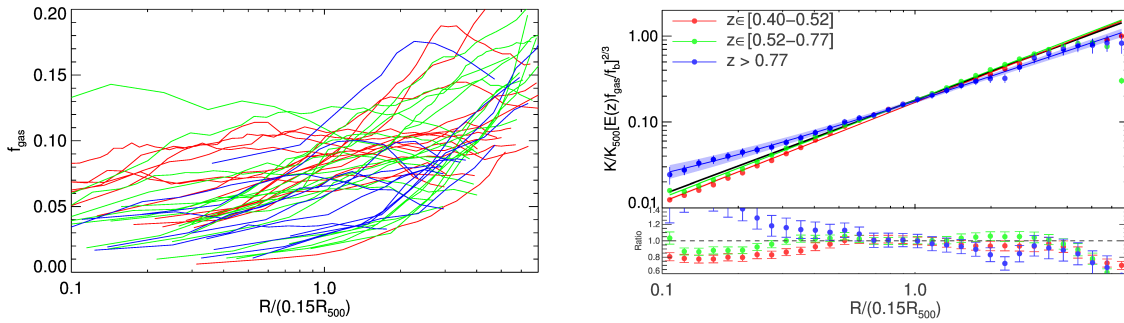


Fig. 9.8 (Left) Gas fraction profile for all our clusters. (Right) Fits in different redshift bins showing the errors on the fits using the shaded area. The blue profile ($z > 0.77$) is compatible with the low redshift profiles for intermediate radii ($R > 0.07R_{500}$) while at low radii there is a difference with the high redshift entropy profile having a flat profile.

The gas fraction f_{gas} is defined at each radial point as the ratio between gas mass and total mass ($f_{gas}(R) = m_{gas}(R)/M_{tot}(R)$) where the gas mass is the integrated density profile and the total mass is recovered from the hydrostatic equilibrium equation. Therefore the gas fraction, like entropy or pressure, can be directly reconstructed from the data and it is shown in Figure 9.8.

Therefore we renormalized the entropy profiles multiplying them by gas fraction profiles ($K \rightarrow K \times (E(z)f_{gas}(R)/f_b)^{2/3}$). The resulting profiles are visible in the last panel of Figure 9.4. The self similarity of the entropy profile is now finally clear in our dataset of clusters

Parameters of Eq. (9.3) and Figure 9.6

bin	$K'_{0.15}$	α'	K'_0	χ^2_{red}
$z \in [0.4, 0.52]$	0.185 ± 0.002	1.06 ± 0.01	0.000 ± 0.000	2.96
$z \in [0.52, 0.77]$	0.189 ± 0.002	1.08 ± 0.01	0.000 ± 0.000	3.25
$z > 0.77$	0.19 ± 0.01	0.85 ± 0.07	0.023 ± 0.009	0.65

Parameters of Eq. (9.4) and Figure 9.8

bin	$K''_{0.15}$	α''	K''_0	χ^2_{red}
$z \in [0.4, 0.52]$	0.169 ± 0.002	1.16 ± 0.01	0.000 ± 0.000	1.66
$z \in [0.52, 0.77]$	0.181 ± 0.002	1.14 ± 0.01	0.000 ± 0.000	1.30
$z > 0.77$	0.167 ± 0.007	1.00 ± 0.05	0.008 ± 0.004	0.31

Table 9.1 Values and errors on the parameters of the fits. For the bin $z > 0.77$ we have a value for the central entropy which indicates the presence of much more NCC systems at high redshift. The exponent α and the term K_{100} are compatible with the prediction of Voit et al. (2005). We also see that the goodness of the fit improves a lot when we correct by the gas fraction

at high redshift. At $0.15R_{500}$, for instance, the scatter is reduced by a factor ~ 3 when the rescaling by the gas fraction is applied.

We then stacked out profiles and we show the resulting entropy radial distribution in the right plot of Figure 9.8. We notice that the stacked profiles are compatible with the non-radiative prediction (Voit et al., 2005) in the radial range $[0.05R_{500}-0.7R_{500}]$, with the two low redshift stacked profile pushing this compatibility down to the lower limit of our analysis. Moreover at large radii, $R > 0.7R_{500}$, all the stacked profiles are flatter than the prediction, indicating some sort of flattening of the entropy profiles.

We fit the stacked entropy profiles with a power law plus a constant and we show the results in Figure 9.8 and in Table 9.1. We notice that the goodness of the fit has improved, with respect to the rescaling without gas fraction, and the parameters we get are closer to the non-radiative prediction.

The slope values we obtain for the two bins at low redshift are slightly larger than 1.1, indicating a profile steeper than the simulated one, in agreement with several recent work (Voit et al. (2005), McDonald et al. (2013), Morandi et al. (2007), Cavagnolo et al. (2009)). However for the highest redshift profile the situation is different, the value of the central entropy is not zero for the bin with the highest redshift, which seems to indicate a high average central entropy K''_0 . The implications of this results will be discussed later on.

9.4 Discussion

In the recent past the dichotomy between the two types of clusters, cool core clusters with a steep density profile and a drop of the temperature in the center, and non cool core clusters with a rather flat density profile and a flat temperature profile in the center, has been studied in numerous work. The particular shape of the density profile reflects in the behaviour of the entropy profile, where CC have a low entropy floor in the center while NCC have a higher one.

9.4.1 Self-similarity

Non-radiative simulations predict from several years that the thermodynamic properties of clusters of galaxies should be self-similar once rescaled to specific physical quantities. In the previous section we have shown that using a proper rescaling we reach self-similarity (see Fig. 9.2). Even when we regroup the data in radial bins, the self-similarity is preserved. However, only a proper rescaling using the gas fraction makes the agreement within 20% above $0.05R_{500}$. This is shown in the bottom panel of Figure 9.6 and 9.8, where we show the ratios between our rebinned data rescaled as indicated in Eq. 9.3 and 9.4, respectively, and the non-radiative prediction in Voit et al. (2005). We observe that, only in the high redshift bin, the rescaling by the gas fraction is needed to recover the self similar behaviour, that is reached between 0.1 and 0.7 R_{500} within 20% from the theoretical value.

The deviations present in the inner part of the profiles may be interpreted as some form of residual energy (Morandi et al. (2007)).

Even though the agreement with simulations is remarkable, we get slightly steeper entropy profiles, 1.15 ± 0.01 for the low redshift bins, while we get a flatter profile in the high redshift bin, with 1.00 ± 0.05 instead than 1.1. This is compatible with the results of Morandi et al. (2007), where they find an outer slope of the entropy profile between 1 and 1.18, while the agreement with the results of Cavagnolo et al. (2009) is excellent in the lower two redshift bins, in fact they have found the slope to be between 1.1 and 1.2. However for the high redshift bins, our results are compatible with both non-radiative predictions (Voit et al., 2005) and observations (Cavagnolo et al., 2009) at the 2σ level.

The excess with respect to Voit et al. (2005) self-similar prediction is present at low radii where most of our data are above the prediction. This extra entropy is more pronounced in low mass systems, as shown in Figure 9.7 and consistent with the results obtained by Pratt et al. (2010).

9.4.2 Angular resolution effect

In a thermalized system, low entropy gas sinks in the center while high entropy gas floats out in the outskirts, producing an entropy profile that increases monotonously with the radius. The net effect is that larger is the central bin considered for the analysis, higher will be the measured value of the entropy. In top panel of Figure 9.9, we plot the value of K_0 for each cluster against the radius of the innermost data point and measure an evident positive correlation (Pearson's rank correlation of 0.79, corresponding to a significance of 7.5×10^{-9} of its deviation from zero that is associated to the case with no correlation). This correlation becomes even more significant if we consider the same points rescaled by the halos' properties. This is shown in the bottom panel of Figure 9.9, where we measure a very significant Pearson's rank correlation of 0.87. A similar result was shown by Panagoulia et al. (2014): the smaller the innermost radial bin, the smaller the central entropy we measure.

However, as we show in Fig. 9.9, the correlation between the rescaled central entropy and the innermost radial bin does not reproduce the expected radial dependence from Voit et al. (2005), suggesting that the flattening has a different origin from the lack of spatial resolution.

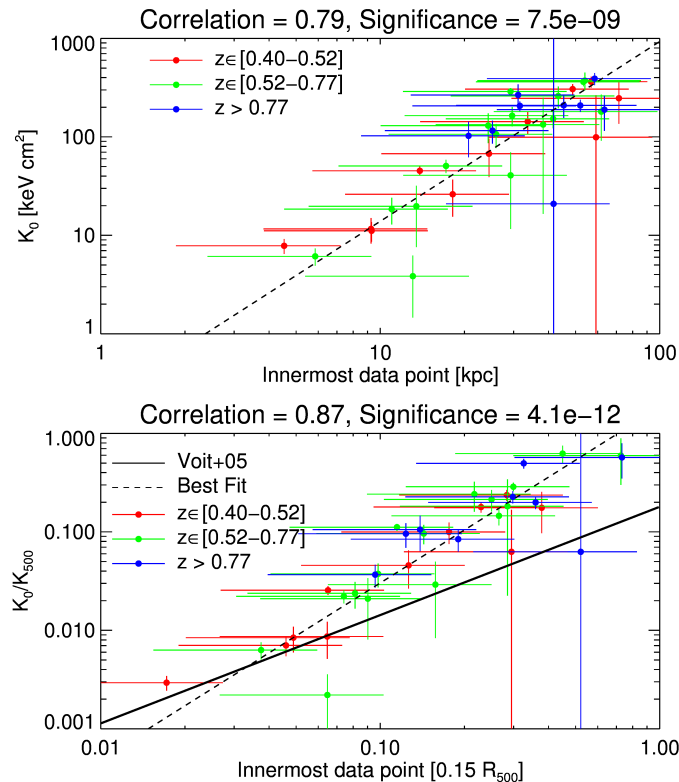


Fig. 9.9 (Top) Central entropy versus the innermost data point. A clear positive correlation is measured. (Bottom) Central entropy versus innermost data point rescaled, an even tighter correlation is present.

9.4.3 Bimodality

Cavagnolo et al. (2009) have shown that the distribution of the values of the cluster central entropy reflects the dichotomy between cool-core and non-cool-core clusters, finding two distinct populations with peaks at 15 keV cm^2 and 150 keV cm^2 . This bimodality has not been confirmed in later work (e.g. Pratt et al., 2010; Santos et al., 2010).

In our work we try to verify the presence of bimodality in the central entropy distribution. In top panel of Figure 9.5, we show the distribution of K_0 . Since we have not many clusters we make a 10000 steps bootstrap of our distribution randomizing the choice of the clusters to be used (allowing repetition). This will allow us to determine whether a bimodal distribution fits our data significantly better than a unimodal one. Therefore at each step of the bootstrap we fit the distribution with a single gaussian and with two gaussians, by comparing their reduced χ^2 we get that 98% of the times the double gaussian fits better than the single one. However this is not a surprise and it is not even what we are looking for to prove the bimodality, but is just an expected result since increasing the the number of fitting parameters should also increase the goodness of the fit. We investigate whether this change of the fit gives a significant improvement in the fitting process.

In order to do this we execute at each step an F-test. This test gives the significance of the improvement in the fitting process. Among the 10000 bootstraps we get a mean value for this test of 0.79 with a dispersion of 0.14, therefore failing to go beyond the 95% required to be a significant improvement. Even though the bimodality cannot be proven, about 10% of the bootstrapped replica of the F-test has proved self similarity, with a significance higher than 95%, these are false positive, which are typical for a bootstrap analysis.

In Figure 9.10 the effect of redshift on the distribution of the central entropy is shown. Due to the small number of clusters in each redshift bin we are not able to prove any evolution of the central entropy with redshift: the number of clusters in each redshift bin is too small to make an accurate statistical analysis. However we report that we have some indication that a well defined evolution may be present.

At high redshift we have a moderate peak at low entropy which represents the cool-core systems, and a quite concentrated peak at about 200 KeV cm^2 which contains half of the clusters at this redshift. In the intermediate redshift bin we have a slightly bigger peak at low entropy and the rest of the distribution is basically flat. At low redshift we just have one peak at low entropy with no other significative peaks.

There is evidence of evolution from many NCC systems at high redshift toward mostly relaxed CC clusters at low redshift. We point out that due to the poor statistic of the sample we are not able to prove this scenario using statistical tests.

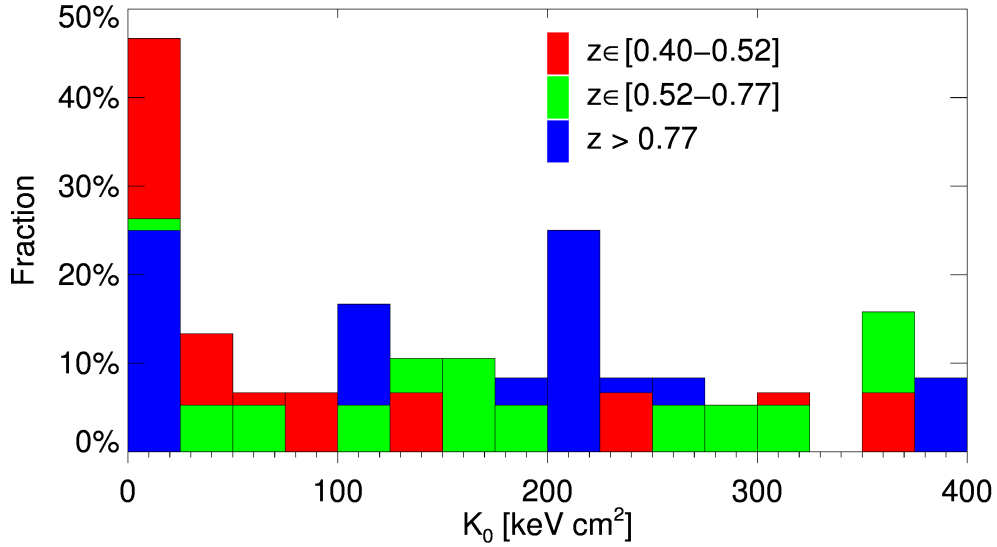


Fig. 9.10 Evolution of the central entropy distribution with redshift. We can clearly see an evolution with evidence of bimodality at high redshift.

9.4.4 Evolution with redshift

We observe an evolution with redshift of the entropy within the central region ($r < 0.1R_{500}$). It suggests that the entropy profiles were flatter at high redshifts in massive objects. However this does not resemble an evolution in the entropy profiles or in the cooling properties of the gas, but it is a confirmation of some results in the cited work above: at $z > 0.77$ the clusters in our dataset are not able to develop a cool core like their low redshift counterparts do, meaning that cool cores were less common in the past. Several studies (e.g. McDonald, 2011; McDonald et al., 2013; Santos et al., 2008, 2010; Vikhlinin et al., 2007) have investigated recently the evolution of the cool-core-ness of clusters, finding that at high redshift there is a lower relative abundance of cool-cores, in particular of the strongest ones.

To characterize our finding we adopt the threshold found by Cassano et al. (2010), using the morphological parameters centroid shift w and the concentration c_{SB} , taken from Amodeo et al. (2016), we classify the clusters with $w < 0.012$ and $c_{SB} > 0.2$ to be relaxed. We point out that 50% of clusters at $z > 0.77$ are not relaxed.

We combine this information, visible in Figure 9.11, together with the evolution of the central entropy distribution, visible in Figure 9.10 to assert that in the low redshift bins 60% of clusters are CC, percentage which reduces to 30% and 25% in the intermediate and high redshift bins respectively.

This result should not be a surprise from the point of view of the hierarchical growth of structure, because at high redshift ($z \sim 1$) clusters were in the middle of their formation

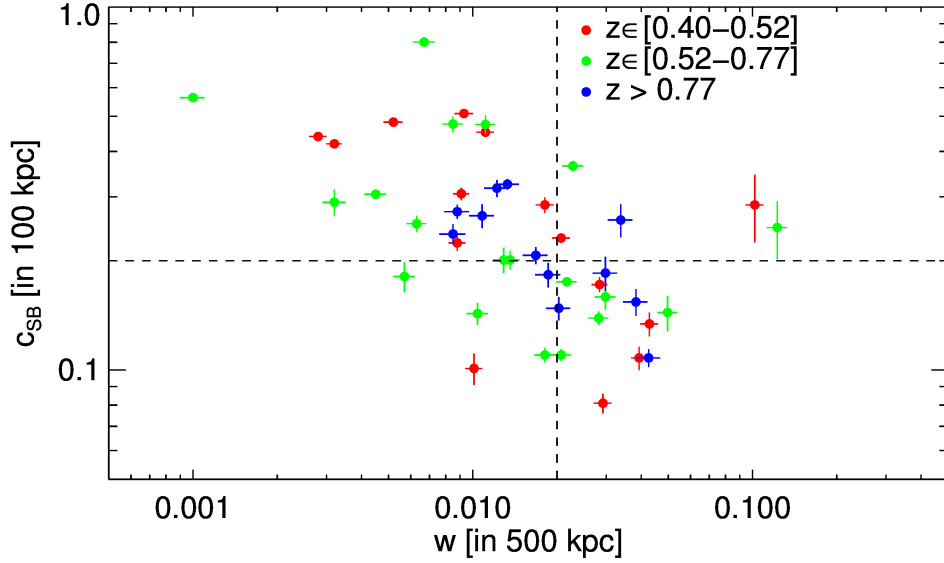


Fig. 9.11 Morphological parameters distribution in the plane of w versus concentration c_{SB}

history and cool core could have easily been destroyed by one of the many merger events, or not even built, if they did not have enough time to relax in the center. Moreover, it is remarkable that even in a X-ray selected sample, like the one we are studying, we get much more NCC than CC. In fact X-ray signal depends on the gas density squared, and therefore it is easier to see a cluster with a peaked density, like the cool core ones.

9.4.5 Pressure

For the same dataset, we study the behaviour of the electronic pressure profile $P(r) = n_e(r) T(r)$.

A generalized NFW profile, as introduced by Nagai et al. (2007), has been widely used to study the radial rescaled pressure profile, resulting in precise best fitting parameters which represents the “universal pressure profile” (see Arnaud et al., 2010).

$$\frac{P(x)}{P_{500}} = \frac{P_0}{(c_{500}x)^\gamma [1 + (c_{500}x)^\alpha]^{\frac{\beta-\gamma}{\alpha}}} \quad (9.5)$$

where $x = R/R_{500}$ and γ , α and β are respectively the central slope, the intermediate slope and the outer slope defined by a scale parameter $r_s = R_{500}/c_{500}$ ($R \ll r_s$, $R \sim r_s$ and $R \gg r_s$ respectively). The best fitting parameters found by Arnaud et al. (2010) were $[P_0, c_{500}, \gamma, \alpha, \beta] = [8.403, 1.177, 0.3081, 1.0510, 5.49]$

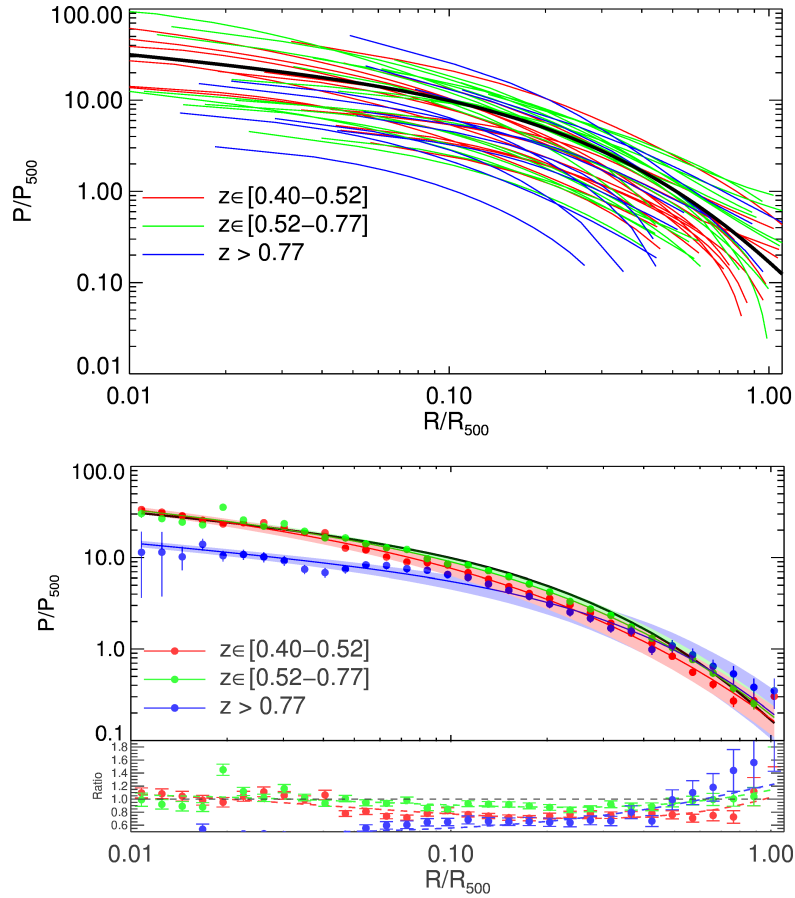


Fig. 9.12 (Top) Pressure profiles for all our clusters rescaled using an overdensity of 500 (color coded with respect to the redshift bin each curve belong, indicated in Figure), compared with the best fit of Arnaud et al. (2010) (black solid line). (Bottom) Stacked pressure profiles (in logarithmic space) compared with the best fit of Arnaud et al. (2010); For the two low redshift bins the agreement with the “universal” pressure profile spans the whole radial range consider in the analysis while for the high redshift bin there is a good agreement only in the outskirts ($R > 0.1R_{500}$).

Pressure is the quantity less affected by the thermal history of the cluster (Arnaud et al., 2010). Indeed McDonald et al. (2014) found no significant evolution of the pressure profile in the analysis of SPT SZ-selected clusters, just a mild flattening of the profile below $0.1R_{500}$. Battaglia et al. (2012), however, suggested from the analysis of cosmological hydrodynamical simulations that a significant evolution of the pressure profile should occur beyond $z = 0.7$, and only outside R_{500} , as consequence of the increasing non-thermal support toward the outskirts of galaxy clusters.

In order to fit our data we use the functional form introduced by Nagai et al. (2007) with the parameters β and γ fixed to the fiducial value found in the work of Arnaud et al.

(2010). We decided to fix these parameters because they are degenerate, and therefore fixing at least one of the slopes is advised in order to have tighter parameters distribution and better comparison (Arnaud et al., 2010).

The pressure profiles are plotted in the top panel of Figure 9.12, with the curve of the universal profile in order to compare. All the profiles show a very similar shape, surrounding the “universal” one from both sides with an apparent discrepancy only in the normalization of the profiles. At each radius the scatter is of about one order of magnitude.

We applied the same procedure described above in the analysis of the entropy profiles on these pressure profiles. We obtain that the stacked curves in the two low redshift bins are compatible with the “universal” pressure profile at all radii and the best fit on these stacked data points comprehend the Arnaud et al. (2010) result in all radii.

On the other hand the high redshift scaled profile is about 25% below the “universal” pressure profile at intermediate radii, $0.07R_{500} < R < 0.7R_{500}$, while the best fit is compatible at any radii above $0.1R_{500}$. For the inner part of these profile we observe a distinctive flattening below $0.1R_{500}$ (Figure 9.12).

Pressure is indeed a thermodynamic properties that is only very little affected by the thermodynamic history of clusters. The observed flattening at high redshift and low radii was also observed in the work of McDonald et al. (2014) and can be easily explained by the little presence of CC clusters at high redshift.

In Table 9.2 we show the best fit of Equation 9.5 where we have kept β and γ fixed to the “universal” pressure profile best fit. We obtain a quite good fit in all the three redshift bins; only the normalization of this functional in the high redshift bin shows a distinct discrepancy with the results of Arnaud et al. (2010). In fact from the bottom panel of Figure 9.12 is evident that the low redshift bins points are almost on top of the “universal” profile, while the high redshift ones are compatible only above $0.1R_{500}$, and below this threshold the discrepancy grows to be factor 2 at $0.01R_{500}$.

Parameters of Eq. 9.5						
bin	P_0	c_{500}	γ	α	β	χ_{red}^2
$z \in [0.4, 0.52]$	8.9 ± 0.3	0.67 ± 0.07	0.308	0.71 ± 0.03	5.49	1.82
$z \in [0.52, 0.77]$	8.6 ± 0.2	0.86 ± 0.07	0.308	0.85 ± 0.03	5.49	2.25
$z > 0.77$	3.4 ± 0.1	0.89 ± 0.17	0.308	1.14 ± 0.12	5.49	1.47
Universal	8.403	1.177	0.308	1.0510	5.49	–

Table 9.2 Values and errors on the parameters of the fits for pressure. We leave β and γ frozen to their “universal” value in order to have better chances at comparing the results. The goodness of the fit is quite decent. The value of the parameters are not too far away from the “universal” results of Arnaud et al. (2010) considering how degenerate they are. We point out that the parameter P_0 for the high redshift bin is significantly smaller than both the other bins and the “universal” value.

9.4.6 Polytropic index

The polytropic index γ , equal to the ratio of specific heats C_P/C_V for an ideal gas, is a common proxy when evaluating the physical state of the gas. It is defined as

$$P_e = \text{const} \cdot n_e^\gamma \quad (9.6)$$

and therefore gives informations about the thermal distribution of the gas, with values of γ expected to be in the range $[1, 5/3]$, with the two extreme values indicating, respectively, an isothermal gas, where thermal conduction is fast enough, and an isentropic gas, when the gas is well mixed and the gas entropy per atom is constant.

The hierarchical growth of structure has several implications on the $c(M, z)$ relation: systems with higher masses are less concentrated and lower concentrations are expected at higher redshifts (e.g. Muñoz-Cuartas et al. (2011)). In the theoretical work of Komatsu and Seljak (2001) they have found a linear relation between concentration and adiabatic index assuming a constant baryon fraction at large radii. Moreover Ascasibar et al. (2006) have shown that c and γ conspire to produce the observed scaling relations, matching the self-similar slope at many overdensities. Therefore studying the evolution of the adiabatic index with redshift and its relation with concentration is fundamental when trying to fully understand the hierarchical structure formation.

We estimate γ by fitting the pressure as function of the gas density with a power law. As a first step, it is calculated for each single cluster. Then, we evaluate the weighted mean in each bin. We also calculate γ for the stacked profiles. In left panel of Figure 9.13, we show

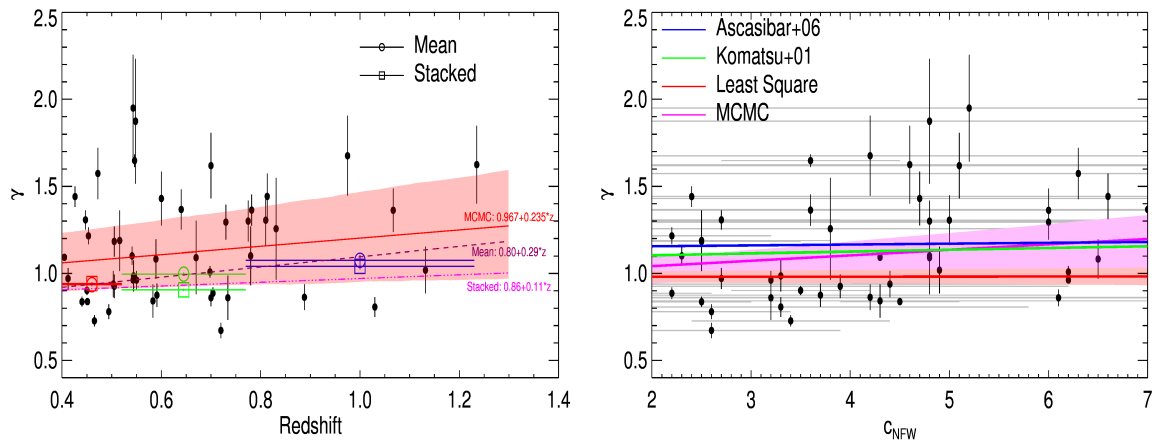


Fig. 9.13 (Left) Polytropic index for all clusters as function of redshift. Data are better fitted by a linear relation: the adiabatic index grows with redshift. (Right) Polytropic index for all cluster against concentration. γ grows with c_{NFW} steeper than what was previously estimated.

the polytropic index as a function of redshift. We measure a positive evolution with redshift, with larger values of γ (by more than $2-\sigma$) at higher redshift (see Table 9.3).

We have also looked for correlations between the polytropic index and the dark matter concentration as recovered from the best-fit with a NFW model in Amodeo et al. (2016). Ascasibar et al. (2006) and Komatsu and Seljak (2001) have shown that between concentration and polytropic index there is a linear relation with slope of 0.005 and 0.01 respectively. In the bottom part of Table 9.3 we fit the polytropic index as a function of concentration. We point out that the MCMC code result is a quite steep dependence, much steeper than what has been shown in the cited works. Nevertheless the uncertainty on the slope is important, 70% of the value. Moreover the intercept we get is much smaller than what has been previously calculated.

Polytropic index γ		
bin	Mean	Stacked
$z \in [0.4, 0.52]$	0.935 ± 0.008	0.942 ± 0.008
$z \in [0.52, 0.77]$	0.996 ± 0.009	0.906 ± 0.006
$z > 0.77$	1.076 ± 0.031	1.041 ± 0.018

$\gamma = \mathbf{m} \cdot \mathbf{z} + \mathbf{q}$		
Method	m	q
Chi-squared	0.05 ± 0.05	0.94 ± 0.03
MCMC	0.24 ± 0.22	0.97 ± 0.14
Mean	0.29 ± 0.05	0.80 ± 0.030
Stacked	0.11 ± 0.03	0.86 ± 0.02

$\gamma = \mathbf{m} \cdot \mathbf{c}_{\text{NFW}} + \mathbf{q}$		
-	m	q
Chi-squared	0.0004 ± 0.0057	0.98 ± 0.03
MCMC	0.031 ± 0.020	0.98 ± 0.09
Ascasibar+06	0.005 ± 0.002	1.145 ± 0.007
Komatsu+01	0.01	1.085

Table 9.3 (Top) Values and errors on the polytropic index for the three redshift bins considering the mean and stacked values. We observe evolution with a significance greater than $2-\sigma$. (Middle) Fit of left panel of Figure 9.13 using different methods. (Bottom) Fit of right panel of Figure 9.13 using different methods and comparing with other works.

9.5 Conclusion

From the sample described in Amodeo et al. (2016), which contains the largest collection of clusters at $z > 0.8$ homogeneously analyzed in their X-ray spectral properties, we have extracted the entropy and pressure profiles of 47 clusters observed with *Chandra* in a redshift range from 0.405 to 1.235.

We observed a higher values of the gas entropy in the central region at higher redshift, that we cannot explain as an effect due to the spatial resolution. A plausible explanation of this result is the fact that at high redshift we observe a lack of cool core clusters with respect to the low redshift sample.

Moreover at intermediate radii, between $0.1R_{500}$ and $0.7R_{500}$, the self similarity is recovered when we use entropy dependent both on redshift and gas fraction. The best fit of the stacked profiles is very similar to the Voit et al. (2005) prediction from non radiative simulations.

We also show that the pressure profiles flattens at high redshift at radii below $0.1R_{500}$, with lower values, by about 50%, than the ones observed at $z > 0.5$.

Overall, these results suggest a scenario in which galaxy clusters are the last gravitationally-bound structures to form according to the hierarchical evolution. They start forming at $z \approx 3$, and at $z \sim 1 - 1.5$ they are still in the middle of their formation. A first implication of this, it is that cool core clusters would have been easily destroyed by merger events, or could not even have been build in time, reducing their relative number at earlier epoch. Moreover, the merging processes ongoing at high redshift would imply that objects at $z \sim 1$ are mostly unrelaxed, with a flatter entropy profile, that produces a clear excess in the inner parts and a deficit in the outskirts. As we show in Figures 9.6 and 9.8, high-redshift clusters have indeed a rather flat stacked entropy profile, supporting the evidence that the floating and sinking of the gas entropy has not been completed yet. The thermodynamical disturbed condition of the high-redshift systems is further supported from the observed flattening of thermal pressure in the inner part of the stacked pressure profile (see Fig. 9.12). Moreover there is evidence for evolution of the polytropic index with redshift and concentration, meaning that at $z \sim 1$ and in systems which are more concentrated, the gas possesses a slightly larger polytropic index, indicating that at high redshift the gas was slightly more isentropic, i.e. the entropy profiles were flatter, as observed.

SUMMARY AND CONCLUSIONS

10.1 Summary

In this thesis, we have extensively explored the properties of galaxy clusters in their outermost regions accessible to X-ray and SZ observations. We have thoroughly exploited the capabilities of *XMM-Newton* and *Planck* to recover at an unprecedented level the thermodynamic properties in the outskirts of galaxy clusters, ranging a very wide radial range, from $0.01R_{500}$ to $2 \times R_{500}$, constraining any statistical and systematic uncertainties to just a few percent over the entire cluster volume. This was possible thanks to the very accurate modeling of the *XMM-Newton* background, see Sect. 3.2, allowing to reduce the systematic uncertainties on the surface brightness profiles to an unprecedented level, smaller than $\sim 5\%$. The large extension of the SZ signal resolved by *Planck* also plays a very big role, extending well beyond the virial radius for these clusters, allows to have well resolved pressure profiles.

We have made use of the density profile corrected by clumpiness (Eckert et al., 2015), to recover the quantities we are interested in. The exquisite quality of these X-ray and SZ dataset enable us to constrain the hydrostatic mass with very high precision, with relatively small uncertainties ($\sim 5\%$ statistical and $\sim 10\%$ systematic), achieving an important level where the systematic uncertainties dominate over the statistical. We have applied hydrostatic equilibrium equation assuming a spherically symmetric distribution of both the ICM and of the dark matter, using mainly 2 methods and 5 mass models. We have demonstrated how the NFW mass profile (Navarro et al., 1996) is the best fit mass model for the majority of these systems, and for the remaining objects it is still indistinguishable from the best fitting mass model. Thus our reference masses are assumed to be the one recovered from the NFW *backward* method (Ettori et al., 2010; Ghirardini et al., 2018b). The applied *forward* method, which does not depend on any mass model, provides consistent results with the reference mass within $\lesssim 5\%$. For a subsample of X-COP, we quantified the discrepancy with masses estimated from other probes, like scaling relation applied to the SZ signal, weak lensing measurements, galaxy dynamics, obtaining an overall remarkable agreement with mean ratio between hydrostatic and other mass probes around 1.0 ± 0.2 (Ettori et al., 2018).

We have demonstrated how the thermodynamic properties of the ICM in a well SZ-selected sample of galaxy clusters are regular and self-similar in the outskirts. Density and pressure are consistent with previous determinations (Eckert et al., 2012; Planck Collaboration et al., 2013, respectively). In particular, the radial profile of the gas entropy is well in agreement with the predictions for entropy generation in galaxy clusters (Tozzi and Norman, 2001; Voit et al., 2005), out to the outermost radial point of our observations, at odds with conclusions generally reached from *Suzaku* observations (Walker et al., 2012b). We suggest that this difference is due to how gas clumping is treated and corrected for in our sample,

which however is not feasible for *Suzaku* given its large PSF. For the first time we have determined the scatter of each thermodynamic quantities as function of radius, showing a typical log-parabola shape. Surprisingly, we find that gas temperature, not pressure, is the least scattered quantity at nearly all radii.

The unprecedented very high data quality allows also for refined analysis, like the unique analysis in azimuthal sectors performed for Abell 2319, Sect. 4.5, which permits to study in detail the azimuthal variation of all the thermodynamic properties for this cluster, revealing clearly the strong deviation of the sectors in the North-West direction, where the merging is still active with clear observable effects. These range from an overall enhanced gas mass fraction to thermodynamic profiles very different from the self-similar expectations, i.e. flat pressure and density, and entropy below the prediction. The presented idea of correcting by the expected gas mass fraction alleviates a lot of tension, bringing pressure and density back in agreement with expectations.

If Abell 2319 has a very high non thermal pressure contamination, we have demonstrated how this is just the exception, because in the entire X-COP sample this cluster is the only one with enhanced gas mass fraction, with average non thermal pressure contamination in the order of $\sim 10\%$, lower than predicted in numerical simulation (Biffi et al., 2016; Nelson et al., 2014a). Nevertheless, recently Vazza et al. (2018) were able to reproduce this result in high-resolution simulations of galaxy clusters, by carefully disentangling the bulk motion from the small-scale turbulent motion. The median mass bias, obtained by comparing the reference hydrostatic masses with the one corrected by in X-COP, is about $1 - b = 0.85 \pm 0.05$, much different from the 0.58 ± 0.04 implied by *Planck* to reconcile CMB cosmology and SZ number counts (Planck Collaboration et al., 2014b, 2016f).

We have shown that the relation between density and pressure is very tight, with scatter of about 15%, and a clear slope change that allows to define core and outskirt regions, with discerning values of $n_0 \sim (2.45 \pm 0.46) \cdot 10^{-3} \text{cm}^{-3}$ for density, or $r_0 \sim (0.19 \pm 0.04)R_{500}$ for radius. Beyond the core ($n < n_0$ or $r > r_0$) the relation between pressure and density is well described by a single power law with index $\Gamma = 1.17 \pm 0.01$, close to the value predicted by numerical simulations (Capelo et al., 2012). Given that NFW is generally our best fitting mass model (Ettori et al., 2018) and given this single power law relation between pressure and density, i.e. a single polytrope, we adopt the model introduced by Bulbul et al. (2010) to fit all together all the thermodynamic quantities, finding a very good agreement with the observed quantities.

Future development for the X-COP project include the completion and submission of the paper on the polytropic state of the ICM, and the extension of the clumpiness profile to the entire X-COP sample, which until now has been done only for A2319. Furthermore, as

stated in Chapter 3, a few objects which fall under the X-COP selection criteria were initially excluded from the sample. The reason for exclusion for A754 and A3667 was that these are clear major mergers, and for A3827 because it has both an apparent size very close to our cut and is a merger along the line of sight (Carrasco et al., 2010). However with the analysis of A2319 we have demonstrated that it is possible to study these objects along several azimuthal directions, and that the data quality from *Planck* is very high and well resolved. Thus adding these three objects to the sample and analyzing them like in the case of A2319 is feasible, and future observations of A754, A3667, and A3827 have been accepted in proposal cycle AO-17 of *XMM-Newton*, even if in priority C.

10.2 Conclusions

The main findings of my work are the following:

- Given the exquisite quality of the X-ray and SZ datasets, their radial extension, and their complementarity, we identify the ongoing merger in Abell 2319 and how it is affecting differently the gas properties in the resolved azimuthal sectors. We have several indications that the merger has injected a high level of non-thermal pressure in this system: (i) the clumping free density profile is above the average profile obtained by stacking Rosat/PSPC observations; (ii) the gas mass fraction recovered using our hydrostatic mass profile exceeds the expected cosmic gas fraction beyond R_{500} ; (iii) the pressure profile is flatter than the fit obtained by the Planck Collaboration; (iv) the entropy profile is flatter than the mean profile predicted from non-radiative simulations; (v) the analysis in azimuthal sectors has revealed that these deviations occur in a preferred region of the cluster. All these tensions are resolved by requiring a relative support of about 40% from non-thermal to the total pressure at R_{200} .
- Our results on the entire X-COP sample indicate that once accreting substructures are properly excised, the properties of the ICM beyond the cooling region ($R > 0.3R_{500}$) follow remarkably well the predictions of simple gravitational collapse and require little non-gravitational corrections.
- The unprecedented accuracy of the hydrostatic mass profiles out to R_{200} allows us (i) to assess the level of systematic errors in the hydrostatic mass reconstruction method, (ii) to evaluate the intrinsic scatter in the NFW $c - M$ relation, (iii) to quantify robustly differences among different mass models, different mass proxies and different gravity scenarios.

- We find that hydrostatic masses require little correction and infer a median non-thermal pressure fraction of $\sim 6\%$ and $\sim 10\%$ at R_{500} and R_{200} , respectively. Our values are lower than the expectations of hydrodynamical simulations, possibly implying a faster thermalization of the gas. The high bias required to match *Planck* CMB and cluster count cosmology is excluded by the data at high significance, unless the most massive halos are missing a substantial fraction of their baryons.
- The entropy and pressure profiles in the high- z lie very close to the baseline prediction from gravitational structure formation. We show that these profiles deviate from the baseline prediction as function of redshift, in particular at $z > 0.75$, where, in the central regions, we observe higher values of the entropy (by a factor of ~ 2.2) and systematically lower estimates (by a factor of ~ 2.5) of the pressure. The effective polytropic index, which retains information about the thermal distribution of the gas, shows a slight linear positive evolution with the redshift and concentration of the dark matter distribution. A prevalence of non-cool core, disturbed systems, as we observe at higher redshifts, can explain such behaviours

10.3 Work produced

The work presented in this thesis has been presented in several published papers listed below:

On the evolution of the entropy and pressure profiles in X-ray luminous galaxy clusters at $z > 0.4$

Ghirardini, V., Ettori, S., Amodeo, S., Capasso, R., & Sereno, M. 2017, *A&A*, 604, A100

The XMM Cluster Outskirts Project (X-COP): Thermodynamic properties, clumpiness and hydrostatic equilibrium in Abell 2319

Ghirardini, V., Eckert, D., Ettori, S., et al. 2018, *A&A*, 614, A7

The universal thermodynamic properties of the intracluster medium over two decades in radius in the X-COP sample

Ghirardini, V., Eckert, D., Ettori, S., et al. 2018, arXiv:1805.00042

The polytropic state of the intracluster medium in the X-COP sample

Ghirardini, V., Ettori, S., Eckert, D., et al. 2018, in preparation

Non-thermal pressure support in X-COP galaxy clusters

Eckert, D., **Ghirardini, V.**, Ettori, S., et al. 2018, arXiv:1805.00034

Hydrostatic mass profiles in X-COP galaxy clusters

Ettori, S., **Ghirardini, V.**, Eckert, D., et al. 2018, arXiv:1805.00035

**REPORT ON THE ACTIVITIES
CARRIED OUT DURING THE PHD**

11.1 Research Activities

Cosmic structures evolve hierarchically from the primordial density fluctuations into larger structures under the action of gravity. Galaxy clusters are the largest bound structures of the universe and the most recent product of structure formation. Baryons fall into the gravitational potential of dark matter halos and heat up to a temperature of the order of $10^7 - 10^8$ K and therefore galaxy clusters are bright extended X-ray emitting sources.

The *XMM-Newton* Cluster Outskirts Project (Eckert et al. 2016) has been designed to grasp the physical conditions of the thermal gas in galaxy cluster outskirts by combining the capability of two European telescopes, *XMM-Newton* and *Planck*. Twelve massive local clusters mapped at high signal to noise ratio by *Planck* were chosen and observed with *XMM-Newton* for a total exposure of 1.2 Msec. Two different and complementary physical mechanism are exploited, bremsstrahlung emission in the X-ray and Sunyaev-Zel'dovich (SZ) effect in the microwave waveband. In this way we retrieve density and pressure of the intracluster medium (ICM) up to cluster's regions which were not explored in the past due to their low signal to noise ratio.

My PhD project is indeed mainly focused on the study of thermodynamic properties of the ICM in the outskirts of the X-COP galaxy clusters. My work resulted in the production of several papers, where, with an international collaboration, we developed novel techniques to model and subtract the *XMM-Newton* background, allowing to reach the virial radius in a complete sample of objects. On top of this, the combination of X-ray and SZ measurements allows to tightly constrain the cluster properties out to very large radii, thus bypassing the need of spectral analysis.

The first cluster analyzed for this sample is Abell 2319, the cluster with the highest signal to noise ratio in *Planck*. This analysis showed several interesting facts, because at first sight all the thermodynamic properties differ from the theoretical expectations. However a detailed analysis in azimuthal sectors has provided a clearer picture of what is happening in this cluster: the ongoing merger event induces throughout the ICM turbulence and in general non gravitational phenomena which changes the observed properties. However when this extra energy input is taken into account the thermodynamic profiles are well in agreement with theoretical prediction.

The same analysis is then applied to the entire sample, in order to obtain baseline redshift zero thermodynamic profiles for all the sample, more accurate and more radially extended than ever before. The thermodynamic properties in the outskirts of this sample are remarkably regular, following tightly the prediction from simulations. For the first time we have computed the scatter of the thermodynamic quantities radially, showing surprisingly

how pressure is a highly scattered thermodynamic quantities, opposite of what is generally believed.

The mass measurement and the estimate of the non thermal contribution resulted in two separate works, one lead by S. Ettori and the other by D. Eckert. In both cases I provided a large contribution, we showed that our mass estimate is very good compared with other mass probes, and that the non thermal contribution in the X-COP sample is very mild, with the exception of A2319.

In the near future we aim at studying the relation between pressure and density in these clusters, i.e. measuring the effective polytropic index. Moreover a few projects will arise in the future since I am strongly involved and co-I with the XMM-Heritage program over a period of 3 years, started in June 2018, will provide a complete sample of the most massive objects in the Universe up to redshift of 0.6.

11.2 Workshops, conferences, and meetings

4-8 JULY 2016	Athens (GR)	European week of astronomy and space science (EWASS)
27 FEBRUARY - 1 MARCH 2017	Turin (IT)	CLUSTER1, 1 st meeting of the Italian cluster community
17 - 21 JULY 2017	Garching (DE)	“Early stages of Galaxy Cluster Formation”
20 - 24 NOVEMBER 2017	Bern (CH)	“Clusters of Galaxies: Physics and Cosmology”
18 - 22 JUNE 2018	Guntersville (USA)	“WHIM and Cluster Outskirts”
10 - 13 SEPTEMBER 2018	Naples (IT)	CLUSTER2, 2 nd meeting of the Italian cluster community
10 - 12 OCTOBER 2018	Bologna (IT)	“Promoting interactions around interacting galaxy clusters”

11.3 Talks

5 JULY 2016	Athens (GR)	3 min presentation at EWASS
21 FEBRUARY 2017	Bologna (IT)	30 min at PhD seminar
28 FEBRUARY 2017	Turin (IT)	20 min talk at CLUSTER 1
12 OCTOBER 2017	Garching (DE)	30 min talk at group meeting
24 NOVEMBER 2017	Bern (CH)	35 min talk at ISSI conference
19 DECEMBER 2017	Bologna (IT)	30 min at PhD seminar
20 JUNE 2018	Guntersville (USA)	20 min talk at workshop
10 SEPTEMBER 2018	Naples (IT)	20 min talk at CLUSTER 2
11 OCTOBER 2018	Bologna (IT)	20 min talk at workshop

11.4 Periods spent Abroad

21 - 25 MARCH 2016	Milan (IT)	in collaboration with F. Gastaldello to learn the basics of the <i>XMM-Newton</i> data reduction
4 - 8 APRIL 2016	Geneva (CH)	in collaboration with D. Eckert to learn the basics of the X-COP pipeline
11 - 16 DECEMBER 2016	Geneva (CH)	in collaboration with D. Eckert to plan and advance the work on the X-COP clusters
15 JULY - 14 NOVEMBER 2017	Garching (DE)	Marco Polo funding, collaborating with D. Eckert and meeting the cluster group at MPE

11.5 Schools and internal courses

18 - 23 SEPTEMBER 2016	Bertinoro (IT)	School of Astrophysics “Francesco Lucchin” Speakers: E. Churazov, F. Nicastro, L. Piro, E. Behar
12 - 16 MARCH 2017	Bologna (IT)	“What we can learn from SKA” Speaker: M. Johnston-Hollitt
29 MAY - 1 JUNE 2017	Bologna (IT)	“A multi-wavelength view of the Galactic Center” Speakers: R. Wijnands, G. Ponti, J. Dexter
12 - 16 JUNE 2017	Milan (IT)	“1st Italian Astrostatistics School” Speakers: S. Andreon, R. Trotta
14 - 17 NOVEMBER 2017	Alicante (ES)	“AHEAD School on High Resolution X-ray Spectroscopy” Speakers: J. Kaastra, J. de Plaa, N. Werner, L. Gu, Y. Naze, G. Bradaudi-Raymont, D. Barret, V. Grinberg
10 - 16 DECEMBER 2017	Tonale (IT)	“Eleventh TRR33 Winter School on Cosmology” Speakers: A. Challinor, T. Hinderer, E. Ishida, K. Koyama, S. Profumo
21 - 25 MAY 2018	Bologna (IT)	“Spectral Energy Distribution of Galaxies” Speaker: C. Maraston

11.6 Publications

On the evolution of the entropy and pressure profiles in X-ray luminous galaxy clusters at $z > 0.4$

Ghirardini, V., Ettori, S., Amodeo, S., Capasso, R., & Sereno, M. 2017, *A&A*, 604, A100

The XMM Cluster Outskirts Project (X-COP): Thermodynamic properties, clumpiness and hydrostatic equilibrium in Abell 2319

Ghirardini, V., Eckert, D., Ettori, S., et al. 2018, *A&A*, 614, A7

The universal thermodynamic properties of the intracluster medium over two decades in radius in the X-COP sample

Ghirardini, V., Eckert, D., Ettori, S., et al. 2018, arXiv:1805.00042

The polytropic state of the intracluster medium in the X-COP sample

Ghirardini, V., Ettori, S., Eckert, D., et al. 2018, in preparation

Non-thermal pressure support in X-COP galaxy clusters

Eckert, D., **Ghirardini, V.**, Ettori, S., et al. 2018, arXiv:1805.00034

Hydrostatic mass profiles in X-COP galaxy clusters

Ettori, S., **Ghirardini, V.**, Eckert, D., et al. 2018, arXiv:1805.00035

Dark matter distribution in X-ray luminous galaxy clusters with Emergent Gravity

Ettori, S., **Ghirardini, V.**, Eckert, D., Dubath, F., & Pointecouteau, E. 2017, MNRAS, 470, L29

Probing Cosmology with Dark Matter Halo Sparsity Using X-ray Cluster Mass Measurements

Corasaniti, P. S., Ettori, S., Rasera, Y., et al. 2018, ApJ 862, 40

REFERENCES

- Abazajian, K. N., Adshead, P., Ahmed, Z., Allen, S. W., Alonso, D., Arnold, K. S., Baccigalupi, C., Bartlett, J. G., Battaglia, N., Benson, B. A., Bischoff, C. A., Borrill, J., Buza, V., Calabrese, E., Caldwell, R., Carlstrom, J. E., Chang, C. L., Crawford, T. M., Cyr-Racine, F.-Y., De Bernardis, F., de Haan, T., di Serego Alighieri, S., Dunkley, J., Dvorkin, C., Errard, J., Fabbian, G., Feeney, S., Ferraro, S., Filippini, J. P., Flauger, R., Fuller, G. M., Gluscevic, V., Green, D., Grin, D., Grohs, E., Henning, J. W., Hill, J. C., Hlozek, R., Holder, G., Holzappel, W., Hu, W., Huffenberger, K. M., Keskitalo, R., Knox, L., Kosowsky, A., Kovac, J., Kovetz, E. D., Kuo, C.-L., Kusaka, A., Le Jeune, M., Lee, A. T., Lilley, M., Loverde, M., Madhavacheril, M. S., Mantz, A., Marsh, D. J. E., McMahon, J., Meerburg, P. D., Meyers, J., Miller, A. D., Munoz, J. B., Nguyen, H. N., Niemack, M. D., Peloso, M., Peloton, J., Pogosian, L., Pryke, C., Raveri, M., Reichardt, C. L., Rocha, G., Rotti, A., Schaan, E., Schmittfull, M. M., Scott, D., Sehgal, N., Shandera, S., Sherwin, B. D., Smith, T. L., Sorbo, L., Starkman, G. D., Story, K. T., van Engelen, A., Vieira, J. D., Watson, S., Whitehorn, N., and Kimmy Wu, W. L. (2016). CMB-S4 Science Book, First Edition. *ArXiv e-prints*.
- Abell, G. O. (1958). The Distribution of Rich Clusters of Galaxies. *ApJS*, 3:211.
- Abell, G. O., Corwin, Jr., H. G., and Olowin, R. P. (1989). A catalog of rich clusters of galaxies. *ApJS*, 70:1–138.
- Adam, R., Arnaud, M., Bartalucci, I., Ade, P., André, P., Beelen, A., Benoît, A., Bideaud, A., Billot, N., Bourdin, H., Bourrion, O., Calvo, M., Catalano, A., Coiffard, G., Comis, B., D’Addabbo, A., Désert, F.-X., Doyle, S., Ferrari, C., Goupy, J., Kramer, C., Lagache, G., Leclercq, S., Macías-Pérez, J.-F., Maurogordato, S., Mauskopf, P., Mayet, F., Monfardini, A., Pajot, F., Pascale, E., Perotto, L., Pisano, G., Pointecouteau, E., Ponthieu, N., Pratt, G. W., Revéret, V., Ritacco, A., Rodriguez, L., Romero, C., Ruppin, F., Schuster, K., Sievers, A., Triqueneaux, S., Tucker, C., and Zylka, R. (2017). Mapping the hot gas temperature in galaxy clusters using X-ray and Sunyaev-Zel’dovich imaging. *A&A*, 606:A64.
- Adam, R., Comis, B., Macías-Pérez, J.-F., Adane, A., Ade, P., André, P., Beelen, A., Belier, B., Benoît, A., Bideaud, A., Billot, N., Blanquer, G., Bourrion, O., Calvo, M., Catalano,

- A., Coiffard, G., Cruciani, A., D'Addabbo, A., Désert, F.-X., Doyle, S., Goupy, J., Kramer, C., Leclercq, S., Martino, J., Mauskopf, P., Mayet, F., Monfardini, A., Pajot, F., Pascale, E., Perotto, L., Pointecouteau, E., Ponthieu, N., Revéret, V., Ritacco, A., Rodriguez, L., Savini, G., Schuster, K., Sievers, A., Tucker, C., and Zylka, R. (2015). Pressure distribution of the high-redshift cluster of galaxies CL J1226.9+3332 with NIKA. *A&A*, 576:A12.
- Akamatsu, H., Hoshino, A., Ishisaki, Y., Ohashi, T., Sato, K., Takei, Y., and Ota, N. (2011). X-Ray Study of the Outer Region of Abell 2142 with Suzaku. *PASJ*, 63:1019.
- Akamatsu, H., Inoue, S., Sato, T., Matsusita, K., Ishisaki, Y., and Sarazin, C. L. (2013). Suzaku X-Ray Observations of the Accreting NGC 4839 Group of Galaxies and a Radio Relic in the Coma Cluster. *PASJ*, 65:89.
- Allen, S. W., Evrard, A. E., and Mantz, A. B. (2011). Cosmological Parameters from Observations of Galaxy Clusters. *ARA&A*, 49:409–470.
- Allen, S. W., Rapetti, D. A., Schmidt, R. W., Ebeling, H., Morris, R. G., and Fabian, A. C. (2008). Improved constraints on dark energy from Chandra X-ray observations of the largest relaxed galaxy clusters. *MNRAS*, 383:879–896.
- Ameglio, S., Borgani, S., Pierpaoli, E., and Dolag, K. (2007). Joint deprojection of Sunyaev-Zeldovich and X-ray images of galaxy clusters. *MNRAS*, 382:397–411.
- Amodeo, S., Ettori, S., Capasso, R., and Sereno, M. (2016). The relation between mass and concentration in X-ray galaxy clusters at high redshift. *A&A*, 590:A126.
- Anders, E. and Grevesse, N. (1989). Abundances of the elements - Meteoritic and solar. *Geochim. Cosmochim. Acta*, 53:197–214.
- Andrade-Santos, F., Jones, C., Forman, W. R., Lovisari, L., Vikhlinin, A., van Weeren, R. J., Murray, S. S., Arnaud, M., Pratt, G. W., Démoclès, J., Kraft, R., Mazzotta, P., Böhringer, H., Chon, G., Giacintucci, S., Clarke, T. E., Borgani, S., David, L., Douspis, M., Pointecouteau, E., Dahle, H., Brown, S., Aghanim, N., and Rasia, E. (2017). The Fraction of Cool-core Clusters in X-Ray versus SZ Samples Using Chandra Observations. *ApJ*, 843:76.
- Andreon, S. (2010). The stellar mass fraction and baryon content of galaxy clusters and groups. *MNRAS*, 407:263–276.
- Arnaud, M., Pointecouteau, E., and Pratt, G. W. (2005). The structural and scaling properties of nearby galaxy clusters. II. The M-T relation. *A&A*, 441:893–903.
- Arnaud, M., Pratt, G. W., Piffaretti, R., Böhringer, H., Croston, J. H., and Pointecouteau, E. (2010). The universal galaxy cluster pressure profile from a representative sample of nearby systems (REXCESS) and the $Y_{SZ} - M_{500}$ relation. *A&A*, 517:A92.
- Ascasibar, Y., Sevilla, R., Yepes, G., Müller, V., and Gottlöber, S. (2006). Adiabatic scaling relations of galaxy clusters. *MNRAS*, 371:193–203.
- Ascasibar, Y., Yepes, G., Müller, V., and Gottlöber, S. (2003). The radial structure of galaxy groups and clusters. *MNRAS*, 346:731–745.

- Auger, M. W., Budzynski, J. M., Belokurov, V., Kuposov, S. E., and McCarthy, I. G. (2013). Are group- and cluster-scale dark matter haloes overconcentrated? *MNRAS*, 436:503–510.
- Bartalucci, I., Arnaud, M., Pratt, G. W., Vikhlinin, A., Pointecouteau, E., Forman, W. R., Jones, C., Mazzotta, P., and Andrade-Santos, F. (2017). Recovering galaxy cluster gas density profiles with XMM-Newton and Chandra. *A&A*, 608:A88.
- Bartelmann, M. (2010). TOPICAL REVIEW Gravitational lensing. *Classical and Quantum Gravity*, 27(23):233001.
- Basu, K., Zhang, Y.-Y., Sommer, M. W., Bender, A. N., Bertoldi, F., Dobbs, M., Eckmiller, H., Halverson, N. W., Holzappel, W. L., Horellou, C., Jaritz, V., Johansson, D., Johnson, B., Kennedy, J., Kneissl, R., Lanting, T., Lee, A. T., Mehl, J., Menten, K. M., Navarrete, F. P., Pacaud, F., Reichardt, C. L., Reiprich, T. H., Richards, P. L., Schwan, D., and Westbrook, B. (2010). Non-parametric modeling of the intra-cluster gas using APEX-SZ bolometer imaging data. *A&A*, 519:A29.
- Battaglia, N., Bond, J. R., Pfrommer, C., and Sievers, J. L. (2012). On the Cluster Physics of Sunyaev-Zel'dovich and X-Ray Surveys. II. Deconstructing the Thermal SZ Power Spectrum. *ApJ*, 758:75.
- Bauer, F. E., Fabian, A. C., Sanders, J. S., Allen, S. W., and Johnstone, R. M. (2005). The prevalence of cooling cores in clusters of galaxies at $z \sim 0.15-0.4$. *MNRAS*, 359:1481–1490.
- Beck, A. M., Murante, G., Arth, A., Remus, R.-S., Teklu, A. F., Donnert, J. M. F., Planelles, S., Beck, M. C., Förster, P., Imgrund, M., Dolag, K., and Borgani, S. (2016). An improved SPH scheme for cosmological simulations. *MNRAS*, 455:2110–2130.
- Bertschinger, E. (1985). Self-similar secondary infall and accretion in an Einstein-de Sitter universe. *ApJS*, 58:39–65.
- Bhattacharya, S., Habib, S., Heitmann, K., and Vikhlinin, A. (2013). Dark Matter Halo Profiles of Massive Clusters: Theory versus Observations. *ApJ*, 766:32.
- Biffi, V., Borgani, S., Murante, G., Rasia, E., Planelles, S., Granato, G. L., Ragone-Figueroa, C., Beck, A. M., Gaspari, M., and Dolag, K. (2016). On the Nature of Hydrostatic Equilibrium in Galaxy Clusters. *ApJ*, 827:112.
- Binney, J. and Tremaine, S. (1987). *Galactic dynamics*.
- Böhringer, H., Schuecker, P., Pratt, G. W., Arnaud, M., Ponman, T. J., Croston, J. H., Borgani, S., Bower, R. G., Briel, U. G., Collins, C. A., Donahue, M., Forman, W. R., Finoguenov, A., Geller, M. J., Guzzo, L., Henry, J. P., Kneissl, R., Mohr, J. J., Matsushita, K., Mullis, C. R., Ohashi, T., Pedersen, K., Pierini, D., Quintana, H., Raychaudhury, S., Reiprich, T. H., Romer, A. K., Rosati, P., Sabirli, K., Temple, R. F., Viana, P. T. P., Vikhlinin, A., Voit, G. M., and Zhang, Y.-Y. (2007). The representative XMM-Newton cluster structure survey (REXCESS) of an X-ray luminosity selected galaxy cluster sample. *A&A*, 469:363–377.
- Bonamente, M., Landry, D., Maughan, B., Giles, P., Joy, M., and Nevalainen, J. (2013). Chandra X-ray observations of Abell 1835 to the virial radius. *MNRAS*, 428:2812–2823.

- Borgani, S., Finoguenov, A., Kay, S. T., Ponman, T. J., Springel, V., Tozzi, P., and Voit, G. M. (2005). Entropy amplification from energy feedback in simulated galaxy groups and clusters. *MNRAS*, 361:233–243.
- Borm, K., Reiprich, T. H., Mohammed, I., and Lovisari, L. (2014). Constraining galaxy cluster temperatures and redshifts with eROSITA survey data. *A&A*, 567:A65.
- Bourdin, H., Mazzotta, P., Kozmany, A., Jones, C., and Vikhlinin, A. (2017). Pressure Profiles of Distant Galaxy Clusters in the Planck Catalogue. *ApJ*, 843:72.
- Brunetti, G. and Jones, T. W. (2014). Cosmic Rays in Galaxy Clusters and Their Nonthermal Emission. *International Journal of Modern Physics D*, 23:1430007–98.
- Bryan, G. L. (2000). Explaining the Entropy Excess in Clusters and Groups of Galaxies without Additional Heating. *ApJ*, 544:L1–L5.
- Bryan, G. L. and Norman, M. L. (1998). Statistical Properties of X-Ray Clusters: Analytic and Numerical Comparisons. *ApJ*, 495:80–99.
- Budzynski, J. M., Kozlov, S. E., McCarthy, I. G., and Belokurov, V. (2014). The similarity of the stellar mass fractions of galaxy groups and clusters. *MNRAS*, 437:1362–1377.
- Bulbul, G. E., Hasler, N., Bonamente, M., and Joy, M. (2010). An Analytic Model of the Physical Properties of Galaxy Clusters. *ApJ*, 720:1038–1044.
- Bullock, J. S., Kolatt, T. S., Sigad, Y., Somerville, R. S., Kravtsov, A. V., Klypin, A. A., Primack, J. R., and Dekel, A. (2001). Profiles of dark haloes: evolution, scatter and environment. *MNRAS*, 321:559–575.
- Burenin, R. A., Vikhlinin, A., Hornstrup, A., Ebeling, H., Quintana, H., and Mescheryakov, A. (2007). The 400 Square Degree ROSAT PSPC Galaxy Cluster Survey: Catalog and Statistical Calibration. *ApJS*, 172:561–582.
- Capelo, P. R., Coppi, P. S., and Natarajan, P. (2012). The polytropic approximation and X-ray scaling relations: constraints on gas and dark matter profiles for galaxy groups and clusters. *MNRAS*, 422:686–703.
- Cappellari, M. and Copin, Y. (2003). Adaptive spatial binning of integral-field spectroscopic data using Voronoi tessellations. *MNRAS*, 342:345–354.
- Carlberg, R. G., Yee, H. K. C., and Ellingson, E. (1997). The Average Mass and Light Profiles of Galaxy Clusters. *ApJ*, 478:462–475.
- Carlstrom, J. E., Holder, G. P., and Reese, E. D. (2002). Cosmology with the Sunyaev-Zel'dovich Effect. *ARA&A*, 40:643–680.
- Carrasco, E. R., Gomez, P. L., Verdugo, T., Lee, H., Diaz, R., Bergmann, M., Turner, J. E. H., Miller, B. W., and West, M. J. (2010). Strong Gravitational Lensing by the Super-massive cD Galaxy in Abell 3827. *ApJ*, 715:L160–L164.
- Cash, W. (1979). Parameter estimation in astronomy through application of the likelihood ratio. *ApJ*, 228:939–947.

- Cassano, R., Ettori, S., Giacintucci, S., Brunetti, G., Markevitch, M., Venturi, T., and Gitti, M. (2010). On the Connection Between Giant Radio Halos and Cluster Mergers. *ApJ*, 721:L82–L85.
- Cavagnolo, K. W., Donahue, M., Voit, G. M., and Sun, M. (2009). Intracluster Medium Entropy Profiles for a Chandra Archival Sample of Galaxy Clusters. *ApJS*, 182:12–32.
- Cavaliere, A. and Fusco-Femiano, R. (1976). X-rays from hot plasma in clusters of galaxies. *A&A*, 49:137–144.
- Cavaliere, A. G., Gursky, H., and Tucker, W. H. (1971). Extragalactic X-ray Sources and Associations of Galaxies. *Nature*, 231:437–438.
- Chaudhuri, A., Nath, B. B., and Majumdar, S. (2012). Energy Deposition Profiles and Entropy in Galaxy Clusters. *ApJ*, 759:87.
- Chiu, I., Mohr, J. J., McDonald, M., Bocquet, S., Desai, S., Klein, M., Israel, H., Ashby, M. L. N., Stanford, A., Benson, B. A., Brodwin, M., Abbott, T. M. C., Abdalla, F. B., Allam, S., Annis, J., Bayliss, M., Benoit-Lévy, A., Bertin, E., Bleem, L., Brooks, D., Buckley-Geer, E., Bulbul, E., Capasso, R., Carlstrom, J. E., Rosell, A. C., Carretero, J., Castander, F. J., Cunha, C. E., D’Andrea, C. B., da Costa, L. N., Davis, C., Diehl, H. T., Dietrich, J. P., Doel, P., Drlica-Wagner, A., Eifler, T. F., Evrard, A. E., Flaugher, B., García-Bellido, J., Garmire, G., Gaztanaga, E., Gerdes, D. W., Gonzalez, A., Gruen, D., Gruendl, R. A., Gschwend, J., Gupta, N., Gutierrez, G., Hlavacek-L, J., Honscheid, K., James, D. J., Jeltema, T., Kraft, R., Krause, E., Kuehn, K., Kuhlmann, S., Kuropatkin, N., Lahav, O., Lima, M., Maia, M. A. G., Marshall, J. L., Melchior, P., Menanteau, F., Miquel, R., Murray, S., Nord, B., Ogando, R. L. C., Plazas, A. A., Rapetti, D., Reichardt, C. L., Romer, A. K., Roodman, A., Sanchez, E., Saro, A., Scarpine, V., Schindler, R., Schubnell, M., Sharon, K., Smith, R. C., Smith, M., Soares-Santos, M., Sobreira, F., Stalder, B., Stern, C., Strazzullo, V., Suchyta, E., Swanson, M. E. C., Tarle, G., Vikram, V., Walker, A. R., Weller, J., and Zhang, Y. (2018). Baryon content in a sample of 91 galaxy clusters selected by the South Pole Telescope at $0.2 < z < 1.25$. *MNRAS*, 478:3072–3099.
- Coupon, J., Arnouts, S., van Waerbeke, L., Moutard, T., Ilbert, O., van Uitert, E., Erben, T., Garilli, B., Guzzo, L., Heymans, C., Hildebrandt, H., Hoekstra, H., Kilbinger, M., Kitching, T., Mellier, Y., Miller, L., Scodeggio, M., Bonnett, C., Branchini, E., Davidzon, I., De Lucia, G., Fritz, A., Fu, L., Hudelot, P., Hudson, M. J., Kuijken, K., Leauthaud, A., Le Fèvre, O., McCracken, H. J., Moscardini, L., Rowe, B. T. P., Schrabback, T., Semboloni, E., and Velander, M. (2015). The galaxy-halo connection from a joint lensing, clustering and abundance analysis in the CFHTLenS/VIPERS field. *MNRAS*, 449:1352–1379.
- Croston, J. H., Arnaud, M., Pointecouteau, E., and Pratt, G. W. (2006). An improved deprojection and PSF-deconvolution technique for galaxy-cluster X-ray surface-brightness profiles. *A&A*, 459:1007–1019.
- Cunha, C., Huterer, D., and Frieman, J. A. (2009). Constraining dark energy with clusters: Complementarity with other probes. *Phys. Rev. D*, 80(6):063532.
- De Grandi, S., Eckert, D., Molendi, S., Girardi, M., Roediger, E., Gaspari, M., Gastaldello, F., Ghizzardi, S., Nonino, M., and Rossetti, M. (2016). A textbook example of ram-pressure stripping in the Hydra A/A780 cluster. *A&A*, 592:A154.

- de Haan, T., Benson, B. A., Bleem, L. E., Allen, S. W., Applegate, D. E., Ashby, M. L. N., Bautz, M., Bayliss, M., Bocquet, S., Brodwin, M., Carlstrom, J. E., Chang, C. L., Chiu, I., Cho, H.-M., Clocchiatti, A., Crawford, T. M., Crites, A. T., Desai, S., Dietrich, J. P., Dobbs, M. A., Doucouliagos, A. N., Foley, R. J., Forman, W. R., Garmire, G. P., George, E. M., Gladders, M. D., Gonzalez, A. H., Gupta, N., Halverson, N. W., Hlavacek-Larrondo, J., Hoekstra, H., Holder, G. P., Holzapfel, W. L., Hou, Z., Hrubes, J. D., Huang, N., Jones, C., Keisler, R., Knox, L., Lee, A. T., Leitch, E. M., von der Linden, A., Luong-Van, D., Mantz, A., Marrone, D. P., McDonald, M., McMahon, J. J., Meyer, S. S., Mocuano, L. M., Mohr, J. J., Murray, S. S., Padin, S., Pryke, C., Rapetti, D., Reichardt, C. L., Rest, A., Ruel, J., Ruhl, J. E., Saliwanchik, B. R., Saro, A., Sayre, J. T., Schaffer, K. K., Schrabback, T., Shirokoff, E., Song, J., Spieler, H. G., Stalder, B., Stanford, S. A., Staniszewski, Z., Stark, A. A., Story, K. T., Stubbs, C. W., Vanderlinde, K., Vieira, J. D., Vikhlinin, A., Williamson, R., and Zenteno, A. (2016). Cosmological Constraints from Galaxy Clusters in the 2500 Square-degree SPT-SZ Survey. *ApJ*, 832:95.
- De Luca, A. and Molendi, S. (2004). The 2-8 keV cosmic X-ray background spectrum as observed with XMM-Newton. *A&A*, 419:837–848.
- Diaz-Rodriguez, J., Eckert, D., Monajemi, H., Paltani, M., and Sardy, S. (2017). Nonparametric estimation of galaxy cluster’s emissivity and point source detection in astrophysics with two lasso penalties. *Submitted to Annals of Applied Statistics*.
- Diemer, B. and Kravtsov, A. V. (2014). Dependence of the Outer Density Profiles of Halos on Their Mass Accretion Rate. *ApJ*, 789:1.
- Diemer, B. and Kravtsov, A. V. (2015). A Universal Model for Halo Concentrations. *ApJ*, 799:108.
- Diemer, B., Mansfield, P., Kravtsov, A. V., and More, S. (2017). The Splashback Radius of Halos from Particle Dynamics. II. Dependence on Mass, Accretion Rate, Redshift, and Cosmology. *ApJ*, 843:140.
- Dolag, K., Bartelmann, M., and Lesch, H. (1999). SPH simulations of magnetic fields in galaxy clusters. *A&A*, 348:351–363.
- Dolag, K., Bartelmann, M., Perrotta, F., Baccigalupi, C., Moscardini, L., Meneghetti, M., and Tormen, G. (2004). Numerical study of halo concentrations in dark-energy cosmologies. *A&A*, 416:853–864.
- Du, W. and Fan, Z. (2014). Effects of Center Offset and Noise on Weak-Lensing Derived Concentration-Mass Relation of Dark Matter Halos. *ApJ*, 785:57.
- Dubois, Y., Devriendt, J., Slyz, A., and Teyssier, R. (2010). Jet-regulated cooling catastrophe. *MNRAS*, 409:985–1001.
- Dunn, R. J. H. and Fabian, A. C. (2008). Investigating heating and cooling in the BCS and B55 cluster samples. *MNRAS*, 385:757–768.
- Dunn, R. J. H., Fabian, A. C., and Taylor, G. B. (2005). Radio bubbles in clusters of galaxies. *MNRAS*, 364:1343–1353.

- Dutton, A. A. and Macciò, A. V. (2014). Cold dark matter haloes in the Planck era: evolution of structural parameters for Einasto and NFW profiles. *MNRAS*, 441:3359–3374.
- Ebeling, H., White, D. A., and Rangarajan, F. V. N. (2006). ASMOOTH: a simple and efficient algorithm for adaptive kernel smoothing of two-dimensional imaging data. *MNRAS*, 368:65–73.
- Eckert, D., Etti, S., Coupon, J., Gastaldello, F., Pierre, M., Melin, J.-B., Le Brun, A. M. C., McCarthy, I. G., Adami, C., Chiappetti, L., Faccioli, L., Giles, P., Lavoie, S., Lefèvre, J. P., Lieu, M., Mantz, A., Maughan, B., McGee, S., Pacaud, F., Paltani, S., Sadibekova, T., Smith, G. P., and Ziparo, F. (2016a). The XXL Survey. XIII. Baryon content of the bright cluster sample. *A&A*, 592:A12.
- Eckert, D., Etti, S., Pointecouteau, E., Molendi, S., Paltani, S., and Tchernin, C. (2017a). The XMM cluster outskirts project (X-COP). *Astronomische Nachrichten*, 338:293–298.
- Eckert, D., Gaspari, M., Vazza, F., Gastaldello, F., Tramacere, A., Zimmer, S., Etti, S., and Paltani, S. (2017b). On the Connection between Turbulent Motions and Particle Acceleration in Galaxy Clusters. *ApJ*, 843:L29.
- Eckert, D., Jauzac, M., Vazza, F., Owers, M. S., Kneib, J.-P., Tchernin, C., Intema, H., and Knowles, K. (2016b). A shock front at the radio relic of Abell 2744. *MNRAS*, 461:1302–1307.
- Eckert, D., Molendi, S., Owers, M., Gaspari, M., Venturi, T., Rudnick, L., Etti, S., Paltani, S., Gastaldello, F., and Rossetti, M. (2014). The stripping of a galaxy group diving into the massive cluster A2142. *A&A*, 570:A119.
- Eckert, D., Molendi, S., and Paltani, S. (2011). The cool-core bias in X-ray galaxy cluster samples. I. Method and application to HIFLUGCS. *A&A*, 526:A79.
- Eckert, D., Molendi, S., Vazza, F., Etti, S., and Paltani, S. (2013). The X-ray/SZ view of the virial region. I. Thermodynamic properties. *A&A*, 551:A22.
- Eckert, D., Roncarelli, M., Etti, S., Molendi, S., Vazza, F., Gastaldello, F., and Rossetti, M. (2015). Gas clumping in galaxy clusters. *MNRAS*, 447:2198–2208.
- Eckert, D., Vazza, F., Etti, S., Molendi, S., Nagai, D., Lau, E. T., Roncarelli, M., Rossetti, M., Snowden, S. L., and Gastaldello, F. (2012). The gas distribution in the outer regions of galaxy clusters. *A&A*, 541:A57.
- Erlar, J., Basu, K., Chluba, J., and Bertoldi, F. (2018). Planck’s view on the spectrum of the Sunyaev-Zeldovich effect. *MNRAS*.
- Etti, S. (2003). Are we missing baryons in galaxy clusters? *MNRAS*, 344:L13–L16.
- Etti, S. (2015). The physics inside the scaling relations for X-ray galaxy clusters: gas clumpiness, gas mass fraction and slope of the pressure profile. *MNRAS*, 446:2629–2639.
- Etti, S. and Balestra, I. (2009). The outer regions of galaxy clusters: Chandra constraints on the X-ray surface brightness. *A&A*, 496:343–349.

- Ettori, S., De Grandi, S., and Molendi, S. (2002). Gravitating mass profiles of nearby galaxy clusters and relations with X-ray gas temperature, luminosity and mass. *A&A*, 391:841–855.
- Ettori, S., Dolag, K., Borgani, S., and Murante, G. (2006). The baryon fraction in hydrodynamical simulations of galaxy clusters. *MNRAS*, 365:1021–1030.
- Ettori, S., Donnarumma, A., Pointecouteau, E., Reiprich, T. H., Giodini, S., Lovisari, L., and Schmidt, R. W. (2013a). Mass Profiles of Galaxy Clusters from X-ray Analysis. *Space Sci. Rev.*, 177:119–154.
- Ettori, S., Gastaldello, F., Leccardi, A., Molendi, S., Rossetti, M., Buote, D., and Meneghetti, M. (2010). Mass profiles and c - M_{DM} relation in X-ray luminous galaxy clusters. *A&A*, 524:A68.
- Ettori, S., Ghirardini, V., Eckert, D., Dubath, F., and Pointecouteau, E. (2017). Dark matter distribution in X-ray luminous galaxy clusters with Emergent Gravity. *MNRAS*, 470:L29–L33.
- Ettori, S., Ghirardini, V., Eckert, D., Pointecouteau, E., Gastaldello, F., Sereno, M., Gaspari, M., Ghizzardi, S., Roncarelli, M., and Rossetti, M. (2018). Hydrostatic mass profiles in X-COP galaxy clusters. *ArXiv e-prints*.
- Ettori, S. and Molendi, S. (2011). X-ray observations of cluster outskirts: current status and future prospects. *Memorie della Societa Astronomica Italiana Supplementi*, 17:47.
- Ettori, S., Morandi, A., Tozzi, P., Balestra, I., Borgani, S., Rosati, P., Lovisari, L., and Terenziani, F. (2009). The cluster gas mass fraction as a cosmological probe: a revised study. *A&A*, 501:61–73.
- Ettori, S., Pratt, G. W., de Plaa, J., Eckert, D., Nevalainen, J., Battistelli, E. S., Borgani, S., Croston, J. H., Finoguenov, A., Kaastra, J., Gaspari, M., Gastaldello, F., Gitti, M., Molendi, S., Pointecouteau, E., Ponman, T. J., Reiprich, T. H., Roncarelli, M., Rossetti, M., Sanders, J. S., Sun, M., Trinchieri, G., Vazza, F., Arnaud, M., Böringher, H., Brighenti, F., Dahle, H., De Grandi, S., Mohr, J. J., Moretti, A., and Schindler, S. (2013b). The Hot and Energetic Universe: The astrophysics of galaxy groups and clusters. *ArXiv e-prints*.
- Evrard, A. E. and Henry, J. P. (1991). Expectations for X-ray cluster observations by the ROSAT satellite. *ApJ*, 383:95–103.
- Farnsworth, D., Rudnick, L., Brown, S., and Brunetti, G. (2013). Discovery of Megaparsec-scale, Low Surface Brightness Nonthermal Emission in Merging Galaxy Clusters Using the Green Bank Telescope. *ApJ*, 779:189.
- Feretti, L., Giovannini, G., Govoni, F., and Murgia, M. (2012). Clusters of galaxies: observational properties of the diffuse radio emission. *A&A Rev.*, 20:54.
- Feroz, F., Hobson, M. P., and Bridges, M. (2009). MULTINEST: an efficient and robust Bayesian inference tool for cosmology and particle physics. *MNRAS*, 398:1601–1614.
- Foreman-Mackey, D., Hogg, D. W., Lang, D., and Goodman, J. (2013a). emcee: The MCMC Hammer. *PASP*, 125:306.

- Foreman-Mackey, D., Hogg, D. W., Lang, D., and Goodman, J. (2013b). emcee: The MCMC Hammer. *PASP*, 125:306–312.
- Forman, W., Kellogg, E., Gursky, H., Tananbaum, H., and Giacconi, R. (1972). Observations of the Extended X-Ray Sources in the Perseus and Coma Clusters from UHURU. *ApJ*, 178:309–316.
- Fruscione, A., McDowell, J. C., Allen, G. E., Brickhouse, N. S., Burke, D. J., Davis, J. E., Durham, N., Elvis, M., Galle, E. C., Harris, D. E., Huenemoerder, D. P., Houck, J. C., Ishibashi, B., Karovska, M., Nicastro, F., Noble, M. S., Nowak, M. A., Primini, F. A., Siemiginowska, A., Smith, R. K., and Wise, M. (2006). CIAO: Chandra’s data analysis system. 6270:62701V.
- Fusco-Femiano, R. and Lapi, A. (2014). Entropy Flattening, Gas Clumping, and Turbulence in Galaxy Clusters. *ApJ*, 783:76.
- Gaspari, M., Brighenti, F., Temi, P., and Etori, S. (2014). Can AGN Feedback Break the Self-similarity of Galaxies, Groups, and Clusters? *ApJ*, 783:L10.
- Gaspari, M., Ruszkowski, M., and Sharma, P. (2012). Cause and Effect of Feedback: Multiphase Gas in Cluster Cores Heated by AGN Jets. *ApJ*, 746:94.
- Ghirardini, V., Eckert, D., Etori, S., Pointecouteau, E., Molendi, S., Gaspari, M., Rossetti, M., De Grandi, S., Roncarelli, M., Bourdin, H., Mazzotta, P., Rasia, E., and Vazza, F. (2018a). The universal thermodynamic properties of the intracluster medium over two decades in radius in the X-COP sample. *ArXiv e-prints*.
- Ghirardini, V., Etori, S., Eckert, D., Molendi, S., Gastaldello, F., Pointecouteau, E., Hurier, G., and Bourdin, H. (2018b). The XMM Cluster Outskirts Project (X-COP): Thermodynamic properties of the intracluster medium out to R_{200} in Abell 2319. *A&A*, 614:A7.
- Ghizzardi, S., Rossetti, M., and Molendi, S. (2010). Cold fronts in galaxy clusters. *A&A*, 516:A32.
- Giodini, S., Pierini, D., Finoguenov, A., Pratt, G. W., Boehringer, H., Leauthaud, A., Guzzo, L., Aussel, H., Bolzonella, M., Capak, P., Elvis, M., Hasinger, G., Ilbert, O., Kartaltepe, J. S., Koekemoer, A. M., Lilly, S. J., Massey, R., McCracken, H. J., Rhodes, J., Salvato, M., Sanders, D. B., Scoville, N. Z., Sasaki, S., Smolcic, V., Taniguchi, Y., Thompson, D., and COSMOS Collaboration (2009). Stellar and Total Baryon Mass Fractions in Groups and Clusters Since Redshift 1. *ApJ*, 703:982–993.
- Gonzalez, A. H., Sivanandam, S., Zabludoff, A. I., and Zaritsky, D. (2013). Galaxy Cluster Baryon Fractions Revisited. *ApJ*, 778:14.
- Gonzalez, A. H., Zaritsky, D., and Zabludoff, A. I. (2007). A Census of Baryons in Galaxy Clusters and Groups. *ApJ*, 666:147–155.
- Gursky, H., Kellogg, E., Murray, S., Leong, C., Tananbaum, H., and Giacconi, R. (1971). A Strong X-Ray Source in the Coma Cluster Observed by UHURU. *ApJ*, 167:L81.

- Hao, J., McKay, T. A., Koester, B. P., Rykoff, E. S., Rozo, E., Annis, J., Wechsler, R. H., Evrard, A., Siegel, S. R., Becker, M., Busha, M., Gerdes, D., Johnston, D. E., and Sheldon, E. (2010). A GMBCG Galaxy Cluster Catalog of 55,424 Rich Clusters from SDSS DR7. *ApJS*, 191:254–274.
- Hernquist, L. (1990). An analytical model for spherical galaxies and bulges. *ApJ*, 356:359–364.
- Heymans, C., Grocutt, E., Heavens, A., Kilbinger, M., Kitching, T. D., Simpson, F., Benjamin, J., Erben, T., Hildebrandt, H., Hoekstra, H., Mellier, Y., Miller, L., Van Waerbeke, L., Brown, M. L., Coupon, J., Fu, L., Harnois-Déraps, J., Hudson, M. J., Kuijken, K., Rowe, B., Schrabback, T., Semboloni, E., Vafaei, S., and Velander, M. (2013). CFHTLenS tomographic weak lensing cosmological parameter constraints: Mitigating the impact of intrinsic galaxy alignments. *MNRAS*, 432:2433–2453.
- Hildebrandt, H., Viola, M., Heymans, C., Joudaki, S., Kuijken, K., Blake, C., Erben, T., Joachimi, B., Klaes, D., Miller, L., Morrison, C. B., Nakajima, R., Verdoes Kleijn, G., Amon, A., Choi, A., Covone, G., de Jong, J. T. A., Dvornik, A., Fenech Conti, I., Grado, A., Harnois-Déraps, J., Herbonnet, R., Hoekstra, H., Köhlinger, F., McFarland, J., Mead, A., Merten, J., Napolitano, N., Peacock, J. A., Radovich, M., Schneider, P., Simon, P., Valentijn, E. A., van den Busch, J. L., van Uitert, E., and Van Waerbeke, L. (2017). KiDS-450: cosmological parameter constraints from tomographic weak gravitational lensing. *MNRAS*, 465:1454–1498.
- Hinshaw, G., Larson, D., Komatsu, E., Spergel, D. N., Bennett, C. L., Dunkley, J., Nolte, M. R., Halpern, M., Hill, R. S., Odegard, N., Page, L., Smith, K. M., Weiland, J. L., Gold, B., Jarosik, N., Kogut, A., Limon, M., Meyer, S. S., Tucker, G. S., Wollack, E., and Wright, E. L. (2013). Nine-year Wilkinson Microwave Anisotropy Probe (WMAP) Observations: Cosmological Parameter Results. *ApJS*, 208:19.
- Hitomi Collaboration, Aharonian, F., Akamatsu, H., Akimoto, F., Allen, S. W., Anabuki, N., Angelini, L., Arnaud, K., Audard, M., Awaki, H., Axelsson, M., Bamba, A., Bautz, M., Blandford, R., Brenneman, L., Brown, G. V., Bulbul, E., Cackett, E., Chernyakova, M., Chiao, M., Coppi, P., Costantini, E., de Plaa, J., den Herder, J.-W., Done, C., Dotani, T., Ebisawa, K., Eckart, M., Enoto, T., Ezoe, Y., Fabian, A. C., Ferrigno, C., Foster, A., Fujimoto, R., Fukazawa, Y., Furuzawa, A., Galeazzi, M., Gallo, L., Gandhi, P., Giustini, M., Goldwurm, A., Gu, L., Guainazzi, M., Haba, Y., Hagino, K., Hamaguchi, K., Harrus, I., Hatsukade, I., Hayashi, K., Hayashi, T., Hayashida, K., Hiraga, J., Hornschemeier, A., Hoshino, A., Hughes, J., Iizuka, R., Inoue, H., Inoue, Y., Ishibashi, K., Ishida, M., Ishikawa, K., Ishisaki, Y., Itoh, M., Iyomoto, N., Kaastra, J., Kallman, T., Kamae, T., Kara, E., Kataoka, J., Katsuda, S., Katsuta, J., Kawaharada, M., Kawai, N., Kelley, R., Khangulyan, D., Kilbourne, C., King, A., Kitaguchi, T., Kitamoto, S., Kitayama, T., Kohmura, T., Kokubun, M., Koyama, S., Koyama, K., Kretschmar, P., Krimm, H., Kubota, A., Kunieda, H., Laurent, P., Lebrun, F., Lee, S.-H., Leutenegger, M., Limousin, O., Loewenstein, M., Long, K. S., Lumb, D., Madejski, G., Maeda, Y., Maier, D., Makishima, K., Markevitch, M., Matsumoto, H., Matsushita, K., McCammon, D., McNamara, B., Mehdipour, M., Miller, E., Miller, J., Mineshige, S., Mitsuda, K., Mitsuishi, I., Miyazawa, T., Mizuno, T., Mori, H., Mori, K., Moseley, H., Mukai, K., Murakami, H., Murakami, T., Mushotzky, R., Nagino, R., Nakagawa, T., Nakajima, H., Nakamori, T., Nakano, T., Nakashima, S., Nakazawa, K., Nobukawa, M., Noda, H., Nomachi, M., O’Dell, S., Odaka,

- H., Ohashi, T., Ohno, M., Okajima, T., Ota, N., Ozaki, M., Paerels, F., Paltani, S., Parmar, A., Petre, R., Pinto, C., Pohl, M., Porter, F. S., Pottschmidt, K., Ramsey, B., Reynolds, C., Russell, H., Safi-Harb, S., Saito, S., Sakai, K., Sameshima, H., Sato, G., Sato, K., Sato, R., Sawada, M., Schartel, N., Serlemitsos, P., Seta, H., Shidatsu, M., Simionescu, A., Smith, R., Soong, Y., Stawarz, L., Sugawara, Y., Sugita, S., Szymkowiak, A., Tajima, H., Takahashi, H., Takahashi, T., Takeda, S., Takei, Y., Tamagawa, T., Tamura, K., Tamura, T., Tanaka, T., Tanaka, Y., Tanaka, Y., Tashiro, M., Tawara, Y., Terada, Y., Terashima, Y., Tombesi, F., Tomida, H., Tsuboi, Y., Tsujimoto, M., Tsunemi, H., Tsuru, T., Uchida, H., Uchiyama, H., Uchiyama, Y., Ueda, S., Ueda, Y., Ueno, S., Uno, S., Urry, M., Ursino, E., de Vries, C., Watanabe, S., Werner, N., Wik, D., Wilkins, D., Williams, B., Yamada, S., Yamaguchi, H., Yamaoka, K., Yamasaki, N. Y., Yamauchi, M., Yamauchi, S., Yaqoob, T., Yatsu, Y., Yonetoku, D., Yoshida, A., Yuasa, T., Zhuravleva, I., and Zoghbi, A. (2016). The quiescent intracluster medium in the core of the Perseus cluster. *Nature*, 535:117–121.
- Hitomi Collaboration, Aharonian, F., Akamatsu, H., Akimoto, F., Allen, S. W., Angelini, L., Audard, M., Awaki, H., Axelsson, M., Bamba, A., Bautz, M. W., Blandford, R., Brenne-
man, L. W., Brown, G. V., Bulbul, E., Cackett, E. M., Canning, R. E. A., Chernyakova,
M., Chiao, M. P., Coppi, P. S., Costantini, E., de Plaa, J., de Vries, C. P., den Herder,
J.-W., Done, C., Dotani, T., Ebisawa, K., Eckart, M. E., Enoto, T., Ezoe, Y., Fabian, A. C.,
Ferrigno, C., Foster, A. R., Fujimoto, R., Fukazawa, Y., Furuzawa, A., Galeazzi, M., Gallo,
L. C., Gandhi, P., Giustini, M., Goldwurm, A., Gu, L., Guainazzi, M., Haba, Y., Hagino,
K., Hamaguchi, K., Harrus, I. M., Hatsukade, I., Hayashi, K., Hayashi, T., Hayashi, T.,
Hayashida, K., Hiraga, J. S., Hornschemeier, A., Hoshino, A., Hughes, J. P., Ichinohe, Y.,
Iizuka, R., Inoue, H., Inoue, S., Inoue, Y., Ishida, M., Ishikawa, K., Ishisaki, Y., Iwai, M.,
Kaastra, J., Kallman, T., Kamae, T., Kataoka, J., Katsuda, S., Kawai, N., Kelley, R. L.,
Kilbourne, C. A., Kitaguchi, T., Kitamoto, S., Kitayama, T., Kohmura, T., Kokubun, M.,
Koyama, K., Koyama, S., Kretschmar, P., Krimm, H. A., Kubota, A., Kunieda, H., Laurent,
P., Lee, S.-H., Leutenegger, M. A., Limousin, O., Loewenstein, M., Long, K. S., Lumb,
D., Madejski, G., Maeda, Y., Maier, D., Makishima, K., Markevitch, M., Matsumoto, H.,
Matsushita, K., McCammon, D., McNamara, B. R., Mehdipour, M., Miller, E. D., Miller,
J. M., Mineshige, S., Mitsuda, K., Mitsuishi, I., Miyazawa, T., Mizuno, T., Mori, H., Mori,
K., Mukai, K., Murakami, H., Mushotzky, R. F., Nakagawa, T., Nakajima, H., Nakamori,
T., Nakashima, S., Nakazawa, K., Nobukawa, K. K., Nobukawa, M., Noda, H., Odaka, H.,
Ohashi, T., Ohno, M., Okajima, T., Ota, N., Ozaki, M., Paerels, F., Paltani, S., Petre, R.,
Pinto, C., Porter, F. S., Pottschmidt, K., Reynolds, C. S., Safi-Harb, S., Saito, S., Sakai,
K., Sasaki, T., Sato, G., Sato, K., Sato, R., Sawada, M., Schartel, N., Serlemitsos, P. J.,
Seta, H., Shidatsu, M., Simionescu, A., Smith, R. K., Soong, Y., Stawarz, L., Sugawara,
Y., Sugita, S., Szymkowiak, A., Tajima, H., Takahashi, H., Takahashi, T., Takeda, S.,
Takei, Y., Tamagawa, T., Tamura, T., Tanaka, K., Tanaka, T., Tanaka, Y., Tanaka, Y. T.,
Tashiro, M. S., Tawara, Y., Terada, Y., Terashima, Y., Tombesi, F., Tomida, H., Tsuboi, Y.,
Tsujimoto, M., Tsunemi, H., Tsuru, T. G., Uchida, H., Uchiyama, H., Uchiyama, Y., Ueda,
S., Ueda, Y., Uno, S., Urry, C. M., Ursino, E., Wang, Q. H. S., Watanabe, S., Werner,
N., Wilkins, D. R., Williams, B. J., Yamada, S., Yamaguchi, H., Yamaoka, K., Yamasaki,
N. Y., Yamauchi, M., Yamauchi, S., Yaqoob, T., Yatsu, Y., Yonetoku, D., Zhuravleva, I.,
and Zoghbi, A. (2018). Atmospheric gas dynamics in the Perseus cluster observed with
Hitomi. *PASJ*, 70:9.
- Hitomi Collaboration, Aharonian, F., Akamatsu, H., Akimoto, F., Allen, S. W., Angelini,
L., Audard, M., Awaki, H., Axelsson, M., Bamba, A., Bautz, M. W., Blandford, R.,

- Brenneman, L. W., Brown, G. V., Bulbul, E., Cackett, E. M., Chernyakova, M., Chiao, M. P., Coppi, P. S., Costantini, E., de Plaa, J., den Herder, J.-W., Done, C., Dotani, T., Ebisawa, K., Eckart, M. E., Enoto, T., Ezoe, Y., Fabian, A. C., Ferrigno, C., Foster, A. R., Fujimoto, R., Fukazawa, Y., Furuzawa, A., Galeazzi, M., Gallo, L. C., Gandhi, P., Giustini, M., Goldwurm, A., Gu, L., Guainazzi, M., Haba, Y., Hagino, K., Hamaguchi, K., Harrus, I. M., Hatsukade, I., Hayashi, K., Hayashi, T., Hayashida, K., Hiraga, J. S., Hornschemeier, A., Hoshino, A., Hughes, J. P., Ichinohe, Y., Iizuka, R., Inoue, H., Inoue, Y., Ishida, M., Ishikawa, K., Ishisaki, Y., Iwai, M., Kaastra, J., Kallman, T., Kamae, T., Kataoka, J., Katsuda, S., Kawai, N., Kelley, R. L., Kilbourne, C. A., Kitaguchi, T., Kitamoto, S., Kitayama, T., Kohmura, T., Kokubun, M., Koyama, K., Koyama, S., Kretschmar, P., Krimm, H. A., Kubota, A., Kunieda, H., Laurent, P., Lee, S.-H., Leutenegger, M. A., Limousine, O., Loewenstein, M., Long, K. S., Lumb, D., Madejski, G., Maeda, Y., Maier, D., Makishima, K., Markevitch, M., Matsumoto, H., Matsushita, K., McCammon, D., McNamara, B. R., Mehdipour, M., Miller, E. D., Miller, J. M., Mineshige, S., Mitsuda, K., Mitsuishi, I., Miyazawa, T., Mizuno, T., Mori, H., Mori, K., Mukai, K., Murakami, H., Mushotzky, R. F., Nakagawa, T., Nakajima, H., Nakamori, T., Nakashima, S., Nakazawa, K., Nobukawa, K. K., Nobukawa, M., Noda, H., Odaka, H., Ohashi, T., Ohno, M., Okajima, T., Ota, N., Ozaki, M., Paerels, F., Paltani, S., Petre, R., Pinto, C., Porter, F. S., Pottschmidt, K., Reynolds, C. S., Safi-Harb, S., Saito, S., Sakai, K., Sasaki, T., Sato, G., Sato, K., Sato, R., Sawada, M., Schartel, N., Serlemitsos, P. J., Seta, H., Shidatsu, M., Simionescu, A., Smith, R. K., Soong, Y., Stawarz, L., Sugawara, Y., Sugita, S., Szymkowiak, A., Tajima, H., Takahashi, H., Takahashi, T., Takeda, S., Takei, Y., Tamagawa, T., Tamura, T., Tanaka, T., Tanaka, Y., Tanaka, Y. T., Tashiro, M. S., Tawara, Y., Terada, Y., Terashima, Y., Tombesi, F., Tomida, H., Tsuboi, Y., Tsujimoto, M., Tsunemi, H., Go Tsuru, T., Uchida, H., Uchiyama, H., Uchiyama, Y., Ueda, S., Ueda, Y., Uno, S., Urry, C. M., Ursino, E., de Vries, C. P., Watanabe, S., Werner, N., Wik, D. R., Wilkins, D. R., Williams, B. J., Yamada, S., Yamaguchi, H., Yamaoka, K., Yamasaki, N. Y., Yamauchi, M., Yamauchi, S., Yaqoob, T., Yatsu, Y., Yonetoku, D., Zhuravleva, I., and Zoghbi, A. (2017). Solar abundance ratios of the iron-peak elements in the Perseus cluster. *Nature*, 551:478–480.
- Hoekstra, H., Herbonnet, R., Muzzin, A., Babul, A., Mahdavi, A., Viola, M., and Cacciato, M. (2015). The Canadian Cluster Comparison Project: detailed study of systematics and updated weak lensing masses. *MNRAS*, 449:685–714.
- Hofmann, F., Sanders, J. S., Nandra, K., Clerc, N., and Gaspari, M. (2016). Thermodynamic perturbations in the X-ray halo of 33 clusters of galaxies observed with Chandra ACIS. *A&A*, 585:A130.
- Hoshino, A., Henry, J. P., Sato, K., Akamatsu, H., Yokota, W., Sasaki, S., Ishisaki, Y., Ohashi, T., Bautz, M., Fukazawa, Y., Kawano, N., Furuzawa, A., Hayashida, K., Tawa, N., Hughes, J. P., Kokubun, M., and Tamura, T. (2010). X-Ray Temperature and Mass Measurements to the Virial Radius of Abell 1413 with Suzaku. *PASJ*, 62:371–389.
- Hudson, D. S., Mittal, R., Reiprich, T. H., Nulsen, P. E. J., Andernach, H., and Sarazin, C. L. (2010). What is a cool-core cluster? a detailed analysis of the cores of the X-ray flux-limited HIFLUGCS cluster sample. *A&A*, 513:A37.
- Hurier, G. (2016). High significance detection of the tSZ effect relativistic corrections. *A&A*, 596:A61.

- Hurier, G., Macías-Pérez, J. F., and Hildebrandt, S. (2013). MILCA, a modified internal linear combination algorithm to extract astrophysical emissions from multifrequency sky maps. *A&A*, 558:A118.
- Ichikawa, K., Matsushita, K., Okabe, N., Sato, K., Zhang, Y.-Y., Finoguenov, A., Fujita, Y., Fukazawa, Y., Kawaharada, M., Nakazawa, K., Ohashi, T., Ota, N., Takizawa, M., Tamura, T., and Umetsu, K. (2013). Suzaku Observations of the Outskirts of A1835: Deviation from Hydrostatic Equilibrium. *ApJ*, 766:90.
- Itoh, N., Kohyama, Y., and Nozawa, S. (1998). Relativistic Corrections to the Sunyaev-Zeldovich Effect for Clusters of Galaxies. *ApJ*, 502:7–15.
- Jeffreys, H. (1961). *The Theory of Probability*.
- Jones, C. and Forman, W. (1984). The structure of clusters of galaxies observed with Einstein. *ApJ*, 276:38–55.
- Kaiser, N. (1986). Evolution and clustering of rich clusters. *MNRAS*, 222:323–345.
- Kalberla, P. M. W., Burton, W. B., Hartmann, D., Arnal, E. M., Bajaja, E., Morras, R., and Pöppel, W. G. L. (2005). The Leiden/Argentine/Bonn (LAB) Survey of Galactic HI. Final data release of the combined LDS and IAR surveys with improved stray-radiation corrections. *A&A*, 440:775–782.
- Kawaharada, M., Okabe, N., Umetsu, K., Takizawa, M., Matsushita, K., Fukazawa, Y., Hamana, T., Miyazaki, S., Nakazawa, K., and Ohashi, T. (2010). Suzaku Observation of A1689: Anisotropic Temperature and Entropy Distributions Associated with the Large-scale Structure. *ApJ*, 714:423–441.
- Kay, S. T., Pearce, F. R., Frenk, C. S., and Jenkins, A. (2002). Including star formation and supernova feedback within cosmological simulations of galaxy formation. *MNRAS*, 330:113–128.
- Kellogg, E., Gursky, H., Tananbaum, H., Giacconi, R., and Pounds, K. (1972). The Extended X-Ray Source at M87. *ApJ*, 174:L65.
- Kelly, B. C. (2007). Some Aspects of Measurement Error in Linear Regression of Astronomical Data. *ApJ*, 665:1489–1506.
- Khedekar, S., Churazov, E., Kravtsov, A., Zhuravleva, I., Lau, E. T., Nagai, D., and Sunyaev, R. (2013). Bias from gas inhomogeneities in the pressure profiles as measured from X-ray and Sunyaev-Zeldovich observations. *MNRAS*, 431:954–965.
- King, I. (1962). The structure of star clusters. I. an empirical density law. *AJ*, 67:471.
- Komatsu, E. and Seljak, U. (2001). Universal gas density and temperature profile. *MNRAS*, 327:1353–1366.
- Kravtsov, A. V. and Borgani, S. (2012). Formation of Galaxy Clusters. *ARA&A*, 50:353–409.
- Kravtsov, A. V., Nagai, D., and Vikhlinin, A. A. (2005). Effects of Cooling and Star Formation on the Baryon Fractions in Clusters. *ApJ*, 625:588–598.

- Kravtsov, A. V., Vikhlinin, A., and Nagai, D. (2006). A New Robust Low-Scatter X-Ray Mass Indicator for Clusters of Galaxies. *ApJ*, 650:128–136.
- Kriss, G. A., Cioffi, D. F., and Canizares, C. R. (1983). The X-ray emitting gas in poor clusters with central dominant galaxies. *ApJ*, 272:439–448.
- Kuntz, K. D. and Snowden, S. L. (2008). The EPIC-MOS particle-induced background spectra. *A&A*, 478:575–596.
- Laganá, T. F., Martinet, N., Durret, F., Lima Neto, G. B., Maughan, B., and Zhang, Y.-Y. (2013). A comprehensive picture of baryons in groups and clusters of galaxies. *A&A*, 555:A66.
- Lamarre, J.-M., Puget, J.-L., Ade, P. A. R., Bouchet, F., Guyot, G., Lange, A. E., Pajot, F., Arondel, A., Benabed, K., Beney, J.-L., Benoît, A., Bernard, J.-P., Bhatia, R., Blanc, Y., Bock, J. J., Bréelle, E., Bradshaw, T. W., Camus, P., Catalano, A., Charra, J., Charra, M., Church, S. E., Couchot, F., Coulais, A., Crill, B. P., Crook, M. R., Dassas, K., de Bernardis, P., Delabrouille, J., de Marcillac, P., Delouis, J.-M., Désert, F.-X., Dumesnil, C., Dupac, X., Efstathiou, G., Eng, P., Evesque, C., Fourmond, J.-J., Ganga, K., Giard, M., Gispert, R., Guglielmi, L., Haissinski, J., Henrot-Versillé, S., Hivon, E., Holmes, W. A., Jones, W. C., Koch, T. C., Lagardère, H., Lami, P., Landé, J., Leriche, B., Leroy, C., Longval, Y., Macías-Pérez, J. F., Maciaszek, T., Maffei, B., Mansoux, B., Marty, C., Masi, S., Mercier, C., Miville-Deschênes, M.-A., Moneti, A., Montier, L., Murphy, J. A., Narbonne, J., Nexon, M., Paine, C. G., Pahn, J., Perdureau, O., Piacentini, F., Piat, M., Plaszczyński, S., Pointecouteau, E., Pons, R., Ponthieu, N., Prunet, S., Rambaud, D., Recouvreur, G., Renault, C., Ristorcelli, I., Rosset, C., Santos, D., Savini, G., Serra, G., Stassi, P., Sudiwala, R. V., Sygnet, J.-F., Tauber, J. A., Torre, J.-P., Tristram, M., Vibert, L., Woodcraft, A., Yurchenko, V., and Yvon, D. (2010). Planck pre-launch status: The HFI instrument, from specification to actual performance. *A&A*, 520:A9.
- Lau, E. T., Kravtsov, A. V., and Nagai, D. (2009). Residual Gas Motions in the Intracluster Medium and Bias in Hydrostatic Measurements of Mass Profiles of Clusters. *ApJ*, 705:1129–1138.
- Lau, E. T., Nagai, D., Avestruz, C., Nelson, K., and Vikhlinin, A. (2015). Mass Accretion and its Effects on the Self-similarity of Gas Profiles in the Outskirts of Galaxy Clusters. *ApJ*, 806:68.
- Lau, E. T., Nagai, D., and Nelson, K. (2013). Weighing Galaxy Clusters with Gas. I. On the Methods of Computing Hydrostatic Mass Bias. *ApJ*, 777:151.
- Lazarian, A. and Brunetti, G. (2011). Turbulence, reconnection and cosmic rays in galaxy clusters. *Mem. Soc. Astron. Italiana*, 82:636.
- Le Brun, A. M. C., McCarthy, I. G., Schaye, J., and Ponman, T. J. (2014). Towards a realistic population of simulated galaxy groups and clusters. *MNRAS*, 441:1270–1290.
- Leauthaud, A., Tinker, J., Bundy, K., Behroozi, P. S., Massey, R., Rhodes, J., George, M. R., Kneib, J.-P., Benson, A., Wechsler, R. H., Busha, M. T., Capak, P., Cortês, M., Ilbert, O., Koekemoer, A. M., Le Fèvre, O., Lilly, S., McCracken, H. J., Salvato, M., Schrabback, T., Scoville, N., Smith, T., and Taylor, J. E. (2012). New Constraints on the Evolution of

- the Stellar-to-dark Matter Connection: A Combined Analysis of Galaxy-Galaxy Lensing, Clustering, and Stellar Mass Functions from $z = 0.2$ to $z = 1$. *ApJ*, 744:159.
- Leccardi, A. and Molendi, S. (2008). Radial temperature profiles for a large sample of galaxy clusters observed with XMM-Newton. *A&A*, 486:359–373.
- Lin, H. W., McDonald, M., Benson, B., and Miller, E. (2015). Cool Core Bias in Sunyaev-Zel'dovich Galaxy Cluster Surveys. *ApJ*, 802:34.
- Lin, Y.-T. and Mohr, J. J. (2004). K-band Properties of Galaxy Clusters and Groups: Brightest Cluster Galaxies and Intracluster Light. *ApJ*, 617:879–895.
- Lin, Y.-T., Mohr, J. J., and Stanford, S. A. (2004). K-Band Properties of Galaxy Clusters and Groups: Luminosity Function, Radial Distribution, and Halo Occupation Number. *ApJ*, 610:745–761.
- Loeb, A. and Mao, S. (1994). Evidence from gravitational lensing for a nonthermal pressure support in the cluster of galaxies Abell 2218. *ApJ*, 435:L109–L112.
- Lovisari, L., Forman, W. R., Jones, C., Ettori, S., Andrade-Santos, F., Arnaud, M., Démoclès, J., Pratt, G. W., Randall, S., and Kraft, R. (2017). X-Ray Morphological Analysis of the Planck ESZ Clusters. *ApJ*, 846:51.
- Ludlow, A. D., Bose, S., Angulo, R. E., Wang, L., Hellwing, W. A., Navarro, J. F., Cole, S., and Frenk, C. S. (2016). The mass-concentration-redshift relation of cold and warm dark matter haloes. *MNRAS*, 460:1214–1232.
- Luo, B., Brandt, W. N., Xue, Y. Q., Lehmer, B., Alexander, D. M., Bauer, F. E., Vito, F., Yang, G., Basu-Zych, A. R., Comastri, A., Gilli, R., Gu, Q.-S., Hornschemeier, A. E., Koekemoer, A., Liu, T., Mainieri, V., Paolillo, M., Ranalli, P., Rosati, P., Schneider, D. P., Shemmer, O., Smail, I., Sun, M., Tozzi, P., Vignali, C., and Wang, J.-X. (2017). The Chandra Deep Field-South Survey: 7 Ms Source Catalogs. *ApJS*, 228:2.
- Mamon, G. A. and Łokas, E. L. (2005). Dark matter in elliptical galaxies - I. Is the total mass density profile of the NFW form or even steeper? *MNRAS*, 362:95–109.
- Mantz, A., Allen, S. W., Ebeling, H., Rapetti, D., and Drlica-Wagner, A. (2010). The observed growth of massive galaxy clusters - II. X-ray scaling relations. *MNRAS*, 406:1773–1795.
- Mantz, A. B., Allen, S. W., and Morris, R. G. (2016). Cosmology and astrophysics from relaxed galaxy clusters - V. Consistency with cold dark matter structure formation. *MNRAS*, 462:681–688.
- Mantz, A. B., Allen, S. W., Morris, R. G., Rapetti, D. A., Applegate, D. E., Kelly, P. L., von der Linden, A., and Schmidt, R. W. (2014). Cosmology and astrophysics from relaxed galaxy clusters - II. Cosmological constraints. *MNRAS*, 440:2077–2098.
- Mantz, A. B., Allen, S. W., Morris, R. G., and von der Linden, A. (2018). Centre-excised X-ray luminosity as an efficient mass proxy for future galaxy cluster surveys. *MNRAS*, 473:3072–3079.

- Markevitch, M., Forman, W. R., Sarazin, C. L., and Vikhlinin, A. (1998). The Temperature Structure of 30 Nearby Clusters Observed with ASCA: Similarity of Temperature Profiles. *ApJ*, 503:77–96.
- Massimi, M. (2018). Three problems about multi-scale modelling in cosmology. *ArXiv e-prints*.
- Mazzotta, P., Rasia, E., Moscardini, L., and Tormen, G. (2004). Comparing the temperatures of galaxy clusters from hydrodynamical N-body simulations to Chandra and XMM-Newton observations. *MNRAS*, 354:10–24.
- McCammon, D., Almy, R., Apodaca, E., Bergmann Tiest, W., Cui, W., Deiker, S., Galeazzi, M., Juda, M., Lesser, A., Mihara, T., Morgenthaler, J. P., Sanders, W. T., Zhang, J., Figueroa-Feliciano, E., Kelley, R. L., Moseley, S. H., Mushotzky, R. F., Porter, F. S., Stahle, C. K., and Szymkowiak, A. E. (2002). A High Spectral Resolution Observation of the Soft X-Ray Diffuse Background with Thermal Detectors. *ApJ*, 576:188–203.
- McDonald, M. (2011). Optical Line Emission in Brightest Cluster Galaxies at $0 < z < 0.6$: Evidence for a Lack of Strong Cool Cores 3.5 Gyr Ago? *ApJ*, 742:L35.
- McDonald, M., Allen, S. W., Bayliss, M., Benson, B. A., Bleem, L. E., Brodwin, M., Bulbul, E., Carlstrom, J. E., Forman, W. R., Hlavacek-Larrondo, J., Garmire, G. P., Gaspari, M., Gladders, M. D., Mantz, A. B., and Murray, S. S. (2017). The Remarkable Similarity of Massive Galaxy Clusters from $z = 0$ to $z = 1.9$. *ApJ*, 843:28.
- McDonald, M., Benson, B. A., Vikhlinin, A., Aird, K. A., Allen, S. W., Bautz, M., Bayliss, M., Bleem, L. E., Bocquet, S., Brodwin, M., Carlstrom, J. E., Chang, C. L., Cho, H. M., Clocchiatti, A., Crawford, T. M., Crites, A. T., de Haan, T., Dobbs, M. A., Foley, R. J., Forman, W. R., George, E. M., Gladders, M. D., Gonzalez, A. H., Halverson, N. W., Hlavacek-Larrondo, J., Holder, G. P., Holzzapfel, W. L., Hrubes, J. D., Jones, C., Keisler, R., Knox, L., Lee, A. T., Leitch, E. M., Liu, J., Lueker, M., Luong-Van, D., Mantz, A., Marrone, D. P., McMahon, J. J., Meyer, S. S., Miller, E. D., Mocanu, L., Mohr, J. J., Murray, S. S., Padin, S., Pryke, C., Reichardt, C. L., Rest, A., Ruhl, J. E., Saliwanchik, B. R., Saro, A., Sayre, J. T., Schaffer, K. K., Shirokoff, E., Spieler, H. G., Stalder, B., Stanford, S. A., Staniszewski, Z., Stark, A. A., Story, K. T., Stubbs, C. W., Vanderlinde, K., Vieira, J. D., Williamson, R., Zahn, O., and Zenteno, A. (2014). The Redshift Evolution of the Mean Temperature, Pressure, and Entropy Profiles in 80 SPT-Selected Galaxy Clusters. *ApJ*, 794:67.
- McDonald, M., Benson, B. A., Vikhlinin, A., Stalder, B., Bleem, L. E., de Haan, T., Lin, H. W., Aird, K. A., Ashby, M. L. N., Bautz, M. W., Bayliss, M., Bocquet, S., Brodwin, M., Carlstrom, J. E., Chang, C. L., Cho, H. M., Clocchiatti, A., Crawford, T. M., Crites, A. T., Desai, S., Dobbs, M. A., Dudley, J. P., Foley, R. J., Forman, W. R., George, E. M., Gettings, D., Gladders, M. D., Gonzalez, A. H., Halverson, N. W., High, F. W., Holder, G. P., Holzzapfel, W. L., Hoover, S., Hrubes, J. D., Jones, C., Joy, M., Keisler, R., Knox, L., Lee, A. T., Leitch, E. M., Liu, J., Lueker, M., Luong-Van, D., Mantz, A., Marrone, D. P., McMahon, J. J., Mehl, J., Meyer, S. S., Miller, E. D., Mocanu, L., Mohr, J. J., Montroy, T. E., Murray, S. S., Nurgaliev, D., Padin, S., Plagge, T., Pryke, C., Reichardt, C. L., Rest, A., Ruel, J., Ruhl, J. E., Saliwanchik, B. R., Saro, A., Sayre, J. T., Schaffer, K. K., Shirokoff, E., Song, J., Šuhada, R., Spieler, H. G., Stanford, S. A., Staniszewski, Z.,

- Stark, A. A., Story, K., van Engelen, A., Vanderlinde, K., Vieira, J. D., Williamson, R., Zahn, O., and Zenteno, A. (2013). The Growth of Cool Cores and Evolution of Cooling Properties in a Sample of 83 Galaxy Clusters at $0.3 < z < 1.2$ Selected from the SPT-SZ Survey. *ApJ*, 774:23.
- Meneghetti, M., Rasia, E., Vega, J., Merten, J., Postman, M., Yepes, G., Sembolini, F., Donahue, M., Ettori, S., Umetsu, K., Balestra, I., Bartelmann, M., Benítez, N., Biviano, A., Bouwens, R., Bradley, L., Broadhurst, T., Coe, D., Czakon, N., De Petris, M., Ford, H., Giocoli, C., Gottlöber, S., Grillo, C., Infante, L., Jouvel, S., Kelson, D., Koekemoer, A., Lahav, O., Lemze, D., Medezinski, E., Melchior, P., Mercurio, A., Molino, A., Moscardini, L., Monna, A., Moustakas, J., Moustakas, L. A., Nonino, M., Rhodes, J., Rosati, P., Sayers, J., Seitz, S., Zheng, W., and Zitrin, A. (2014). The MUSIC of CLASH: Predictions on the Concentration-Mass Relation. *ApJ*, 797:34.
- Merloni, A., Predehl, P., Becker, W., Böhringer, H., Boller, T., Brunner, H., Brusa, M., Dennerl, K., Freyberg, M., Friedrich, P., Georgakakis, A., Haberl, F., Hasinger, G., Meidinger, N., Mohr, J., Nandra, K., Rau, A., Reiprich, T. H., Robrade, J., Salvato, M., Santangelo, A., Sasaki, M., Schwobe, A., Wilms, J., and German eROSITA Consortium, t. (2012). eROSITA Science Book: Mapping the Structure of the Energetic Universe. *ArXiv e-prints*.
- Mernier, F., de Plaa, J., Pinto, C., Kaastra, J. S., Kosec, P., Zhang, Y.-Y., Mao, J., and Werner, N. (2016a). Origin of central abundances in the hot intra-cluster medium. I. Individual and average abundance ratios from XMM-Newton EPIC. *A&A*, 592:A157.
- Mernier, F., de Plaa, J., Pinto, C., Kaastra, J. S., Kosec, P., Zhang, Y.-Y., Mao, J., Werner, N., Pols, O. R., and Vink, J. (2016b). Origin of central abundances in the hot intra-cluster medium. II. Chemical enrichment and supernova yield models. *A&A*, 595:A126.
- Milgrom, M. (1983). A modification of the Newtonian dynamics as a possible alternative to the hidden mass hypothesis. *ApJ*, 270:365–370.
- Milgrom, M. and Sanders, R. H. (2016). Perspective on MOND emergence from Verlinde’s “emergent gravity” and its recent test by weak lensing. *ArXiv e-prints*.
- Mitchell, R. J., Culhane, J. L., Davison, P. J. N., and Ives, J. C. (1976). Ariel 5 observations of the X-ray spectrum of the Perseus Cluster. *MNRAS*, 175:29P–34P.
- Molendi, S. and Pizzolato, F. (2001). Is the Gas in Cooling Flows Multiphase? *ApJ*, 560:194–200.
- Montes, M. and Trujillo, I. (2014). Intracluster Light at the Frontier: A2744. *ApJ*, 794:137.
- Morandi, A., Ettori, S., and Moscardini, L. (2007). X-ray and Sunyaev-Zel’dovich scaling relations in galaxy clusters. *MNRAS*, 379:518–534.
- Morandi, A., Sun, M., Forman, W., and Jones, C. (2015). The galaxy cluster outskirts probed by Chandra. *MNRAS*, 450:2261–2278.
- Moretti, A., Campana, S., Lazzati, D., and Tagliaferri, G. (2003). The Resolved Fraction of the Cosmic X-Ray Background. *ApJ*, 588:696–703.

- Mroczkowski, T., Dicker, S., Sayers, J., Reese, E. D., Mason, B., Czakon, N., Romero, C., Young, A., Devlin, M., Golwala, S., Korngut, P., Sarazin, C., Bock, J., Koch, P. M., Lin, K.-Y., Molnar, S. M., Pierpaoli, E., Umetsu, K., and Zemcov, M. (2012). A Multi-wavelength Study of the Sunyaev-Zel'dovich Effect in the Triple-merger Cluster MACS J0717.5+3745 with MUSTANG and Bolocam. *ApJ*, 761:47.
- Muñoz-Cuartas, J. C., Macciò, A. V., Gottlöber, S., and Dutton, A. A. (2011). The redshift evolution of Λ cold dark matter halo parameters: concentration, spin and shape. *MNRAS*, 411:584–594.
- Muldrew, S. I., Hatch, N. A., and Cooke, E. A. (2015). What are protoclusters? - Defining high-redshift galaxy clusters and protoclusters. *MNRAS*, 452:2528–2539.
- Nagai, D., Kravtsov, A. V., and Vikhlinin, A. (2007). Effects of Galaxy Formation on Thermodynamics of the Intracluster Medium. *ApJ*, 668:1–14.
- Nagai, D. and Lau, E. T. (2011). Gas Clumping in the Outskirts of Λ CDM Clusters. *ApJ*, 731:L10.
- Nandra, K., Barret, D., Barcons, X., Fabian, A., den Herder, J.-W., Piro, L., Watson, M., Adami, C., Aird, J., Afonso, J. M., and et al. (2013a). The Hot and Energetic Universe: A White Paper presenting the science theme motivating the Athena+ mission. *ArXiv e-prints*.
- Nandra, K., Barret, D., Barcons, X., Fabian, A., den Herder, J.-W., Piro, L., Watson, M., Adami, C., Aird, J., Afonso, J. M., and et al. (2013b). The Hot and Energetic Universe: A White Paper presenting the science theme motivating the Athena+ mission. *ArXiv e-prints*.
- Navarro, J. F., Frenk, C. S., and White, S. D. M. (1996). The Structure of Cold Dark Matter Halos. *ApJ*, 462:563.
- Navarro, J. F., Frenk, C. S., and White, S. D. M. (1997). A Universal Density Profile from Hierarchical Clustering. *ApJ*, 490:493–508.
- Nelson, K., Lau, E. T., and Nagai, D. (2014a). Hydrodynamic Simulation of Non-thermal Pressure Profiles of Galaxy Clusters. *ApJ*, 792:25.
- Nelson, K., Lau, E. T., Nagai, D., Rudd, D. H., and Yu, L. (2014b). Weighing Galaxy Clusters with Gas. II. On the Origin of Hydrostatic Mass Bias in Λ CDM Galaxy Clusters. *ApJ*, 782:107.
- Neto, A. F., Gao, L., Bett, P., Cole, S., Navarro, J. F., Frenk, C. S., White, S. D. M., Springel, V., and Jenkins, A. (2007). The statistics of Λ CDM halo concentrations. *MNRAS*, 381:1450–1462.
- Nevalainen, J., David, L., and Guainazzi, M. (2010). Cross-calibrating X-ray detectors with clusters of galaxies: an IACHEC study. *A&A*, 523:A22.
- Oegerle, W. R., Hill, J. M., and Fitchett, M. J. (1995). Observations of High Dispersion Clusters of Galaxies: Constraints on Cold Dark Matter. *AJ*, 110:32.
- Oguri, M. and Takada, M. (2011). Combining cluster observables and stacked weak lensing to probe dark energy: Self-calibration of systematic uncertainties. *Phys. Rev. D*, 83(2):023008.

- Ostriker, J. P., Bode, P., and Babul, A. (2005). A Simple and Accurate Model for Intracluster Gas. *ApJ*, 634:964–976.
- Ota, N., Nagai, D., and Lau, E. T. (2018). Constraining hydrostatic mass bias of galaxy clusters with high-resolution X-ray spectroscopy. *PASJ*, 70:51.
- Panagoulia, E. K., Fabian, A. C., and Sanders, J. S. (2014). A volume-limited sample of X-ray galaxy groups and clusters - I. Radial entropy and cooling time profiles. *MNRAS*, 438:2341–2354.
- Pfrommer, C., Springel, V., Jubelgas, M., and Ensslin, T. A. (2007). Cosmic Ray Feedback in Hydrodynamical Simulations of Galaxy and Galaxy Cluster Formation. In Metcalfe, N. and Shanks, T., editors, *Cosmic Frontiers*, volume 379 of *Astronomical Society of the Pacific Conference Series*, page 221.
- Pierre, M., Pacaud, F., Adami, C., Alis, S., Altieri, B., Baran, N., Benoist, C., Birkinshaw, M., Bongiorno, A., Bremer, M. N., Brusa, M., Butler, A., Ciliegi, P., Chiappetti, L., Clerc, N., Corasaniti, P. S., Coupon, J., De Breuck, C., Democles, J., Desai, S., Delhaize, J., Devriendt, J., Dubois, Y., Eckert, D., Elyiv, A., Ettori, S., Evrard, A., Faccioli, L., Farahi, A., Ferrari, C., Finet, F., Fotopoulou, S., Fourmanoit, N., Gandhi, P., Gastaldello, F., Gastaud, R., Georgantopoulos, I., Giles, P., Guennou, L., Guglielmo, V., Horellou, C., Husband, K., Huynh, M., Iovino, A., Kilbinger, M., Koulouridis, E., Lavoie, S., Le Brun, A. M. C., Le Fevre, J. P., Lidman, C., Lieu, M., Lin, C. A., Mantz, A., Maughan, B. J., Maurogordato, S., McCarthy, I. G., McGee, S., Melin, J. B., Melnyk, O., Menanteau, F., Novak, M., Paltani, S., Plionis, M., Poggianti, B. M., Pomarede, D., Pompei, E., Ponman, T. J., Ramos-Ceja, M. E., Ranalli, P., Rapetti, D., Raychaudury, S., Reiprich, T. H., Rottgering, H., Rozo, E., Rykoff, E., Sadibekova, T., Santos, J., Sauvageot, J. L., Schimd, C., Sereno, M., Smith, G. P., Smolčić, V., Snowden, S., Spergel, D., Stanford, S., Surdej, J., Valageas, P., Valotti, A., Valtchanov, I., Vignali, C., Willis, J., and Ziparo, F. (2016). The XXL Survey. I. Scientific motivations - XMM-Newton observing plan - Follow-up observations and simulation programme. *A&A*, 592:A1.
- Pillepich, A., Reiprich, T. H., Porciani, C., Borm, K., and Merloni, A. (2018). Forecasts on dark energy from the X-ray cluster survey with eROSITA: constraints from counts and clustering. *MNRAS*, 481:613–626.
- Plagge, T., Benson, B. A., Ade, P. A. R., Aird, K. A., Bleem, L. E., Carlstrom, J. E., Chang, C. L., Cho, H.-M., Crawford, T. M., Crites, A. T., de Haan, T., Dobbs, M. A., George, E. M., Hall, N. R., Halverson, N. W., Holder, G. P., Holzappel, W. L., Hrubes, J. D., Joy, M., Keisler, R., Knox, L., Lee, A. T., Leitch, E. M., Lueker, M., Marrone, D., McMahon, J. J., Mehl, J., Meyer, S. S., Mohr, J. J., Montroy, T. E., Padin, S., Pryke, C., Reichardt, C. L., Ruhl, J. E., Schaffer, K. K., Shaw, L., Shirokoff, E., Spieler, H. G., Stalder, B., Staniszewski, Z., Stark, A. A., Vanderlinde, K., Vieira, J. D., Williamson, R., and Zahn, O. (2010). Sunyaev-Zel'dovich Cluster Profiles Measured with the South Pole Telescope. *ApJ*, 716:1118–1135.
- Planck Collaboration, Adam, R., Ade, P. A. R., Aghanim, N., Akrami, Y., Alves, M. I. R., Argüeso, F., Arnaud, M., Arroja, F., Ashdown, M., and et al. (2016a). Planck 2015 results. I. Overview of products and scientific results. *A&A*, 594:A1.

- Planck Collaboration, Adam, R., Ade, P. A. R., Aghanim, N., Akrami, Y., Alves, M. I. R., Argüeso, F., Arnaud, M., Arroja, F., Ashdown, M., and et al. (2016b). Planck 2015 results. I. Overview of products and scientific results. *A&A*, 594:A1.
- Planck Collaboration, Adam, R., Ade, P. A. R., Aghanim, N., Arnaud, M., Ashdown, M., Aumont, J., Baccigalupi, C., Banday, A. J., Barreiro, R. B., and et al. (2016c). Planck 2015 results. VII. High Frequency Instrument data processing: Time-ordered information and beams. *A&A*, 594:A7.
- Planck Collaboration, Ade, P. A. R., Aghanim, N., Armitage-Caplan, C., Arnaud, M., Ashdown, M., Atrio-Barandela, F., Aumont, J., Aussel, H., Baccigalupi, C., and et al. (2014a). Planck 2013 results. XXIX. The Planck catalogue of Sunyaev-Zeldovich sources. *A&A*, 571:A29.
- Planck Collaboration, Ade, P. A. R., Aghanim, N., Armitage-Caplan, C., Arnaud, M., Ashdown, M., Atrio-Barandela, F., Aumont, J., Baccigalupi, C., Banday, A. J., and et al. (2014b). Planck 2013 results. XX. Cosmology from Sunyaev-Zeldovich cluster counts. *A&A*, 571:A20.
- Planck Collaboration, Ade, P. A. R., Aghanim, N., Arnaud, M., Ashdown, M., Atrio-Barandela, F., Aumont, J., Baccigalupi, C., Balbi, A., Banday, A. J., and et al. (2013). Planck intermediate results. V. Pressure profiles of galaxy clusters from the Sunyaev-Zeldovich effect. *A&A*, 550:A131.
- Planck Collaboration, Ade, P. A. R., Aghanim, N., Arnaud, M., Ashdown, M., Aumont, J., Baccigalupi, C., Balbi, A., Banday, A. J., Barreiro, R. B., and et al. (2011). Planck early results. VIII. The all-sky early Sunyaev-Zeldovich cluster sample. *A&A*, 536:A8.
- Planck Collaboration, Ade, P. A. R., Aghanim, N., Arnaud, M., Ashdown, M., Aumont, J., Baccigalupi, C., Banday, A. J., Barreiro, R. B., Barrena, R., and et al. (2016d). Planck 2015 results. XXVII. The second Planck catalogue of Sunyaev-Zeldovich sources. *A&A*, 594:A27.
- Planck Collaboration, Ade, P. A. R., Aghanim, N., Arnaud, M., Ashdown, M., Aumont, J., Baccigalupi, C., Banday, A. J., Barreiro, R. B., Bartlett, J. G., and et al. (2016e). Planck 2015 results. XIII. Cosmological parameters. *A&A*, 594:A13.
- Planck Collaboration, Ade, P. A. R., Aghanim, N., Arnaud, M., Ashdown, M., Aumont, J., Baccigalupi, C., Banday, A. J., Barreiro, R. B., Bartlett, J. G., and et al. (2016f). Planck 2015 results. XXIV. Cosmology from Sunyaev-Zeldovich cluster counts. *A&A*, 594:A24.
- Planck HFI Core Team, Ade, P. A. R., Aghanim, N., Ansari, R., Arnaud, M., Ashdown, M., Aumont, J., Banday, A. J., Bartelmann, M., Bartlett, J. G., Battaner, E., Benabed, K., Benoît, A., Bernard, J.-P., Bersanelli, M., Bhatia, R., Bock, J. J., Bond, J. R., Borrill, J., Bouchet, F. R., Boulanger, F., Bradshaw, T., Bréelle, E., Bucher, M., Camus, P., Cardoso, J.-F., Catalano, A., Challinor, A., Chamballu, A., Charra, J., Charra, M., Chary, R.-R., Chiang, C., Church, S., Clements, D. L., Colombi, S., Couchot, F., Coulais, A., Cressiot, C., Crill, B. P., Crook, M., de Bernardis, P., Delabrouille, J., Delouis, J.-M., Désert, F.-X., Dolag, K., Dole, H., Doré, O., Douspis, M., Efstathiou, G., Eng, P., Filliard, C., Forni, O., Fosalba, P., Fourmond, J.-J., Ganga, K., Giard, M., Girard, D., Giraud-Héraud, Y., Gispert, R., Górski, K. M., Gratton, S., Griffin, M., Guyot, G., Haissinski, J., Harrison, D., Helou,

- G., Henrot-Versillé, S., Hernández-Monteagudo, C., Hildebrandt, S. R., Hills, R., Hivon, E., Hobson, M., Holmes, W. A., Huppenberger, K. M., Jaffe, A. H., Jones, W. C., Kaplan, J., Kneissl, R., Knox, L., Lagache, G., Lamarre, J.-M., Lami, P., Lange, A. E., Lasenby, A., Lavabre, A., Lawrence, C. R., Leriche, B., Leroy, C., Longval, Y., Macías-Pérez, J. F., Maciaszek, T., MacTavish, C. J., Maffei, B., Mandolesi, N., Mann, R., Mansoux, B., Masi, S., Matsumura, T., McGehee, P., Melin, J.-B., Mercier, C., Miville-Deschênes, M.-A., Moneti, A., Montier, L., Mortlock, D., Murphy, A., Nati, F., Netterfield, C. B., Nørgaard-Nielsen, H. U., North, C., Noviello, F., Novikov, D., Osborne, S., Paine, C., Pajot, F., Patanchon, G., Peacocke, T., Pearson, T. J., Perdureau, O., Perotto, L., Piacentini, F., Piat, M., Plaszczynski, S., Pointecouteau, E., Pons, R., Ponthieu, N., Prézeau, G., Prunet, S., Puget, J.-L., Reach, W. T., Renault, C., Ristorcelli, I., Rocha, G., Rosset, C., Roudier, G., Rowan-Robinson, M., Rusholme, B., Santos, D., Savini, G., Schaefer, B. M., Shellard, P., Spencer, L., Starck, J.-L., Stassi, P., Stolyarov, V., Stompor, R., Sudiwala, R., Sunyaev, R., Sygnet, J.-F., Tauber, J. A., Thum, C., Torre, J.-P., Touze, F., Tristram, M., van Leeuwen, F., Vibert, L., Vibert, D., Wade, L. A., Wandelt, B. D., White, S. D. M., Wiesemeyer, H., Woodcraft, A., Yurchenko, V., Yvon, D., and Zacchei, A. (2011). Planck early results. IV. First assessment of the High Frequency Instrument in-flight performance. *A&A*, 536:A4.
- Planelles, S., Borgani, S., Dolag, K., Ettori, S., Fabjan, D., Murante, G., and Tornatore, L. (2013). Baryon census in hydrodynamical simulations of galaxy clusters. *MNRAS*, 431:1487–1502.
- Planelles, S., Fabjan, D., Borgani, S., Murante, G., Rasia, E., Biffi, V., Truong, N., Ragone-Figueroa, C., Granato, G. L., Dolag, K., Pierpaoli, E., Beck, A. M., Steinborn, L. K., and Gaspari, M. (2017). Pressure of the hot gas in simulations of galaxy clusters. *MNRAS*, 467:3827–3847.
- Pointecouteau, E. and Silk, J. (2005). New constraints on modified Newtonian dynamics from galaxy clusters. *MNRAS*, 364:654–658.
- Postman, M., Lubin, L. M., Gunn, J. E., Oke, J. B., Hoessel, J. G., Schneider, D. P., and Christensen, J. A. (1996). The Palomar Distant Clusters Survey. I. The Cluster Catalog. *AJ*, 111:615.
- Pratt, G. W., Arnaud, M., Piffaretti, R., Böhringer, H., Ponman, T. J., Croston, J. H., Voit, G. M., Borgani, S., and Bower, R. G. (2010). Gas entropy in a representative sample of nearby X-ray galaxy clusters (REXCESS): relationship to gas mass fraction. *A&A*, 511:A85.
- Pratt, G. W., Böhringer, H., Croston, J. H., Arnaud, M., Borgani, S., Finoguenov, A., and Temple, R. F. (2007). Temperature profiles of a representative sample of nearby X-ray galaxy clusters. *A&A*, 461:71–80.
- Pratt, G. W., Croston, J. H., Arnaud, M., and Böhringer, H. (2009). Galaxy cluster X-ray luminosity scaling relations from a representative local sample (REXCESS). *A&A*, 498:361–378.
- Predehl, P., Andritschke, R., Böhringer, H., Bornemann, W., Bräuninger, H., Brunner, H., Brusa, M., Burkert, W., Burwitz, V., Cappelluti, N., Churazov, E., Dennerl, K., Eder,

- J., Elbs, J., Freyberg, M., Friedrich, P., Fürmetz, M., Gaida, R., Hälker, O., Hartner, G., Hasinger, G., Hermann, S., Huber, H., Kendziorra, E., von Kienlin, A., Kink, W., Kreykenbohm, I., Lamer, G., Lapchov, I., Lehmann, K., Meidinger, N., Mican, B., Mohr, J., Mühlegger, M., Müller, S., Nandra, K., Pavlinsky, M., Pfeffermann, E., Reiprich, T., Robrade, J., Rohé, C., Santangelo, A., Schächner, G., Schanz, T., Schmid, C., Schmitt, J., Schreib, R., Schrey, F., Schwobe, A., Steinmetz, M., Strüder, L., Sunyaev, R., Tenzer, C., Tiedemann, L., Vongehr, M., and Wilms, J. (2010). eROSITA on SRG. In *Space Telescopes and Instrumentation 2010: Ultraviolet to Gamma Ray*, volume 7732 of *Proc. SPIE*, page 77320U.
- Rasia, E., Borgani, S., Ettori, S., Mazzotta, P., and Meneghetti, M. (2013). On the Discrepancy between Theoretical and X-Ray Concentration-Mass Relations for Galaxy Clusters. *ApJ*, 776:39.
- Rasia, E., Borgani, S., Murante, G., Planelles, S., Beck, A. M., Biffi, V., Ragone-Figueroa, C., Granato, G. L., Steinborn, L. K., and Dolag, K. (2015). Cool Core Clusters from Cosmological Simulations. *ApJ*, 813:L17.
- Rasia, E., Ettori, S., Moscardini, L., Mazzotta, P., Borgani, S., Dolag, K., Tormen, G., Cheng, L. M., and Diaferio, A. (2006). Systematics in the X-ray cluster mass estimators. *MNRAS*, 369:2013–2024.
- Rasia, E., Lau, E. T., Borgani, S., Nagai, D., Dolag, K., Avestruz, C., Granato, G. L., Mazzotta, P., Murante, G., Nelson, K., and Ragone-Figueroa, C. (2014). Temperature Structure of the Intracluster Medium from Smoothed-particle Hydrodynamics and Adaptive-mesh Refinement Simulations. *ApJ*, 791:96.
- Rasia, E., Meneghetti, M., Martino, R., Borgani, S., Bonafede, A., Dolag, K., Ettori, S., Fabjan, D., Giocoli, C., Mazzotta, P., Merten, J., Radovich, M., and Tornatore, L. (2012). Lensing and x-ray mass estimates of clusters (simulations). *New Journal of Physics*, 14(5):055018.
- Read, A. M., Rosen, S. R., Saxton, R. D., and Ramirez, J. (2011). A new comprehensive 2D model of the point spread functions of the XMM-Newton EPIC telescopes: spurious source suppression and improved positional accuracy. *A&A*, 534:A34.
- Reiprich, T. H. (2003). Cosmological Implications and Physical Properties of an X-Ray Flux-Limited Sample of Galaxy Clusters. *ArXiv Astrophysics e-prints*.
- Reiprich, T. H., Basu, K., Ettori, S., Israel, H., Lovisari, L., Molendi, S., Pointecouteau, E., and Roncarelli, M. (2013). Outskirts of Galaxy Clusters. *Space Sci. Rev.*
- Rettura, A. (2017). Mass-Richness relations for X-ray and SZE-selected clusters at $0.4 < z < 2.0$ as seen by Spitzer at 4.5 μ m. In *Exploring Dark Matter and Dark Ages with Lensing Clusters*, page 15.
- Rines, K. J., Geller, M. J., Diaferio, A., and Hwang, H. S. (2016). HeCS-SZ: The Hectospec Survey of Sunyaev-Zeldovich-selected Clusters. *ApJ*, 819:63.
- Roncarelli, M., Ettori, S., Borgani, S., Dolag, K., Fabjan, D., and Moscardini, L. (2013). Large-scale inhomogeneities of the intracluster medium: improving mass estimates using the observed azimuthal scatter. *MNRAS*, 432:3030–3046.

- Rosati, P., Borgani, S., and Norman, C. (2002). The Evolution of X-ray Clusters of Galaxies. *ARA&A*, 40:539–577.
- Rossetti, M., Gastaldello, F., Eckert, D., Della Torre, M., Pantiri, G., Cazzoletti, P., and Molendi, S. (2017). The cool-core state of Planck SZ-selected clusters versus X-ray-selected samples: evidence for cool-core bias. *MNRAS*, 468:1917–1930.
- Ruppin, F., Adam, R., Comis, B., Ade, P., André, P., Arnaud, M., Beelen, A., Benoît, A., Bideaud, A., Billot, N., Bourrion, O., Calvo, M., Catalano, A., Coiffard, G., D’Addabbo, A., De Petris, M., Désert, F.-X., Doyle, S., Goupy, J., Kramer, C., Leclercq, S., Macías-Pérez, J. F., Mauskopf, P., Mayet, F., Monfardini, A., Pajot, F., Pascale, E., Perotto, L., Pisano, G., Pointecouteau, E., Ponthieu, N., Pratt, G. W., Revéret, V., Ritacco, A., Rodriguez, L., Romero, C., Schuster, K., Sievers, A., Triqueneaux, S., Tucker, C., and Zylka, R. (2017). Non-parametric deprojection of NIKA SZ observations: Pressure distribution in the Planck-discovered cluster PSZ1 G045.85+57.71. *A&A*, 597:A110.
- Salucci, P. and Burkert, A. (2000). Dark Matter Scaling Relations. *ApJ*, 537:L9–L12.
- Salveti, D., Marelli, M., Gastaldello, F., Ghizzardi, S., Molendi, S., De Luca, A., Moretti, A., Rossetti, M., and Tiengo, A. (2017). A Systematic Analysis of the XMM-Newton Background: II. Properties of the in-Field-Of-View Excess Component. *ArXiv e-prints*.
- Sanderson, A. J. R., O’Sullivan, E., and Ponman, T. J. (2009). A statistically selected Chandra sample of 20 galaxy clusters - II. Gas properties and cool core/non-cool core bimodality. *MNRAS*, 395:764–776.
- Sanderson, A. J. R., Ponman, T. J., Finoguenov, A., Lloyd-Davies, E. J., and Markevitch, M. (2003). The Birmingham-CfA cluster scaling project - I. Gas fraction and the M-T_X relation. *MNRAS*, 340:989–1010.
- Sanderson, A. J. R., Ponman, T. J., and O’Sullivan, E. (2006). A statistically selected Chandra sample of 20 galaxy clusters - I. Temperature and cooling time profiles. *MNRAS*, 372:1496–1508.
- Santos, J. S., Rosati, P., Tozzi, P., Böhringer, H., Ettori, S., and Bignamini, A. (2008). Searching for cool core clusters at high redshift. *A&A*, 483:35–47.
- Santos, J. S., Tozzi, P., Rosati, P., and Böhringer, H. (2010). The evolution of cool-core clusters. *A&A*, 521:A64.
- Sayers, J., Mroczkowski, T., Zemcov, M., Korngut, P. M., Bock, J., Bulbul, E., Czakon, N. G., Egami, E., Golwala, S. R., Koch, P. M., Lin, K.-Y., Mantz, A., Molnar, S. M., Moustakas, L., Pierpaoli, E., Rawle, T. D., Reese, E. D., Rex, M., Shitanishi, J. A., Siegel, S., and Umetsu, K. (2013). A Measurement of the Kinetic Sunyaev-Zel’dovich Signal Toward MACS J0717.5+3745. *ApJ*, 778:52.
- Schellenberger, G., Reiprich, T. H., Lovisari, L., Nevalainen, J., and David, L. (2015). XMM-Newton and Chandra cross-calibration using HIFLUGCS galaxy clusters . Systematic temperature differences and cosmological impact. *A&A*, 575:A30.

- Sembolini, F., Yepes, G., Pearce, F. R., Knebe, A., Kay, S. T., Power, C., Cui, W., Beck, A. M., Borgani, S., Dalla Vecchia, C., Davé, R., Elahi, P. J., February, S., Huang, S., Hobbs, A., Katz, N., Lau, E., McCarthy, I. G., Murante, G., Nagai, D., Nelson, K., Newton, R. D. A., Perret, V., Puchwein, E., Read, J. I., Saro, A., Schaye, J., Teyssier, R., and Thacker, R. J. (2016). nIFTy galaxy cluster simulations - I. Dark matter and non-radiative models. *MNRAS*, 457:4063–4080.
- Sereno, M. (2016). A Bayesian approach to linear regression in astronomy. *MNRAS*, 455:2149–2162.
- Sereno, M., Covone, G., Izzo, L., Ettori, S., Coupon, J., and Lieu, M. (2017a). PSZ2LenS. Weak lensing analysis of the Planck clusters in the CFHTLenS and in the RCSLenS. *MNRAS*, 472:1946–1971.
- Sereno, M. and Ettori, S. (2015). Comparing masses in literature (CoMaLit) - I. Bias and scatter in weak lensing and X-ray mass estimates of clusters. *MNRAS*, 450:3633–3648.
- Sereno, M., Ettori, S., Meneghetti, M., Sayers, J., Umetsu, K., Merten, J., Chiu, I.-N., and Zitrin, A. (2017b). CLUMP-3D: three-dimensional lensing and multi-probe analysis of MACS J1206.2-0847, a remarkably regular cluster. *MNRAS*, 467:3801–3826.
- Sereno, M., Giocoli, C., Ettori, S., and Moscardini, L. (2015). The mass-concentration relation in lensing clusters: the role of statistical biases and selection effects. *MNRAS*, 449:2024–2039.
- Serlemitsos, P. J., Smith, B. W., Boldt, E. A., Holt, S. S., and Swank, J. H. (1977). X-radiation from clusters of galaxies - Spectral evidence for a hot evolved gas. *ApJ*, 211:L63–L66.
- Serra, A. L. and Diaferio, A. (2013). Identification of Members in the Central and Outer Regions of Galaxy Clusters. *ApJ*, 768:116.
- Shaw, L. D., Nagai, D., Bhattacharya, S., and Lau, E. T. (2010). Impact of Cluster Physics on the Sunyaev-Zel’dovich Power Spectrum. *ApJ*, 725:1452–1465.
- Shi, X. (2016). Locations of accretion shocks around galaxy clusters and the ICM properties: insights from self-similar spherical collapse with arbitrary mass accretion rates. *MNRAS*, 461:1804–1815.
- Shi, X., Komatsu, E., Nelson, K., and Nagai, D. (2015). Analytical model for non-thermal pressure in galaxy clusters - II. Comparison with cosmological hydrodynamics simulation. *MNRAS*, 448:1020–1029.
- Simionescu, A., Allen, S. W., Mantz, A., Werner, N., Takei, Y., Morris, R. G., Fabian, A. C., Sanders, J. S., Nulsen, P. E. J., George, M. R., and Taylor, G. B. (2011). Baryons at the Edge of the X-ray-Brightest Galaxy Cluster. *Science*, 331:1576.
- Simionescu, A., Werner, N., Mantz, A., Allen, S. W., and Urban, O. (2017). Witnessing the growth of the nearest galaxy cluster: thermodynamics of the Virgo Cluster outskirts. *MNRAS*, 469:1476–1495.

- Smith, A. G., Hopkins, A. M., Hunstead, R. W., and Pimbblet, K. A. (2012). Multiscale probability mapping: groups, clusters and an algorithmic search for filaments in SDSS. *MNRAS*, 422:25–43.
- Smith, G. P., Mazzotta, P., Okabe, N., Ziparo, F., Mulroy, S. L., Babul, A., Finoguenov, A., McCarthy, I. G., Lieu, M., Bahé, Y. M., Bourdin, H., Evrard, A. E., Futamase, T., Haines, C. P., Jauzac, M., Marrone, D. P., Martino, R., May, P. E., Taylor, J. E., and Umetsu, K. (2016). LoCuSS: Testing hydrostatic equilibrium in galaxy clusters. *MNRAS*, 456:L74–L78.
- Snowden, S. L., Mushotzky, R. F., Kuntz, K. D., and Davis, D. S. (2008). A catalog of galaxy clusters observed by XMM-Newton. *A&A*, 478:615–658.
- Sommer, M. W. and Basu, K. (2014). A comparative study of radio halo occurrence in SZ and X-ray selected galaxy cluster samples. *MNRAS*, 437:2163–2179.
- Springel, V., Di Matteo, T., and Hernquist, L. (2005). Modelling feedback from stars and black holes in galaxy mergers. *MNRAS*, 361:776–794.
- Stanford, S. A., Elston, R., Eisenhardt, P. R., Spinrad, H., Stern, D., and Dey, A. (1997). An IR-Selected Galaxy Cluster at $z=1.27$. *AJ*, 114:2232.
- Storm, E., Jeltama, T. E., and Rudnick, L. (2015). A radio and X-ray study of the merging cluster A2319. *MNRAS*, 448:2495–2503.
- Struble, M. F. and Rood, H. J. (1999). A Compilation of Redshifts and Velocity Dispersions for ACO Clusters. *ApJS*, 125:35–71.
- Sunyaev, R. A. and Zeldovich, Y. B. (1972). The Observations of Relic Radiation as a Test of the Nature of X-Ray Radiation from the Clusters of Galaxies. *Comments on Astrophysics and Space Physics*, 4:173.
- Tauber, J. A., Mandolesi, N., Puget, J.-L., Banos, T., Bersanelli, M., Bouchet, F. R., Butler, R. C., Charra, J., Crone, G., Dodsworth, J., and et al. (2010). Planck pre-launch status: The Planck mission. *A&A*, 520:A1.
- Tchernin, C., Eckert, D., Ettori, S., Pointecouteau, E., Paltani, S., Molendi, S., Hurier, G., Gastaldello, F., Lau, E. T., Nagai, D., Roncarelli, M., and Rossetti, M. (2016). The XMM Cluster Outskirts Project (X-COP): Physical conditions of Abell 2142 up to the virial radius. *A&A*, 595:A42.
- Tozzi, P. and Norman, C. (2001). The Evolution of X-Ray Clusters and the Entropy of the Intracluster Medium. *ApJ*, 546:63–84.
- Truong, N., Rasia, E., Mazzotta, P., Planelles, S., Biffi, V., Fabjan, D., Beck, A. M., Borgani, S., Dolag, K., Gaspari, M., Granato, G. L., Murante, G., Ragone-Figueroa, C., and Steinborn, L. K. (2018). Cosmological hydrodynamical simulations of galaxy clusters: X-ray scaling relations and their evolution. *MNRAS*, 474:4089–4111.
- Urban, O., Simionescu, A., Werner, N., Allen, S. W., Ehlert, S., Zhuravleva, I., Morris, R. G., Fabian, A. C., Mantz, A., Nulsen, P. E. J., Sanders, J. S., and Takei, Y. (2014). Azimuthally resolved X-ray spectroscopy to the edge of the Perseus Cluster. *MNRAS*, 437:3939–3961.

- Urban, O., Werner, N., Simionescu, A., Allen, S. W., and Böhringer, H. (2011). X-ray spectroscopy of the Virgo Cluster out to the virial radius. *MNRAS*, 414:2101–2111.
- van der Burg, R. F. J., Hoekstra, H., Muzzin, A., Sifón, C., Balogh, M. L., and McGee, S. L. (2015). Evidence for the inside-out growth of the stellar mass distribution in galaxy clusters since $z \sim 1$. *A&A*, 577:A19.
- Vazza, F., Angelinelli, M., Jones, T. W., Eckert, D., Brüggén, M., Brunetti, G., and Gheller, C. (2018). The turbulent pressure support in galaxy clusters revisited. *MNRAS*, 481:L120–L124.
- Vazza, F., Brüggén, M., Gheller, C., Hackstein, S., Wittor, D., and Hinz, P. M. (2017). Simulations of extragalactic magnetic fields and of their observables. *Classical and Quantum Gravity*, 34(23):234001.
- Vazza, F., Brunetti, G., Kritsuk, A., Wagner, R., Gheller, C., and Norman, M. (2009). Turbulent motions and shocks waves in galaxy clusters simulated with adaptive mesh refinement. *A&A*, 504:33–43.
- Vazza, F., Eckert, D., Simionescu, A., Brüggén, M., and Ettori, S. (2013). Properties of gas clumps and gas clumping factor in the intra-cluster medium. *MNRAS*, 429:799–814.
- Vazza, F., Roediger, E., and Brüggén, M. (2012). Turbulence in the ICM from mergers, cool-core sloshing, and jets: results from a new multi-scale filtering approach. *A&A*, 544:A103.
- Vazza, F., Roncarelli, M., Ettori, S., and Dolag, K. (2011). The scatter in the radial profiles of X-ray luminous galaxy clusters as diagnostic of the thermodynamical state of the ICM. *MNRAS*, 413:2305–2313.
- Verlinde, E. P. (2016). Emergent Gravity and the Dark Universe. *ArXiv e-prints*.
- Vikhlinin, A., Burenin, R., Forman, W. R., Jones, C., Hornstrup, A., Murray, S. S., and Quintana, H. (2007). Lack of Cooling Flow Clusters at $z > 0.5$. In Böhringer, H., Pratt, G. W., Finoguenov, A., and Schuecker, P., editors, *Heating versus Cooling in Galaxies and Clusters of Galaxies*, page 48.
- Vikhlinin, A., Forman, W., and Jones, C. (1999). Outer Regions of the Cluster Gaseous Atmospheres. *ApJ*, 525:47–57.
- Vikhlinin, A., Kravtsov, A., Forman, W., Jones, C., Markevitch, M., Murray, S. S., and Van Speybroeck, L. (2006). Chandra Sample of Nearby Relaxed Galaxy Clusters: Mass, Gas Fraction, and Mass-Temperature Relation. *ApJ*, 640:691–709.
- Vikhlinin, A., Kravtsov, A. V., Burenin, R. A., Ebeling, H., Forman, W. R., Hornstrup, A., Jones, C., Murray, S. S., Nagai, D., Quintana, H., and Voevodkin, A. (2009). Chandra Cluster Cosmology Project III: Cosmological Parameter Constraints. *ApJ*, 692:1060–1074.
- Voges, W., Aschenbach, B., Boller, T., Bräuninger, H., Briel, U., Burkert, W., Dennerl, K., Enghauser, J., Gruber, R., Haberl, F., Hartner, G., Hasinger, G., Kürster, M., Pfeffermann, E., Pietsch, W., Predehl, P., Rosso, C., Schmitt, J. H. M. M., Trümper, J., and Zimmermann, H. U. (1999). The ROSAT all-sky survey bright source catalogue. *A&A*, 349:389–405.

- Voit, G. M. (2005). Tracing cosmic evolution with clusters of galaxies. *Reviews of Modern Physics*, 77:207–258.
- Voit, G. M. and Bryan, G. L. (2001). On the Distribution of X-Ray Surface Brightness from Diffuse Gas. *ApJ*, 551:L139–L142.
- Voit, G. M., Kay, S. T., and Bryan, G. L. (2005). The baseline intracluster entropy profile from gravitational structure formation. *MNRAS*, 364:909–916.
- von der Linden, A., Mantz, A., Allen, S. W., Applegate, D. E., Kelly, P. L., Morris, R. G., Wright, A., Allen, M. T., Burchat, P. R., Burke, D. L., Donovan, D., and Ebeling, H. (2014). Robust weak-lensing mass calibration of Planck galaxy clusters. *MNRAS*, 443:1973–1978.
- Walker, S. A., Fabian, A. C., Sanders, J. S., and George, M. R. (2012a). Further X-ray observations of the galaxy cluster PKS 0745-191 to the virial radius and beyond. *MNRAS*, 424:1826–1840.
- Walker, S. A., Fabian, A. C., Sanders, J. S., and George, M. R. (2012b). Galaxy cluster outskirts: a universal entropy profile for relaxed clusters? *MNRAS*, 427:L45–L49.
- Walker, S. A., Fabian, A. C., Sanders, J. S., George, M. R., and Tawara, Y. (2012c). X-ray observations of the galaxy cluster Abell 2029 to the virial radius. *MNRAS*, 422:3503–3515.
- Willingale, R., Starling, R. L. C., Beardmore, A. P., Tanvir, N. R., and O’Brien, P. T. (2013). Calibration of X-ray absorption in our Galaxy. *MNRAS*, 431:394–404.
- Willson, M. A. G. (1970). Radio observations of the cluster of galaxies in Coma Berenices - the 5C4 survey. *MNRAS*, 151:1–44.
- Zappacosta, L., Buote, D. A., Gastaldello, F., Humphrey, P. J., Bullock, J., Brighenti, F., and Mathews, W. (2006). The Absence of Adiabatic Contraction of the Radial Dark Matter Profile in the Galaxy Cluster A2589. *ApJ*, 650:777–790.
- Zhang, Y.-Y., Reiprich, T. H., Schneider, P., Clerc, N., Merloni, A., Schwobe, A., Borm, K., Andernach, H., Caretta, C. A., and Wu, X.-P. (2017). HIFLUGCS: X-ray luminosity-dynamical mass relation and its implications for mass calibrations with the SPIDERS and 4MOST surveys. *A&A*, 599:A138.
- Zhuravleva, I., Churazov, E., Kravtsov, A., Lau, E. T., Nagai, D., and Sunyaev, R. (2013). Quantifying properties of ICM inhomogeneities. *MNRAS*, 428:3274–3287.
- Zibetti, S., White, S. D. M., Schneider, D. P., and Brinkmann, J. (2005a). Intergalactic stars in $z \sim 0.25$ galaxy clusters: systematic properties from stacking of Sloan Digital Sky Survey imaging data. *MNRAS*, 358:949–967.
- Zibetti, S., White, S. D. M., Schneider, D. P., and Brinkmann, J. (2005b). Intergalactic stars in $z \sim 0.25$ galaxy clusters: systematic properties from stacking of Sloan Digital Sky Survey imaging data. *MNRAS*, 358:949–967.
- Zu, Y. and Mandelbaum, R. (2015a). Mapping stellar content to dark matter haloes using galaxy clustering and galaxy-galaxy lensing in the SDSS DR7. *MNRAS*, 454:1161–1191.

- Zu, Y. and Mandelbaum, R. (2015b). Mapping stellar content to dark matter haloes using galaxy clustering and galaxy-galaxy lensing in the SDSS DR7. *MNRAS*, 454:1161–1191.
- ZuHone, J. A., Miller, E. D., Bulbul, E., and Zhuravleva, I. (2018). What Do the Hitomi Observations Tell Us About the Turbulent Velocities in the Perseus Cluster? Probing the Velocity Field with Mock Observations. *ApJ*, 853:180.
- Zwicky, F. (1933). Die Rotverschiebung von extragalaktischen Nebeln. *Helvetica Physica Acta*, 6:110–127.
- Zwicky, F. (1937). On the Masses of Nebulae and of Clusters of Nebulae. *ApJ*, 86:217.

LIST OF FIGURES

1.1	Evolution of the energy densities in <i>Planck</i> 2015 cosmology	5
1.2	Evolution of a dark matter density field around a cluster.	6
1.3	The anisotropies of the cosmic microwave background as observed by <i>Planck</i>	7
1.4	Multiwavelength observation of Abell 370	10
2.1	The relation between cluster mass and observable properties.	20
2.2	Cool core bias illustrated	21
2.3	Entropy profile from simulations and as observed by <i>Suzaku</i>	27
3.1	Artistic representation of <i>XMM-Newton</i> and <i>Planck</i>	35
3.2	Flow chart of the <i>XMM-Newton</i> pipeline in X-COP	36
3.4	Adaptively smoothed images of the X-COP clusters	45
4.1	Image in X-ray soft energy band of Abell 2319	55
4.2	Surface brightness profiles using the mean and median	55
4.3	Density, abundance, and temperature profiles for A2319	56
4.6	Comptonization map and correlation matrix for A2319	60
4.7	Comptonization map of Abell 2319	60
4.8	Clumpiness profiles for Abell 2319	62
4.9	Temperature profiles from X-ray data, SZ data, and from best fit	63
4.10	Systematic uncertainties on temperature and abundance	64
4.11	Rescaled pressure profile for A2319	66
4.12	Best fitting mass reconstruction in A2319	68
4.13	Rescaled entropy profiles in A2319	72
4.14	Residual image and definition of sectors in A2319	74
4.15	Thermodynamic properties in azimuthal sectors in A2319	77
4.16	Azimuthal scatter and residual clumpiness profiles	78
4.20	Non thermal pressure support in A2319	83
4.21	Effect of rescaling the thermodynamics using the true mass of A2319	87
5.3	Density profiles in the X-COP cluster sample	101
5.5	Pressure profiles in the X-COP cluster sample	104

5.7	Temperature profiles in the X-COP cluster sample	108
5.9	Entropy profiles in the X-COP cluster sample	112
5.11	Intrinsic scatter in the X-COP sample	116
5.13	Functional form fit dividing X-COP in CC and NCC clusters	119
6.1	X-COP data: density, pressure, and temperature	134
6.2	Bayesian evidence for 5 mass model and relative error on the masses	137
6.3	Mass-concentration relation in X-COP	139
6.4	Comparison between reference <i>backward</i> NFW and other mass estimate	144
6.5	Comparison of the mass reconstructed using EG and MOND	144
7.1	Gas mass fraction profiles in X-COP	152
7.2	Baryon depletion factor in the300 simulation	153
7.3	Stellar mass fraction in the literature	155
7.4	Gas mass fraction at R_{500} and R_{200}	159
7.5	Non-thermal pressure fraction in X-COP clusters	160
7.6	Gas fraction at R_{500} using different mass proxies and biases	162
8.1	Pressure against density in X-COP	171
8.2	Politropic index as function of radius	174
8.3	Functional form fit on pressure vs density	176
8.4	Comparisong of the fit in the outskirts	179
8.5	Posterior on the NFW politropic fit in the outskirts	180
8.6	NFW polytropic with $\Gamma(r)$	182
9.1	Redshift and mass distribution for this sample	187
9.2	Entropy profiles in redshift bins	188
9.3	Spatial extension of the measurements	190
9.4	The effect of rescaling on the entropy profiles	192
9.5	Distribution of best fitting parameters	193
9.6	Fit on entropy binned and rescaled	195
9.7	Entropy at fixed radii as function of mass	196
9.8	Fit on entropy binned and rescaled using gas mass fraction	196
9.9	Central entropy against innermost data point	199
9.10	Evolution of central entropy with redshift	201
9.11	Morphological parameters distribution	202
9.12	Pressure and rescaled pressure profiles	203
9.13	Evolution of polytropic index with redshift	206

LIST OF TABLES

3.1	Master table presenting the basic properties of the X-COP sample.	46
4.1	Information on A2319's observations	54
4.4	Best fitting parameters for pressure profile in A2319	65
4.5	Results for several mass reconstruction techniques in Abell 2319	67
4.6	Best fitting parameters for entropy profile in A2319	71
4.7	Mass of A2319 with or without merging region	85
4.8	Fit on non thermal pressure parameters	85
5.1	Basic properties of the X-COP sample.	94
5.2	Piecewise best fit on the thermodynamic quantities in X-COP	114
5.3	Functional form best fit on the thermodynamic quantities in X-COP	118
6.1	Best fit parameters for the various mass models	141
6.2	Measured masses in X-COP at reference radii	142
6.3	Systematic differences of mass models compared to reference	142
7.1	Baryon depletion factor in the300 simulation	154
7.2	Measured non-thermal pressure fraction in X-COP	158
8.1	Polytropic index in radial and density ranges	173
8.2	Best fitting parameters for NFW polytropic functional form	178
9.1	Fit results on rescaled entropy profiles	197
9.2	Fitting results on the rescaled pressure profiles	205
9.3	Measurements and parametrization of polytropic index	207

ACKNOWLEDGEMENTS

First and foremost, I would like to thank my beloved Veronica for this awesome life she is making me live in, for her support, and for her patience with all my extravagance.

I would like to thank my dear friend Giorgio for his long lasting friendship, his crazy infectious passions, like the one for baking bread with my very own sourdough starter Maui. I am also thankful toward my close friends Damiano, Francesco, and Daniela.

I am grateful to Stefano for his guidance during these 3 years of PhD, for his patience and brilliance in making me fell in love with galaxy clusters. I acknowledge also Dominique for his scientific support, and his knowledge, which lead to the ferment and rising of X-COP.

I am grateful to my family for the support they have granted me for all these years of studying, including that one from my dogs: from the crazy border collie Pascal to the once alive mutts Nerina and Giove. A special thanks goes to the peope of the “Pratello”, my ex flat mates Adriana, Katia, and Federica, with all the fat food we have prepared.

I want also to thank Giacomo, Riccardo, Alessia, and Alberto for being very good office colleagues, and all the other Bolognese PhD in astrophysics.

